Karlsruhe Institute of Technology

Tritium Sorption on the KATRIN Rear Wall: Effects, Dynamics and Mitigation

Zur Erlangung des akademischen Grades eines
Doktors der Naturwissenschaften (Dr. rer. nat)
von der KIT-Fakultät für Physik
des Karlsruher Instituts für Technologie (KIT)
angenommene
Dissertation
von
M. Sc.

Max Josef Aker

aus Malsch

Referent:	Prof. Dr. Guido Drexlin Institut für Experimentelle Teilchenphysik Karlsruhe Institut für Technologie
Korreferentin:	JProf. Dr. Loredana Gastaldo Kirchhoff-Institut für Physik Universität Heidelberg

Tag der mündlichen Prüfung: 13.12.2024

Declaration of Authorship

Herewith I affirm that I wrote the current thesis on my own and without the usage of any other sources or tools than the cited ones and that this thesis has not been handed neither in this nor in equal form at any other official commission.

Erklärung der Selbstständigkeit

Hiermit versichere ich, die vorliegende Arbeit selbstständig angefertigt zu haben und keine Hilfsmittel jenseits der kenntlich gemachten verwendet zu haben. Weiterhin habe ich weder diese noch eine äquivalente Version dieser Arbeit bei einer anderen Prüfungskommission vorgelegt.

Karlsruhe, den 4. November 2024

Max Aker

Abstract

Neutrino oscillations have confirmed that neutrinos possess a non-zero mass, a discovery that challenges the Standard Model (SM) of particle physics. While several theoretical frameworks attempt to explain neutrino mass generation, and oscillation experiments offer insights into the mass differences between neutrino states, their absolute mass and ordering remain unresolved. Experiments, using high-precision β-spectroscopy of the kinematic endpoint of the tritium decay, have sought to directly determine the neutrino mass. Currently, this effort is led by the Karlsruhe Tritium Neutrino (KATRIN) experiment, which has recently set a new upper limit on the effective neutrino mass at $m_\nu < 0.45\,\mathrm{eV/c^2}$, based on its first five measurement campaigns. By the end of its data-taking program in late 2025, KATRIN aims to achieve a sensitivity of better than $0.3\,\mathrm{eV/c^2}$.

To reach this goal, it is crucial to account for and mitigate various systematic effects that could otherwise increase the uncertainty in the neutrino mass measurement. One such source of systematic uncertainty stems from the so-called Rear Wall - a gold-coated stainless steel disk that defines the reference potential for the β-electrons in the experiment. The Rear Wall is exposed to electrons, tritium molecules, and tritium (cluster-)ions, leading to tritium accumulation on its surface due to adsorption. This adsorbed tritium generates a secondary β-spectrum, which differs in shape from the primary spectrum originating from the gaseous tritium source of KATRIN. The superposition of these two spectra distorts the measured β-spectrum, causing a systematic shift in the determined m_ν^2 value.

The main objective of this thesis is to mitigate the effects of this secondary β-spectrum. In this work, tritiated amorphous carbon (aC:T) was identified as the most likely contributor to the accumulation, with an Electron Beam Induced Deposition (EBID) mechanism proposed as the primary formation process. This was tested through multiple complementary dedicated measurements. Based on these insights, a two-part mitigation strategy was developed and implemented into the current operations and analysis framework of KATRIN.

The first approach is mitigation within the KATRIN analysis chain. By performing so-called Rear Wall scans when the tritium source is empty (at less than 10^{-5} of the nominal gas density), a complete characterization of the secondary spectrum was possible. Although each scan required several days of data collection, it was found that the shape of the spectrum remained constant, with only its amplitude changing due to ongoing tritium accumulation on the Rear Wall. This allowed the development of a measurement strategy combining Rear Wall scans during maintenance phases and shorter, more frequent Rear Wall rate measurements throughout the neutrino mass measurement campaigns. These Rear Wall rate measurements require only a few minutes of measurement time to accurately asses the amplitude of the secondary spectrum, as they focus on a single point deep in the β-spectrum, where the recorded rate is high. An empirical model based on the EBID accumulation process was developed to interpolate and extrapolate the evolution of the amplitude of the spectrum, based on the integral tritium throughput. By combining the Rear Wall scans and the Rear Wall rate model, accurate input parameters for the KATRIN

m_ν analysis were calculated, treating the secondary spectrum as a background signal, and reducing its impact below the uncertainty budget.

The second approach is the direct mitigation of the secondary spectrum by removing the accumulated tritium from the Rear Wall surface. Various decontamination techniques were tested, with UV/ozone cleaning proving to be the most effective, by being capable of reducing the surface activity by three orders of magnitude in less than a week.

In conclusion, a comprehensive strategy has been developed, combining direct Rear Wall cleaning and indirect analytical mitigation of the secondary β-spectrum. This approach ensures that the contribution of the secondary spectrum is accurately assessed in the m_ν analysis, supporting KATRIN to meet its predicted sensitivity for the effective neutrino mass.

Contents

List of Figures

List of Tables

1 Introduction

Neutrinos, with their intriguing properties, have continually reshaped our understanding of fundamental physics - from their very discovery to the present day. In the Standard Model (SM) of particle physics, neutrinos are considered massless [For21]. However, the observation of neutrino oscillations provided clear evidence that neutrinos have mass, as shown by landmark experiments [McD02; Fuk98a], thereby pointing to physics beyond the SM. While modifications to the SM can account for neutrino mass generation [Zyl20; Zub20], neither these theories nor neutrino oscillation data provide insight into the absolute neutrino mass, with oscillation measurements only constraining mass differences. This gap has motivated ongoing efforts to directly determine the absolute mass of neutrinos [Di 24].

One approach to measure the neutrino mass directly is through model-independent, high-precision β-spectroscopy of tritium decay [Fer34; Ott08]. Following earlier experiments [Wil91; Kra05; Ase11], the Karlsruhe Tritium Neutrino (KATRIN) experiment [Ake21a] is currently the most advanced in pursuing this method. In KATRIN, the β-electrons originate from the decay of T_2, which is circulated within a Windowless Gaseous Tritium Source (WGTS) capable of maintain a stable activity of up to 10^{11} Bq [Mar20]. These β-electrons are then adiabatically guided along magnetic field lines towards the main spectrometer (MS), which operates based on the Magnetic Adiabatic Collimation with an Electrostatic filter (MAC-E) principle [Bea80; Lob85; Pic92a], working as a high-pass filter to enable high-precision electron energy selection before detection by the Focal Plane Detector (FPD). This setup allows KATRIN to analyze the tritium β-spectrum with unprecedented accuracy, searching for the subtle imprint of m_ν near its kinematic endpoint which is the signature of the neutrino mass [Kle19]. It recently set the most stringent upper limit on the effective electron antineutrino mass [Ake24a]:

$$m_\nu < 0.45\,\mathrm{eV/c^2} \text{ at } 90\,\% \text{ CL}. \tag{1.1}$$

with a projected final sensitivity better than $0.3\,\mathrm{eV/c^2}$ at 90 % CL. To reach this level of precision, it is essential to minimize all sources of systematic uncertainties. One such source is related to the surface of the Rear Wall [Bab14; Sch16]. This gold-coated stainless steel disc forms the physical boundary of the tritium source opposite of the main spectrometer and plays a critical role in defining the starting potential of the β-electrons generated in the WGTS [Sch16; Mac21; Ake21a]. As the termination point of the tritium source, the Rear Wall is exposed to impinging electrons, tritium molecules, and tritium (cluster-)ions, raising concerns about potential tritium accumulation on its surface.

Initial estimates suggested that this effect would be negligible for KATRIN, given the low hydrogen adsorption properties of gold [Bab14]. However, the phenomenon of tritium buildup, commonly known as the "tritium memory effect," has been observed on gold surfaces in previous studies [Nis89; Mat85]. This prompted preparatory experiments using dedicated setups, which revealed significant tritium accumulation on gold-coated samples [Röl15]. Indeed, shortly after KATRIN began operating with tritium, tritium accumulation on the Rear Wall was detected, generating a secondary β-spectrum distinct from the primary spectrum produced by the tritium in the WGTS [Fri20].

Although initially minimal, this accumulation has grown with continued operation. As both spectra overlap, the result is a distortion of the measured β-spectrum that introduces a systematic effect on the m_ν^2 measurment.

Mitigating this effect and the uncertainties arising from it is the central aim of the work reported in this thesis. The approach is divided into several key tasks:

- Identification of the underlying processes to form the basis of a mitigation strategy,
- Quantitative characterization of the secondary spectrum, with a focus on its evolution, to enable indirect mitigation by integrating it into the KATRIN analysis chain and
- Development of a procedure to remove tritium from the Rear Wall, directly mitigating its effect.

This thesis is structured as follows: Chapter 2 gives the basics of neutrino physics and an overview of mass generation mechanisms. Chapter 3 introduces main the components of the KATRIN experiment and the relevant underlying principles. In Chapter 4, the impact of the secondary β-spectrum on KATRIN's m_ν analysis is examined, and the key characteristics of this spectrum, which must be quantified for analytical treatment, are identified. The fundamental processes of tritium adsorption and possible facilitating factors are discussed in Chapter 5, leading to the development of a working hypothesis regarding the underlying tritium accumulation process. This hypothesis provides predictions that are evaluated in the subsequent chapters. In Chapter 6 both the direct and indirect mitigation strategies are presented. First, it describes methods for characterizing the secondary spectrum and its temporal and spatial evolution. Second, it outlines the results of developed procedures to remove accumulated tritium from the Rear Wall. In Chapter 7, the dynamics of the secondary spectrum are analyzed. This includes the description of accumulated tritium over time and the evaluation of dedicated measurements to better understand the processes leading to tritium accumulation. Finally, Chapter 8 summarizes the results of this work, highlights open questions, offers an outlook on future research, and emphasizes the significance of the developed procedures for future sterile neutrino searches using tritium.

2 Neutrino Physics

The discovery of the neutrino was triggered by the interplay between J. Chadwick and W. Pauli, which subsequently laid the groundwork for E. Fermi's formulation of his successful theory of beta decay. To this day, the neutrino continues to captivate scientists, inspiring numerous research efforts aimed at unraveling its mysteries. In Section 2.1, the history of the neutrino discovery is briefly reviewed and the particle is situated within the broader context of our current understanding of particle physics. Section 2.2 delves into the intriguing discovery of neutrino oscillation and its implications, particularly concerning the neutrino mass. Finally, Section 2.3 outlines a method for determining the neutrino mass m_ν through tritium β-spectroscopy, a technique employed by the KATRIN experiment.

2.1 Standard Model and Neutrinos

The continuous energy spectrum of β-electrons, first reported by J. Chadwick in 1914 [Cha14], posed a challenge to the conservation of energy. If only two particles were involved in the decay, the energy distribution would be discrete. To resolve this, W. Pauli postulated in 1930 the existence of a new neutral, light particle to account for the continuous energy spectrum observed in β-decay [Pau64].

In 1932, J. Chadwick discovered the neutron [Cha32a; Cha32b], which paved the way for E. Fermi's theory of β-decay [Fer34], being the foundation of todays description of the process as:

$$n \rightarrow p + e^- + \bar{\nu}_e. \tag{2.1}$$

The newly proposed particle was named the "neutrino" to reflect its neutral charge and small mass, which was estimated to be much smaller than that of the electron.

The neutrino was experimentally detected for the first time in the 1950s by F. Reines and C. L. Cowan, using a nuclear reactor at Savannah River in South Carolina as strong anti-neutrino source [Cow56]. They utilized the neutrino capture reaction:

$$p + \bar{\nu}_e \rightarrow n + e^+, \tag{2.2}$$

and verified the process by detecting the correlated emission of two photons due to e^+e^- annihilation, accompanied by a third photon emitted after a delay due to the de-excitation of Cd following capture of the created neutron.

Just a few years later, in 1962, the AGS neutrino experiment discovered the muon neutrino [Dan62]. In this experiment, a proton accelerator produced pions, which decayed into

muons and their associated (anti-)muon neutrinos. Behind a steel target that stopped any incoming muons, a spark chamber detected only muon signatures. This confirmed the existence of the muon neutrino, as the observed muons had to result from interactions with neutrinos. The absence of electrons, alongside the creation of muons, could only be explained by the presence of a distinct type of neutrino.

The tau neutrino was discovered in 2000 by the DONUT collaboration [Kod01]. Using a proton accelerator, D_S mesons were created, which decayed into $\tau^{\pm}$ and their corresponding (anti-)tau neutrinos. These neutrinos passed through a shielding and entered a detector containing steel and photosensitive emulsion targets. Upon interaction of the neutrinos with nucleons, τ are created and tracked in this detector. The short lifetime of the τ led to a detectable "kink" in their trajectory, allowing them to be identified, which proved the existence of the tau neutrinos.

These three neutrino flavors are the only ones discovered so far, with further measurements consistently indicating the existence of just three light neutrino flavors. One such example is the investigation of the decay width of the Z boson, which can decay into neutrinos and thus gives insight into the number of neutrinos. The decay width can be expressed as [ALE06]

$$\Gamma_Z = \Gamma_{\text{had}} + 3\Gamma_{\ell\ell} + \Gamma_{\text{inv}}, \tag{2.3}$$

with the partial width of hadronic decays Γ_{had}, decays into charged leptons $\Gamma_{\ell\ell}$ and decays into particles invisible to most detectors, like the neutrinos Γ_{inv}. Assuming only neutrinos as the invisible Z decay products, the number of light neutrino species N_ν can be expressed as:

$$\Gamma_{\text{inv}} = N_\nu \Gamma_{\nu\bar{\nu}}, \tag{2.4}$$

and

$$R^0_{\text{inv}} = \frac{\Gamma_{\text{inv}}}{\Gamma_{\ell\ell}} = N_\nu \left(\frac{\Gamma_{\nu\bar{\nu}}}{\Gamma_{\ell\ell}} \right). \tag{2.5}$$

This ratio R^0_{inv} can be measured by examining the Z resonance using e^-e^+ colliders. The cross-section for the Z production depends on the partial widths in Equation (2.3). By calculating the ratio of partial widths for neutrinos and charged leptons, the number of light neutrino species is determined to be $N_\nu = 2.984 \pm 0.008$ [ALE06].

The existence of these three neutrino flavors is central to our modern understanding of the Standard Model (SM) of particle physics [Mün19]. Developed throughout the second half of the 20th century, the SM provides a quantum field theory framework for particle interactions. It classifies all known elementary particles into two main categories: fermions and bosons, as depicted in Figure 2.1, and explains the electromagnetic force, strong nuclear force and weak nuclear force. Apart from gravity, the SM thus incorporates three of the four fundamental forces.

Despite the success of the SM, not all properties of neutrinos can be explained within its framework. One such property is the helicity, which describes the relationship between the spin and momentum of a particle. Helicity can be left-handed or right-handed, and under a

parity transformation (which flips spatial coordinates), helicity should reverse. However, this doesn't happen with neutrinos, revealing an unexpected violation of parity.

Wu-Experiment: In 1957, C. S. Wu conducted a famous experiment using the β-decay of ${}^{60}_{27}\mathrm{Co}$ [Wu57]:

$$ {}^{60}_{27}\mathrm{Co} \rightarrow {}^{60}_{28}\mathrm{Ni}^{*} + \mathrm{e}^{-} + \bar{\nu}_{\mathrm{e}}, \tag{2.6} $$

where both the β-electron and the neutrino carry a spin $S = 1/2$. Wu aligned the spins of cobalt atoms using an external magnetic field and found that the electrons were preferentially emitted in the opposite direction of the spin of the cobalt nucleus. This demonstrated a maximal violation of parity for processes involving neutrinos, as the electrons exhibited a clear directional preference, which contradicts parity symmetry.

Goldhaber-Experiment: A year later, M. Goldhaber investigated the reaction [Gol58]:

$$ {}^{152\mathrm{m}}\mathrm{Eu} + \mathrm{e}^{-} \rightarrow {}^{152}\mathrm{Sm}^{*} + \nu_{\mathrm{e}}. \tag{2.7} $$

By analyzing the circular polarization of photons emitted during the de-excitation of the excited Sm^{*} nucleus. M. Goldhaber demonstrated that only left-handed neutrinos are produced. This further confirmed the violation of parity in weak interactions involving neutrinos.

While helicity depends on the observer's frame of reference (and can be flipped for massive particles by changing the velocity of the reference frame), chirality is an intrinsic quantum mechanical property that remains invariant under Lorentz transformations. In these experiments, neutrinos were found to exist only in one chirality (left-handed for neutrinos and right-handed for antineutrinos), which, according to the SM, implies that they should be massless.

According to the Higgs mechanism for mass generation [Hig64; Cha12; Aad12], massless neutrinos should not interact with the Higgs field, since such interactions require a change in chirality. The results from Wu and Goldhaber's experiments show that neutrinos, which have only one chirality, would not be able to interact with the Higgs field, further suggesting their masslessness in the SM context. However, the discovery of neutrino oscillations implies that neutrinos do, in fact, have mass, challenging this assumption within the SM.

2.2 Neutrino Oscillation and Mass

This section covers the discovery of neutrino oscillation in Section 2.2.1 and discusses its substantial implications, particularly in relation to neutrino mass as described in Section 2.2.2. This section concludes with an overview of various experimental approaches aimed at determining the neutrino mass in Section 2.2.3.

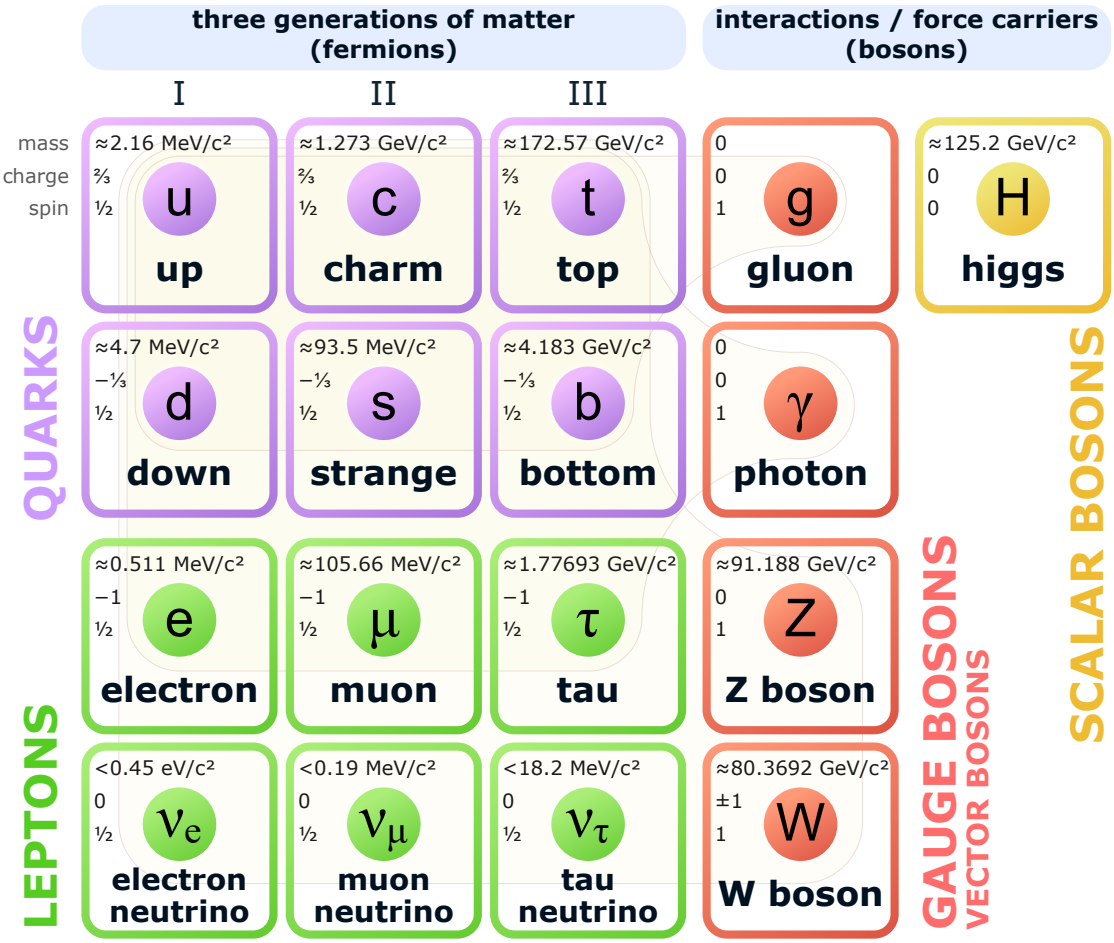

Figure 2.1: Particles of the Standard Model. This overview categorizes the particles according to their flavor, spin and interactions. The bosons that mediate those interactions are visually connected to the involved particles by a lightly colored outline. Information regarding the mass, charge and spin of the respective particles is provided. This data is sourced from [Nav24; Ake24a] and the image is obtained from [Com24] and is public domain.

2.2.1 Neutrino Oscillation

According to the SM leptons can be grouped in three generation-doublets as depicted in Figure 2.1,

$$\begin{pmatrix} \nu_e \\ e^- \end{pmatrix} \quad \begin{pmatrix} \nu_\mu \\ \mu^- \end{pmatrix} \quad \begin{pmatrix} \nu_\tau \\ \tau^- \end{pmatrix}. \tag{2.8}$$

This separation into neutrino families is particularly important for interpreting the results of the Homestake experiment by R. Davis et al. [Dav68], which aimed to measure the flux of solar neutrinos. Generated primarily as electron neutrinos in the core of the sun through

nuclear fusion that fuses hydrogen nuclei into helium, these neutrinos were detected via the reaction:

$$\bar{\nu}_e + {}^{37}\mathrm{Cl} \rightarrow {}^{37}\mathrm{Ar}^{+} + e^{-}, \tag{2.9}$$

The ^{37}Ar nucleus produced in this reaction decays with a half-life of 35 days into an excited ^{37}Cl atom, allowing for the detection of the Auger electrons emitted during its decay. This method enabled the quantification of the solar neutrino interactions. However, the experiment detected only about one-third of the expected neutrino flux predicted by the SM and solar models [Cle98; Bah82]. This discrepancy became known as the solar neutrino deficit.

The solution to this deficit came in the form of neutrino oscillations, which were experimentally confirmed by two key experiments:

Super-Kamiokande: The Super-Kamiokande experiment provided the first experimental proof of neutrino oscillation [Fuk98b]. It measured both solar and atmospheric neutrinos by detecting the Cherenkov radiation produced when neutrinos interacted with water. By analyzing the shape and intensity of the Cherenkov light, the type of neutrino interaction was identified, and the direction of the incoming neutrino could be reconstructed. The experiment observed a deficit in the atmospheric ν_μ flux passing through the Earth compared to those coming from the sky. This discrepancy was explained by the oscillation of ν_μ during their passage through the Earth into a different neutrino flavor, which was not detected.

Sudbury Neutrino Observatory (SNO): The SNO experiment further confirmed the existence of neutrino oscillation [Ahm01]. Similar to Super-Kamiokande, SNO detected Cherenkov radiation from neutrino interactions with heavy water, which enabled it to register both Cherenkov light and neutrons. This made it sensitive to all three neutrino flavors by exploiting different neutrino interactions - one interaction that was sensitive only to ν_e and others that were sensitive to all flavors. By combining these measurements, SNO was able to measure the total solar neutrino flux, confirming the predicted values and solving the solar neutrino deficit [Aha05]. Additionally, it proved the admixture of muon and tau neutrinos in the solar neutrino flux, providing direct evidence of ν_e oscillation.

These findings revealed that neutrinos are not always detected in the same flavor state in which they were produced. Instead, they undergo flavor-changing oscillations as they propagate through space. This discovery provided an explanation for why electron neutrinos (ν_e) emitted from the Sun could transform into muon or tau neutrinos (ν_μ or ν_τ) before being detected on Earth, thus solving the solar neutrino deficit. This breakthrough confirmed that the total number of neutrinos emitted by the Sun was consistent with theoretical predictions once these oscillations were taken into account.

These oscillations imply that neutrinos have mass, while the SM originally assumed neutrinos to be massless. The existence of neutrino mass is crucial for the theory of neutrino oscillations, which is discussed in Section 2.2.1.1. Following this Section 2.2.1.2 outlines the

conclusions regarding neutrino mass that can be inferred from the observation of neutrino oscillation parameters.

2.2.1.1 Flavor and Mass Eigenstates

In the framework of neutrino oscillations, the flavor states - which are the states associated with the electron, muon, and tau neutrinos - are not the same as the mass states, but rather they exist as a superposition of each other. The flavor eigenstates, $|\nu_\alpha\rangle$ (where $\alpha \in \mathrm{e}, \mu, \tau$), correspond to their electrically charged partner leptons, and these states define the interactions that neutrinos undergo. However, for neutrino propagation through space, the relevant states are the mass eigenstates, $|\nu_i\rangle$ (with $i \in 1, 2, 3$). The flavor states can be expressed as a superposition of the mass states, as follows:

$$|\nu_i\rangle = \sum_\alpha U_{\alpha i} |\nu_\alpha\rangle, \tag{2.10}$$

and in reverse:

$$|\nu_\alpha\rangle = \sum_i U^*_{\alpha i} |\nu_i\rangle. \tag{2.11}$$

where the elements $U_{\alpha i}$ form a unitary matrix known as the PMNS matrix:

$$U = \begin{pmatrix} U_{\mathrm{e}1} & U_{\mathrm{e}2} & U_{\mathrm{e}3} \\ U_{\mu 1} & U_{\mu 2} & U_{\mu 3} \\ U_{\tau 1} & U_{\tau 2} & U_{\tau 3} \end{pmatrix}, \tag{2.12}$$

named after Pontecorvo, Maki, Nakagawa, and Sakata, who first proposed the possibility of neutrino-antineutrino oscillations [Pon58] and flavor mixing [Mak62]. The PMNS matrix can be parameterized in terms of the mixing angles θ_{ij} and a CP-violating phase δ_{CP}:

$$U = \begin{pmatrix} 1 & 0 & 0 \\ 0 & \mathrm{c}_{23} & \mathrm{s}_{23} \\ 0 & -\mathrm{s}_{23} & \mathrm{c}_{23} \end{pmatrix} \begin{pmatrix} \mathrm{c}_{13} & 0 & \mathrm{s}_{13}\mathrm{e}^{-i\delta_{\mathrm{CP}}} \\ 0 & 1 & 0 \\ -\mathrm{s}_{13}\mathrm{e}^{-i\delta_{\mathrm{CP}}} & 0 & \mathrm{c}_{13} \end{pmatrix} \begin{pmatrix} \mathrm{c}_{12} & \mathrm{s}_{12} & 0 \\ -\mathrm{s}_{12} & \mathrm{c}_{12} & 0 \\ 0 & 0 & 1 \end{pmatrix}, \tag{2.13}$$

where $\mathrm{c}_{ij} = \cos(\theta_{ij})$ and $\mathrm{s}_{ij} = \sin(\theta_{ij})$ represent the cosine and sine of the respective mixing angles.

If neutrinos are Majorana particles, meaning they are their own antiparticles, the PMNS matrix requires further extension to include the Majorana phases α and β [Zub20]:

$$U_{\mathrm{Majorana}} = \begin{pmatrix} 1 & 0 & 0 \\ 0 & \mathrm{e}^{i\alpha} & 0 \\ 0 & 0 & \mathrm{e}^{i\beta} \end{pmatrix}. \tag{2.14}$$

To observe neutrino oscillations experimentally, like in Super-Kamiokande and SNO, the probabilities of flavor oscillations need to be derived by considering the evolution of the

mass eigenstates during propagation. The transition probability is obtained by solving the Schrödinger equation using a plane wave approach [Zub20], where also the mass differences are incorporated. The solution, simplified for ultra-relativistic neutrinos, which is the case relevant for most experiments, can be expressed as:

$$P_{\alpha\to\beta} = \left|\langle \nu_\beta | \nu_\alpha\,(t,x)\rangle\right|^2 = \sum_{i,j} U^*_{\alpha i} U_{\beta i} U_{\alpha j} U^*_{\beta i} \mathrm{e}^{-\frac{i}{\hbar}\cdot\frac{\Delta m^2_{ij} c^3 L}{2E}}, \tag{2.15}$$

where $\Delta m^2_{ij} = m^2_i - m^2_j$ represents the difference in squared masses of the neutrino mass eigenstates.

Given that the oscillation scales of solar and atmospheric neutrinos differ by more than an order of magnitude [Nav24], it is often useful to simplify the discussion by considering only two mass and flavor eigenstates.

For example, the oscillation probability for ν_e to oscillate into ν_μ, considering a single mixing angle θ and assuming no CP violation, is given by:

$$P_{\nu_e\to\nu_\mu} = \sin^2(2\theta)\cdot\sin^2\left(\frac{\Delta m^2_{12}}{4}\cdot\frac{L}{E}\right), \tag{2.16}$$

where the probability depends on the squared mass difference Δm^2_{12}, the distance traveled L, and the neutrino energy E. The characteristic oscillation length L_0 can be determined from the second term of Equation (2.16):

$$L_0 = 4\pi\hbar c\frac{E}{\Delta m^2} = 2.48\frac{E/\mathrm{MeV}}{\Delta m^2/\mathrm{eV}^2}\mathrm{m}. \tag{2.17}$$

Numerous neutrino oscillation experiments have been conducted to probe neutrino properties, with the results listed in Table 2.1. However, these experiments are sensitive to the difference of squared masses (Δm^2), not the absolute neutrino mass. Consequently, while they reveal much about oscillations, they do not directly determine the mass scale of neutrinos.

2.2.1.2 Mass Hierarchy

Because neutrino oscillation experiments provide information only in the form of differences in squared masses, the absolute ordering of the neutrino masses remains uncertain. This opens the possibility for different mass hierarchies. However, observations of the MSW (Mikheyev-Smirnov-Wolfenstein) resonance in solar neutrino data [Wol78; Mik86] have established that $m_1 < m_2$, fixing the order of the first two mass states [Zub20]. Using this information, the data can be arranged into two possible scenarios:

- Normal Ordering (NO): $m_1 < m_2 < m_3$, or
- Inverted Ordering (IO): $m_3 < m_1 < m_2$.

Table 2.1: Overview of parameters obtained from oscillation experiments. Listed are the best-fit values derived from a comprehensive analysis of globally available data from various oscillation experiments. The data is sourced from [Nav24; Est24].

Oscillation Parameter	Normal Ordering	Inverted Ordering
$\sin^2\theta_{12}$	0.307 ± 0.013	$0.308^{+0.012}_{-0.011}$
$\sin^2\theta_{23}$	$0.558^{+0.015}_{-0.021}$	$0.553^{+0.016}_{-0.024}$
$\sin^2\theta_{13}$	$(2.19 \pm 0.07) \cdot 10^{-2}$	$0.223\ 10^{+0.000\ 56}_{-0.000\ 56}$
δ_{CP} in πrad	1.19 ± 0.22	$1.52^{+0.12}_{-0.14}$
Δm^2_{21} in $(\mathrm{eV/c^2})^2$	$(7.53 \pm 0.18) \cdot 10^{-5}$	$(7.53 \pm 0.18) \cdot 10^{-5}$
Δm^2_{32} in $(\mathrm{eV/c^2})^2$	$(2.455 \pm 0.028) \cdot 10^{-3}$	$(-2.529 \pm 0.029) \cdot 10^{-3}$

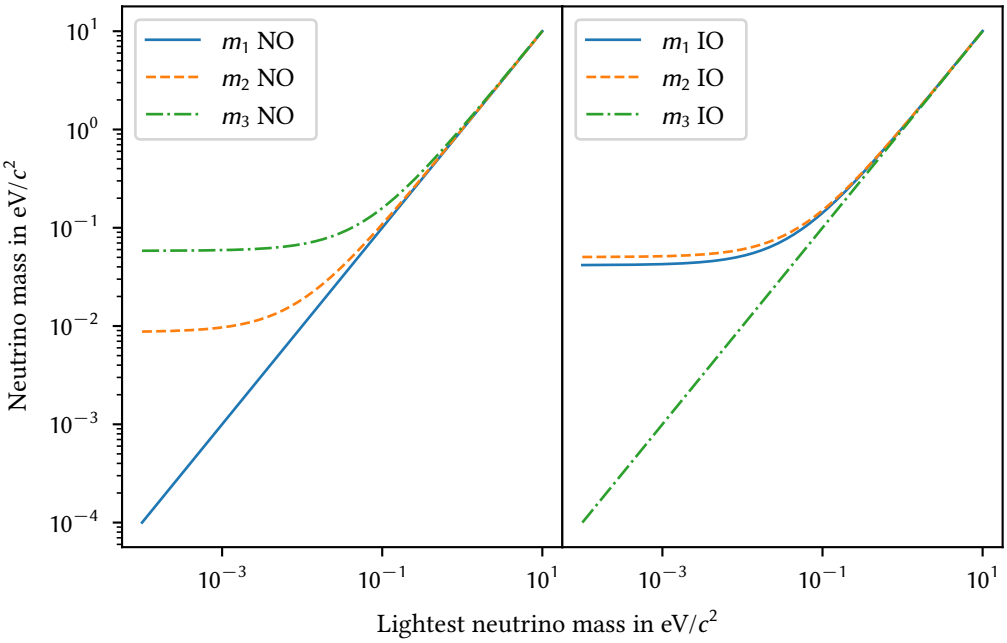

Figure 2.2: Comparison of normal and inverted mass ordering. The values of each of the three neutrino mass eigenstates are depicted as a function of the mass of the lightest neutrino. The mass values are calculated based on the data displayed in Table 2.1.

The differences in squared masses listed in Table 2.1 allow both mass hierarchy scenarios to be visualized as functions of the smallest neutrino mass. This relationship is illustrated in Figure 2.2.

In addition to the ordering of masses, a distinction can be made regarding the absolute scale of the neutrino masses. When the smallest neutrino mass (m_1 for NO or m_3 for IO) is much larger than the mass splittings - i.e., $m_1^2 \gg |\Delta m^2_{31}|$ for NO and $m_3^2 \gg |\Delta m^2_{32}|$ for IO - the neutrino masses are referred to as degenerate, meaning the masses of all three neutrino states would be approximately equal. One important constraint on the absolute

mass of neutrinos can be derived from the largest mass splitting. This provides a lower limit on the mass of the heaviest neutrino eigenstate [Est19; Est24]. For NO:

$$m_3 > \sqrt{|\Delta m^2_{31}|} = 0.05\,\text{meV/c}^2, \tag{2.18}$$

and

$$m_2 > \sqrt{|\Delta m^2_{32}|} = 0.05\,\text{meV/c}^2 \tag{2.19}$$

for IO.

2.2.2 Neutrino Mass Generation

The previous sections provided a summary of the initial indication that neutrinos possess mass, a fact that is incompatible with the SM in its current form. To address this, it is helpful to first understand how fermions in the SM acquire mass, which is discussed in Section 2.2.2.1, followed by two examples of how the neutrino mass problem can be resolved with minimal extensions to the SM, as covered in Section 2.2.2.2. The primary source for this discussion is [Zyl20], unless otherwise noted.

2.2.2.1 Fermionic Masses in the SM - the Yukawa Coupling

In the SM, fermions acquire mass through the Yukawa coupling to the Higgs field ϕ, via spontaneous symmetry breaking. For the lightest charged lepton (the electron), this coupling can be expressed as:

$$-\mathcal{L}_{\text{Yukawa}} = \lambda_e \bar{L}_e \phi e_R + \text{h.c.} \tag{2.20}$$

where $L_e = (\nu_{e,L}, e_L)$ is the left-handed lepton doublet, which contains both the left-handed electron neutrino and the left-handed electron, and e_R is the right-handed electron. The free coupling constant, λ_e, governs the interaction strength.

Once the Higgs field acquires a vacuum expectation value, v, due to electroweak symmetry breaking, the Yukawa coupling becomes:

$$-\mathcal{L}_{\text{Yukawa}} = \lambda_e \frac{v}{\sqrt{2}} \left[\bar{e}_R e_L + \bar{e}_L e_R\right] \tag{2.21}$$

where the vacuum expectation value is $v \approx 246\,\text{GeV}$ [Nav24]. As expressed in Equation (2.21), the Yukawa interaction term only applies to fermions that have both left- and right-handed components. However, since the SM lacks right-handed neutrinos, no Yukawa term can be constructed for neutrinos, leaving them massless in the SM framework.

2.2.2.2 Sterile Neutrinos

The issue of neutrino mass generation in the SM could be resolved by introducing additional neutrino states beyond the SM. A particularly simple extension involves introducing right-handed neutrinos, which do not interact via the weak force, leaving only gravitational interactions. These hypothetical particles are referred to as "sterile" neutrinos. With the addition of right-handed neutrinos, a Dirac mass term analogous to the mass generation mechanism for charged leptons (as shown in Equation (2.21)) can be introduced:

$$\mathcal{L}_{\mathcal{D}} = -m_D \bar{\nu}_L \nu_R + \text{h.c.} \tag{2.22}$$

For this model to account for the smallness of the observed neutrino masses, the coupling constant λ_ν must be extremely small, on the order of $\lambda_\nu \sim 10^{-11}$ [Zyl20].

Alternatively, a combination of Dirac and Majorana mass terms can be considered [Zub20]. While Majorana mass terms blur the distinction between neutrinos and antineutrinos, the distinction between left- and right-handed neutrinos is retained. The addition of Majorana mass terms results in two heavy, sterile neutrinos ($N_{L,R}$) with distinct masses m_L and m_R. This is described by the following Lagrangian:

$$\mathcal{L} = \frac{1}{2} \begin{pmatrix} \bar{\nu}_L & \bar{N}_L^C \end{pmatrix} \begin{pmatrix} m_L & m_D \\ m_D & m_R \end{pmatrix} \begin{pmatrix} \nu_R^C \\ N_R \end{pmatrix} + \text{h.c.}, \tag{2.23}$$

where C denotes the charge conjugation operator, transforming the neutrinos into their corresponding antiparticles.

The mass eigenvalues are derived by diagonalizing the mass matrix, leading to two real mass eigenvalues:

$$\tilde{m}_{1,2} = \frac{1}{2} \left((m_L + m_R) \pm \sqrt{(m_L - m_R)^2 + 4m_D^2} \right) \tag{2.24}$$

Three distinct cases can be identified from this expression [Zub20; Zyl20; Pov15]:

1. **Pure Dirac Case**: If $m_L = m_R = 0$, then $\tilde{m}_{1,2} = m_D$. In this case, the neutrino is a Dirac particle, which can be thought of as a pair of degenerate Majorana neutrinos.
2. **Pure Majorana Case**: If $m_D = 0$, the mass eigenvalues are simply $\tilde{m}_{1,2} = m_{L,R}$. In this case, the neutrinos have a purely Majorana nature.
3. **Seesaw Mechanism**: If $m_R \gg m_D$ and $m_L = 0$, the two mass eigenvalues become $m_1 = \frac{m_D^2}{m_R}$ and $m_2 \approx m_R$. Here, m_1 corresponds to the mass of the active neutrino (which participates in weak interactions), while m_2 represents the much heavier sterile neutrino. In this scenario, the active neutrino mass is suppressed by the mass of the sterile neutrino, explaining the small neutrino masses observed in experiments.

2.2.3 Experimental Determination of the Neutrino Mass

Since none of the mechanisms presented in the previous section inherently predict the neutrino mass, several experiments are currently underway, aiming to determine it. These experiments follow various approaches, such as using cosmological observations (discussed in Section 2.2.3.1), investigating neutrinoless double β-decay (outlined in Section 2.2.3.2), or employing direct kinematic β-decay measurements (as shown in Section 2.2.3.3).

2.2.3.1 Cosmological Observations

Neutrinos are extremely abundant in the universe, with a density of $336\,\mathrm{cm}^{-3}$ remaining today from the big bang [Bil10]. Although their individual masses are tiny, their sheer number allows them to have a significant impact on the evolution of large-scale structures in the universe. Since neutrinos interact rarely and have a low mass, they are capable of escaping dense matter clumps and carrying away energy. This behavior, which can influence structure formation, is described by the free streaming length, a parameter that depends, among other things, on the sum of the light neutrino mass eigenvalues and described how far neutrinos can travel without significant interactions or clustering due to gravity [Bil10].

Cosmological observations are sensitive to the sum of the neutrino masses rather than individual mass eigenstates. Their mass impacts several observable phenomena, which have been measured using various astrophysical surveys and satellites. Key examples include [Nav24]:

- **Matter Power Spectrum**: The power spectrum quantifies density fluctuations in the universe, and the mass of neutrinos contributes to the suppression of small-scale structures. Relevant features include:
  1. **Baryon Acoustic Oscillations (BAO)**: BAO measures density fluctuations that occurred in the early universe, creating a characteristic scale found in the spatial distribution of galaxies. The BAO scale, investigated by the Baryon Oscillation Spectroscopic Survey (BOSS), is sensitive to changes in the expansion rate and growth of structure, which both provide a sensitive probe of neutrino masses [Ala21; Bri22].
  2. **Weak Gravitational Lensing**: The weak lensing of background light by large-scale structure, as investigated by the Dark Energy Survey (DES), offers another avenue to constrain neutrino mass [Abb18; Abb22].
- **Temperature Anisotropies in the Cosmic Microwave Background (CMB)**: Neutrinos leave their mark on the CMB through the late Integrated Sachs-Wolfe effect [Sac67], which impacts the large-scale temperature fluctuations. This effect is measured by satellite missions like Planck [Agh20] or earth-bound installations like the Atacama Cosmology Telescope [Mad24].

- **Supernova Redshift Surveys**: Surveys such as Pan-STARRS1 [Ton12], the Sloan Digital Sky Survey (SDSS) [Yor00], and the Hubble Space Telescope [BAH86] investigate the redshift of distant supernovae to determine the expansion history of the universe, which also helps constrain the sum of neutrino masses [Sco18].

The impact of neutrino mass on these cosmological observables has allowed experiments to place constraints on the sum of the neutrino masses. Current results, as reported in [Nav24], give:

$$\sum m_\nu < \text{ (0.082 to 0.54) eV/c}^2 \text{ at 95 \% CL.} \tag{2.25}$$

The precise value depends on the specific combination of datasets and assumptions used. In fact, the Particle Data Group (PDG) lists up to 12 different values of the neutrino mass sum, reflecting the inherent model dependence of these constraints [Nav24].

Understanding the ramifications of the underlying models used to derive cosmological constraints on neutrino mass is critical, especially in light of ongoing debates such as the Hubble tension [Di 21]. The underlying reason for the discrepancy between local and early-universe measurements of the Hubble constant could directly affect how neutrino mass is inferred from cosmological data [Nav24].

2.2.3.2 Neutrino-Less Double β-Decay

A more exotic method to explore the neutrino mass is by investigating neutrinoless double beta decay ($0\nu\beta\beta$).

In standard double beta decay, which is a second-order weak process, two neutrons in a nucleus decay simultaneously into two protons, two electrons, and two electron-antineutrinos:

$$(A, Z) \rightarrow (A, Z+2) + \mathrm{e}^- + \mathrm{e}^- + \bar{\nu}_\mathrm{e} + \bar{\nu}_\mathrm{e} \tag{2.26}$$

However, in the case of a Majorana neutrino, which is its own antiparticle, the process could occur without emitting neutrinos [Fur39]. This is because, as a Majorana particle, the neutrino would not violate lepton number conservation, when annihilating with another neutrino. In such a case, the following decay could take place:

$$(A, Z) \rightarrow (A, Z+2) + \mathrm{e}^- + \mathrm{e}^- \tag{2.27}$$

In this process, a virtual neutrino emitted by one neutron is immediately absorbed as an antineutrino at another neutron, resulting in the emission of only two electrons. Without any neutrinos to carry away energy, the decay would produce a mono-energetic spectrum in the electron emissions, if the nuclear recoil is neglected.

To date, no $0\nu\beta\beta$ event has been observed. However, the absence of such an observation, along with the amount of target material used in experiments, allows to place upper limits

Table 2.2: 0νββ experiments and their respective results. None of the experiments reported a detected event, leading to the listed upper limits for $m_{\beta\beta}$, which are derived from the total observation time and the total isotope mass.

Experiment	Isotope	Upper limit for $m_{\beta\beta}$	Reference
GERDA[1)]	^{76}Ge	(79 to 180) meV/c^2 at 95 % CL	[Ago20]
CUORE[2)]	^{128}Te	(90 to 305) meV/c^2 at 90 % CL	[Ada22]
KamLAND-Zen[3)]	^{136}Xe	(35 to 156) meV/c^2 at 95 % CL	[Abe23]
AMoRE[4)]	^{100}Mo	(210 to 610) meV/c^2 at 95 % CL	[Agr24]

[1)] GERmanium Detector Array
[2)] Cryogenic Underground Observatory for Rare Events
[3)] Kamioka Liquid Scintillator ANtineutrino Detector-Zen
[4)] Advanced Mo-based Rare process Experiment

on the decay rate. The half-life of this process is directly related to the Majorana neutrino mass:

$$\left(T_{1/2}^{0\nu}\right)^{-1} \propto |m_{\beta\beta}|^2 \tag{2.28}$$

This relation enables the derivation of limits on the effective Majorana mass. Four experiments recently provided upper limits of their search for $0\nu\beta\beta$ events of different isotopes, as listed in Table 2.2.

While this method of determining the neutrino mass in a laboratory is less reliant on theoretical models compared to approaches using cosmological observations, it is fully contingent on the assumption that neutrinos are Majorana particles.

2.2.3.3 Neutrino Mass Determination Using the β-Decay Kinematic

Another largely model-independent method to determine the neutrino mass in a laboratory, without the reliance on the Majorana nature of neutrinos required for $0\nu\beta\beta$-decay, is through high-precision measurements of weak decays like β-decay or electron capture.

The β-decay is a process where a nucleus transitions by emitting an electron (or positron) and a corresponding neutrino (or antineutrino), with the reaction written as:

$$(A, Z) \rightarrow (A, Z+1) + \mathrm{e}^- + \bar{\nu}_\mathrm{e}, \tag{2.29}$$

$$(A, Z) \rightarrow (A, Z-1) + \mathrm{e}^+ + \nu_\mathrm{e}, \tag{2.30}$$

and the electron capture as:

$$(A, Z) + \mathrm{e}^- \rightarrow (A, Z-1) + \nu_\mathrm{e}. \tag{2.31}$$

In the case of β-decay, the Q-value is defined as the energy difference between the parent and daughter nuclei:

$$Q = (m(A, Z) - m(A, Z+1))\, c^2 \tag{2.32}$$

For a massless neutrino and no excitation of the daughter nucleus, the so-called endpoint energy E_0 can be expressed as

$$E_0 = Q - E_{\text{rec}} \tag{2.33}$$

where E_{rec} is the recoil energy of the nucleus. If the neutrino has a non-zero mass, the shape of the β-spectrum near the endpoint E_0 will be affected, resulting in a shift that provides information about the neutrino mass.

This approach is currently pursued by several experiments, utilizing either (molecular) tritium ($^3H_2$ ot T_2) [Ake21a], which has an endpoint energy of 18.6 keV [Med23], or ^{163}Ho via electron capture (Equation (2.31)) [Gas14; Vel19; Bor23], which has a Q-value of (2863.2 ± 0.6) eV [Sch24b]. The next section will provide a detailed description how to determine the neutrino mass using tritium β-spectroscopy.

2.3 Direct Kinematic m_ν Determination using Tritium β-Spectroscopy

Prominent examples of direct kinematic neutrino mass determination, as discussed in Section 2.2.3.3, include the Mainz [Kra05], Troitsk [Ase11], and Los Alamos [Wil91] experiments. The efforts of the Mainz and Troitsk experiments culminated in an upper limit of $m_\nu = 2$ eV [Ott08], and are further supplemented by the ongoing KATRIN experiment, which will be described in detail in Chapter 3.

All of these experiments utilized the tritium β-decay:

$$T \rightarrow {}^3He^+ + e^- + \bar{\nu}_e. \tag{2.34}$$

While the rationale for choosing tritium is discussed in Section 3.1, this section focuses on outlining the necessary theoretical framework to extract the neutrino mass from the tritium β-spectrum.

This reaction provides a pathway for direct, kinematic, and largely model-independent determination of the neutrino mass. It does not depend on fundamental assumptions such as the Majorana nature of neutrinos but instead relies solely on the well-understood β-decay model [For21].

Fermi's golden rule allows calculation of the energy distribution Γ for the β-electron emitted by the decaying tritium nucleus of a T_2 molecule [Fer34; Ott08]. Assuming natural

units $\hbar = c = 1$, it can be expressed as:

$$\frac{d\Gamma}{dE} = \frac{G_{\mathrm{F}}^2 \cos^2(\theta_{\mathrm{C}})}{2\pi^3} |M_{\mathrm{nuc}}|^2 F(Z,E)(E+m_{\mathrm{e}}) \cdot \sqrt{(E+m_{\mathrm{e}})^2 - m_{\mathrm{e}}^2} \cdot \sum_i \zeta_i \epsilon_i \sqrt{\epsilon_i^2 - m_{\nu}^2} \Theta(\epsilon_i - m_{\nu}) \,. \tag{2.35}$$

In this expression:

G_{F}	: Fermi coupling constant
θ_{C}	: Cabibbo angle
$\lvert M_{\mathrm{nuc}}\rvert^2$	: Nuclear matrix element
$F(Z,E)$	: Fermi function
ζ_i	: Probability to occupy molecular final state
$\epsilon_i = E_0 - V_i - E$	: Neutrino energy, with the molecular excitation energy V_i
$\Theta(\epsilon_i - m_i)$	: Heaviside function to ensure energy conversation
m_i	: Neutrino mass eigenstates (i = 1,2,3)

The molecular Final-State Distribution (FSD) is included in the equation with ζ_i and V_i, where ζ_i describes the probability that a given energy V_i from the β-decay of T_2 will be retained as excitation energy in the molecular daughter ion $^3HeT^+$ [Dos06; Sae00].

The resulting β-electron-spectrum is shown in Figure 2.3, illustrating both the case of a vanishing neutrino mass and a non-zero mass of $m_{\nu} = 1$ eV. This highlights the distinctive signature of the neutrino mass in the spectrum, manifesting as a subtle shift in the shape near the endpoint region.

High-precision measurements focus on the endpoint region, which contains only about $2 \cdot 10^{-13}$ of the total emitted electrons within 1 eV around E_0. By comparing the gathered data to a model based on Equation (2.35), it becomes possible to extract the neutrino mass from the tritium β-spectrum [Kle19].

This simplified explanation provides a direct approach to measuring the neutrino mass by analyzing the shape of the electron spectrum near the endpoint. For a more detailed explanation, the reader is referred to [Ake21b].

It should be noted that throughout the remainder this work, no distinction is made between the mass of a neutrino and the mass of an antineutrino. Consequently, the term "neutrino" will be used indiscriminately to refer to both neutrinos and antineutrinos.

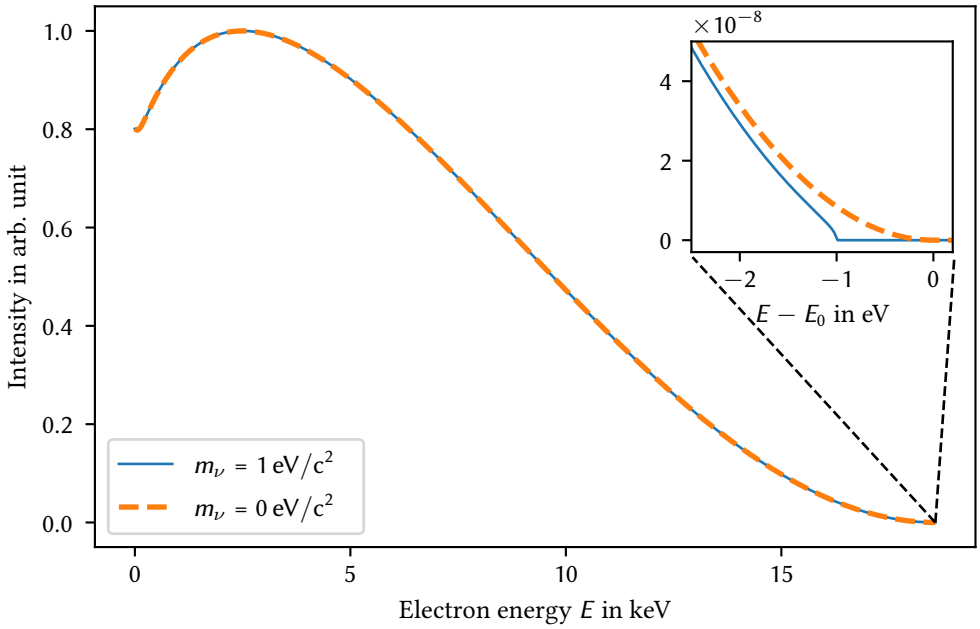

Figure 2.3: Impact of the neutrino mass on the tritium β-spectrum. The shape of the spectrum can be calculated using Equation (2.35). A non-vanishing neutrino mass alters the shape near the endpoint, resulting in a shift.

3 The KATRIN Experiment

The Karlsruhe Tritium Neutrino (KATRIN) experiment is specifically designed to determine the neutrino mass using tritium β-spectroscopy, as described in Section 2.3. It is the direct successor to the Mainz [Kra05] and Troitsk [Ase11] neutrino mass experiments, which collectively established an upper limit on the neutrino mass of $2\,\mathrm{eV/c^2}$. KATRIN is hosted in the Tritium Laboratory Karlsruhe (TLK) and features an ultra-stable high luminosity tritium source with up to $10^{11}\,\mathrm{Bq}$ and a high-resolution MAC-E filter[1] with an energy resolution on the order of eV. It is expected to achieve a final sensitivity of better than $0.3\,\mathrm{eV/c^2}$ at 90 % CL [Ake24a].

Unless otherwise indicated, [Ake21a; Ang05] will serve as the source for the content in the following sections.

An overview of the experimental setup, approximately 70 m in length, is shown in Figure 3.1. The setup consists of the Source and Transport Section (STS), which includes the Rear Section (RS), the Windowless Gaseous Tritium Source (WGTS), and the transport and pumping section on one end, while the Spectrometers and Detector Section (SDS) is located on the other end.

The measurement principle is based on tritium β-decay. The β-electrons are generated in the WGTS, a component that is described in more detail in Section 3.1. These electrons are then guided in a magnetic flux tube either "downstream" along the beam line towards the detector or "upstream" towards the Rear Wall. In the downstream path, electrons pass through the Differential Pumping Section (DPS) and the Cryogenic Pump Section (CPS), as discussed in Section 3.2. These sections are designed to prevent tritium from entering the SDS. In this part of the setup, explained in Section 3.3, the Main Spectrometer (MS) functions as a high-pass filter, applying a blocking potential that allows only electrons with sufficient energy to pass towards the Focal Plane Detector (FPD), where they are detected.

Conversely, in the upstream direction, the RS is responsible for calibration and monitoring, as explained in Section 3.4, with the Rear Wall serving as its core component, detailed in Section 3.5.

To measure the integral tritium β-spectrum, the rate of electrons reaching the FPD at different retarding potentials U_{ret} applied to the MS is measured repeatedly. The specific measurement points and times are defined by the Measurement Time Distribution (MTD). Each cycle of the MTD consists of a series of measurement points together referred to

[1] Magnetic Adiabatic Collimation with an Electrostatic filter

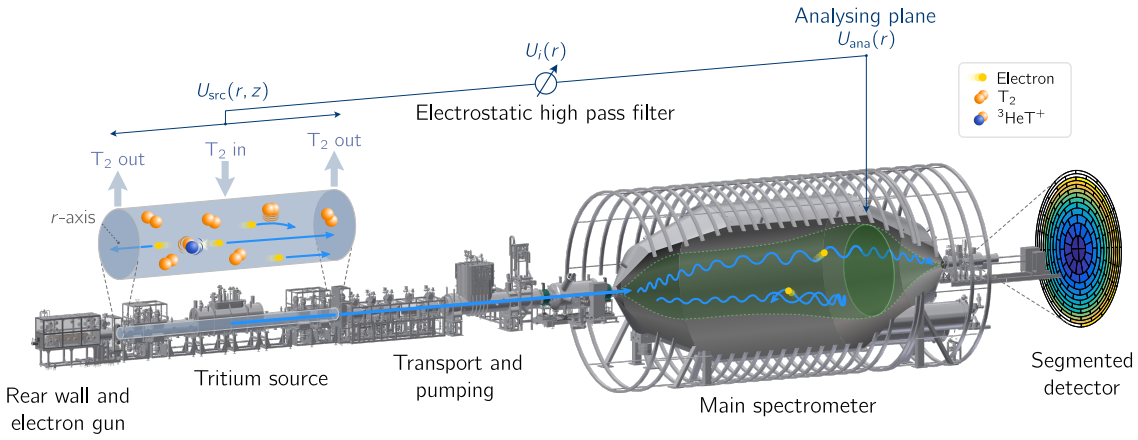

Figure 3.1: Illustration of the KATRIN experiment. Tritium inside the source emits β-electrons which are transported adiabatically towards the main spectrometer. This MAC-E filter acts as an electrostatic high-pass filter for the electrons, allowing for measurement of the integral tritium β-spectrum with the FPD. Illustration as published in [Ake22a] under the CC BY 4.0 license http://creativecommons.org/licenses/by/4.0/.

as a "run," with a typical duration of 3.5 h. These "KATRIN neutrino mass campaigns" (KNM) recorded during a measurement campaign - designated KNM1, KNM2, and so forth - are combined for subsequent analysis. Typically, a maintenance phase occurs between measurement campaigns.

3.1 The Windowless Gaseous Tritium Source

As mentioned in Section 2.3, KATRIN uses tritium β-decay to determine m_ν. Tritium is a favorable β-emitter for neutrino mass determination due to several advantageous properties [Ott08]:

- **Short half-life** of about 12.3 a due to the superallowed transition T→^{3}He. This means that a comparatively low inventory of radioactive material is sufficient to establish a high decay rate [Luc00].
- **Low Q value** of about 18.6 keV, which results in a low endpoint energy E_0 of the spectrum. This minimizes the relative proportion between the absolute energy of the events of interest and the actual effect of the neutrino mass on the spectrum [Mye15].
- **Simple theoretical description of the decay**, as tritium has an atomic number of $Z = 1$ [Zub20], which minimizes Coulomb interactions between the decay electron and the nucleus. Using a gaseous tritium source containing T_2 further enhances this

advantage, as the simple structure of the molecule and its daughter molecule $^3HeT^+$ allows quantitative calculation of the final state distribution [Sae00; Dos06; Dre13; Bod15].

To provide tritium for the measurement, KATRIN utilizes its Windowless Gaseous Tritium Source (WGTS), with an activity of up to $1 \cdot 10^{11}$ Bq [Ake21a]. The WGTS can be operated at different temperatures, such as 30 K, 80 K, and 100 K, and allows for the addition of ^{83m}Kr to tritium for calibration measurements. This facilitates the quantification of various source parameters otherwise not directly accessible, such as plasma density and the electron energy-loss function [Alt20; Rod23]. To prevent krypton from freezing out, the beam tube is operated at temperatures between 80 K and 100 K in this mode.

The tritium source is established by circulating tritium through the source tube, forming a column of gas. Continuous injection of tritium into the center of the source tube and evacuation at both ends by differential pumping sections (DPS1-R/F) creates a stationary gas profile [Mar20], resulting in constant activity within the source. The activity is determined by the number of tritium atoms inside the WGTS, which is represented by the column density ρd. The number of tritium atoms N_T can be expressed as:

$$N_\mathrm{T} = \rho d \cdot A_\mathrm{WGTS} \cdot \varepsilon_\mathrm{T} \cdot 2, \tag{3.1}$$

where A_WGTS is the cross-sectional area of the WGTS, and

$$\varepsilon_\mathrm{T} = \frac{N_{\mathrm{T}_2} + \frac{1}{2}\left(N_\mathrm{HT} + N_\mathrm{DT}\right)}{\sum_i N_i} \tag{3.2}$$

represents the tritium purity in the gas which is continuously monitored by a Laser-Raman-System [Zel24; Ake20a]. The tritium purity typically varies between (97 to 99) % [Ake24a]. The gas mixture usually contains all isotopologues Q_2, where Q can be H, D, or T. However, since the tritium concentration is high, T will be used throughout this work for simplicity, even in cases where it could be H or D.

The column density is stable to better than 0.1 % h^{-1}[Stu21], and the high purity of tritium gas can be maintained largely due to the specifically for this task designed KATRIN Loop System. A simplified schematic of the Inner Loop System is shown in Figure 3.2.

Pure tritium from the Outer Loop System flows into the intermediate buffer vessel B2. The gas then passes through a regulation valve into the pressure-stabilized buffer vessel B1. From B1, the tritium is injected into the source via the tritium injection capillary. The tritium then streams toward the far ends of the source tube, where it is evacuated and passed through a palladium membrane filter (permeator), which is only permeable to hydrogen isotopes [Got70; Bor05]. Any non-hydrogen impurities are filtered out, allowing the purified tritium to be reused, while the waste is removed for reprocessing.

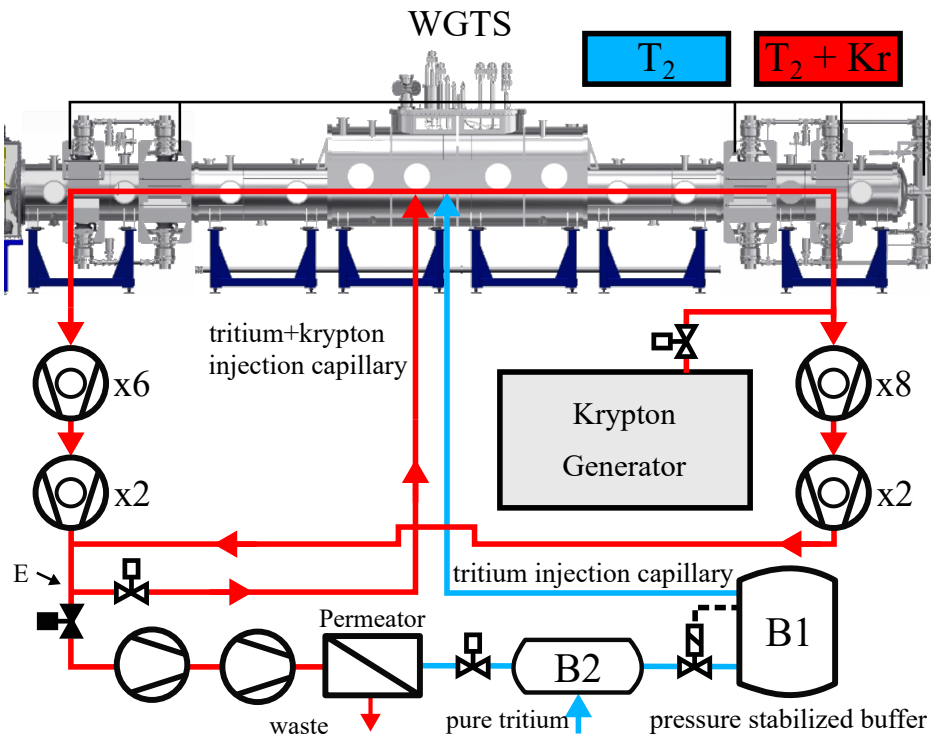

Figure 3.2: Schematic of the inner loop, depicting the tritium circulation path of for different operation modes of the WGTS. Illustration adapted from [Mar22] under the CC BY 4.0 license http://creativecommons.org/licenses/by/4.0/.

An additional operational mode is realized by splitting the gas stream into roughly equal parts (see E in Figure 3.2), re-injecting one part of the gas pumped out from the source back into the source via the tritium+krypton injection capillary, while the other part passes through the permeator and is then re-injected via the tritium injection capillary. Initially designed for mixed calibration measurements with tritium and krypton, this configuration has been adapted as the standard circulation mode from KNM4 onwards and is known as the "80 K mode" [Ake24a]. This mode allows for measurements to be conducted under the same conditions as krypton calibration measurements, including operating at krypton-compatible temperatures of 80 K. Another difference from the "30 K mode" is that part of the gas stream bypasses the permeator, potentially leading to a reduced removal of impurities, such as hydrocarbons.

An in-depth explanation of the loop system and the working principles of the various subsystems can be found in [Stu10; Mar20; Mar22].

The electrons originating from the decay of tritium are adiabatically guided towards the SDS by a magnetic flux tube generated by a magnetic field of 2.5 T, created by superconducting solenoids surrounding the source tube.

3.2 The Transport Section

While the electrons emitted in the WGTS need to be adiabatically guided towards the SDS and be able to reach their destination unobstructed, it is crucial to reduce the tritium flow from the injection point to the spectrometer by 14 orders of magnitude. Any residual tritium entering the spectrometer would create a significant background source. Electrons produced in the spectrometer would originate from a different starting potential, causing their energy to shift towards higher values compared to those emitted in the WGTS.

Any tritium gas that is not removed by the pumps at the end of the WGTS is pumped out by the Differential Pumping Section (DPS) and Cryogenic Pump Section (CPS), before being returned to the Outer Loop for reprocessing [Wel17]. During full operation, the KATRIN source has a tritium throughput of about 40 grams per day [Wel17; Stu21].

3.2.1 Differential Pumping Section

The DPS is responsible for reducing the tritium flow by seven orders of magnitude before it reaches the CPS. The first stage, DPS1-F, located at the end of the WGTS, achieves a reduction in tritium flow by two orders of magnitude. Further pumping is performed by the DPS2-F [Ake21a].

Since windows would obstruct the path of the electrons, the DPS is designed to permit the unobstructed guidance of electrons while blocking the flow of neutral T_2.It achieves this by forming a chicane, ensuring that neutral tritium collides with the beam tube walls, hindering its flow and facilitating pumping by six Turbomolecular Pumps (TMPs), which reduce the tritium flux by five orders of magnitude. The DPS also contains five superconducting solenoids, with the second and second-to-last solenoids tilted by 20°, creating a magnetic field of more than 5 T to guide the electrons through the chicane.

To prevent tritiated ions from following the magnetic guiding field, as the electrons do, an additional electrode system is installed inside the DPS beam tube. Ring electrodes apply a potential between (5 to 40) V to block the ions, while dipole electrodes induce an $E \times B$ drift, moving ions onto dedicated metal surfaces where they are neutralized [Fri20]. The neutralized tritium is then pumped out by the TMPs.

3.2.2 Cryogenic Pumping Section

The primary goal of the CPS is to further reduce the tritium flow by at least seven orders of magnitude, resulting in a maximum allowed tritium flow of less than $1 \cdot 10^{-14}$ mbar L s^{-1} after this section.

The CPS features a chicane similar to the DPS, consisting of five segments, with two segments tilted by 15°. This configuration ensures that any neutral tritium collides with the walls. Electrons continue to be guided adiabatically by superconducting magnets.

All CPS segments are housed inside a cryostat, cooled to (3 to 4) K [Röt23; Ake21a]. The beam tube walls are gold-plated and covered with a condensed layer of argon frost, which serves as a cryosorption pump to capture tritium [Kaz08; Gil09; Jan15].

As tritium accumulates on the walls, a threshold of 1 Curie ($3.7 \cdot 10^{10}$ Bq) is defined to comply with radiation safety regulations. Under standard measurement conditions, this threshold would be reached after more than one year of operation [Ake21a]. To avoid surpassing this limit, the argon layer is periodically regenerated by warming the beam tube walls and purging the system with helium. This procedure effectively removes the argon and tritium, after which a new argon frost layer is prepared, following the process described in [Jan15; Röt19].

3.3 The Spectrometer and Detector Section

The Spectrometers and Detector Section (SDS) of KATRIN consists of two MAC-E filters, the Pre-Spectrometer (PS) and Main Spectrometer (MS), as well as the Focal Plane Detector (FPD), as shown in Figure 3.1. The PS can be used for coarse filtering of low-energy electrons but has been set to a reduced potential since KNM4 to achieve further background reduction [Ake24a]. Essentially, the PS functions similarly to a smaller version of the MS and is also equipped with a picoamperemeter connected to the inner electrode system, which allows in-situ monitoring of the residual ion flux entering the spectrometer section [Kle19]. The MS is responsible for the precise energy determination of electrons near the endpoint region by functioning as a high-pass filter. Electrons that pass this filter are subsequently detected by the FPD.

3.3.1 Pre and Main Spectrometer

Both the PS and MS operate under the principle of MAC-E filter [Bea80; Lob85; Pic92a]. In this technique, a combination of magnetic fields produced by superconducting solenoids at the entrance and exit of the spectrometer, and an electric potential to create a potential barrier, is used to filter the electrons based on their energy. A schematic of the magnetic field, the corresponding components, and the paths of different electrons, illustrating the MAC-E filter principle, is shown in Figure 3.3. To shape the electro-magnetic field, the MS is surrounded by the Low Field Correction System (LFCS) and contains Inner Electrodes (IE).

The working principle of a MAC-E filter is as follows: An electron arriving from the Source and Transport Section (STS) is guided by the magnetic field towards the center of the spectrometer where the analyzing plane is located. In this process, the magnetic gradient force

$$\vec{F} = \vec{\nabla}\left(\vec{\mu} \cdot \vec{B}\right) \tag{3.3}$$

transforms the cyclotron energy ($E_\perp$) of the electron into longitudinal energy ($E_\parallel$), while conserving the total energy. This is achieved as long as the relative change in the magnetic field strength is small over the electron cyclotron radius. In such a case, the process is adiabatic, and the magnetic moment (μ) is conserved:

$$\mu = \frac{E_\perp}{B} = \text{const.} \tag{3.4}$$

The field configuration is designed in such a way that $E_\perp$ becomes minimal at the analyzing plane, where the magnetic field (B) is reduced to about 0.5 mT, as shown in Figure 3.3. An electron can only pass through the analyzing plane if its energy (E) exceeds the applied electrostatic blocking potential (U_{max}):

$$E_\parallel = E \cdot \cos^2\theta > e \cdot U_{\text{max}}, \tag{3.5}$$

where θ is the pitch angle of the electron. Electrons that do not meet this condition are reflected. The energy resolution is given by

$$\frac{\Delta E}{E} = \frac{B_{\text{min}}}{B_{\text{max}}}, \tag{3.6}$$

from which follows $\Delta E = 0.93\,\text{eV}$ at 18.6 keV according to design configuration.

For electrons with high surplus energy, the process can become non-adiabatic. This effect is of particular interest for the measurements discussed in Section 6.1.2.2, and is detailed in [Hub21].

During KNM3, the Shifted Analyzing Plane (SAP) configuration was introduced, as shown in Figure 3.4, and is explained in detail in [Lok22; Ake24b]. This setting serves the suppression of background. However, this configuration results in a broader filter width for the spectrometer, with $\Delta E = 2.8\,\text{eV}$, due to the higher magnetic field of 0.63 mT in the analyzing plane, as given by Equation (3.6). Nevertheless, the higher magnetic field is beneficial for probing deeper into the beta spectrum due to an increased suppression of non-adiabatic effects, as discussed in Section 6.1.2.2. The asymmetric geometry of the analyzing plane also necessitates a patch-wise analysis of the data.

3.3.2 Focal Plane Detector

The Focal Plane Detector (FPD) is a silicon p-i-n diode wafer, segmented into 148 pixels [Ams15], and can be subdivided into 14 patches to account for the asymmetry in the potential under the SAP setting, as shown in Figure 3.5. The FPD is located behind the pinch magnet, which generates the highest magnetic field B_{pch} along the entire KATRIN beamline with $B_{pch} = 4.2\,\text{T}$, merging the field lines after the MS, guiding all transmitted electrons towards the FPD. The FPD itself is again housed inside the detector magnet,

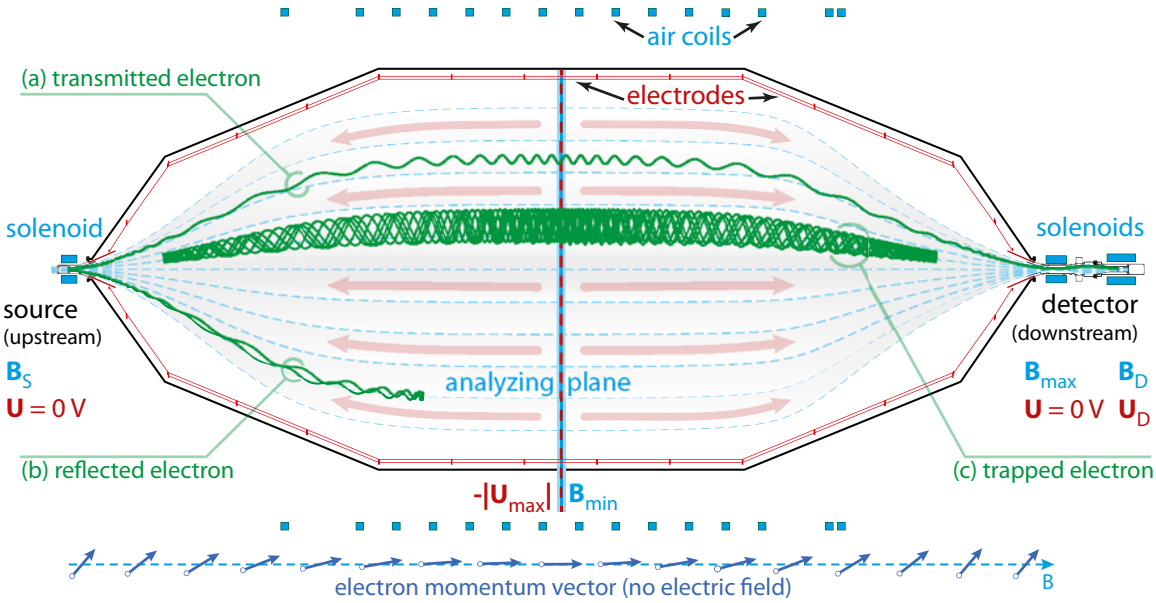

Figure 3.3: The MAC-E filter principle. Superconducting solenoid magnets together with electrodes and normal-conducting solenoids (air coils) shape the magnetic and electric fields adiabatically align the electron momenta, maximizing the parallel component in the analyzing plane. Depending on their energy and the applied potential U_{max} the electrons can pass and reach the detector (a) or are reflected (b) . Electrons originated from inside the spectrometer volume may remain trapped due to the magnetic bottle effect at both ends (c). Illustration as published in [Ake21a] under the CC BY 4.0 license http://creativecommons.org/licenses/by/4.0/.

achieving the same field strengths. The value of B_{pch} along with the strength of the field in which the electron is emitted, B_{source}, defines the maximum acceptance angle [Gro15]:

$$\theta_{\text{max}} = \sin^{-1}\sqrt{\frac{B_{\text{source}}}{B_{\text{pch}}}}. \tag{3.7}$$

All electrons which are emitted with a polar angle above this will be reflected at the pinch magnet and will not reach the detector.

The detector has a high efficiency of $\varepsilon_{\text{FPD}} \geq 90\,\%$ for electrons in the signal region and is regularly calibrated using an ^{241}Am calibration γ-source. Electrons reaching the detector are further accelerated by a Post-Acceleration Electrode (PAE) applying an additional potential of 10 kV.

A detailed description of the detector hardware, Data Acquisition (DAQ) system, and associated software, can be found in [Ams15; Ake21a]. However, in the scope of this work, measurements with high rates were performed, where pile-up is a concern (see Section 6.1.2.2). Therefore, the filtering applied for event registration is summarized here, based on [Ams15; Ake21a].

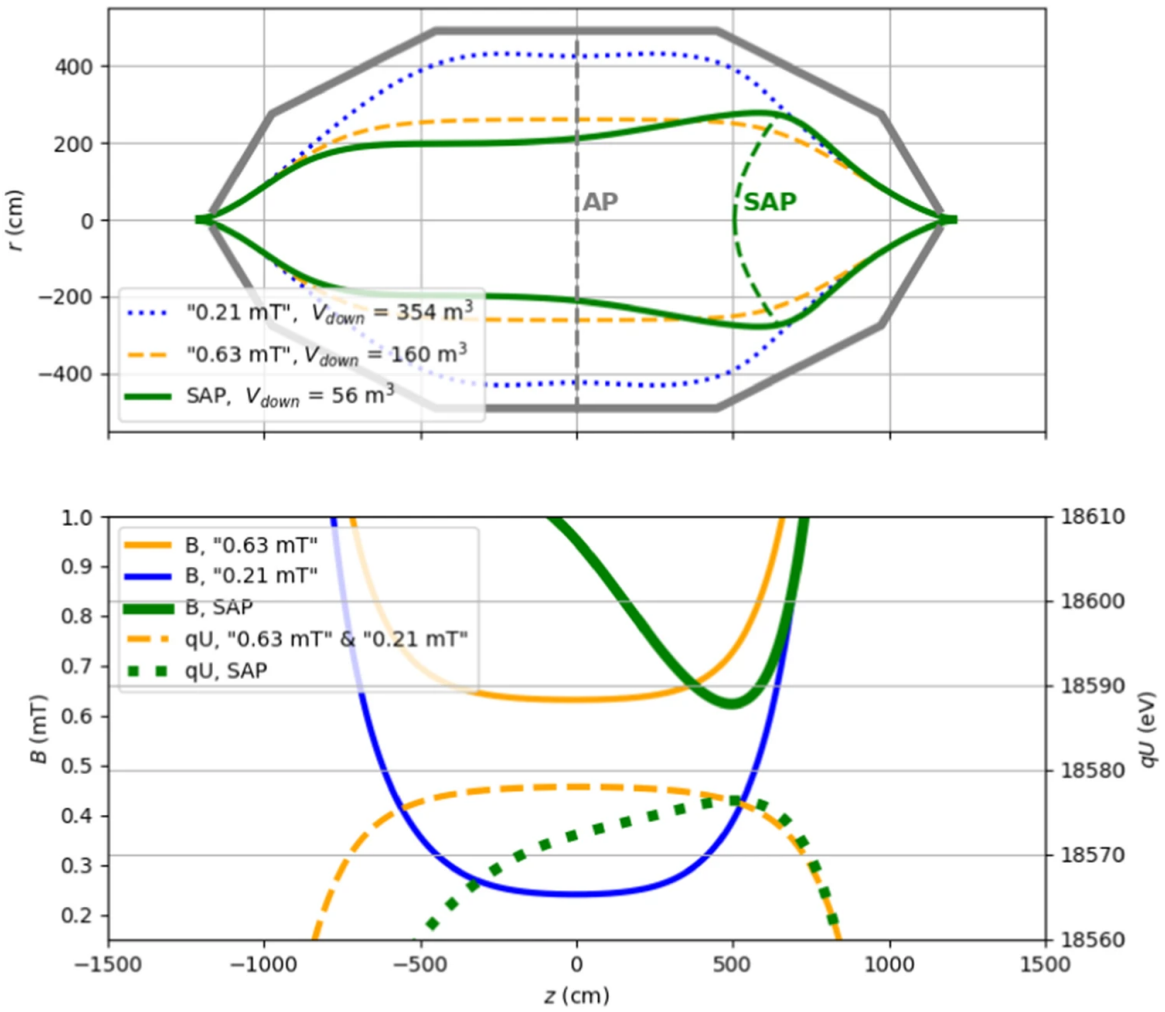

Figure 3.4: Shifted analyzing plane configuration. The upper panel depicts the magnetic flux tube geometries and the respective analyzing plane for different settings in comparison to the main spectrometer. V_{down} is the downstream flux tube volume. In the lower panel the electric retarding potential and the magnetic field for different settings is depicted. Illustration as published in [Lok22] under the CC BY 4.0 license http://creativecommons.org/licenses/by/4.0/.

When an electron hits the detector, it produces a step response in the signal, with the step height proportional to the electron energy. The typical rise time of this signal is on the order of 100 ns, while the fall time is on the order of 1 ms.

A series of trapezoidal filters detects steps in the digitized waveform, defined by the shaping length L and gap length G, measured in Analog-to-Digital Converter ADC time bins. The filtered signal output S_i is calculated from a moving sum of previous trace values. The output of the first filter reaches its maximum L time bins after the step, indicating the step height. A second filter with a shaping length of $L/2$ produces a zero-crossing at the peak of first filter. Triggers occur when zero-crossings in the second filter align with

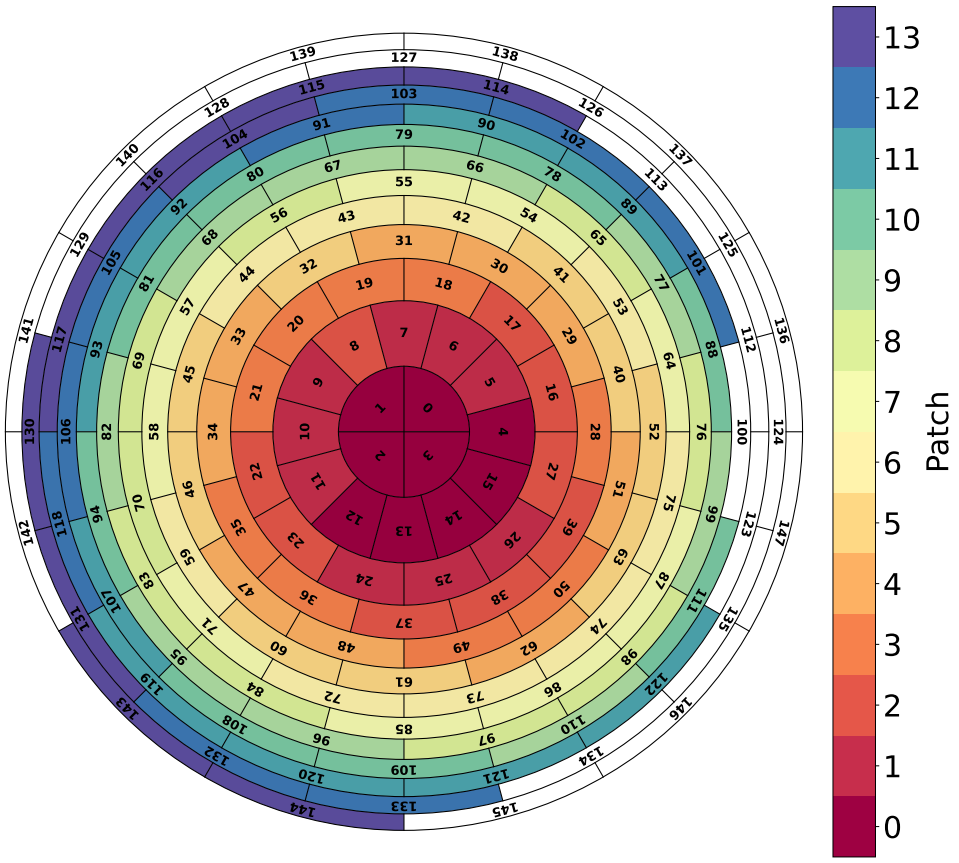

Figure 3.5: SAP-Patches with their assigned pixels on the segmented pixel map of the FPD. The assignment of pixels to their respective patches is determined based on the transmission properties of the spectrometer for electrons detected at each pixel. White pixels are excluded from the analysis.

energy thresholds in the first. Larger L values optimize energy resolution, while shorter L improves timing. Figure 3.6 shows the application of this cascade to a sample signal, including a single detected electron and two electrons arriving within the shaping length.

Initially, a cascade of two filters was used, where the zero-crossing of the output of the second filter triggered the recognition of an event if the corresponding value of the first filter output was above a threshold. The value of the first filter output was then used as the energy measurement. In the case of pile-up, as shown in Figure 3.6b, two electrons

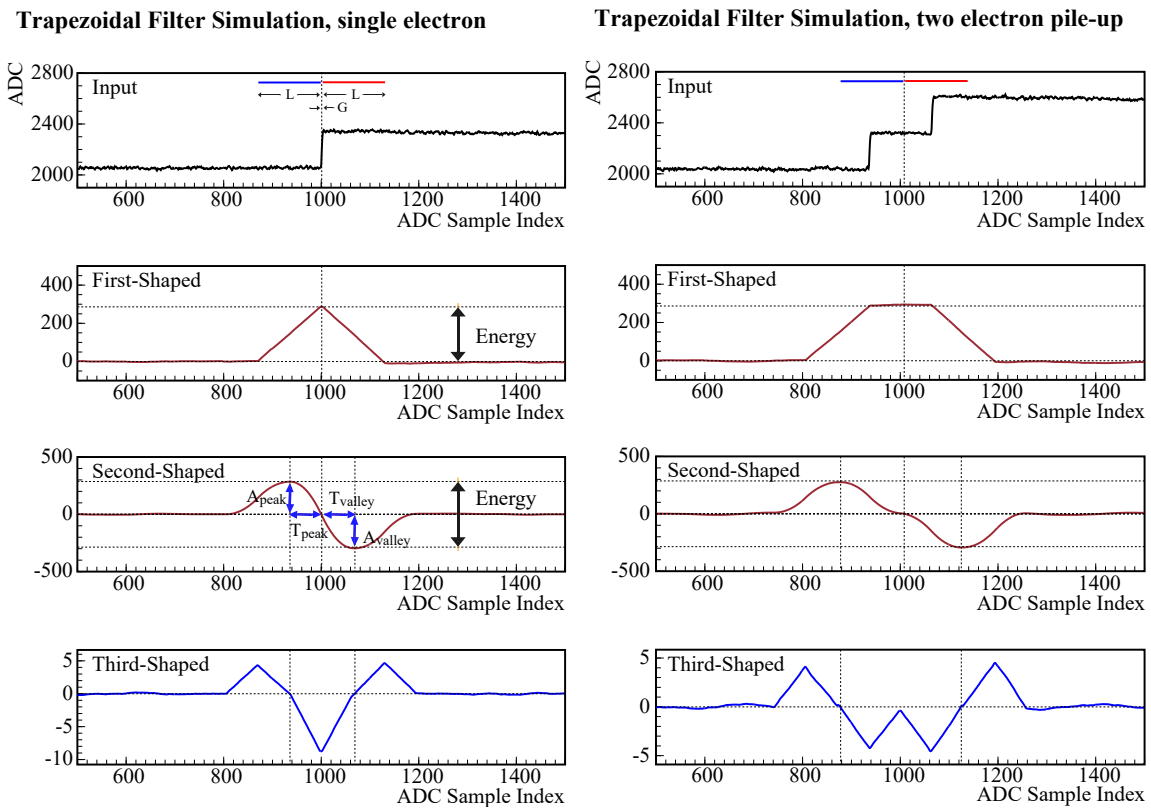

(a) Single-electron event

(b) Two-electron pileup

Figure 3.6: Simulation of the trapezoidal filter behavior on a single-electron and two-electron event, for three subsequent application of the filter. Illustration as published in [Ake21a] under the CC BY 4.0 license http://creativecommons.org/licenses/by/4.0/.

arriving within the shaping length would be recognized as a single event, with an energy equivalent to that of a single electron.

However, the shape of the second filter output contains additional information about the energy. To make use of this, a third layer of trapezoidal filter was added. For each trigger, the amplitudes and timestamps of the peak and valley - denoted as A_{peak}, T_{peak}, A_{valley}, and T_{valley} - of the second filter output are recorded for each zero-crossing of the third filter output. This allows for correction of some pile-up events, increasing the rate limit from 1 kcps/pixel to 100 kcps/pixel, according to simulations.

3.4 Rear Section

Opposite to the SDS on the other end of the WGTS is the Rear Section (RS), which contains several calibration and monitoring devices for the WGTS column density and electromag-

netic characteristics along the beamline. A central part of the RS is the gold coated Rear Wall. Due to its importance for both, KATRIN and this work, the Rear Wall is discussed in detail in Section 3.5. This section continues the technical discussion of the RS and its components peripheral to the Rear Wall. The RS can be subdivided into three main sections: the Rear Wall chamber, the mid chamber and the e-gun chamber.

3.4.1 The Electron Gun

At the far end of the RS is the e-gun chamber, housing the electron gun (e-gun), which is an angular selective, monoenergetic electron source used for Column Density (CD) measurements and determination of the energy loss function experienced by electrons traveling through the WGTS [Sch21]. This is needed to define the response function that combines the theoretical spectrum described in Section 2.3 with the recorded β-spectrum [Kle19]. The E-gun produces photoelectrons by UV illumination of a metallic cathode at a constant rate [Beh17]. The light is delivered through an optical fiber to the back of the thin photocathode surface, where photoemission occurs. The electrons are then accelerated to the desired energy and steered using dedicated electrodes [Ake21a]. Electrons are magnetically guided through a central hole in the Rear Wall into the flux tube in the WGTS, and magnetic dipole coils located in the WGTS allow steering of the electron beam in both vertical and horizontal directions, enabling selection of the pitch angle θ between 0° and 90° at the pinch magnet. The energy width of the electron beam is less than 0.5 eV [Ake21a]. To ensure a sufficiently good vacuum, particularly for the high-voltage components of the electron gun, additional pumping capacities are required. These are housed in the so-called mid-chamber, which is located directly adjacent to the electron gun chamber.

3.4.2 UV Illumination of the Rear Wall

Connected to the mid-chamber by a long DN-CF63 pipe passing through the Re-Condenser Superconducting Magnet (RSCM) is the Rear Wall chamber, which links to the WGTS DPS1-R. While its primary function is to house the Rear Wall, it also contains additional monitoring tools and instrumentation. Adjacent to the Rear Wall are additional features, including an optical port and a UV lamp. Initially, a Cermax® xenon lamp[2] was used, which was later replaced by two MiniZ[3] mercury-UV (Hg-UV) lamps. The lamps are located behind two vacuum viewports[4] at a distance of roughly 550 mm. A sophisticated optical setup was designed for the former lamp to ensure homogeneous illumination of the Rear Wall [Ful20]. The Cermax® lamp provides approximately 0.3 W of UV power in the wavelength range of (200 to 266) nm to produce photoelectrons from the Rear Wall. These photoelectrons were used to probe the electrical potential inside the beamline and to

[2]Perkin Elmer, 06484 CT, United States., Type Cermax® PE1000DUV (lifetime 1000 h)
[3]RBD Instruments, 97701 OR, United States. miniZ Water Vapor Desorption System
[4]HPFS Corning code 7980

desorb bound water and possibly other species on the Rear Wall (see Section 5.2.3). Later, the lamp was replaced by two MiniZ Hg-UV lamps with 24 W of electrical power, emitting discrete lines at wavelengths of 185 nm and 253 nm.

3.4.3 β-Induced X-ray Spectrometry

Two Beta-Induced X-ray Spectrometry (BIXS) systems monitor the source activity, as described in detail in [Röl15]. These systems utilize a Silicon Drift Detector (SDD)[5]

The functional principle of BIXS involves the detection of X-rays emitted as a result of tritium β-electrons interacting with materials [Mat07]. These X-rays are created via two main processes:

Characteristic X-Rays When β-electrons interact with matter, they transfer energy through ionization and inelastic scattering [Bet32]. After ionization, an electron from a higher orbital may fill the vacancy, releasing energy as a photon. The energy is characteristic of the corresponding atom and involved orbital [Hak01]. For atoms with atomic number $Z \geq 4$, these energies fall in the X-ray region.

Bremsstrahlung: Additionally, β-electrons can be deflected by the Coulomb field of atoms. Since the electrons are accelerated during this process, they emit electromagnetic radiation (bremsstrahlung). The radiative energy loss per path length is given by:

$$\left(\frac{dE}{dx}\right)_{\text{Rad}} = \frac{4n\text{a}Z^2\alpha^3(\hbar c)^2 E}{m_\text{e}^2 c^4} \ln\frac{a(E)}{Z^{1/3}}, \tag{3.8}$$

where n_a is the atomic density, Z is the atomic number of the material, α is the fine structure constant, and a accounts for the impact parameter of the scattering [Dem17]. The intensity distribution of bremsstrahlung is continuous and can be described by Kramers' rule:

$$I(\lambda)d\lambda = K\left(\frac{\lambda}{\lambda_\text{min}} - 1\right)\frac{1}{\lambda^2}d\lambda, \tag{3.9}$$

where K is a material-specific constant, and λ_min is the minimum wavelength that a photon can have if an electron with a given energy E_e transfers it completely to the photon [Lag77; Kra23]. The energy and wavelength of a photon are reciprocally dependent:

$$\lambda \propto \frac{1}{E_\gamma} \implies d\lambda \propto \frac{1}{E_\gamma^2}dE_\gamma, \tag{3.10}$$

$$\lambda_\text{min} \propto \frac{1}{E_{\gamma,\text{max}}} = \frac{1}{E_\text{e}}. \tag{3.11}$$

[5] KETEK, 81737 München, AXAS-M

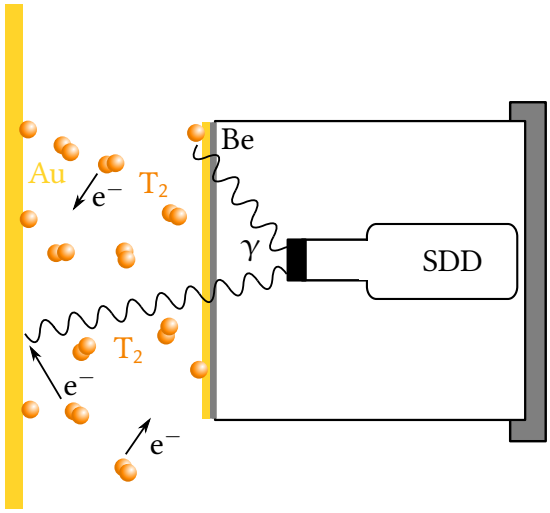

Figure 3.7: Schematic representation of the BIXS principle. Tritium β-electrons interact with the gold surface of the Rear Wall or the gold-coated Be windows, generating X-rays. These X-rays pass through the Be window, which is transparent to them, allowing the SDD to detect and measure the tritium activity.

Inserting these relationships into Equation (3.9) yields:

$$I(E_\gamma)dE_\gamma = K' \left(\frac{E_e}{E_\gamma} - 1 \right) dE_\gamma, \tag{3.12}$$

which describes the intensity distribution of bremsstrahlung caused by an electron with energy E_e in a single collision.

The bremsstrahlung spectrum for tritium β-electrons is obtained by convolving the energy spectrum of the decay electrons (Equation (2.35)) with Kramers' rule (Equation (3.12)). The resulting X-ray photons have energies up to $E_0 = 18.6\,\text{keV}$, meaning bremsstrahlung falls within the X-ray region. Multiple collisions occur in thicker layers, causing an overlap of multiple bremsstrahlung spectra. X-rays interacting further with material can induce X-ray fluorescence, giving the recorded BIX spectrum its shape.

The SDD detects these X-rays, with the recorded intensity being proportional to the underlying tritium activity. To protect the detector from contamination, it is positioned behind a Be window that blocks tritium but allows X-rays to pass through (see Section 3.4.3). To further enhance the signal, these windows are gold-coated, yielding a higher X-ray intensity for electrons impinging on them.

The main signal from BIXS results from β-electrons emitted in the source being guided to the Rear Wall by magnetic fields, where they create X-rays, a portion of which are then detected by the SDDs. However, tritium accumulated on the Rear Wall also contributes to

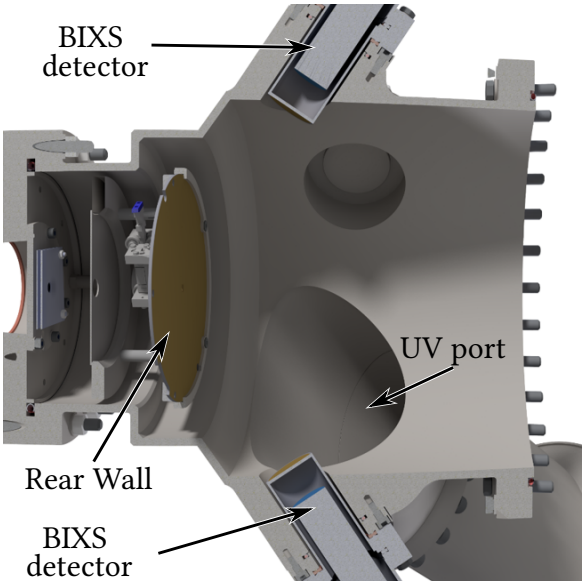

Figure 3.8: Rear Wall Chamber The Rear Wall is mounted along the symmetry axis of the Rear Wall chamber, with two SDDs positioned behind additional gold-coated beryllium (Be) windows. An optical port for UV illumination is also directed towards the Rear Wall.

the signal, and tritium accumulated on the Be windows produces an even stronger signal due to the proximity to the detector, which increases the portion of X-rays reaching the detector. Consequently, BIXS experiences a memory effect [Röl15], but on the other hand, it can also be used as a tool to monitor tritium on the Rear Wall.

3.5 The KATRIN Rear Wall

The Rear Wall is located in the Rear Wall chamber, where it terminates the tritium source. The RSCM is positioned behind it. The Rear Wall is mounted on ceramic rods to ensure electrical insulation, as depicted in Figure 3.8. The Rear Wall chamber is directly adjacent to the differential pumping section DPS1-R and is separated from the WGTS by valve V0, which allows for isolation of the RS from the WGTS when needed. The Rear Wall itself is an Au-sputter coated stainless steel disc with a diameter of 145 mm and a 1 µm thick gold coating, featuring a central 5 mm hole serving as a passage for e-gun electrons.

At the Rear Wall, a significant portion of the circulated tritium is already pumped out, with the DPS1-R primarily defining the pressure in the Rear Wall chamber during nominal tritium circulation, which is around $1 \cdot 10^{-5}$ mbar. Additional pumping capacities are available through the connection to the mid chamber with its own vacuum system, especially if valve V0 is closed.

The primary β-electrons from tritium decay and the secondary electrons from ionization of tritium can leave the KATRIN beamline almost exclusively through the Rear Wall, due to the magnetic field confining their movement to be along the longitudinal direction, and the retarding potential of the spectrometers. Electrons emitted in the upstream direction and those reflected by the tandem spectrometer ultimately impinge on the Rear Wall. The same applies to the ions that migrate towards the RS from the WGTS.

The entire flux tube is mapped onto the Rear Wall, which plays a crucial role in determining and manipulating the starting potential experienced by β-electrons in the cold tritium plasma within the WGTS. This starting potential directly influences the kinetic energy of the β-electrons. In the tritium source, a neutral gas coexists with a cold plasma resulting from the ionization of gas molecules [Kuc16; Kel22]. While a bias voltage of up to $\pm 500\,\mathrm{V}$ can be applied to the Rear Wall to influence this potential inside the plasma. The potential further depends on the work function difference between the Rear Wall and the stainless steel surface of the beam tube [Mac21; Sac20]. The implications of the work function within the scope of this work are further discussed in Section 5.3.2.

Gold was chosen as the ideal Rear Wall material due several reasons[Bab14]:

- Its high atomic number Z results in a higher bremsstrahlung intensity due to impinging electrons, increasing BIXS rates.
- Gold is a good conductor with a homogeneous work function, facilitating manipulation of the starting potential of the β-electrons.
- It is chemically inert, with only low and weak tritium adsorption expected.

Additionally, a picoammeter is used to measure the current flowing through the Rear Wall. The Rear Wall can also be heated to temperatures up to 120 °C.

In conclusion, the Rear Wall plays a critical role in defining the starting potential of the β-electrons in the KATRIN experiment, influencing the precision of neutrino mass measurements. Furthermore, it serves as a signal enhancing component for the BIXS system or can serve to produce photo-electrons. However, previous studies have shown that even gold, chosen for its low tritium adsorption, does adsorb tritium over time [Röl15]. The following chapter explores the impact of this tritium adsorption on the Rear Wall and its potential implications for the accurate determination of the neutrino mass.

4 The Influence of Tritium Adsorbed to the Rear Wall on the Neutrino Mass Analysis

The unique experimental setup of KATRIN, as detailed in Chapter 3, enables high-precision measurements of the tritium β-spectrum, leading to an unprecedented sensitivity for model-independent determination of the effective neutrino mass. The analysis of the first five measurement campaigns, recently published in [Ake24a], yielded a best-fit value of

$$m_\nu^2 = -0.14^{+0.13}_{-0.15}\,\mathrm{eV}^2/\mathrm{c}^4, \tag{4.1}$$

which sets the upper bound of the neutrino mass to

$$m_\nu < 0.45\,\mathrm{eV}/\mathrm{c}^2 \tag{4.2}$$

at 90 % CL. This marked the first KATRIN m_ν analysis where the impact of tritium sorption on the Rear Wall was observed and had a measurable effect on the results.

The decay of T_2 in the WGTS creates the primary β-spectrum which serves as the central input for the m_ν analysis. However, a secondary β-spectrum, with a different spectral shape, emerges from tritium adsorbed onto the Rear Wall. Since the decay of both types of tritium occurs within the flux tube, their β-electrons reach the FPD and cannot be distinguished from each other. This overlap between the primary and secondary spectra leads to a distortion of the measured spectrum.

The following sections will assess the uncertainties and evaluate the possible distortions due to tritium adsorption on the Rear Wall and its effect on the measured β-spectrum.

In Section 4.1, an assessment of all uncertainties relevant to the neutrino mass analysis is given to gauge the magnitude of the impact needed for these effects to be significant. Section 4.2 discusses how the secondary spectrum overlaps with the primary spectrum and which impact this has on the measured spectrum. An estimation of the potential shift in m_ν^2 due to this distortion, if left untreated, is also provided. Finally, in Section 4.3, the detailed shape of the secondary spectrum is discussed, and a concept is presented for characterizing this spectrum in order to incorporate it into the m_ν analysis. This leads to the definition of the objective of this work, which is outlined in Section 4.4.

4.1 Overview of Uncertainties of the m_ν Determination

In this section, the scope of effects that the secondary spectrum causes is assessed and it is determined how significant they must be to impact the overall uncertainty in the neutrino mass analysis.

Table 4.1 provides an overview of the uncertainties associated with the m_ν determination, as presented in [Ake24a]. The total uncertainty is dominated by statistical error, followed by uncertainties of the column density, the energy-loss function, the time-dependent background rate, and source-potential variations.

Compared to the previous publication [Ake22a], there has been a noticeable improvement in statistical uncertainty due to the additional gathered events during the KNM3-5 campaigns. Additionally, systematic uncertainties were improved. The background level has been reduced by a factor of two due to adjustments in the analyzing plane settings [Lok22]. Furthermore, advancements in calibration methods, along with improvements in the Final-State Distribution (FSD) uncertainty were made.

A new entry in this uncertainty breakdown is the residual tritium background from the Rear Wall. Campaign-specific estimations of the impact of this residual tritium (see detailed discussion in Section 4.2.2) indicate a potential shift Δm_ν^2 of up to $0.073\,\mathrm{eV}^2/\mathrm{c}^4$. While the overall shift across the first five campaigns would be lower, this reduction is partly due to cleaning procedures applied to the Rear Wall. By incorporating both these cleanings and additional measures as part of a mitigation strategy developed and implemented in the scope of this work, the impact of residual tritium was effectively minimized, resulting in a systematic uncertainty contribution of only $0.004\,\mathrm{eV}^2/\mathrm{c}^4$ - well within the uncertainty budget.

The next sections will delve into how the mitigation strategy was devised and its role in minimizing the influence of tritium adsorption on the Rear Wall in the neutrino mass analysis.

4.2 Distortion of Spectral Shape and Its Impact on m_ν

In the previous section, an overview of uncertainties is provided, including the contribution of the secondary spectrum as one of the key systematic effects influencing the total uncertainty in the determined m_ν^2 value. While this contribution appears minimal in the uncertainty breakdown, it only remains so due to the countermeasures implemented which is discussed in detail throughout this work. To trace the evolution of tritium accumulation on the Rear Wall from a source of significant impact to a well-controlled systematic with minimal residual effects, it is crucial to understand the underlying mechanisms affecting neutrino mass determination.

Table 4.1: Overview of the m_ν^2 uncertainties based on Monte Carlo generated data. Data obtained from [Ake24a]. For a comprehensive breakdown of the individual contributions to the uncertainty in m_ν^2, along with a detailed discussion of additional effects that are beyond the scope of this work, the reader is referred to the original source.

Effect	68.3 % CL uncertainty on m_ν^2 in eV^2/c^4
Statistical uncertainty	0.108
Non-Poissonian background	0.015
Column density × inelastic cross section	0.052
Energy-loss function	0.034
Scan-step-duration-dependent background	0.027
Source-potential variations	0.022
qU-dependent background slope	0.007
Analyzing-plane magnetic field and potential	0.006
Source magnetic field	0.004
Maximum magnetic field	0.004
Rear Wall residual tritium background	**0.004**
Molecular final-state distribution	
Activity fluctuations	
Detector efficiency	< 0.002
Retarding-potential stability and reproducibility	
Theoretical corrections	

Section 4.2.1 discusses the impact of a secondary β-spectrum overlapping the primary spectrum. Section 4.2.2 quantifies this effect using data recorded during the KNM1-5 campaigns.

4.2.1 Overlap of Two β-Spectra

When a secondary β-spectrum with a different endpoint superimposes on the primary β-spectrum, it distorts the overall measured spectrum, which is subsequently analyzed according to the method outlined in Section 2.3. Figure 4.1 provides a schematic illustration of this overlap. The figure depicts the endpoint-near regions of two stylized β-spectra: the primary T_2 spectrum and a secondary spectrum, such as one originating from the Rear Wall with a shifted E_0. Together, these two spectra combine into a convolved spectrum, which carries the imprint of the higher E_0 from the secondary spectrum.

At lower electron energies, far from E_0, the relative influence of the secondary spectrum on the measured spectrum is relatively minor. However, near E_0, the distortion becomes more pronounced. As contribution of the secondary spectrum increases, the shape of the measured spectrum deviates more significantly from the primary spectrum, leading to a noticeable shift of the effective E_0. As noted in Section 2.3, the region close to the

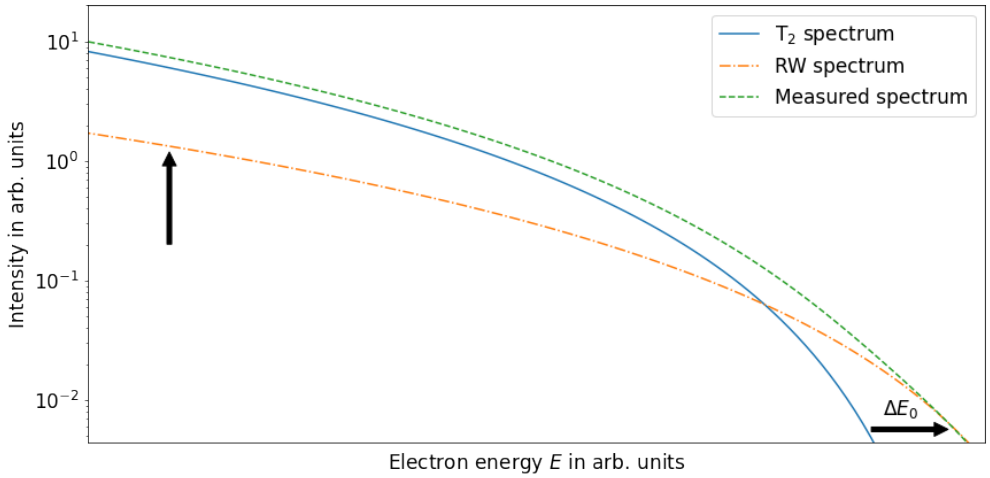

Figure 4.1: Simplified schematic depiction of the overlap of two distinct tritium β-spectra. The primary T_2 spectrum (solid line) is overlaid with a secondary spectrum (dash-dotted line) that has a different endpoint, E_0, emitted by tritium accumulated on the Rear Wall. This results in a distorted measured spectrum (dashed line). Additional corrective measures are necessary to reconstruct the true shape of the primary spectrum. The illustration is intentionally exaggerated to highlight how the spectral distortion, caused by the increasing contribution of the secondary spectrum, leads to a measurable shift in the apparent endpoint, E_0. Additional effects, including the increased scattering probability due to the longer travel path for β-electrons of the secondary spectrum are not included.

endpoint is where the neutrino mass most strongly affects the spectrum. Consequently, any distortion in this critical region introduces a systematic effect, leading to an absolute shift in the determined m_ν^2 value [Köl].

In the following section, we estimate the magnitude of this distortion based on data collected during the KNM1-5 measurement campaigns.

4.2.2 Estimated Shift on m_ν^2

Estimating the impact on the neutrino mass when the contribution of the Rear Wall spectrum is neglected in the analysis is not straightforward, as the underlying FSD of the tritium on the Rear Wall is unknown. To address this, a simulation-based approach using empirical data as input was employed[1]. Two Monte Carlo generated spectra were generated: one representing the properties of the T_2 spectrum corresponding to the respective measurement campaign, and the other based on the Rear Wall spectrum, which was recorded while

[1]This analysis was conducted by the co-authors of the "Rear wall report for the KNM1-5 neutrino mass analysis", Internal Report by M. Aker, B. Daniel, S.Hickford, L. Köllenberger, B. Lehnert, G. Li, D. Parno and A. Schwemmer, 2023, KATRIN Collaboration

Table 4.2: Estimated m_ν^2 bias due to neglected Rear Wall spectrum, for each of the measurement campaigns KNM1-5.[2]The last row indicates the estimated bias due to neglecting KNM1 and KNM2 in the overall KNM1-5 analysis.

Campaign	Δm_ν^2 in eV^2/c^4
KNM1	0.002
KNM2	0.017
KNM3a	0.058
KNM3b	0.044
KNM4	0.073
KNM5	0.032
KNM1-5 analysis	0.002

the WGTS was evacuated (see Chapter 6 for a detailed discussion of tritium measurements on the Rear Wall).

For both spectra, the resulting experiment response was simulated, with the secondary spectrum adjusted to reflect the starting magnetic field at the Rear Wall ($B_{\mathrm{RW}} = 1.23\,\mathrm{T}$) and accounting for the fact that all electrons must traverse the full WGTS, leading to more scattering events. Both spectra were then stacked and fit with the regular analysis model. The results were compared to those of only the primary spectrum, revealing a bias in the m_ν^2 estimates. These biases are summarized in Table 4.2.

The impact of the secondary spectrum on m_ν^2 increases over the measurement campaigns, correlating with the gradual accumulation of tritium on the Rear Wall where a larger contribution from the secondary spectrum causes a greater shift, as discussed in Section 4.2.1. A notable outlier in this trend is KNM3a, which exhibits a larger bias, followed by a smaller bias in KNM3b. This discrepancy is likely due to the different CD settings applied during KNM3a and KNM3b, affecting the outcome of the estimation. A larger CD in KNM3b leads to a higher scattering probability for the β-electrons originating from the Rear Wall, which reduces the impact. The decline in bias during KNM5 is attributed to the first cleaning of the Rear Wall, which reduced the amplitude of the secondary spectrum. The detailed rate evolution is discussed further in Chapter 7.

4.2.3 Differences in the Final State Distribution of Adsorbed and Gaseous Tritium

The Final-State Distribution (FSD) represents the distribution of energy left in the daughter molecular states after decay, and deviations from the expected FSD can lead to an inaccurate

[2]Values taken from "Rear wall report for the KNM1-5 neutrino mass analysis", Internal Report by M. Aker, B. Daniel, S.Hickford, L. Köllenberger, B. Lehnert, G. Li, D. Parno and A. Schwemmer, 2023, KATRIN Collaboration

determination of E_0, which affects the neutrino mass fit [Nde24]. In the gaseous state, the decay of T_2 induces excitations in the electronic, rotational, and vibrational states of the daughter molecule, along with external effects such as recoil [Ott08]. These transitions can be computed using ab initio quantum mechanical methods [Sae00], allowing for a well-defined FSD to be integrated into the neutrino mass analysis [Ake21b]. However, for tritium in a condensed state, as e.g. adsorbed on surfaces, such as the Rear Wall, the situation becomes significantly more complex. In addition to molecular excitations, there are interactions with neighboring atoms and the substrate, making the FSD for adsorbed tritium much harder to predict and more challenging to incorporate into neutrino mass analysis [Ott08].

In condensed sources, such as tritium adsorbed onto the Rear Wall there is a greater likelihood of electronic excitation of nearby atoms or molecules in addition to the excitations in the tritiated molecule itself. Solid-state effects, such as local lattice relaxation after the decay of bound tritium, can lead to a significantly different FSD compared to the gaseous state [Nde24; Ott08]. These additional interactions complicate the understanding of how energy is partitioned between the β-electron and the recoiling molecular system.

Without accurate knowledge of the FSD for adsorbed tritium, it becomes difficult to model the Rear Wall spectrum with precision as the endpoint fit parameter depends - to a good approximation - on the mean of the FSD [Ake21b]. A key challenge arises from the fact that the underlying FSD of adsorbed tritium remains largely unknown, especially when considering the possibility of different tritiated species such as tritiated hydrocarbons being present on the Rear Wall surface. As a result, describing the Rear Wall spectrum from theory includes large uncertainties.

While some tests have been conducted using various FSD models (see an excerpt in Figure 4.2), many of them do not include rotational and vibrational excitations or even solid-state effects that might be relevant for adsorbed tritium. Using these incomplete FSD models has already been investigated and resulted in the shifts in the measured endpoint energy E_0 as expected and no improvement of the fit quality. However, the limited statistics collected from the Rear Wall spectrum do not provide sufficient sensitivity to accurately probe the underlying FSD.

Given the limitations of current FSD models for adsorbed tritium the currently pursued approach focuses on more empirical methods, as explained in the next section.

4.3 Characterization of the Rear Wall Spectrum for the Neutrino Mass Analysis

The precise characterization of the Rear Wall spectrum is crucial for quantifying its impact on the measured β-spectrum, which in turn influences the accuracy of the neutrino mass determination. Key parameters for the description of the Rear Wall spectrum include the

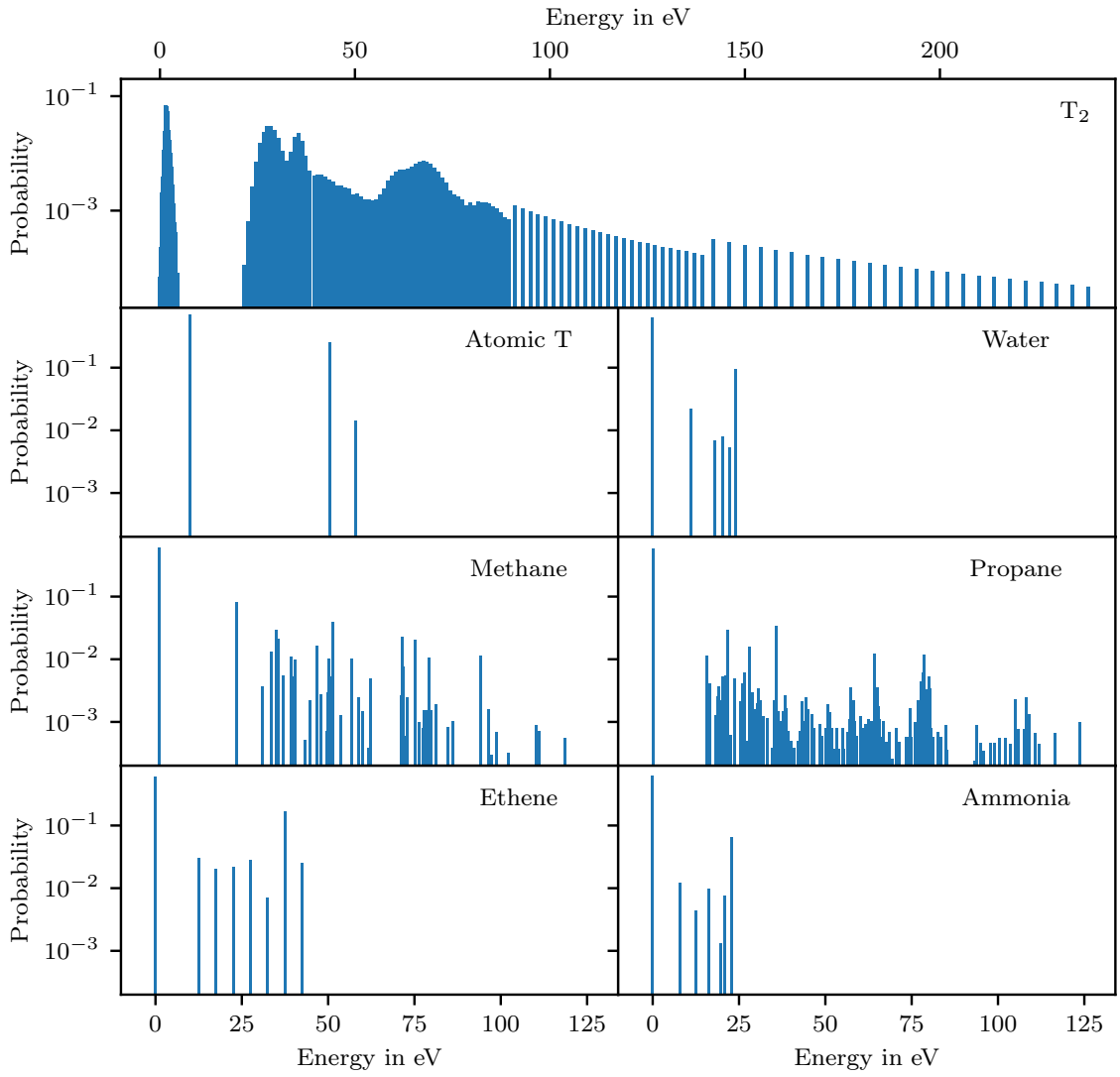

Figure 4.2: Discretized FSD of different tritiated molecules, as available in literature. In comparison the detailed T_2 FSD including rotational and vibrational excitation states used for the KATRIN m_ν analysis on top [Sae00]. The FSD of tritiated water [Iku77], methane [Cla92], propane [Hol92] and ethene [Kap88] lack those excitations. The FSD of atomic T [Ber71] is completely described without those excitations.

endpoint energy E_0 and the shape parameter $w_{\mathrm{GR,RW}}$, which accounts for uncertainties in the FSD, as well as the overall signal amplitude A_s. Properly considering these parameters is essential for minimizing systematic uncertainties and ensuring that the distortion introduced by the Rear Wall spectrum can be effectively accounted for.

The Rear Wall spectrum is characterized empirically through dedicated measurements. While the measurement procedure is detailed in Section 6.1.1, this section focuses on the

key spectrum parameters used for the characterization. The endpoint energy E_0 and the shape parameter $w_{\text{GR,RW}}$ is discussed in Section 4.3.1, and the signal intensity is covered in Section 4.3.2.

4.3.1 Endpoint Energy E_0

In β-decay, the endpoint energy E_0 defines the maximum kinetic energy that the emitted electron can reach.

For tritium decay, it is given by $E_0 = Q - E_{\text{rec}}$ [Ott08], where Q represents the decay energy and E_{rec} is the recoil energy of the daughter molecule. The recoil energy can be expressed as $E_{\text{rec}} \approx E \cdot \frac{m_e}{M_d}$ [Ang05], where M_d is the mass of the daughter molecule. In the case of tritium adsorbed on the Rear Wall (e.g., bound in some larger molecule), the mass M_d of the daughter molecule, is typically larger than that of the gaseous T_2 decay products, which leads to a higher endpoint energy E_0.

This difference in endpoint energy can result in a systematic shift in the measured spectrum, affecting the neutrino mass fit. In the case of the Rear Wall spectrum, the endpoint $E_{0,\text{RW}}$ is determined through fitting, where the neutrino mass m_ν is fixed to zero. However, as discussed in Section 4.2.3, uncertainties in the FSD of adsorbed tritium can lead to inaccuracies in determining $E_{0,\text{RW}}$, introducing a potential source of systematic error.

To address the uncertainties in modeling the FSD for surface-bound tritium, an additional free parameter is introduced: the FSD shape parameter $w_{\text{GR,RW}}$ [Köl]. This parameter scales the relative amplitude of the ground and excited states, effectively shifting the mean of the FSD. This allows for flexibility in the fit, compensating for the effect that an incorrect or unknown FSD might have on the determination of $E_{0,\text{RW}}$. Both parameters, $E_{0,\text{RW}}$ and $w_{\text{GR,RW}}$ are strongly anti-correlated, with a correlation value of roughly -0.96[3]. This approach takes the uncertainties arising from the complex interactions of tritium adsorbed on the Rear Wall into account.

4.3.2 Signal Amplitude A_s

The signal intensity of the Rear Wall spectrum is another critical parameter that must be properly characterized in order to assess its contribution to the overall measured β-spectrum. The stronger the signal from the Rear Wall spectrum, the more significant is its contribution to the measured spectrum. The normalization factor, A_s, typically accounts for the number of tritium atoms present in the source and also depends on other factors such as the acceptance angle θ_{max} of emitted electrons. However, since the Rear Wall spectrum is much smaller than the main signal from the gaseous tritium, it can only be measured when the source is evacuated of tritium. To make the intensity of the Rear Wall signal

[3] "Rear wall report for the KNM1-5 neutrino mass analysis", Internal Report by M. Aker, B. Daniel, S.Hickford, L. Köllenberger, B. Lehnert, G. Li, D. Parno and A. Schwemmer, 2023, KATRIN Collaboration

comparable to the primary tritium spectrum, a virtual reference is introduced [Köl]. This reference value corresponds to a column density of $\rho d_{\mathrm{RW}} = 3.75 \cdot 10^{21}\ \mathrm{m}^{-2}$, allowing the normalization factor $A_{\mathrm{s,\,RW}}$ to be expressed as:

$$\hat{A}_{\mathrm{s,RW}} = A_{\mathrm{s,RW}} \frac{\rho d_{\mathrm{RW}}}{\rho d_{\mathrm{KNM}i}}, \tag{4.3}$$

where $\hat{A}_{\mathrm{s,RW}}$ is comparable to the signal amplitude of the respective primary spectrum. The detailed process for measuring the Rear Wall spectrum is further described in Section 6.1.1.

Properly normalizing the signal intensity of the Rear Wall spectrum is essential for understanding how much it contributes to the total measured spectrum, allowing the effects of this secondary spectrum to be disentangled from the primary gaseous tritium spectrum by properly including it into the fit model. This is key to ensuring that the primary β-spectrum, which is most relevant to the neutrino mass analysis, can be isolated and analyzed without significant distortion.

4.4 Objective of this Work

The central objective of this work is the **development and implementation of a comprehensive strategy to mitigate the impact of tritium accumulated on the Rear Wall on the KATRIN m_ν analysis**. The accumulation of tritium on the Rear Wall introduces a secondary β-spectrum that distorts the measured data, affecting the accuracy of the m_ν determination. To address this challenge, the work is structured around several key objectives:

- **Understanding the Accumulation Process:** The first step is to develop a fundamental understanding of the underlying process of tritium accumulation on the Rear Wall. Similar processes in conditions comparable to the rear section of the KATRIN experiment described in literature will be identified and reviewed and a theoretical model for tritium accumulation will be developed in Chapter 5. This model will be tested throughout this work to ensure its accuracy in describing the behavior of tritium on the Rear Wall.
- **Development of Characterization Methods:** In order to accurately assess the impact of the Rear Wall spectrum on the measured β-spectrum, specific methods and measurements will be developed to characterize the secondary spectrum in Section 6.1 This includes identifying key parameters such as the endpoint $E_{0,\,\mathrm{RW}}$ and shape of the Rear Wall spectrum as well as its total amplitude, ensuring these are well understood and can be effectively incorporated into the neutrino mass analysis.
- **Direct Mitigation of Tritium Accumulation:** Practical methods for removing tritium from the Rear Wall will be explored and developed in Section 6.2. This includes

evaluating different cleaning techniques and their implementation as operational strategy to reduce the presence of tritium and minimize its impact on the experiment.

- **Characterization of the Evolution of the Secondary Spectrum:** The temporal evolution of the secondary β-spectrum will be studied in detail to describe how the spectrum changes over time and during β-scans in Chapter 7. This understanding is crucial for predicting the behavior of the spectrum during experiments and accurately estimating its impact on the data.
- **Providing Inputs for the m_ν Analysis:** By combining the knowledge gained from characterizing the secondary spectrum, mitigation techniques, and understanding the accumulation process, the work aims to develop a comprehensive approach to incorporating the Rear Wall spectrum into the KATRIN m_ν analysis in Section 7.4. This ensures that its impact is minimized and that the neutrino mass measurement is as accurate as possible.

A secondary goal of this work is to compile relevant knowledge gathered from the investigations performed within its scope into a broader understanding of the interaction between tritium and surfaces, which leads to tritium accumulation. The model developed in the next chapter will serve as the starting point for this endeavor. Based on this model, a set of predictions regarding the behavior of the accumulated tritium will be derived at the conclusion of the next chapter. These predictions will be evaluated throughout this work and further supplemented by insights gained into underlying processes that require additional efforts to fully uncover.

5 Tritiated Amorphous Carbon on the RW - Fundamentals and a Working Hypothesis

This chapter provides an overview of interactions of tritium with solid surfaces, highlighting both fundamental concepts and practical implications in the scope of the KATRIN experiment. Section 5.1 covers the underlying processes of tritium sorption on metal surfaces and focuses on the tritium-gold interactions that are expected to occur on the gold coated Rear Wall. In Section 5.2 amorphous carbon (aC) is introduced, with a focus on its growth process and the properties that influence tritium sorption and retention. In Section 5.3 a model describing the tritium accumulation and retention on the KATRIN Rear Wall is presented. From this model predictions relating the temporal and spatial behavior, spectral properties of the accumulated tritium and its dynamics during potential cleaning attempts are derived. Those predictions are compared to the experimental findings in Chapter 6 and Chapter 7.

5.1 General Concepts of Tritium Interactions on Metal Surfaces

The concepts of interest regarding the accumulation of tritium on the Rear Wall can be summarized under the notion of sorption. Sorption encompasses adsorption, absorption and desorption. Adsorption and absorption describe the accumulation of substances at the interfaces of different phases while desorption describes the reversed process [Hay64; Tom78]. In the scope of the present work the focus is set on the solid-gas interface as it is relevant to the Rear Wall and therefore the KATRIN experiment as a whole. The fundamental principles of those processes are discussed in Section 5.1.1. A more specific view on the sorption dynamics of hydrogen on gold surfaces is provided in Section 5.1.2.

5.1.1 Fundamental Principles of Sorption Processes

Adsorption processes depend on physical and chemical properties of both the adsorbate and the adsorbent, as well as the temperature of the system and the gas pressure. The interaction of gaseous particles with a solid body at its interface is mediated by forces acting between the gas molecules and the atoms on the surface of the solid. In the case of adsorption those forces attract the gas molecules, referred to as the adsorbate causing

them to adhere to the surface, referred to as the adsorbent [Tom78]. Based on the nature of the adhering forces, adsorption can be classified into physisorption and chemisorption [Atk13], which is discussed in Section 5.1.1.1 and Section 5.1.1.2, respectively.

In pronounced cases, adsorption can lead to multiple layers of adsorbate forming on the surface [Bar11]. Due to the short range of the adhering forces involved in chemisorption, multilayer adsorption is primarily a result of physisorption. However, depending on pressure and temperature, a weakly chemisorbed layer can sometimes form on top of already adsorbed layers in certain systems [Tom78].

5.1.1.1 Physisorption

The general properties of physisorption can be summarized as follows [Atk13; Iba06]:

- **Weak Binding:** Physisorption characteristically exhibits weak interactions between the adsorbate and the adsorbent. The mediating forces are dominantly van der Waals forces, which are significantly weaker than covalent or ionic bonds.
- **Reversibility:** The weak nature of the adhering forces lead to physisorption being a generally reversible process. The adsorbed molecules can easily desorb from the surface when the temperature is increased or the pressure is decreased.
- **Low Activation Energy:** The energy barrier for physisorption is relatively low, meaning that it can occur at lower temperatures compared to chemisorption.
- **Non-Specific Binding:** Due to the binding being mediated by the non-specific acting van der Waals forces, physisorption does not require specific chemical compatibility between the adsorbate and the adsorbent, making it applicable to a wide range of substances.

The acting van der Waals forces are based on fluctuations of the charge distribution of an atom [Zan88]. H. Ibach [Iba06] explains the formed potential in great detail. This explanation is summarized below. The fluctuation of the atomic charge distribution generates a dynamic dipole moment. This dipole moment generates an electric field that induces another dipole moment in a second atom [Pau20]. Consequently, an attraction is created between the two atoms, which depends on the distance r between them. This attraction is proportional to r^{-6}. Due to the Pauli exclusion principle, a repulsion arises at short distances between the atoms, which counteracts the attraction from the dipole moments. The repulsive contribution increases exponentially as the distance decreases. Often, this exponential dependence is approximated by a r^{-12} dependence. This results in the Lennard-Jones potential, with the equilibrium potential $-V_0$ occurring at the distance r_0:

$$V(r) = V_0 \left(\left(\frac{r_0}{r} \right)^{12} - \left(\frac{r_0}{r} \right)^{6} \right) \tag{5.1}$$

Considering the van der Waals forces of all the atoms in the solid yields the surface

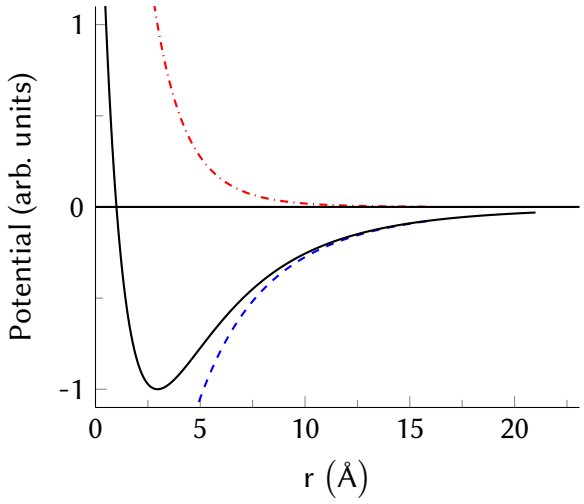

Figure 5.1: Behavior of the van der Waals Potential as a function of the distance r between the gas atom and the surface, according to Equation (5.2). The potential is composed of the attractive term due to dipole moments (blue dashed line) and the repulsive term resulting from the Pauli exclusion principle (red dash-dotted line). A minimum occurs a few angstroms away from the surface [Zan88].

potential

$$V_{\text{surf.}}\left(\vec{r}_{\text{atom}}\right) = V_0 \sum_{\alpha} \left(\left(\frac{r_0}{|\vec{r}_{\text{atom}} - \vec{r}_{\alpha}|} \right)^{12} - 2 \left(\frac{r_0}{|\vec{r}_{\text{atom}} - \vec{r}_{\alpha}|} \right)^{6} \right). \tag{5.2}$$

Figure 5.1 depicts how the interplay of the attraction of the dipol moments and the repulsion due to the Pauli principle forms a van der Waals potential. In the distance of a few Å to the surface a minimum is formed which results in a bond due to physisorption [Zan88].

5.1.1.2 Chemisorption

Some of the key properties of chemisorption are contrary compared to physisorption [Hay64; Tom78]:

- **Strong Binding:** The adsorbate forms chemical (covalent or ionic) bonds with the adsorbent, which are significantly stronger than the van der Waals forces involved in physisorption.
- **Irreversibility:** The strong adherent forces leads to significant energy required to reverse the adsorption. Once the chemical bonds are formed, the adsorbate is not easily desorbed from the surface.
- **High Activation Energy:** The formation of chemical bonds typically requires some activation energy. This leads to chemisorption generally occuring at higher temperatures than physisorption or requiring some other energy source.

- **Specific Binding:** Due to the chemical nature of the bonding, chemisorption is highly specific, depending on the chemical compatibility between the adsorbate and the adsorbent.

Chemisorption, in special cases, can be an endothermic process, unlike physisorption [Atk13]. Moreover, due to the nature of the bonds involved, the range of chemisorption is more limited compared to physisorption. Consequently, adsorption typically saturates once a monolayer is accumulated, unless the adsorbate itself is suitable to act as adsorbent.

In his "resonant level model", A. Zangwill [Zan88] introduces a simple framework for describing charge transfer and chemical bonding between gas molecules and metal surfaces (see Figure 5.2). This model is summarized in the following paragraph:

The adsorbate is represented by a potential well with a single bound state at energy $-|\varepsilon_a|$. For the adsorbent, the free-electron gas model is assumed. At a sufficiently large distance between the adsorbate and the adsorbent, both maintain their electronic structures. However, at shorter distances, the electronic wavefunctions of the adsorbate and the charge density on the metallic surface overlap. The combined system then possesses mixed eigenstates of the original systems, causing the sharp atomic state to broaden into a resonance. Through tunneling effects, charge exchange with the metal becomes possible. The energy level of the resonance shifts from ε_a to a new energy E. The nature of the surface bond depends on the relationship between the values of E and the Fermi energy E_F of the metal.

For large values of $|E - E_\mathrm{F}|$, a charge transfer occurs from the adsorbate to the adsorbent, resulting in an ionic bond. When the values of E and E_F are close, the adsorbate and adsorbent share electrons, forming a covalent bond. Figure 5.2 illustrates the latter case, and the shift from ε_a to E is neglected here, to simplify the depiction. The electronic structure of the entire system can also influence the difference $\varepsilon_\mathrm{a} - E$. Hydrogen chemisorption on thin Au films occurs in the presence of surface Au atoms of a low coordination number. Such an adsorbent can be obtained during thin Au film deposition on a glass support maintained at low temperature 78 K [Sto99]. The Au-H bond strength was found to be $\Delta E(Me - H) \approx 1\,\mathrm{eV}$ [Mil06].

5.1.2 Ad- and Desorption of Tritium on Gold Surfaces

The interaction of hydrogen with gold, particularly regarding adsorption or the formation of discrete Au-H bonds, has not been widely studied, and experimental data is scarce [Duś93; Sch14].

Hydrogen adsorption on metals generally exhibits distinct behaviors depending on whether the hydrogen is present in its atomic or molecular form. Experimental and theoretical studies have shown that molecular hydrogen adsorption is often an activated process [McL73; Ver00]. For instance, hydrogen adsorption on gold is characterized by an activation energy

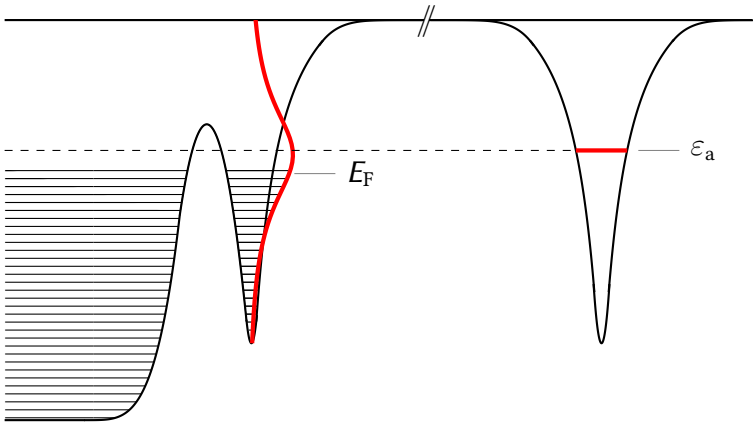

Figure 5.2: Schematic representation of energy levels according to the "resonant level model" adapted from [Zan88]. A single atom is represented by a potential well with a bound state ε_a (right). As the atom approaches a surface, the energy states overlap and mix (left). The sharp energy level of the electron broadens into a resonance (red), and tunneling effects occur. If the energy level ε_a is close to the Fermi energy E_F of the solid, a covalent bond forms. If the difference is large, an ionic bond is created.

value of 130 kJ mol^{-1}, making it an endothermic process with bond energies significantly lower than those of hydrogen with other transition metals [Ver00].

In contrast, atomic hydrogen can easily adsorb onto metal surfaces and can even be absorbed beneath the surface. Studies have demonstrated that atomic hydrogen adsorbed on thin Au films at 90 K increases the work function by approximately 120 mV at a coverage of around 0.2, with complete desorption occurring below 200 K [Pri63].

Furthermore, molecular hydrogen does not adsorb on gold surfaces at temperatures above 75 K [Sto92; Pri63]. This highlights the significant difference in adsorption behavior between atomic and molecular hydrogen, which is crucial for understanding the processes involved in hydrogen and tritium interaction with gold surfaces.

5.1.2.1 Adsorption Induced Dissociation of H_2

Adsorption of hydrogen on gold and other noble metals presents distinct challenges compared to transition metals. For transition metals, hydrogen molecules adsorb dissociatively over a wide temperature range (from about (50 to 500) K) [Chr88]. However, on noble metals like gold, spontaneous dissociative hydrogen adsorption does not occur due to a significant activation energy barrier [Har88].

This barrier arises because, as a hydrogen molecule approaches the surface of a noble metal, its 1s orbital overlaps with the outer tails of the electron wave functions of the metal. According to the Pauli exclusion principle, the metal electrons must adjust to remain orthogonal to the orbital of the hydrogen, increasing their energy and thus creating an activation barrier. This contrasts with transition metals, which have unfilled d-bands

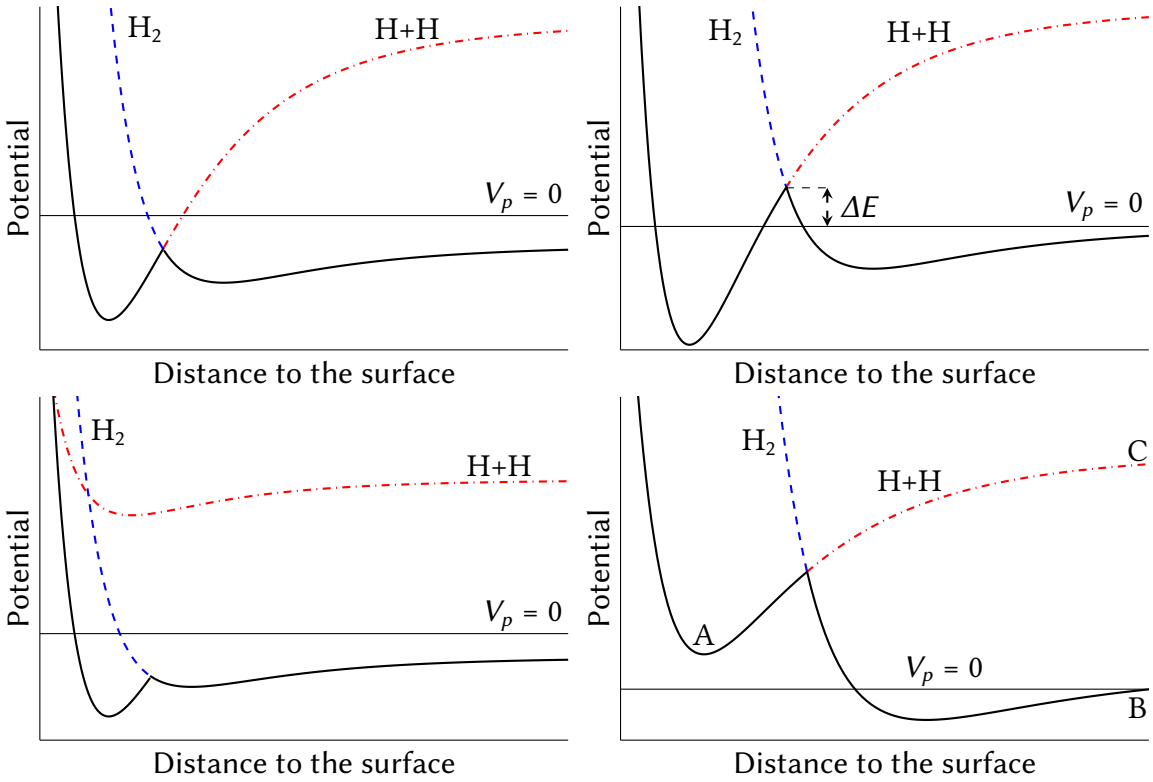

Figure 5.3: Schematic representation of the potential for dissociative adsorption. Blue dashed line: The van der Waals potential associated with physisorption between the molecule and the surface. Red dash-dotted line: Binding potential of dissociated atoms. Thick black solid line: The minimum of all involved potentials, representing the adsorption potential. The diagram illustrates cases of spontaneous dissociation of molecules (top left), activated dissociation (top right), molecular chemisorption (bottom left), and hydrogen adsorption on gold (bottom right). Diagrams based on [Zan88; Tom78].

allowing s-electrons to transfer into the d-band without energy loss, avoiding the energy increase and facilitating hydrogen adsorption [Duś93].

For noble metals, without such d-band holes, the s-electrons cannot transfer, leading to stronger Pauli repulsion and a higher activation barrier. Therefore, to achieve hydrogen chemisorption on noble metals like gold, one must use highly energetic hydrogen molecules or directly use hydrogen atoms to bypass the dissociation step.

The activated dissociation process of H_2 on noble metals is described by J. Harris [Har86] as an interaction between a metal dimer M_2 and a hydrogen molecule (H_2). Initially, the molecular orbitals of both the metal and hydrogen are distinct, with bonding and anti-bonding levels. As H_2 approaches M_2, these levels mix, resulting in bonding and anti-bonding combinations between M_2 and H_2.

As the separation between M_2 and H_2 decreases further, the energy of the system increases due to Pauli repulsion, as described earlier. Eventually, a critical point is reached where a

level crossing occurs: the M-H bonding level falls below the M-M and H-H bonding levels. This results in a sudden change in the electronic configuration, leading to the dissociation of H_2 into two MH units. This dissociation process is highly activated and involves a sudden change in the symmetry of the state, making it a "symmetry forbidden" reaction.

Dissociative adsorption can be qualitatively described using a Lennard-Jones model [Zan88]. In the initial physisorption stage, the molecule follows the van der Waals potential towards its minimum (represented by the blue dashed lines in Figure 5.3). The potential energy of the molecule at a large distance from the surface,$V_p = 0$, is shown as a horizontal thin line. If the molecule dissociates, the energy of the individual atoms would be higher than this level. As the atoms approach the surface, this energy decreases due to van der Waals forces (red dash-dotted line). If the atoms chemically bond with the surface, a pronounced minimum can form. The energy of the adsorbate then follows the minimum of all involved potentials (solid line).

If the two curves intersect below V_p, the molecule dissociates spontaneously (top left in Figure 5.3). If the transition occurs above V_p, as shown at the top right in the figure, the molecule is initially bound as a whole via physisorption. An activation energy ΔE, such as from high temperatures or radiochemical processes, is required for the system to reach the energetically favorable state of atomic chemisorption.

Another possibility is shown at the bottom left of Figure 5.3. Here, dissociation of the molecule is not energetically favorable, so chemisorption occurs directly following physisorption with the entire molecule.

The bottom right graph represents the situation for hydrogen adsorption on gold [Tom78]: The energy of two adsorbed H atoms (A) is higher than that of a free H_2 molecule (B) but lower than that of two free H atoms (C). Consequently, the atoms will only desorb without excitation if they recombine into a hydrogen molecule on the surface. Chemisorption occurs if the H_2 molecules dissociate before interacting with the surface and if the surface is sufficiently cold. The dissociation can occur thermally or as a result of radiochemical processes.

5.1.2.2 Desorption

Given that the temperature of the Rear Wall exceeds the temperatures reported for hydrogen adsorption on gold and is also higher than the temperature at which complete desorption occurs, the desorption mechanisms are discussed briefly.

Hydrogen desorption processes from gold are thoroughly discussed by Y. Koga and L. Harrison [Kog84]. Their explanation is excerpted below.

The presumption for this discussion is, that an adsorbed H_2 molecule dissociates and is held weakly as a precursor state to chemisorption. When the thermal energy is large relative to the barrier height, adatoms can freely move across the surface without being influenced by its atomic structure. At intermediate temperatures, adatoms become more

localized but frequently hop to neighboring sites. This mobility facilitates desorption via the Langmuir-Hinshelwood recombination mechanism, which predominates at higher coverages where adatom collisions are more likely. In this mechanism, two adatoms on the surface meet, recombine into a molecule, and then desorb.

Another relevant process is the Rideal-Eley mechanism, where an adatom recombines with a gaseous hydrogen atom impinging on the surface and subsequently desorbs.

The desorption rate for the Langmuir-Hinshelwood mechanism is proportional to the concentration of adatoms in quadrature, resulting in a hyperbolic desorption rate in vacuum, as numerically calculated by M. Babutzka [Bab14]. Since there is a lack of gaseous atoms for recombination, no desorption via the Rideal-Eley mechanism is expected during evacuation. Combined with the observation that the atomization process on the surface is pressure-dependent, this leads to the possibility of an equilibrium between adsorption and desorption during hydrogen or tritium exposure on a gold surface.

For the conditions at the Rear Wall, with a gold surface area of 141 cm^2, corresponding to approximately $2.14 \cdot 10^{17}$ surface sites, the equilibrium surface coverage is calculated as $\Theta = 6.83 \cdot 10^{-5}$ [Bab14]. This implies that the expected surface coverage is extremely low, corresponding to only about 0.05 % of a monolayer. According to the aforementioned numerical model, the adsorbed layer should be completely desorbed after approximately 500 s [Bab14].

5.2 Adsorbed Amorphous Carbon as Facilitating Basis for Tritium Adsorption

Despite the literature suggesting that hydrogen sorption on gold surfaces is generally negligible, significant adsorption of tritium has been observed on various gold-coated systems [Röl15; Ake20b] and specifically on the Rear Wall itself [Ake23]. This discrepancy between expectations and experimental findings can be explained by the presence of amorphous carbon (aC) as an intermediate layer that facilitates tritium adsorption.

An overview of aC, its characteristics, and formation processes relevant to the KATRIN experiment are discussed in Section 5.2.1. Section 5.2.2 elaborates on how amorphous carbon, can enhance tritium retention on surfaces where direct adsorption on gold would typically be minimal. In Section 5.2.3, cleaning methods aimed at removing accumulated tritium and counteracting re-accumulation by reducing the available amount of amorphous carbon are presented and the underlying processes discussed.

This section aims to reconcile the observed discrepancies between theoretical expectations of only negligible tritium accumulation occurring on gold surfaces and experimental realities, highlighting the role of amorphous carbon as a complicating factor.

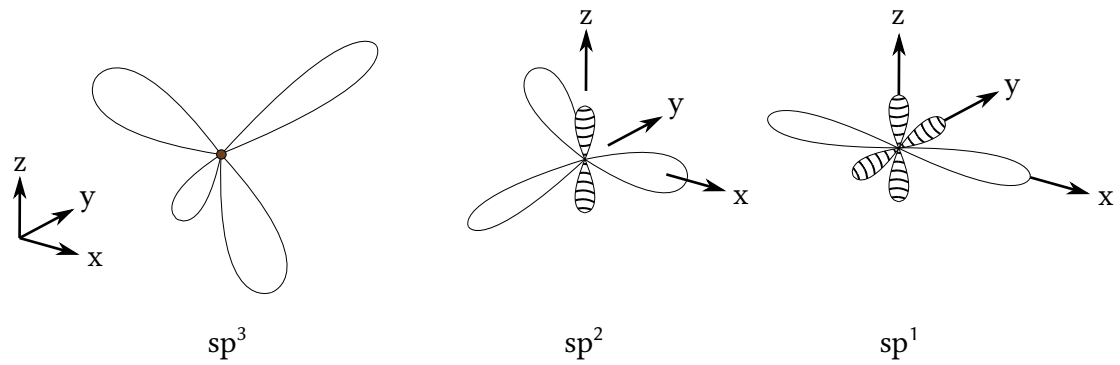

Figure 5.4: Schematic representation of sp^3, sp^2 and sp^1 hybridization of the carbon atom. The white orbitals are capable of forming strong σ bonds, while the striped one will form π bonds with adjacent atoms.

5.2.1 Amorphous Carbon and its Formation on the Rear Wall

Carbon is capable of bonding with other atoms in various configurations, namely sp^1, sp^2, and sp^3, as depicted in Figure 5.4 [Rob86]. In the sp^3 configuration, each of the carbon's four valence electrons is part of a tetrahedrally directed sp^3 hybrid orbital, forming strong sigma (σ) bonds with adjacent atoms. At sp^2 sites, three of the four electrons form trigonally directed sp^2 hybrids, which create σ bonds, while the fourth electron resides in a p_z orbital, normal to the σ bonding plane, forming weaker π bonds with adjacent p_z orbitals. In the sp^1 configuration, two electrons form σ bonds, and two others are left in orthogonal p_y and p_z orbitals to create π bonds. A σ bond between two atoms is called a single bond, while a $\sigma - \pi$ bond pair is referred to as a double bond. Hydrocarbons containing only single bonds are classified as "saturated", whereas those with double bonds, such as ethylene ($H_2C{=}CH_2$) or aromatic rings like benzene (C_6H_6), are termed "unsaturated".

These bonding variations enable carbon to form highly ordered compounds such as graphene, graphite, and diamond but also another unorganized structure called amorphous carbon (aC). While aC encompasses a wide range of properties [Jan85; Das91; Sil03], a common feature is the absence of long-range lattice order. Additionally, aC shows a high density of unsatisfied valences (unpaired electrons), known as dangling bonds [Jan85]. Those dangling bonds are prone to hydrogenation, which leads to their passivation and formation of hydrogenated amorphous carbon (aC:H).

Amorphous carbon generally consists of a mix of sp^3 and sp^2 bonding configurations, with little evidence of sp^1 [Rob86]. Some sp^1 bonding can be observed in aC:H structures, such as -C≡CH. According to J. Robertson [Rob03], the bonding in aC:H can be described as follows: Carbon sp^3 sites form a continuous network of C-C bonds, with most sp^3 sites bonded to one or more hydrogen atoms. The sp^2 sites form small clusters within this matrix.

The ratio between sp^3 and sp^2 bonding determines the material's optical and electrical properties and thus serves as a primary classification metric for amorphous carbon [Jac93; Rob02a]. When considering hydrogenated amorphous carbon (aC:H), the classification becomes more complex, as hydrogen content plays a significant role. This leads to a ternary phase diagram, as shown in Figure 5.5. The aC:H films can contain between 30 % and 60 % hydrogen, with about 30 % of carbon sites in an sp^2 configuration [Rob86].

These two factors - the sp^3/sp^2 ratio and the hydrogen content - define the short-range order in aC. However, they do not fully determine its structure [Rob86]. Common nomenclature for different categories of aC and aC:H includes:

- Graphite-like amorphous carbon (GAC),
- sp^3-rich tetrahedral amorphous carbon (ta-C),
- Diamond-like amorphous carbon (DAC or sometimes also DLC) and
- Polymer-like amorphous carbon (PAC),

each named after the carbon structures their dominant bond types are found in.

5.2.1.1 Properties of Amorphous Carbon

Amorphous carbon can exhibit a wide range of physical properties. Some forms of aC achieve high hardness, up to 65 GPa while others remain soft [Wad80; Sil03]. The material's density can range from (0.6 to 3.2) $\mathrm{g\,cm^{-3}}$, depending on its sp^3/sp^2 ratio and hydrogen content [Sil03].

The dangling bond density in aC is relatively high, though it can be passivated by hydrogen, making the material more chemically inert [Jan85].

The electrical properties of aC are highly dependent on deposition parameters. Conductivity at room temperature can vary by up to 12 orders of magnitude [Das91]. Higher hydrogen content tends to impede the formation of conductive sp^2 clusters, making the material more insulating, whereas films with lower hydrogen and higher sp^2 content exhibit better electrical conductivity.

5.2.1.2 Growth of Amorphous Carbon on the Rear Wall

While aC and particularly aC:H layers are commonly produced industrially using hydrocarbon plasma processes, this section will focus on scenarios where aC and aC:H are unintentionally created as contaminants [Rob02a; Kon16], which are relevant to the KATRIN experiment. As examples for those scenarios, processes involving electron induced aC and aC:H production are chosen. Those processes occur in accelerators, where e.g. photoelectrons are created by synchrotron radiation [Bol83]. Additionally those processes are a well known phenomenon in electron microscopes [Enn53; Har70; Din05]. The formation of aC/aC:H layers have been reported on steel [Enn54] and on gold [Cha10; Bol83].

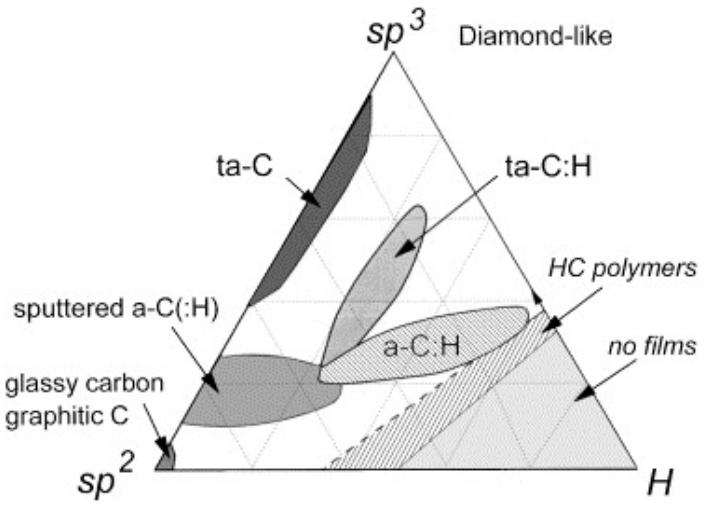

Figure 5.5: Ternary phase diagram of bonding in amorphous carbon–hydrogen alloys. The classification of aC:H structures is based on the ratio of sp^3 and sp^2 centers and the hydrogen content, as those properties significantly define the properties of the creates structure. Reprinted from Materials Science and Engineering: R: Reports, 37, J. Robertson, Diamond-like amorphous carbon, Pages 129-281, Copyright (2002), with permission from Elsevier [Rob02b].

Particularly interesting is the latter scenario, since a commonly used energy range for electrons in scanning electron microscopes is (5 to 30) keV [Sch12]. This range overlaps with the energy distribution of the β-electrons impinging on the Rear Wall, suggesting that similar conditions for the growth of aC and aC:H layers are present. Crucial factors for this growth include the presence of a vacuum environment and adsorbed hydrocarbons as precursor molecules, both of which are also met in the KATRIN RS. A significant reservoir of hydrocarbons is expected on the walls of a vacuum system as large as the KATRIN RS. Other sources include outgassing hydrocarbons from the Kapton® insulation of electrical components within the RS and from Viton™ parts in valve V1. Moreover, interactions between tritium and the carbon in the stainless steel walls of the system lead to the formation of tritiated methane [Stu21].

Given that all the conditions for the formation of aC/aC:H on samples irradiated by an electron microscope are also present on the KATRIN Rear Wall, the formation of these layers is expected on the Rear Wall as well. This process can be described analogously to the growth observed under an electron microscope which was detailed by W. Ding et al. [Din05]. This so-called Electron Beam Induced Deposition (EBID) process is schematically depicted in Figure 5.6.

The β-electrons impinge on the Rear Wall surface, which is coated with weakly adsorbed precursor molecules (P/P*). New molecules can arrive at the electron facing surface of the Rear Wall either by adsorption (A) or due to surface diffusion (M). The latter process plays a major role in the transport of mobile adsorbates along the surfaces of samples in electron microscopes [Het17]. Impinging β-electrons then scatter on the Rear Wall gold layer.

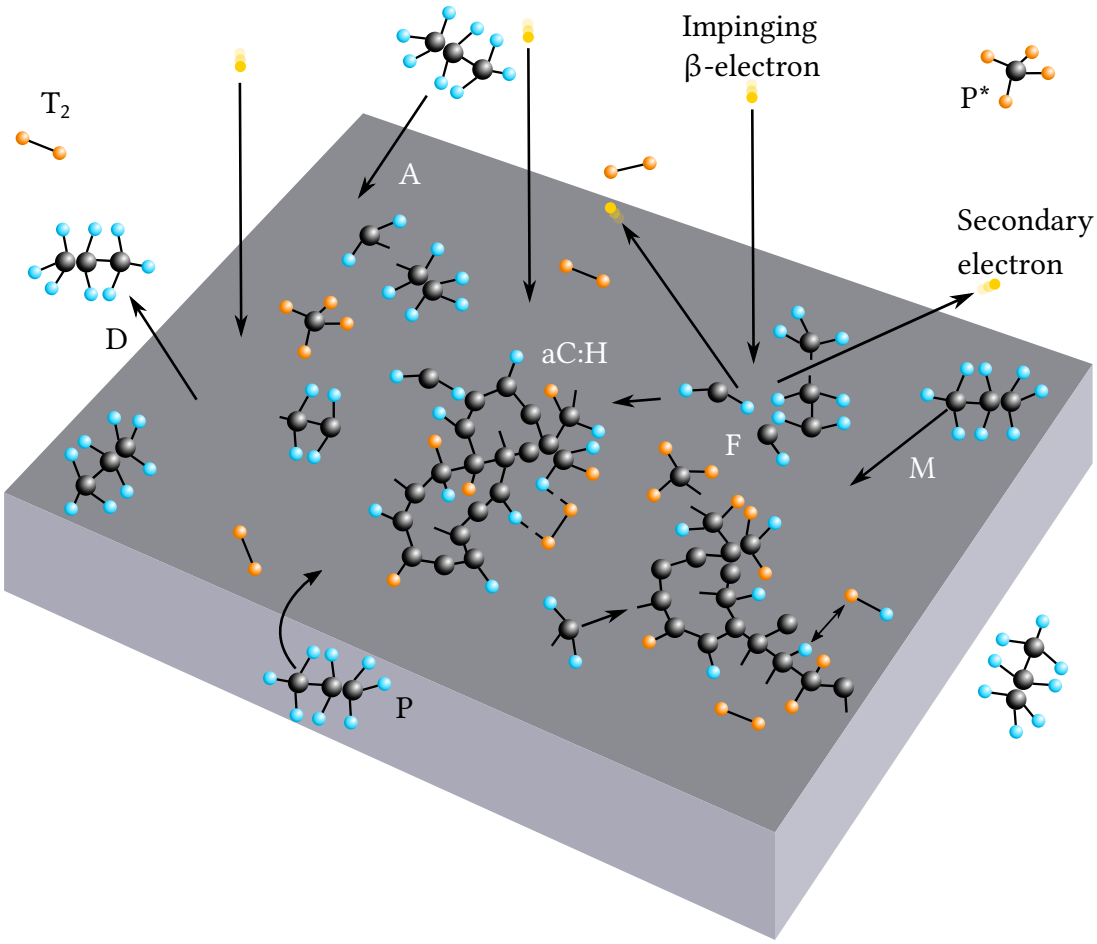

Figure 5.6: Electron induced aC:H formation. Impinging β-electrons create secondary electrons which dissociate tritiated (P*) and non-tritiated precursor molecules (P). The so-created fragments (F) polymerize forming aC:H on the surface, which can be further tritiated by nearby T_2. The growth of the aC:H layer depends on the adsorption (A), desorption (D) and migration (M) speeds of the precursor molecules. Adapted from [Din05].

During those processes secondary electrons are created, of which a significant amount are within an energy interval of (0 to 50) eV, according to simulations[1]. Electrons with these energies have a nearly optimal cross section to dissociate adsorbed hydrocarbons upon collision. Parts of the so-created fragments (F) can then polymerize on the irradiated surface, leading to the formation of aC:H.

According to S. Hettler et al. [Het17] this process leads to a local depletion of adsorbed hydrocarbons on the irradiated surface, creating a concentration gradient of adsorbed molecules. The polarizability of the fragments and charges induced by the impinging electrons possibly enhance this gradient further. Together, those effects result in surface

[1]D. Batzler: "Production of secondary electrons on the KATRIN Rear Wall". Personal communication. IAP-TLK, Karlsruhe Institute of Technology, Germany, 2024

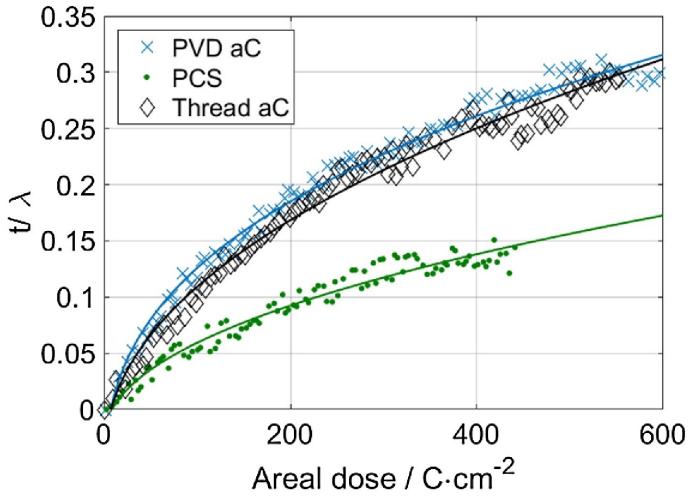

Figure 5.7: Growth rate of aC under an electron microscope. The plot shows the relative thickness (t/λ) over areal dose d_A for a PVD aC (blue, crosses), Thread aC (black, diamonds) and PCS (green, dots) thin film. The solid lines represents a fit of the function $t(d_\mathrm{A} = d_\mathrm{A}^a)$. Reprinted from Micron, 96, S. Hettler et al., Carbon contamination in scanning transmission electron microscopy and its impact on phase-plate applications, Pages 38-47, Copyright (2017), with permission from Elsevier [Het17].

diffusion of adsorbates from surrounding areas towards the irradiated area. Eventually, a quasi-steady state is reached between arriving molecules and the decomposition reaction induced by the β-electrons and secondary electrons leading to a constant deposition rate. The time required to reach this quasi-steady state depends on various factors, such as the surface diffusion coefficient or the initial adsorbate density.

The growth of aC layers on different substrates inside an electron microscope as a function of the areal dose d_A, as observed by Hettler et al., is depicted in Figure 5.7. The different substrates are aC deposited by electron beam evaporation (PVD aC) and by carbon-thread evaporation (Thread aC) and a sputtered $Pd_{77.5}Cu_6Si_{16.5}$ (PCS) film. For all samples an initial strong growth is visible, that later diminishes and converges towards a more linear increase, which coincides with the expectations of the model proposed by the authors. The authors described the data with a function for the plotted relative thickness $t/\lambda(d_\mathrm{A} = d_\mathrm{A}^a)$ and reported an result of $a \approx 0.5$.

Despite the differences in experimental conditions compared to those present at the Rear Wall, such as the different substrate and the fact that the areal dose rate is more than ten orders of magnitude higher than that at the Rear Wall surface, the underlying effects remain the same. The data in the plot, which depicts an exposure time of roughly 100 s, provides a qualitative understanding of the growth behavior which can be expected in KATRIN. While the specific conditions likely are different, this comparison offers valuable insights into the expected deposition dynamics on the Rear Wall.

5.2.2 Tritiation Processes of Amorphous Carbon

Three main processes of tritium accumulation due to the presence or growth of amorphous carbon (aC) can be identified:

- Direct formation of aC:T,
- Isotope exchange reactions and
- Adsorption of tritium on aC.

Which are discussed in Sections 5.2.2.1 to 5.2.2.3. All these processes contribute to an increase in activity alongside the growth of aC and may occur simultaneously. In reality, it is likely that a combination of these processes is responsible for the tritium accumulation.

5.2.2.1 Direct Formation of aC:T

The high purity and large amount of gaseous tritium in the KATRIN sources results in the formation of highly tritiated hydrocarbons within the WGTS [Stu21]. Any aC:H layer that grows from these tritiated hydrocarbons as precursor molecules will bind the contained tritium to the Rear Wall, leading to tritium accumulation with the growth of the aC layer. In industrial aC:H coating application, hydrogen is typically mixed into the plasma used for layer deposition [Jan85]. Although in KATRIN the formation process is driven by EBID, the presence of tritium near the hydrocarbon fragments forming the aC may still lead to tritium incorporation in the growing aC:H structure, even when the precursor molecules themselves are not tritiated.

5.2.2.2 Isotope Exchange Reactions

In addition tritium can also bind to surfaces through exchange reactions [Tan17]. In this process, tritium atoms from the gas phase replace hydrogen atoms from hydrocarbons or aC:H already present on the surface (see Figure 5.8). It has been observed that exposure of a hydrogen saturated aC:H film to a deuterium flux at room temperature results in isotopic exchange of hydrogen for deuterium [Wit96].

In similar constellations involving surface-bound water, isotope exchange is known to continue until the ratio of H to T in both the gas phase and on the surface is balanced [Nak01]. Given the high tritium concentration in the WGTS, it is expected that this process will continue until the aC:H layer on the Rear Wall is fully tritiated.

Dong et al. [Don15] investigated isotope exchange reactions resulting in the tritiation of hydrocarbons using density functional theory and transition state theory. Their calculations include two mechanisms.

- **Direct Exchange:**
  In this mechanism, isotope exchange occurs via a four-membered ring transition state, as illustrated in Figure 5.9. Here methane was chosen as an example since

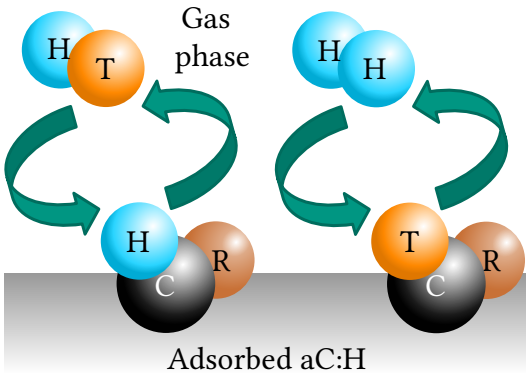

Figure 5.8: Schematic representation of isotope exchange with adsorbed aC:H (based on [Tan17]). Tritium atoms exchange with hydrogen atoms. The reactions can proceed in both directions, depending on the H to T ratio.

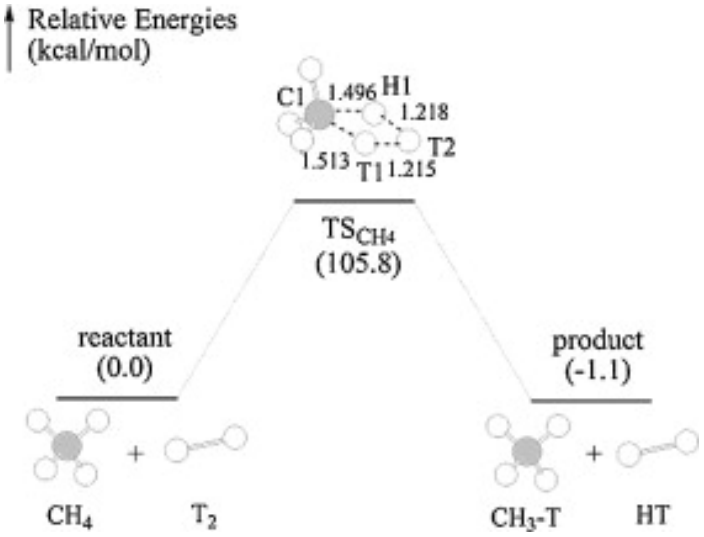

Figure 5.9: Reaction path of T-H isotope exchange of methane. Reprinted from Journal of Hazardous Materials, 287, L. Dong et al., Theoretical investigation of isotope exchange reaction in tritium-contaminated mineral oil in vacuum pump, Pages 42-50, Copyright (2015), with permission from Elsevier [Don15].

it is the simplest hydrocarbon molecule. The reaction starts with the T_2 molecule approaching the C atom to form a bond. Via hydrogen migration, a T-H exchange occurs, which is then followed by the expulsion of a HT molecule.

- **Hydrogenation-Dehydrogenation:**
  Hydrocarbons with unsaturated double bonds can undergo isotope exchange via a two-step process [Don15]. First hydrogenation adds T_2 to the C=C center (e.g. according to Reaction 5.3). In the second step dehydrogenation occurs and is released from a different position (Reaction 5.4).

Table 5.1: Isotope exchange mechanisms of selected hydrocarbon molecules. The involved mechanism, product, and branching ratio (%) of the different molecules of the T-H exchange reaction. Data taken from [Don15].

Species	Exchange mechanism	Product	Branching ratio
CH_4	Direct	CH_3T	–
C_2H_4	Hydrogenation-dehydrogenation	C_2H_3T	–
C_6H_6	Direct	C_6H_5T	–
CH_3COCH_3	Hydrogenation-dehydrogenation	CH_3COCH_2T	–
C_2H_5OH	Direct	$CH_2T\text{-}CH_2OH$	≈ 0
		$CH_3CHT\text{-}OH$	≈ 0
		CH_3CH_2OT	100
CH_3COOH	Direct	$CH_2T\text{-}COOH$	≈ 0
CH_3CHO	Direct	CH_3COOT	100
	Hydrogenation-dehydrogenation	$CH_2T\text{-}CHO$	≈ 0
		CH_3TCO	100

$$H_2C{=}CH_2 + T_2 \rightarrow TH_2C\text{-}CH_2T \tag{5.3}$$
$$TH_2C\text{-}CH_2T \rightarrow HTC{=}CH_2 + HT \tag{5.4}$$

In Table 5.1 various hydrocarbons investigated by L. Dong et al. are listed alongside their preferred isotope exchange mechanisms and the resulting products. Although oxygen-containing molecules are not expected in the Rear Wall environment, they are included in the table to demonstrate the universality of these processes.

Isotope exchange reactions can also be initiated by molecules ionized by radiation. An example reaction chain leading to tritiated methane triggered by the presence of T_2^+ is given below [Wex63]:

$$T_2^+ + CH_4 \rightarrow CH_2T^+ + H_2 + T \tag{5.5}$$
$$T_2^+ + CH_4 \rightarrow CHT_2^+ + H_2 + H \tag{5.6}$$
$$CH_2T^+ + CH_4 \rightarrow C_2H_4T^+ + H_2 \tag{5.7}$$
$$CHT_2^+ + CH_4 \rightarrow C_2H_3T_2^+ + H_2 \tag{5.8}$$
$$C_2H_4T^+ + e^- \rightarrow CH_2T + CH_2 \tag{5.9}$$
$$CH_2T + CH_4 \rightarrow CH_3T + CH_3 \tag{5.10}$$

Although methane is used as an example in this case, the passivation of radicals in Reactions 5.7 and 5.8 does not necessarily require methane; other hydrocarbon fragments

on the Rear Wall can also participate in similar reactions. Ionization of hydrocarbons can trigger similar reactions such as:

$$C_2H_5^+ + T_2 \rightarrow C_2H_4T^+ + TH \tag{5.11}$$
$$C_2H_4T^+ + e^- \rightarrow CH_2T + CH_3 \tag{5.12}$$

Further isotope exchange can occur via radiation-induced radical formation [Uda92]. Below are example reactions where R represents a group attached to carbon within a hydrocarbon molecule:

$$RCH \xrightarrow{\beta} RC \cdot H^+ + e^- \tag{5.13}$$
$$RC \cdot H^+ + e^- \rightarrow RC + H \tag{5.14}$$
$$T_2 \xrightarrow{\beta} 2T \tag{5.15}$$
$$RC + T \rightarrow RCT \tag{5.16}$$

When T_2 decays, it forms the stable molecular ion $^3HeT^+$ in about half of the cases [Fie92; Jon99; Sae00; Lin20]. After recombination with an electron, this molecule decays within 10 ns into atomic helium and tritium. In the remaining cases, atomic tritium (ionized or neutral) is produced directly following the β-decay. This atomic tritium, along with the tritium formed in Reactions 5.5 and 5.16, can contribute to tritiation of hydrocarbon species on the Rear Wall.

5.2.2.3 Adsorption of Tritium on aC

This third process involves the tritiation of an existing amorphous carbon (aC) structure through the chemisorption of tritium, with several mechanisms contributing to this process, which are discussed in the next paragraphs.

A detailed atomistic description of aC reactivity is challenging due to its disordered nature. However, first principle studies have identified the most reactive sites for hydrogen chemisorption, showing high adsorption energies ranging from (2.42 to 4.15) eV for specific sp^1 and sp^2 configurations [Car18]. Less reactive sp^3 configurations, in contrast, exhibit lower adsorption energies around 0.83 eV. Especially those high adsorption energies indicate significant potential for tritiation within an existing aC layer. Experimental studies verify that hydrogen and deuterium atoms efficiently hydrogenate sp^1 and sp^2 carbon centers, such as unsaturated CH groups, located on the surface of the aC layer [Wit96].Those hydrogenation reactions occur with negligible activation energy barriers and are in certain cases able to cleave C-C bonds [Jar09].

Further tritiation possibilities arise from the presence of dangling bonds. The disordered structure of aC contains these unsatisfied valence electrons of carbon atoms, making

them highly reactive, with the addition cross section of a H atom to a dangling bond being $\sigma_{\text{add}} = (1.3 \text{ to } 4.5)\,\text{Å}^2$ [Küp95]. Additionally, the continuous generation of secondary electrons from the Rear Wall creates new dangling bonds, offering even more opportunities for tritium to bond with the aC structure. Incident hydrogen atoms, which can penetrate the aC film up to about two nanometers, are known to passivate these broken bonds effectively [Hop05].

Spontaneous H_2 splitting on amorphous carbon surfaces has also been demonstrated through DFT calculations, indicating that tritiation of aC on the Rear Wall doesn't necessarily depend on the presence of atomic tritium but can also occur through interactions with molecular tritium [Che24].

Tritium in the aC:T structure exhibits low mobility, as predicted by DFT and AIMD calculations at 300 K, which makes aC:T an effective retainer of tritium activity on the Rear Wall [Che24]. However, there are potential escape paths for tritium within the aC:T structure. Repeated bond-breaking and re-passivation events can lead to the formation of volatile hydrocarbon species at or near the surface. These species can then diffuse to the surface and desorb from the film [Hop05]. Additionally, hydrogen etching of aC:T, where both hydrogen atoms and ions react with aC, can result in volatile reaction products that leave the aC film.

Incoming hydrogen can further lead to the dissociation of surface-bound hydrogen through hydrogen abstraction. However, the cross-section for this process is relatively low, around $0.05\,\text{Å}^2$, and is considerably smaller than the likelihood of hydrogen adding to the newly created dangling bond [Küp95]. These dangling bonds can recombine to form new C-C bonds, meaning that hydrogen abstraction can theoretically reduce the hydrogen content in the amorphous carbon layer. However, for this recombination to occur, structural changes within the amorphous network are required. This process leads to a stoichiometric limit of H/C ≈ 1, representing the upper bound for hydrogen-induced reduction of the hydrogen content in the layer [Keu03].

For ion-stimulated etching, the removal probability is approximately 0.1 carbon atoms per incident hydrogen atom. In contrast, for atomic hydrogen etching alone, the removal probability is significantly lower, ranging between 10^{-4} and 10^{-6} carbon atoms per incident hydrogen atom [Leu21], with ion energies of (10 to 20) eV [Bra12].

5.2.3 Cleaning Procedures to Reduce Surface-Near Tritium Activity

Some tritium removal from the Rear Wall could theoretically occur due to etching by tritium ions. The tritium ions in the WGTS are mostly thermal and primarily consist of cluster ions, e.g. T_3^+, T_5^+. However, it remains uncertain whether significant etching actually takes place. Studies have shown that an incoming flux of low-energy hydrogen ions can enhance the erosion yield of atomic hydrogen when etching graphite, but it can also inhibit the erosion yield in the case of etching a aC:H film [Von96]. Furthermore, these tritium cluster

ions dissociate upon neutralization, releasing free tritium atoms, which are then available for further tritiation [Bab14]. Therefore, no substantial tritium removal is expected from this process.

To effectively mitigate the accumulation of tritium, active measures are necessary. Considering the tritiation mechanisms discussed in Section 5.2.2, decontamination techniques based on similar mechanisms are explored. These methods fall into two categories:

1. Direct tritium removal from the adsorbent and
2. Removal of the aC:T entirely.

The available options are discussed in the following.

5.2.3.1 Direct Tritium Removal from the Adsorbent

The least invasive methods focus on using isotope exchange reactions or dissociation of hydrogen from aC to remove tritium by UV illumination.

- **Isotope Exchange Reactions:** Exposing the aC:T layer on the Rear Wall to pure hydrogen/deuterium gas can trigger isotope exchange reactions, where tritium is replaced by hydrogen/deuterium and removed from the aC:T layer. Additionally, exposure to water vapor [Tor02] can reduce tritium in cases where residual surface water has become tritiated. This method leverages the concentration gradient to drive the exchange, resulting in diminishing decontamination rates over the progress of the procedure.
- **UV Illumination:** UV light is considered to be able to desorb tritium from aC:T by breaking C-T bonds [Oya01a]. However, there are reports attributing this etching effect to ozone formation directly on the surface instead of direct interaction of the UV light with the substrate [Ish97]. Although not primarily focused on tritium removal, previous investigations on the Rear Wall have shown no significant impact on surface properties, such as the work function, due to UV illumination [Sch16].

Both of these methods, while removing tritium from the Rear Wall, face re-accumulation challenges. After removal, re-adsorption of tritium is expected to happen quickly, as the isotope exchange is driven by the concentration gradient, and hydrogen dissociation from aC leaves reactive dangling bonds that can bond with new tritium.

5.2.3.2 Removal of aC:T to Reduce Tritium Adsorption Sites

A more robust, yet more invasive approach is to remove the aC:T layer entirely using UV/ozone cleaning, thereby diminishing the adsorption possibilities for tritium on the Rear Wall.

UV/ozone cleaning is an effective method for removing hydrocarbons from surfaces through UV-ozonolysis, the combined use of UV light and ozone [Vig85]. This method is commonly

used in electron microscopy to mitigate carbon contamination [Hoy11] and has been effectively used to remove tritiated carbon contaminations by various groups [Shu01; Gen02; Lar22].

The process involves multiple chemical steps, including the formation and dissociation of ozone, followed by the decomposition of the carbon structure through the Criegee mechanism.

- **Ozone Formation:** UV light at 185 nm dissociates molecular oxygen (O_2) into atomic oxygen (O). This atomic oxygen then combines with O_2 to generate ozone (O_3) [Vig85].
- **Ozone Dissociation:** UV light at 254 nm dissociates O_3 into O_2 and atomic oxygen (O) [Vig85], producing a highly reactive oxygen radical that can break down hydrocarbon chains [Li22].
- **Criegee Mechanism:** The functionality of UV-ozonolysis is driven by the Criegee mechanism [Cri75]. This process is depicted in for an exemplary reaction in Figure 5.10. It begins with O_3 adding across a carbon-carbon double bond. This forms an unstable cyclic compound called the primary ozonide (see 1 in Figure 5.10).

  In the next step, the primary ozonide decomposes into a carbonyl oxide (Criegee intermediate) and a carbonyl compound (either an aldehyde or a ketone), as shown in the first elements on the left path in Figure 5.10. The precise details of the reaction pathways require more minute investigation [Gel98]. This is especially true in cases like those depicted in Figure 5.10 (steps 2-3), where a crossover experiment results in a labeled oxygen atom appearing in different positions depending on the actual reaction path. However, for the scope of this work, it is sufficient to note that the intermediates typically react to form secondary ozonides. These ozonides eventually break down into smaller, volatile molecules. Some Criegee intermediates may also decompose or isomerize into dioxiranes, which further break down into volatile products [Che22; Cre98].

Regardless of the specific underlying reactions - whether oxygen radicals breaking down hydrocarbon chains or the decomposition of structures via the Criegee mechanism - the cleaning effect is achieved by fragmenting the carbon compounds into smaller, volatile hydrocarbons. These fragments desorb from the surface and can then be removed from the system through evacuation.

5.3 Expected Dynamics of Tritiated aC on the Rear Wall

Significant tritium sorption on a gold surface is not expected without the presence of a carrier substrate. To explain the observed persistent tritium accumulation on the Rear Wall, a carrier material is required. As discussed in Section 5.2.1 and Section 5.2.2, the formation aC:T is a plausible scenario given the environmental parameters within the KATRIN Rear

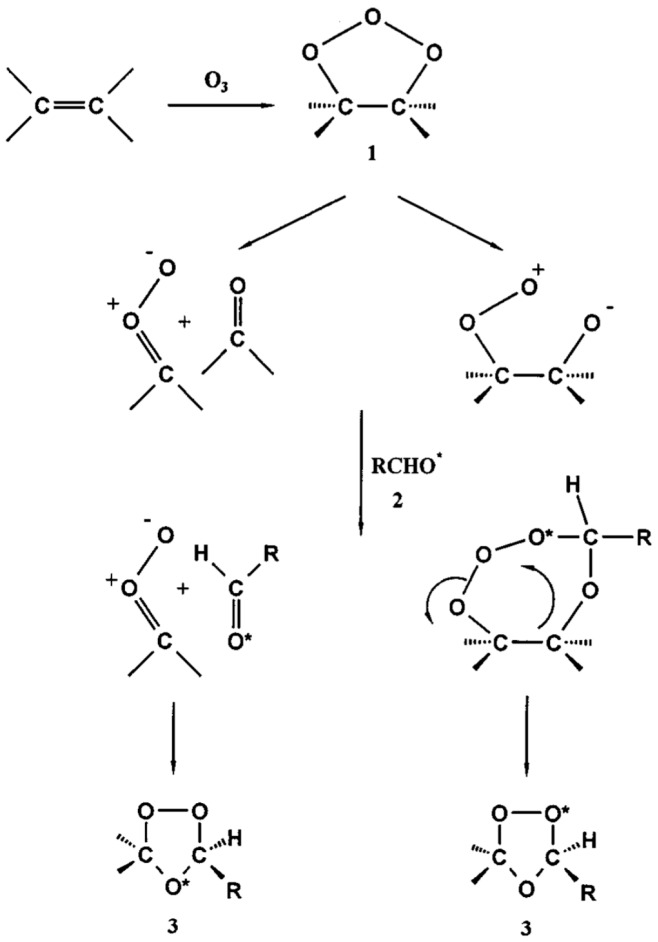

Figure 5.10: Formation of Criegee intermediates (1) and their further reaction path if allowed to react with a labelled aldehyde (2). Depending on the underlying mechanism the oxygen label in different regions of the resulting secondary ozonide (3). Reprinted from European Journal of Organic Chemistry, 1998, Stefan Berger and Christian Geletneky, The Mechanism of Ozonolysis Revisited by ^{17}O-NMR Spectroscopy, Pages 1625-1627, ©WILEY-VCH Verlag GmbH, D-69451 Weinheim, 1998, with permission from John Wiley and Sons [Gel98].

Wall chamber. Based on these considerations, a working hypothesis - closely resembling the EBID processes occurring in electron microscopes - is presented in Section 5.3.1, followed by verifiable predictions derived from this hypothesis in Section 5.3.2.

5.3.1 Working Hypothesis of the Underlying aC:T Formation Process

Multiple processes likely occur in parallel, contributing to tritium accumulation on the Rear Wall. Identifying and verifying the precise contribution of each process would require

sophisticated instrumentation, which is currently unavailable due to spatial and other constraints and is not justified by the effort required. However, the main aspects and outcomes relevant to the KATRIN experiment can be measured and will be discussed in later chapters. The proposed process consists of the following five mechanisms:

1. **Precursor Hydrocarbons:** A reservoir of both tritiated and non-tritiated hydrocarbons is available in the KATRIN system. This reservoir includes hydrocarbons initially present on system surfaces, those outgassing from components such as Kapton® and Viton™, and hydrocarbons generated through radiochemical reactions between tritium and the carbon in the stainless steel walls, as discussed in Section 5.2.1.
2. **Hydrocarbon Migration:** The hydrocarbons migrate towards the Rear Wall within the KATRIN system. While direct adsorption of gas-phase hydrocarbons onto the Rear Wall is expected, significant migration of hydrocarbons occurs via surface diffusion, driven by a concentration gradient.
3. **Secondary Electron Production:** Beta-electrons impinging on the Rear Wall generate secondary electrons with energies of $\mathcal{O}(10\,\mathrm{eV})$.
4. **Hydrocarbon Dissociation and Polymerization:** Hydrocarbons on the Rear Wall are dissociated by these secondary electrons. The resulting fragments polymerize on the Rear Wall surface, forming aC:H, which becomes firmly bound to the Rear Wall. The amorphous structure of the growing layer and continuous bond-breaking by secondary electrons create dangling bonds.
5. **Accumulation of Tritium:** Tritiation of the aC:H layer occurs through several mechanisms, including the accumulation of tritiated precursor hydrocarbons, tritium bonding with dangling bonds, and isotope exchange reactions, leading to a progressively tritiated aC:H layer.

This hypothesis lays the foundation for understanding the processes responsible for tritium accumulation on the Rear Wall and sets the stage for verifiable predictions in the next section.

5.3.2 Predicted Effects of the Electron Induced aC:T Formation Process

The underlying process, outlined in Section 5.3.1 can be used to derive the following nine predictions:

Prediction 1 **Tritium Accumulation:** Tritium will accumulate on the Rear Wall as the dosage increases, similar to the layer growth observed by S. Hettler et al. [Het17], shown in Figure 5.7. This accumulation can be observed as an increasing number of β-electrons emitted from the Rear Wall while the WGTS is evacuated. The growth of this Rear Wall rate is expected to initially show saturation behavior, then transition into a linear growth phase as a

steady deposition rate is reached, as discussed in Section 5.2.1. To reflect the long exposure times during KATRIN operation and the prominence of the quasi-steady state, Equation (5.17) is chosen to describe the rate evolution, where f represents the tritium throughput.

$$R_{\mathrm{RW}}(f) = a \cdot \exp\left(-k \cdot f\right) + b \cdot f \tag{5.17}$$

Prediction 2 **Shift of the β-Spectrum:** Tritium bound to carbon will produce a β-spectrum with a higher endpoint, as discussed in Section 4.3.1.

Prediction 3 **Electron-Induced Tritium Accumulation:** Accumulation is driven by the EBID process and thus only occurs in regions where electrons impinge on the surface.

Prediction 4 **Tritium Retention:** Tritium is firmly bound within the aC:T matrix, so no significant reduction in tritium is expected due to:

- Purging of the system with inert carrier gases,
- Desorption in an evacuated system,
- Heating and
- UV illumination in an evacuated system. Altough this is expected according to the findings of Y. Oya et al. [Oya01a] the effect is though disfavored by the earlier mentioned findings of [Ish97] and [Sch16].

Prediction 5 **Tritium Removal:** Reduction of the observed activity can be expected by methods which either extract tritium from the aC:T matrix or remove the aC:T altogether, e.g.:

- Isotope exchange,
- UV/ozone cleaning, which is known to effectively remove aC:H.

Prediction 6 **Quick Regeneration After Cleaning:** If the aC layer is not completely removed during cleaning, quick regeneration of tritium accumulation is expected. This is due to newly created dangling bonds and increased hydrocarbon migration along surfaces driven by a higher concentration gradient. The second effect also results in quick reformation of the aC:T layer if the previous layer was completely removed.

Prediction 7 **Activity Distribution:** Depending on the initial distribution of precursor hydrocarbons on the Rear Wall, the spatial distribution of tritium accumulation may vary. After sufficient cleaning, this distribution should approach a more homogeneous state as the initial layer is removed.

Prediction 8 **Exhaustion of Hydrocarbon Reservoir:** After extensive cleaning, the hydrocarbon reservoir within the system should be depleted. This will result in: a) A cessation of tritium accumulation, with the final saturation level dependent on the remaining hydrocarbons and other tritium binding

mechanisms on gold (as discussed in Section 5.1.2). b) Observable desorption of weakly bound tritium on gold in an evacuated system.

Prediction 9 **Change of Work Function:** While the exact work function of the growing layer is unknown, for ta-C a range of (4 to 5) eV is reported [Har00]. While this is near the work function of gold, the accumulation of aC:T on the Rear Wall can result in a decrease of the work function, depending on the properties of the growing layer. An increase of the work function is expected when the Rear Wall is cleaned.

Prediction 1 and Prediction 2 are crucial for understanding the impact on the KATRIN analysis, as they provide insights into how the secondary β-spectrum influences the determination of the neutrino mass. Adequately addressing these predictions is essential for mitigating any potential effects on the analysis.

Predictions 3 to 5, on the other hand, center on the critical role of aC:T, specifically how this material facilitates tritium accumulation and retention on the Rear Wall. Confirmation of Predictions 1 through 5 is fundamental to validating the working hypothesis, as any deviations would challenge its validity and necessitate modifications.

Predictions 6 through 8 describe the dynamics of the adsorbate, which are sensitive to system conditions and may vary based on several hard to quantify parameters, e.g. the availability of precursor hydrocarbons. Discrepancies between the predicted and observed behaviors provide deeper insights into the processes involved and shed light on otherwise inaccessible factors that may be influencing the system.

Predictions 1 to 8 were tested as part of this work and are discussed in Chapter 6 and Chapter 7. The exact sections containing the corresponding results are detailed in Table 5.2.

Testing Prediction 9 is beyond the scope of this work, as it has been the focus of earlier investigations [Sac20] and remains an ongoing area of research. However, the importance

Table 5.2: Overview of Predictions 1-9 with references to the relevant sections where the corresponding results are discussed.

Prediction	Relevant section
Prediction 1: Tritium Accumulation	7.1.2.2
Prediction 2: Shift of the β-Spectrum	6.1.1
Prediction 3: Electron-Induced Tritium Accumulation	7.2.2.1
Prediction 4: Tritium Retention	6.2.2
Prediction 5: Tritium Removal	6.2.2
Prediction 6: Quick Regeneration After Cleaning	7.1.2.1 and 7.1.2.2
Prediction 7: Activity Distribution	7.1.2.5
Prediction 8: Exhaustion of Hydrocarbon Reservoir	7.1.2.2 and 7.1.2.3
Prediction 9: Change of Work Function	-

and impact of the work function are briefly discussed here. As outlined in Section 3.5, the work function of the Rear Wall plays a crucial role in determining the starting potential of tritium β-electrons in the WGTS. The difference between the work function of the Rear Wall and that of the beam tube walls is particularly significant [Mac21]. Changes over time can lead to a shift in the spectrum's endpoint, resulting in a broadening of the resulting combined spectrum, which causes issues similar to those of the residual spectrum, as discussed in Section 4.2.

Additionally, plasma and Q-value analysis [Ake24a] require that the work function values during m_ν measurements and systematics measurements, such as those involving krypton, remain consistent. Initial measurements of the work function were possible [Sac20] but became challenging after KATRIN began operation due to tritium background. These measurements showed work function values approximately 1 eV lower than expected for pure Au, which can be attributed to surface impurities [Ake21a], as indicated by Prediction 9. This discrepancy necessitates long-term extrapolation of the work function values [Ake24a].

During operation of KATRIN, a drift in the work functions was observed. Ideally, cleaning procedures would reduce this drift by depleting the reservoirs of impurities that accumulate on the surface, in line with Prediction 8.

6 Accumulated Tritium on the Rear Wall: Observation and Removal

In order to mitigate the systematic impact on KATRIN's neutrino mass result caused by the secondary tritium β-spectrum created by tritium adsorbed on the Rear Wall, two complementary approaches are pursued. Firstly, the contribution to the measured spectrum, which results from the overlap of the primary spectrum from the gaseous tritium and the secondary spectrum, is considered in the analysis. This necessitates a comprehensive understanding of the secondary spectrum, including its characteristics and its overall impact to the measured spectrum. Secondly, as a direct countermeasure to the secondary spectrum the adsorbed tritium is removed from the Rear Wall. Section 6.1 describes how the secondary spectrum is measured, how the data is analyzed and discusses the characteristics of the secondary spectrum. In Section 6.2 the results of investigated Rear Wall cleaning procedures are reported. The decontamination effectiveness of each of multiple investigated procedures are presented and a suitable candidate for repeated cleanings is identified. In Section 6.3 the obtained results are probed to gain insights on the underlying state of tritium bound to the Rear Wall.

6.1 Rate and β-Spectrum of Tritium on the Rear Wall

In this section different approaches to describe and quantify the observable β-decay electrons of tritium accumulated on the Rear Wall are presented. The emitted β-electrons can be directly observed using the KATRIN FPD, which, together with the main spectrometer, allows for recording of the integral β-spectrum, which is discussed in Section 6.1.1. The details of the performed measurements are outlined as well as the spectral shape and the discovered differences to the spectrum of β-electrons being emitted from the gaseous tritium source. The method to determine the activity on the Rear Wall using the FPD is presented in Section 6.1.2. This method is complemented by indirect observation via Beta-Induced X-ray Spectrometry (BIXS) which allows for continuous monitoring when the beam line is not available. A conversion factor is derived that allows quantification of tritium accumulated on the Rear Wall based on the rate of β-electrons from the Rear Wall observed with the FPD. Considered uncertainties and systematic effects are discussed.

6.1.1 The Spectrum of Tritium on the Rear Wall

After a prolonged period of tritium circulation, measurements were conducted with KATRIN while tritium circulation was halted and residual gas was evacuated from the WGTS. The results revealed a secondary spectrum that closely resembles that of tritium. Due to the flux tube's constraints regarding the propagation of electrons the only possible origin is tritium adsorbed on Rear Wall, since electrons emitted from beam tube walls would be magnetically reflected. This is verified by measurements with valve V0 closed which separates the Rear Wall chamber from the WGTS, resulting in a significantly reduced observed rate, confirming the Rear Wall as the source.

As discussed in Section 2.3 the neutrino mass analysis is sensitive to the shape of the recorded tritium β-spectrum. Thus, it is important to investigate the shape of the secondary spectrum, which overlaps the primary spectrum from gaseous tritium distorting its shape and leading to systematic bias on m_ν. The shape of the spectrum can be expressed using the parameters discussed in Section 4.3. The rate of the observed secondary spectrum is approximately two orders of magnitude lower compared to the measured spectrum recorded during nominal operation of the WGTS. Since the rate is low and the available measurement time is limited, efforts have been made to sufficiently describe the secondary spectrum despite the low statistics.

Focus was set to determine the endpoint of the secondary spectrum $E_{0,\mathrm{RW}}$ as the main characteristic for describing the secondary spectrum. This parameter can still be resolved sufficiently well with low statistics. An optimized MTD was developed to achieve maximal sensitivity on the endpoint for those so-called Rear Wall scans. The MTD consists of equidistant measurement points spaced 4 eV apart, spanning the range from (18 454 to 18 574) eV, and five more points in 2 eV steps up to 18 584 eV. Each point has an acquisition time of 2.5 min. Apart from the dedicated MTD and the empty source, the Rear Wall bias voltage is set to 0 V for those measurements. All the other parameters of the measurement setup correspond to those of the standard β-scans. The transition from performing scans in NAP setting to SAP setting was also applied to the Rear Wall scans. Consequently, some early scans were conducted in NAP mode, followed by subsequent scans in SAP mode. With a measurement time of 4 h per scan, coupled with the time required for evacuating the source firstly and allowing it to reach equilibrium afterwards, the Rear Wall scans are typically performed during dedicated systematics campaigns close to maintenance phases. This approach minimize the disruption of the β-scanning. Depending on the accumulated amount of tritium on the Rear Wall the measurement time to reach sufficiently high statistics varies, resulting in total measurement times of two to four days per Rear Wall scan measurement.

In Figure 6.1 the secondary spectrum of a Rear Wall scan is depicted next to the measured spectrum recorded during nominal operation, with the best fit for each dataset and the resulting endpoint being highlighted. Both fits were performed using the FSD for gaseous T_2. Since this is not the expected form of bound tritium on the Rear Wall as discussed in

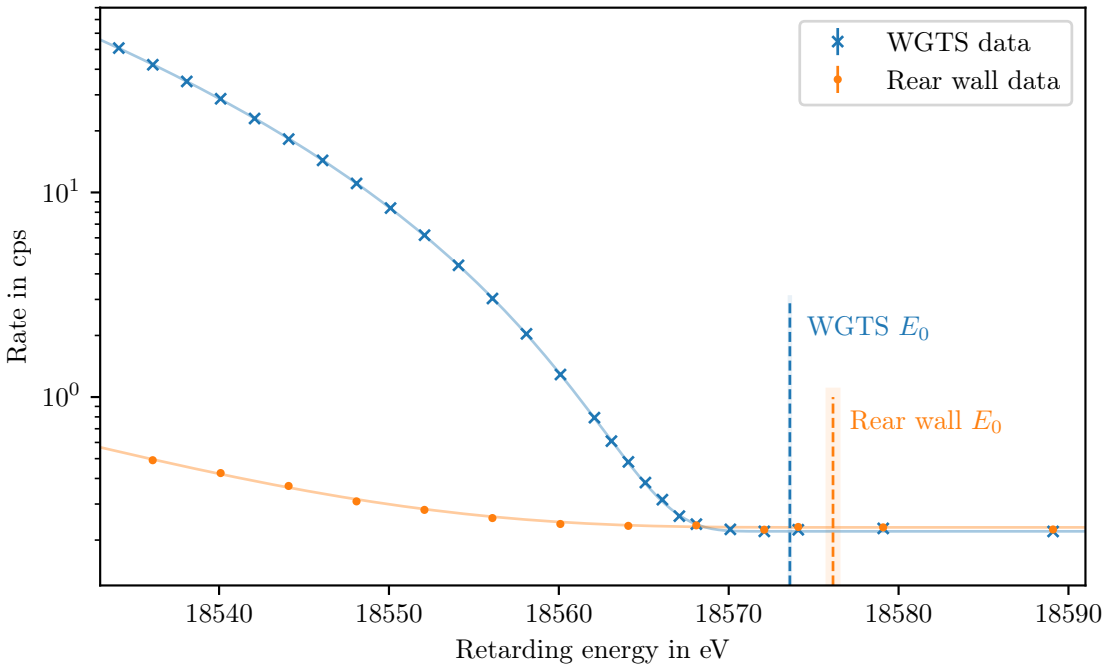

Figure 6.1: Comparison of the Rear Wall-spectrum with the spectrum of gaseous tritium. The data was recorded during KNM3 in the NAP-setting. The fit applied used the T_2 FSD. The uncertainty on the respective endpoint results ($E_{0,\mathrm{WGTS}}$ = (18 573.60 ± 0.05) eV, $E_{0,\mathrm{RW}}$ = (18 576.14 ± 0.36) eV) is marked with the shaded area, the uncertainties on the data points are small. The analysis for this data was performed by S. Hickford.

Chapter 5 for fits to the Rear Wall scan data an additional parameter is introduced. This FSD shape parameter $w_{\mathrm{GR,RW}}$ adds a degree of freedom to the FSD to accommodate for differences between the FSD of T_2 and the true but unknown FSD of the residual tritium bound on the Rear Wall. The other two fit parameters are the respective endpoint and the signal amplitude, with the endpoint being strongly correlated to the FSD shape parameter (see Section 4.3.1). The different experimental conditions for the Rear Wall scans are reflected by adjustment of a few relevant parameters. The origin of the β-electrons being the Rear Wall requires two changes to be considered for the fit. Firstly, the starting magnetic field of the electrons is set to the field present at the Rear Wall, $B_{\mathrm{RW}} = 1.23\,\mathrm{T}$. Secondly, the path length of the electrons passing through the WGTS is doubled, as they need to pass the entire WGTS. This impacts correction for losses due to synchrotron radiation. The scattering probability is set to zero due to the absence of gas in the source as scattering partner. Since the signal parameter is scaled using the column density in the m_ν analysis a similar, virtual scaling is performed to allow for direct comparison of the Rear Wall signal to the WGTS signal as discussed in Section 4.3.2.

Besides the above mentioned lower rate, the resulting $E_{0,\mathrm{RW}}$ is found to be approximately (2.5 ± 0.4) eV higher compared to E_0 for the data shown in Figure 6.1, which shows data

recorded during KNM3 in the NAP setting. This affirms Prediction 2. This statistically significant deviation underlines the importance of considering the residual spectrum in the m_ν analysis to mitigate the distortion of the measured spectrum by the secondary spectrum with a different shape. The higher value of $E_{0,\mathrm{RW}}$ compared to E_0 is expected for tritium being bound in a larger molecule, like in hydrocarbons or tritiated amorphous carbon as was discussed in Section 5.2. It further indicates that the tritium is located on the surface and is not embedded deeper within the bulk material. In the latter case β-electrons escaping the material would experience energy loss due to scattering, resulting in a shift of the entire spectrum towards lower energies.

6.1.1.1 Time Evolution

The aforementioned Rear Wall scans have been conducted repeatedly to assess the stability of the shape of the spectrum as a prerequisite to minimize the time designated for these measurements. Changes in the shape over time would necessitate more frequent measurements. Figure 6.2 illustrates the evolution of the three fit parameters for the Rear Wall scans performed up to KNM6. Both KaFit and Fitrium, the fitting programs utilized in the KATRIN analysis chain, have been employed to analyze the recorded Rear Wall spectra, yielding highly consistent results[1]. The Rear Wall underwent cleaning once within the depicted timeframe, as indicated in the plot by the dotted line. Further details regarding the cleaning procedure, its effectiveness and insights gained are discussed in Section 6.2. As previously discussed the endpoints for all the scans are significantly higher relative to the endpoint obtained from the spectrum of gaseous T_2. Furthermore for all measurements the results for the endpoint and FSD shape parameter, respectively, agree with each other within the expected statistical fluctuation, showing no discernible trend over time or impact from the Rear Wall cleaning. The signal parameter increases over time due to the accumulation of tritium and is significantly reduced after the cleaning. The accumulation dynamics are discussed in detail in Section 7.1.

The consistency of the shape defining parameters of the spectrum, the endpoint and the FSD shape parameter, allows for a split approach of determining the contribution of residual tritium to the data used for the m_ν analysis. This split approach is described in the next section.

6.1.2 Determination of the Rear Wall Activity

The Rear Wall scans presented in the previous section provide detailed information about the spectral properties of the β-electrons emitted by adsorbed tritium on the Rear Wall. This information is necessary to gain a better understanding of the underlying physical

[1] "Rear wall report for the KNM1-5 neutrino mass analysis", Internal Report by M. Aker, B. Daniel, S.Hickford, L. Köllenberger, B. Lehnert, G. Li, D. Parno and A. Schwemmer, 2023, KATRIN Collaboration

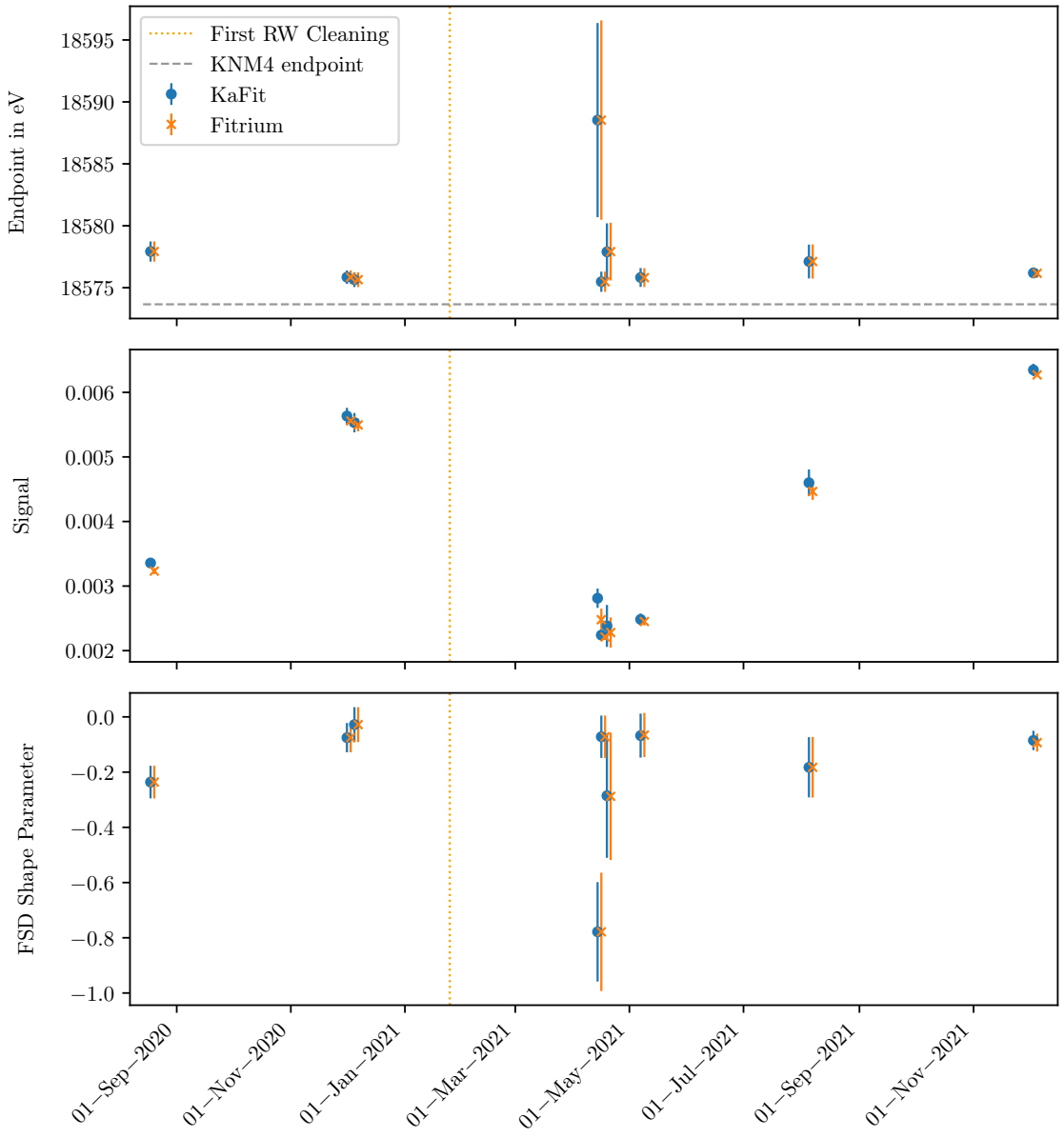

Figure 6.2: Evolution of the Rear Wall spectrum parameters for the Rear Wall scans performed up to KNM6. As a reference the KNM4 endpoint is marked as gray dashed line. The orange dotted line marks the time the first Rear Wall cleaning was performed, with the second following after the displayed timeframe. The KaFit and Fitrium results are derived from the same data and slightly shifted sideways for better visibility. Values taken from "Rear wall report for the KNM1-5 neutrino mass analysis", Internal Report by M. Aker, B. Daniel, S.Hickford, L. Köllenberger, B. Lehnert, G. Li, D. Parno and A. Schwemmer, 2023, KATRIN Collaboration.

processes and also to integrate the secondary spectrum into the neutrino mass analysis of KATRIN. However, performing those measurements with the goal to obtain information

concerning the temporal evolution is not feasible due to the extensive measurement time required.

The spectral shape is dependent on the molecular state of the bound tritium which is not expected to change over short time frames without actively changing the system by e.g. performing cleaning procedures. This is reflected in the data of the subsequent Rear Wall scans presented in the previous section, which show no significant change in the spectrum parameters (see Figure 6.2). Thus, it is sufficient to perform Rear Wall scans with larger time intervals between them, typically at the start and end of a measurement campaign and prior to and following any cleaning procedure. Besides its shape, the total contribution, i.e. the absolute rate of the Rear Wall spectrum is of importance. Due to accumulation of tritium this parameter is expected to vary over time. This time-dependent behavior needs to be observed in order to correctly describe the overall impact of the secondary spectrum in the neutrino mass analysis and to understand the underlying processes of the tritium accumulation. A second, more time-efficient method is required to monitor the evolution of activity on the Rear Wall. Two complementary measurement principles can be utilized for this: Measurement using BIXS on the one hand and using the FPD to perform so-called Rear Wall rate measurements on the other hand. For the latter a low $U_{ret} = 14\,\mathrm{kV}$ is applied at the MS, in order to obtain high count rates at the detector which allows for short measurement durations with low statistical uncertainty. In Table 6.1 an overview of the key aspects of the utilized measurements is given. A detailed explanation of the measurement of residual tritium on the Rear Wall using BIXS or the FPD is given in Section 6.1.2.1 and Section 6.1.2.2, respectively. An estimation of the tritium activity based on the measured rate by the FPD is presented in 6.1.2.3.

6.1.2.1 Monitoring Accumulated Tritium on the Rear Wall with BIXS

The functional principle of BIXS and its setup is explained in Section 3.4.3. The field of view of the SDDs encompasses various areas, primarily focusing on the Rear Wall, with a dominant portion covered, while smaller sections include portions of the vessel walls. During nominal operation of the tritium source the main signal consists of X-rays being dominantly created by β-electrons being magnetically guided to the Rear Wall which outweighs any secondary signals. In order to interpret BIXS readings in the scope of investigating the amount of tritium accumulated on the Rear Wall a more differentiated approach must be taken.

While the main contribution to the signal is still expected to originate from the Rear Wall the amplitude is two to three orders of magnitude smaller, when measuring the residual tritium signal with the source empty. This causes additional contributions to the signal stemming from the stainless steel vessel walls and from the gold coated Be windows directly in front of SDDs to significantly contribute. While the contribution from the former can be estimated due to characteristic X-rays from the steel, it is not possible to distinguish a signal from the latter from the Rear Wall-signal, since both generate the same X-ray spectra. Due

Table 6.1: Comparison of different measurement principles to monitor the Rear Wall activity. While monitoring with BIXS can be performed passively as long as the WGTS is evacuated, the Rear Wall rate measurements (second column) and the Rear Wall scan (third column) are active measurements.

	BIXS	FPD (low U_{ret})	FPD (scan)
Detection method	X-rays	e^-	e^-
Spatial resolution	No	Yes[1)]	Yes
Area in field of view	RW + Vessel walls	RW[1)]	RW
Beamline required	No[2)]	Yes	Yes
Typical rates	(1 to 10) cps[2)]	(2 to 2000) kcps	$\mathcal{O}(1\,\text{cps})$
Measurement time	100 s (continuous)	10 min	2 h
Application	Monitoring during decontamination	Activity evolution over time	Determination of spectral properties

[1)] Slight shift in mapping to pixels.
[2)] Readings vary depending on beamline configuration.

to the location outside of the magnetic flux tube the Be windows are expected to experience a lower activity buildup since the proposed formation process as described in Section 5.2 requires directly impinging electrons. Additionally, the windows orientation facing away from the WGTS prevents direct flight paths of tritium coming from the source. Those effects are opposed by the higher probability of a decay occurring on the Be windows being detected, due to its proximity to the detectors. Interpretation of BIXS readings also varies drastically depending on the current B-field configuration. During nominal field settings electrons being emitted from outside the flux tube cannot reach the Rear Wall. This reduces the impact of tritium accumulated on the vessel walls on the BIXS readings. Additionally, electrons emitted by tritium on the Rear Wall downstream are confined to the flux tube and are mostly either reflected by the retarding potential at the MS or backscattered if one of the valves is closed, further enhancing the signal. The main advantage of BIXS regarding the investigation of tritium adsorbed on the Rear Wall is its availability even when beamline valves are closed or the B-fields are ramped down. This enables BIXS to continuously monitor the Rear Wall activity during any cleaning procedures which are discussed in Section 6.2, while the FPD is not available. However, compared to the Rear Wall rate measurements the data gathered with BIXS lacks spectral and spatial resolution of the underlying residual spectrum.

6.1.2.2 Observing the Rear Wall Rate with the FPD

Additionally to the measurement discussed in Section 6.1.1 the FPD can be utilized to quickly assess the amount of tritium adsorbed on the Rear Wall by performing the so-called Rear Wall rate measurements. For this kind of measurement, the higher rate obtained

at lower retarding potentials applied to the MS is exploited. At a retarding potential of $U_{\text{ret}} = 14\,\text{kV}$ the rate is increased by roughly a factor of 10^5 compared to measurements near the endpoint, like the Rear Wall scans. This allows to gather about (10^6 to 10^9) counts in the measurement time of 10 min, which leads to a statistical uncertainty of less than 0.1 % for the entire detector for the lowest rate measured. The average relative uncertainty per pixel varies between (0.03 to 1.1) %. Due to the low retarding potential, electrons with high surplus energy $E_{\text{sur}} = E_\beta - qU_{\text{ret}}$ pass the analyzing plane. High surplus energies lead to non-adiabatic transport conditions inside the main spectrometer which results to transmission losses of electrons [Pra12; Hub21]. According to A. Huber [Hub21] the surplus energies resulting from measurements performed at U_{ret} =14 kV result in a decline of the transmission probability of up to ≈10 % if measured in the standard NAP setting. This effect, however, completely diminishes if the MAX LFCS[2] setting is applied. In addition to the nominal pixel selection of KATRIN the pixels 134 and 144 are rejected for those measurements. Unusual high rates are recorded for those pixels during Rear Wall rate measurements, which persist when valve V0 is closed, indicating that at least parts of the field lines connecting to those pixels collide with the beam tube wall.

The short measurement time makes repeated measurements throughout a campaign feasible. The major part of the time required for performing Rear Wall rate measurements is needed for the evacuation of the WGTS beforehand, which is discussed in Section 6.1.2.2.1. Additionally, further effects that could impact the result of a Rear Wall rate measurement need to be considered: High Rear Wall rates can lead to pile-up effects in the detector. A procedure to correct for those effects and the accompanying uncertainty are presented in Section 6.1.2.2.2. The impact of the field settings on the measured Rear Wall rate is quantified in Section 6.1.2.2.3. The effect of deviations in U_{ret} on the recorded rate is estimated in Section 6.1.2.2.4.

6.1.2.2.1 The Effect of Residual Gas on Rear Wall Activity Measurements In order to reliably and comparably determine the signal stemming from tritium on the Rear Wall surface, it is necessary to completely evacuate the WGTS. Any residual gas still inside the source during the measurement of the Rear Wall rate causes a background rate. Figure 6.3 shows an example of the FPD rate decline recorded during the pumpdown of the WGTS, with the data acquisition being started with some delay to the begin of the evacuation. A model in the form of $R(t) = R_1 \exp\left(k\left(t + t_0\right)\right) + R_{\text{RW}}$ is fit to the data. The fit accurately describes the rate trend, with $-k$ varying in an interval of ($4.6 \cdot 10^{-3}$ to $5.1 \cdot 10^{-3}$) s^{-1} for different measurements. $R_1 = 1$ cps is fixed to stabilize the fit. While k describes the system inherent evacuation speed, t_0 is primarily dependent on the time difference between starting of the evacuation and initialization of the data acquisition. The most crucial parameter is R_{RW} which describes the Rear Wall rate towards which the measured rate converges. For comparable measurement results the Rear Wall rate measurements have to be performed

[2]The exact configuration of the setting can be found in Table A.1

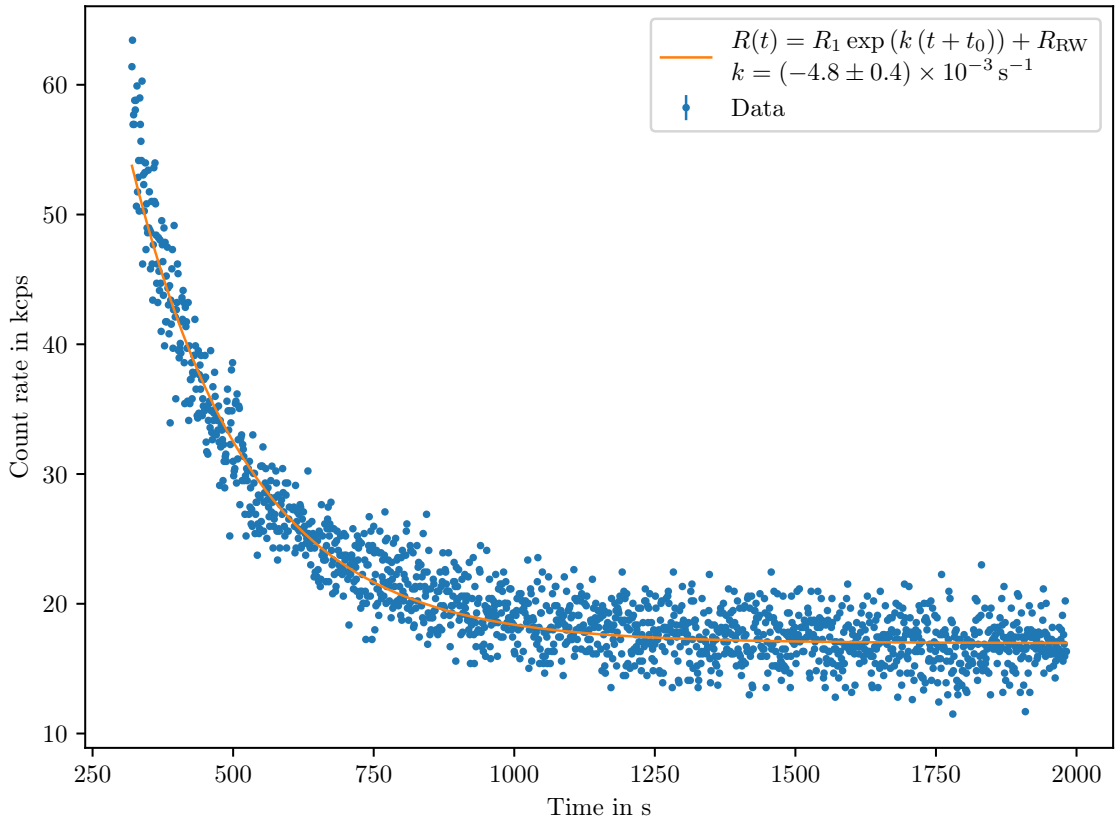

Figure 6.3: Rate trend during WGTS evacuation, recorded at U_{ret} = 17 800 V. While the time constant of the exponential rate decline depends on the procedure of the WGTS evacuation, the offset towards the rate converges varies depending on the activity accumulated on the Rear Wall. The uncertainties on the data points are small, so the error bars are not visible.

after the rate stabilized. Since the time Δt from start of the evacuation until the rate converges to the Rear Wall rate $\lim_{t \to \Delta t} R(t) = R_{\mathrm{RW}}$ depends on the Rear Wall rate itself, the required waiting time to start the Rear Wall rate measurement varies. For low Rear Wall activities waiting times of up to one hour are required to achieve rate measurements without significant trend.

6.1.2.2.2 Pile-up Correction for High Rear Wall Rates While the low retarding potential of $U_{\mathrm{ret}} = 14\,\mathrm{kV}$ allows for the accumulation of high statistics in short times, high activities on the Rear Wall can lead to pile-up occurring on the detector. To ensure consistency in the taken data sets, the retarding potential is maintained independently from the observed Rear Wall rate and the corrections for potential loss of counts are applied

during the data analysis. An empiric model has been developed by S. Enomoto[3] to describe and account for possible pile-up losses. The correction procedure consists of the following steps:

1. The FPD events are counted in an region of interest $[E_{\text{th}}, E_{\text{max}}]$ with the maximum energy resolved by the FPD $E_{\text{max}} = 400\,\text{keV}$ and the lower threshold

$$E_{\text{th}} = \frac{1}{2}\left(E_0 - \frac{3}{4}\left(E_0 - qU_{\text{ret}}\right) + qV_{\text{PAE}}\right), \tag{6.1}$$

   where $E_0 = 18\,575\,\text{eV}$ and $V_{\text{PAE}} = 10\,000\,\text{V}$.

2. This rate is corrected by the factor

$$\frac{1}{\epsilon_{\text{PU}}} \tag{6.2}$$

   with

$$\epsilon_{\text{PU}} = 1 - WR \tag{6.3}$$

   where R is the event rate for a pixel and $W = L + G + 25\,\text{ns} = 1.828\,\mu\text{s}$ with L being the shaping length and G being the gap length of the trapezoidal filter (see Section 3.3).

This procedure is applicable to data recorded down to $U_{\text{ret}} \approx 14\,\text{kV}$ and yields an correction error of less than 0.5 % for a rate up to 50 kcps/pixel. Since this uncertainty is by nature fully correlated for all data points in any dataset consisting of multiple Rear Wall rates it is, contrary to the other uncertainties discussed in this section, only applied to the final input parameters for the Rear Wall contribution to the KATRIN analysis chain (see Section 7.4.1).

6.1.2.2.3 Impact of Field Settings on the Recorded Rate As mentioned earlier the Rear Wall rate measurements are performed in the LFCS configuration called the *MAX setting* to mitigate effects of the non-adiabatic motion of electrons in the MS. Subsequent measurements of the Rear Wall rate in the MAX, NAP and SAP setting have been performed to investigate the impact of different configurations. The inner electrodes have been set to the asymmetrical SAP-like setting for the MAX and SAP setting, while for the NAP setting a symmetrical 130 V setting was applied. All measurements resulted in a total rate of around 2.5 Mcps registered by the FPD with the measurement in the MAX setting recording 0.2 % higher rates as the NAP setting and 5.0 % higher rates than the SAP setting. The statistical uncertainties on these rates are negligible compared to the observed differences.

In Figure 6.4, the relative rate differences between the measurement in the MAX setting and the NAP (a) or SAP (b) setting are shown in the FPD pixel map. While the comparison with the NAP setting shows a weakly pronounced dipolar trend, the overall relative rate

[3] S. Enomoto: "FPD Pile-up Correction for Low-qU Measurements". Personal communication. Department of Physics, University of Washington, WA, USA, 2023

differences are small. The comparison with the SAP setting shows an increasing rate with higher radii for the MAX setting, with the rate being up 20 % higher on the outer rings. This can be attributed to non-adiabatic effects occurring in the SAP-setting. Besides the general loss of transmission probability due to an non-perpendicular orientation of the non-adiabatic electron momentum at the analyzing plane. Additionally, electrons with a high E_{sur} which deviate from the symmetry axis of the MS are subject to an azimuthal drift [Pra11; Pic92a]. This drift increases with the distance to the symmetry axis and leads to the radial pattern seen in Figure 6.4b. Drifting electrons may exit the area of detection, leading to a lower recorded rate. This effect is stronger in the SAP setting but largely mitigated by the high B-fields of the MAX setting. The increase of the effect with increasing distance to the symmetry axis results in a higher rate loss for greater radii in the SAP setting, leading to the observed pattern. This effect is further mitigated in the MAX setting as the higher B-field strength reduces the spatial extension of the flux tube, thereby decreasing the average distance of propagating electrons to the symmetry axis [Hub21].

In both plots the shift of rate in the two left pixels of the bullseye can be explained by a change of the mapping of the central hole in the Rear Wall to the neighboring pixel. While typically the e-gun beam passes the hole, it also acts as an aperture for electrons emitted by tritium accumulated behind the Rear Wall. This results in a somewhat focused electron beam that is susceptible to changes in mapping due to alterations in the field setting.

Additional to the LFCS setting, the setting of the inner electrodes can affect the recorded rate. During the course of the development of the Rear Wall rate measurements in the MAXS setting the applied voltages to the steep cone inner electrodes have been changed. Three different settings were applied:

Setting 1: The asymmetrical SAP-like setting,

Setting 2: A symmetrical 40 V setting, comparable to the NAP setting,

Setting 3: A symmetrical 130 V setting.

The symmetrical 130 V setting was selected as standard. To guarantee comparable data a empirical conversion factor $\xi_{1/2}$ was computed to convert the rates measured in Setting 1/Setting 2 to an equivalent rate expected to be measured in Setting 3. This conversion factor was determined by subsequently performing Rear Wall rate measurements in each of the settings and comparison of the observed rate. For the uniform correction factors the following results were obtained:

- ξ_1 =0.9987,
- ξ_2 =1.0088.

Those corrections for the entire detector are in the sub-percent level for both settings, with the patch-wise correction factors reaching maximal values of up to 0.20 %(0.56 %) for the SAP-like setting (40 V setting). The applied corrections are also regarded as additional uncertainties.

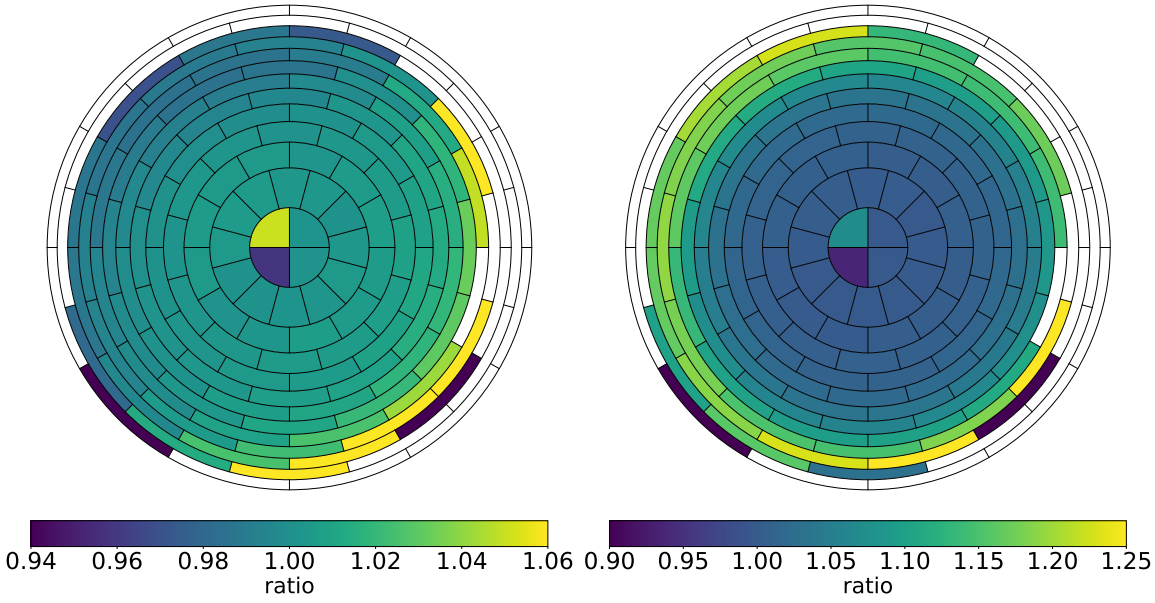

(a) MAX/NAP (b) MAX/SAP

Figure 6.4: Comparison of different LFCS settings for Rear Wall rate measurements. The pixelmaps show the ratio of the rates measured in the MAX setting to the rates measured in the NAP (a) and the SAP (b) setting. For both plots the scale has been adapted to emphasize the dipolar or radial trend.

6.1.2.2.4 Uncertainty due to MS Voltage Deviations To adequately consider deviations in U_{ret} in the Rear Wall rate measurements a basic model on the basis of deep scans performed of Rear Wall spectrum was developed. The deep scan was performed with measurement points in 500 V separation and an acquisition time of 150 s per point. A cubic polynomial $R_U(U_{\text{ret}}) = aU_{\text{ret}}^3 + bU_{\text{ret}}^2 + cU_{\text{ret}} + d$ was fit as a simplified model of the tritium β-spectrum to deep scan data. The region of interest is 3 kV around the setpoint $U_{\text{ret,RW}} = 14\,\text{kV}$. The resulting fit is depicted in Figure 6.5 with the resulting fit parameters $a = -1.10 \cdot 10^{-6}\,\text{cps/V}^3$, $b = 5.85 \cdot 10^{-2}\,\text{cps/V}^2$, $c = -1.04 \cdot 10^{3}\,\text{cps/V}$, $d = 6.17 \cdot 10^{6}\,\text{cps}$, with negligible uncertainties on each. The structure in the residuals reflect the simplified nature of this model. However, the description is sufficiently accurate to be used as an estimation of the uncertainties on the Rear Wall rate based on the deviation of the actual average U_{ret} from the desired set-point at $U_{\text{ret,RW}}$. Those deviations mostly occur since operation in a non-standard setting is more prone to operator errors. Caution has been given regarding the correct consideration of the inner electron settings and the deviating behavior of the HV post regulation due to temperature changes occurring for high voltage changes. The uncertainty $\sigma_{\Delta U}$ on the rate R is computed by extrapolating the expected rate difference due to the deviation of U_{ret}

$$\sigma_{\Delta U} = R\left(1 - \frac{R_U(U_{\text{ret}})}{R_U(U_{\text{ret,RW}})}\right).$$

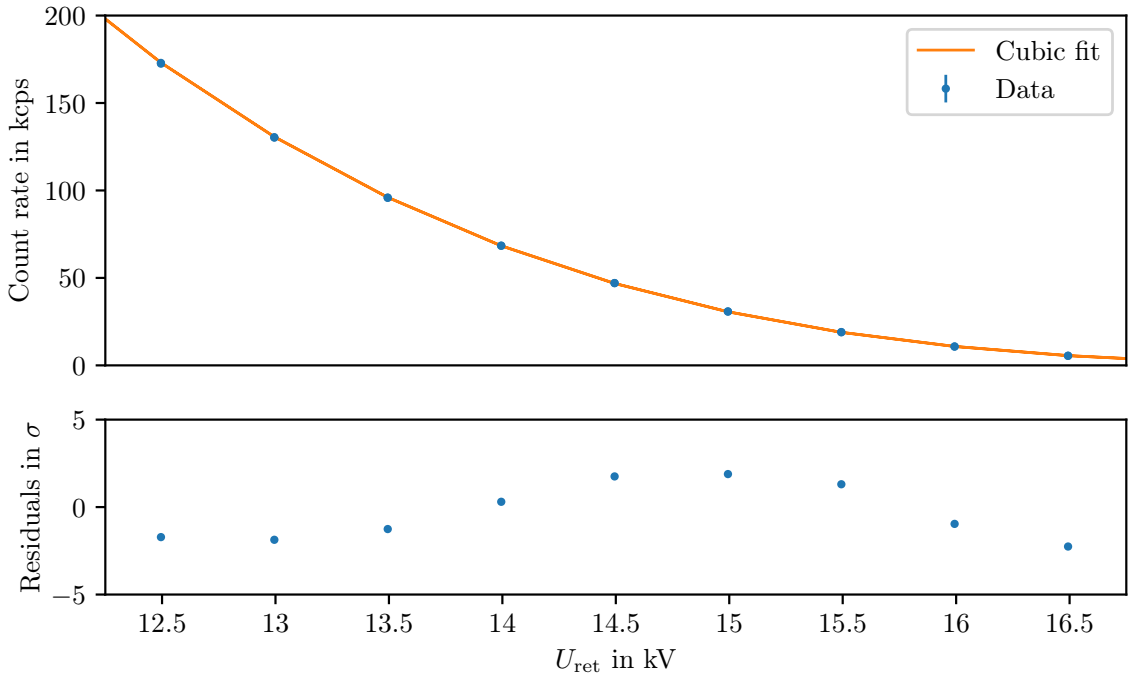

Figure 6.5: Cubic interpolation of the Rear Wall spectrum at low $U_{\mathbf{ret}}$ around $U_{\mathrm{ret,RW}}$. While the cubic model is simplified, it sufficiently describes the spectrum to estimate uncertainties caused by deviations in the retarding potential. The uncertainties on the data points are small, so the error bars are not visible.

This uncertainty is then added in quadrature to the statistical uncertainty and the uncertainty induced by the correction of the IE settings.

6.1.2.3 Activity Estimation

Lastly, the Rear Wall rate measurements can be used to quantify the activity deposited onto the Rear Wall. The previously discussed corrections are applied to the Rear Wall rate, which is used to compute the input for the KATRIN analysis chain. However, to gain further insight into the underlying processes of tritium accumulation and removal on the Rear Wall it can be helpful to calculate the actual tritium activity on the Rear Wall. The tritium activity can be used to quantify the amount of substance which allows probing different models for the activity growth on the Rear Wall. While only a lower limit on the activity can be given due to limitations of the sensitivity of electrons being emitted deeper inside the material due to energy less of electrons, consideration of surface near activity is sufficient. Apart from the aforementioned extrapolation of the recorded Rear Wall rate to the expected rate over the entire spectrum additional considerations are necessary. Electrons being emitted by surface-bound tritium on the Rear Wall have no preferred direction of flight. Based on an isotropic angular distribution electrons emitted in

downstream direction are either magnetically reflected or guided towards the FPD, if their emission angle is smaller or equal the acceptance angle. Electrons emitted toward the Rear Wall undergo scattering. About 28 % of the electrons with $E_{\text{kin}\geq 14\,\text{keV}}$ moving downstream were initially emitted towards the Rear Wall. Depending on the angle of reflection, some of these electrons may again reach the FPD. Due to the lower magnetic field $B_{\text{RW}} = 1.23\,\text{T}$ at the Rear Wall compared to the field $B_{\text{src}} = 3.6\,\text{T}$ in the WGTS, the acceptance angle of interest is lower with $\theta_{\text{max, RW}} \approx 33^\circ$ (see Sections 3.1 and 3.3.2). Since the reflection of electrons being emitted towards the Rear Wall affects their energy and angular distribution GEANT4 [Ago03; All06; All16] simulations have been conducted to allow for a connection of the Rear Wall rate and the actual Rear Wall activity. For those simulations $N = 10^9$ electrons starting directly on Rear Wall surface were simulated, with the angle distribution being isotropic and the energies distribution matching the tritium β-spectrum. Only single scattering events were considered. Three different scenarios were simulated:

1. A pure gold surface,
2. A 20 nm carbon layer on a gold surface,
3. A 50 nm carbon layer on a gold surface.

The results of the angular-spectral distribution of all electrons moving downstream after maximal one scattering process is depicted in Figure 6.6a for the pure gold scenario. The region of interest containing the electrons capable of reaching the FPD due to sufficient kinetic energy and falling within the acceptance angle is marked with a dashed rectangle. Figure 6.6b shows a comparison of the angular distribution of all electrons with an energy $E_{\text{kin}} \geq 14\,\text{keV}$ for the three different scenarios. The sum of all events in the region of interest

$$N_\Sigma = \sum_{E_{\text{kin}}\geq 14\,\text{keV}, \theta \leq 33^\circ} N_i$$

together with the initial number of electrons N is used to calculate an extrapolation factor, which allows to convert the measured Rear Wall rate to a lower limit of activity on the Rear Wall in Becquerel. The extrapolation factor $r_{\text{act}} = \frac{N}{N_\Sigma}$ yields for the three scenarios:

1. $r_{\text{act,Au}} = 386$,
2. $r_{\text{act,20 nm C}} = 402$ and
3. $r_{\text{act,50 nm C}} = 417$.

The increasing value of r_{act} for an increasing thickness of the carbon layer can be explained with the worse backscattering characteristics of carbon, which can also be observed in Figure 6.6b. Due to the lower Z of carbon compared to gold, the scattering probability for the electrons is reduced, leading to a lower direct backscattering probability. Additionally the electrons penetrate deeper into the material, further reducing the probability of an electron leaving the material in downstream direction. A reduced backscattering probability in turn leads to a fewer events being registered by the FPD per decay on the Rear Wall, leading to a higher conversion factor of FPD rate to tritium activity on the Rear Wall. These

factors allow for a rough estimation of a lower bound for activity accumulated on the Rear Wall surface (see Section 6.2.3 and Section 7.3). However, this estimation does not account for tritium that may have migrated deeper into the Rear Wall material. Nor does it consider second-order effects such as electrons emitted downstream, magnetically reflected back to the Rear Wall, and subsequently backscattered within the acceptance angle. Additionally, further dedicated study is required to quantify the decrease in detection efficiency of the FPD due to backscattering of electrons with high E_{sur}.

While the actual Rear Wall activity is not required for the KATRIN analysis chain it allows for crosschecking models developed to understand the tritium accumulation process on the Rear Wall enables us to contextualize the results of the next section.

6.2 Removal of Tritiated Hydrocarbons from the Rear Wall

Removal of adsorbed tritium on the Rear Wall is the preferred countermeasure to minimize the systematic effects on the neutrino mass analysis. This approach entails a direct reduction of the secondary spectrum background, without introducing additional uncertainties inherent in analytical background consideration. Since only β-electrons with energies near E_0 are of interest and electrons being emitted by tritium absorbed deeper within the bulk material experience energy loss during their escape, this work focuses on decontamination techniques for surface-near bound tritium. Different techniques have been investigated to find the most effective process to decontaminate the Rear Wall with minimal impact on the operation of KATRIN and to gain insight on the state of bound tritium as described in Chapter 5. This section provides an overview of the investigated decontamination techniques and presents results of the applied decontamination procedures. The results are then examined with regard to the underlying adsorption process of the contamination. Results shown in this section have partly already been published [Ake23].

6.2.1 Overview of Investigated Decontamination Techniques

The decontamination procedures for the Rear Wall need to meet the following requirements to guarantee a minimal impact on the KATRIN operations and data taking:

- The process has to be performed in-situ, since a removal of the Rear Wall from the system would be excessively time-consuming.
- The procedure should have no significant impact on the vacuum system or built in components.
- It must be achievable using the existing system, as modifying the system or implementing additional tools would not be feasible.

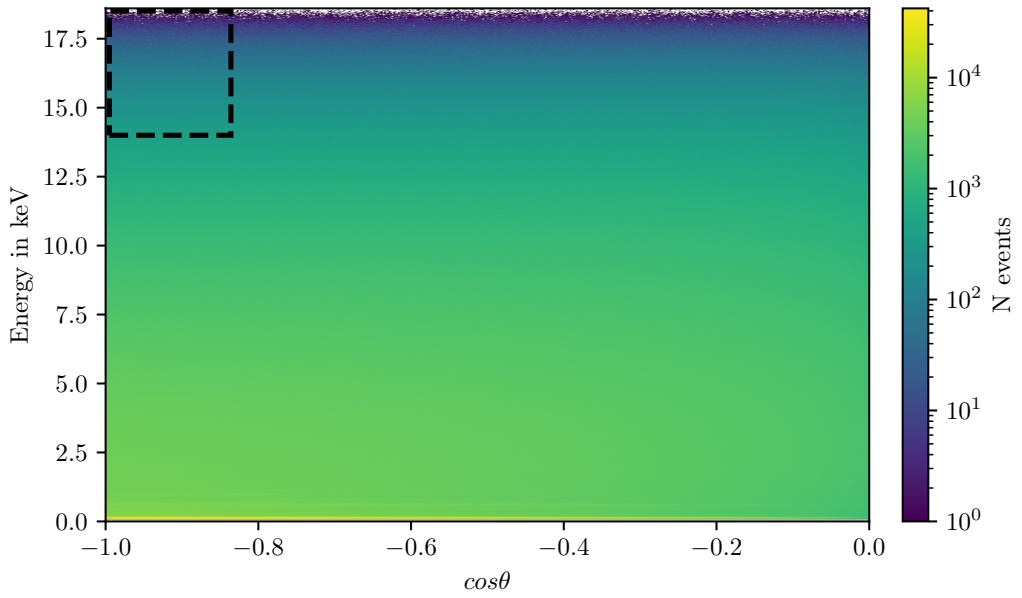

(a) Angular-spectral distribution.

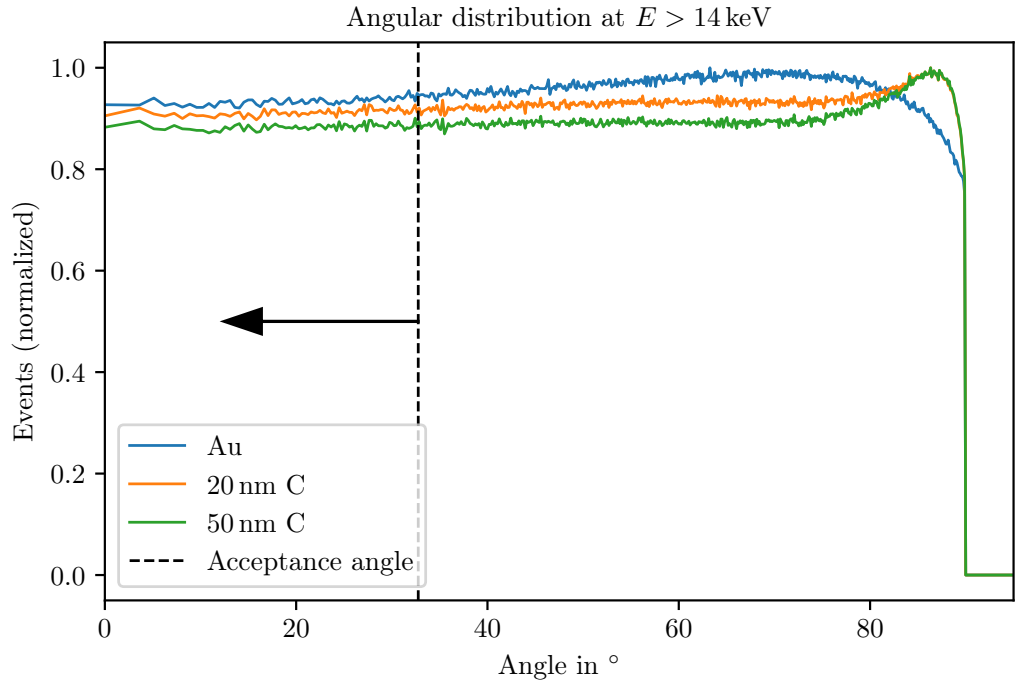

(b) Angular distribution for $E > 14\,\mathrm{keV}$ for different surface conditions.

Figure 6.6: Angular-spectral distribution of electrons emitted on the Rear Wall surface. A total of $1 \cdot 10^9$ electrons with isotropic angular distribution and an energy distribution following the tritium β-spectrum are simulated on top of the Rear Wall surface. Any electron being propagated in downstream direction after a maximum of one scattering process is counted. The area enclosed in dashed lines depicts the area of interest for the Rear Wall rate measurements. Data provided by D. Batzler.

- The time scale of the process should permit to conduct it during the maintenance phases.
- A significant reduction of contamination levels has to be achievable, to reduce the impact of the residual tritium on the KATRIN m_ν analysis.

Another crucial requirement is minimizing the impact of the decontamination procedure on parameters affecting the m_ν measurement, particularly the stability of the Rear Wall's work function, which plays a vital role as discussed in Section 5.3.2. Some cleaning techniques may alter the work function, as anticipated by Prediction 9. This is considered in the execution of the decontamination process to minimize any effect, as mentioned in Section 6.2.3. Since work function changes cannot be entirely avoided during surface decontamination, they are closely monitored through dedicated measurements, which are also part of the Q-value determination process [Ake24a]. However, as these measurements go beyond the scope of this work, they are not discussed in further detail here.

The available system is depicted in Figure 6.7. The Rear Wall chamber is located between the WGTS, from which it can be separated by valve V0 and the so-called mid-chamber (not shown) which provides a vacuum system, that allows evacuation of the system down to less than 10^{-6} mbar. The vacuum system has access ports which allows for injection of various gases. The Rear Wall is mounted on a holder close to the connection to the mid-chamber. An optical port allows illumination of the Rear Wall with light with discrete emission lines at wavelengths of 185 and 253 nm by two miniZ Hg-UV lamps with each 24 W of electrical power. Two BIXS systems allow continuous inline monitoring of the activity within the Rear Wall chamber. The gate valve is closed during the decontamination process, thereby preventing activity monitoring by the FPD. The walls of the primary system (grey) can be heated up to (100 to 110) °C. With separate heaters the Rear Wall can reach a maximal temperature of 165 °C.

The following decontamination procedures have been selected based on the discussion in Sections 5.2.2 and 5.2.3 and were performed in subsequent steps:

- **Prolonged evacuation**: Evacuation of the system over a long period of time gives insight into the contribution of residual tritium gas in the Rear Wall chamber which could contribute to the observed rate. The stability of the rate monitored during evacuation also yields information regarding possible outgassing of tritium from the vessel walls which can give insight into the nature of the bounding mechanism.
- **Illumination of surfaces with UV light**: Illumination of the contaminated surfaces with UV light during evacuation of the system could lead to desorption of weakly bound molecules and partly to dissociation of C-T bonds, leading to desorption of tritiated remnants, which in turn are removed due to the evacuation, causing the observed rate to decline.
- **Heating of surfaces**: The presence of tritium bound as adsorbed HTO can be determined if after heating of the surfaces a decrease of the rate can be observed.

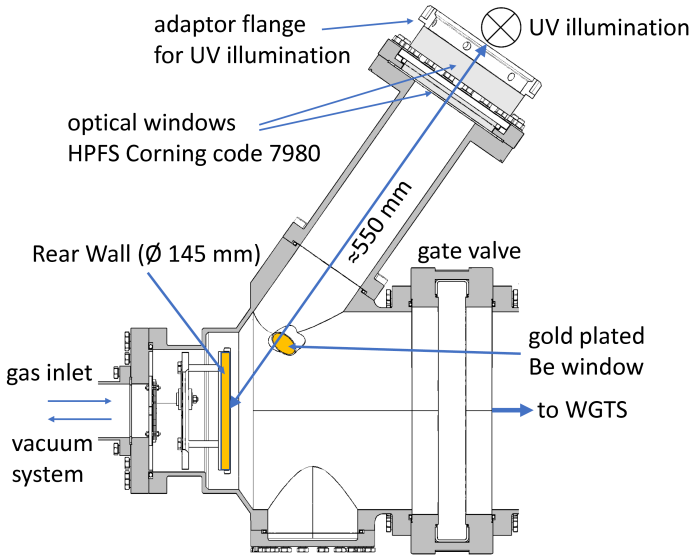

Figure 6.7: Cross-sectional drawing of the Rear Wall chamber, depicting the gold coated Rear Wall and Be window (yellow) of one of the BIXS systems. To the left the system is connected via a DN63 tube to the so-called mid chamber, which provides capabilites for gas injection and evacuation. The upper part portrays the optical port, where two MiniZ lamps are located behind two vacuum view ports HPFS Corning code 7980 in roughly 550 mm distance to the Rear Wall. The connection of the system to the WGTS can be closed using a gate valve, which is done during the entire decontamination process. Illustration as published in [Ake23] under the CC BY 4.0 license http://creativecommons.org/licenses/by/4.0/.

- **Purging with 6 mbar N_2 and air as carriergas**: Purging with carrier gas increases the effectiveness of purging the system from residual tritium gas by expelling remaining trace amounts.
- **Repeated exposure to 20 mbar D_2**: Surface trapped tritium can be removed utilizing the isotope exchange effect.
- **Exposure to 40 mbar air**: Filtered air with residual humidity can act as both a carrier gas and a reactant to bind tritium in gaseous molecules. Additionally, H_2O in the air serves as partner molecule for isotope exchange or further chemical reactions.
- **Exposure to 100 mbar air combined with UV illumination**: Strongly bound tritium, especially in stable hydrocarbons or aC:T can be removed by UV/ozone cleaning.

Table 6.2 lists the sequence of decontamination procedures conducted in the investigation, together with the corresponding duration and obtained decontamination effect.

Table 6.2: Overview of investigated decontamination procedures and their parameters. The observed rate reduction was determined using the corresponding BIXS rates with accumulated data of 15 min, 1 h or 2 h, depending on the available time-gap between the previous and following the procedure. The heating (Step 2) overlaps all other procedures, it was activated during Step 1 and continued throughout the entire investigation. All other procedures were performed subsequently in the order they are listed.

Step	Procedure/Medium	Pressure (mbar)	Duration (h)	Rate reduction relative to previous rate (%)
1	Evacuation	$<10^{-6}$	960	1.5 [2)]
2	Heating	$<10^{-6}$	504	3 [1)]
3	N_2/Air	6	1.5	-
4	Evacuation	$<10^{-6}$	20	-
5	Air	6	7	6.4
6	Evacuation	$<10^{-6}$	17	-
7	D_2	20	7.5	-
8	Evacuation	$<10^{-6}$	16	-
9	D_2	20	23	4.6
10	Evacuation	$<10^{-6}$	4.5	-
11	Air	40	21.5	24.3
12	Air + UV	100	4.5	34
13	Air	100	15	7
14	Air + UV	100	54	94
15	Evacuation	$<10^{-6}$	27	25 [3)]
16	Air + UV	7	20	55
17	Evacuation	$<10^{-6}$	4	35 [3)]

[1)] Given reduction observed within $\approx$ 1 d, procedure continues until end of the last Step.
[2)] Start predates beginning of heating. The given reduction is calculated from start to begin of Step 1.
[3)] Due to removal of gaseous activity due to previous decontamination procedure.

6.2.2 Rate Development During the Decontamination of the Rear Wall

Three dedicated Rear Wall decontamination procedures were carried out in the scope of this work. This section focuses on the procedures themselves, discussing the effectiveness of different techniques and the insights gained. The impact of these procedures on the dynamics of the Rear Wall rate evolution is explored in Section 7.1.

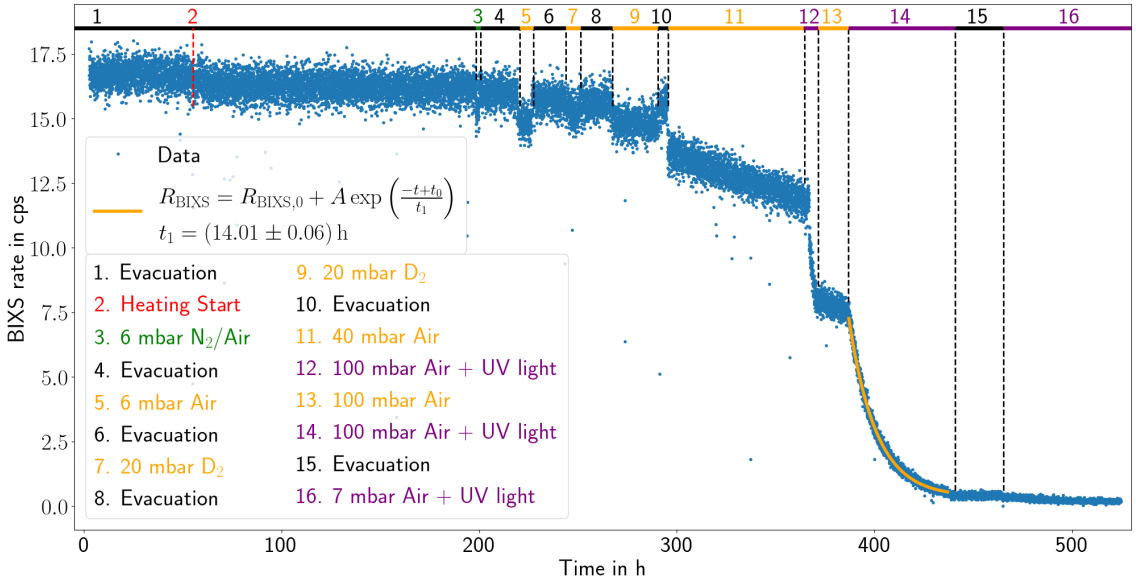

Figure 6.8: Evolution of the BIXS count rate during the Rear Wall decontamination investigation. For each investigated procedure the corresponding period is marked and denoted with numbers, as detailed in the legend. With the heating being applied continuously following the marked start. Prior to the data shown in the plot the Rear Wall was illuminated with UV over a timespan of 4 d. During this period the rate declined by less than 2.5 %.

6.2.2.1 First Rear Wall decontamination

The first dedicated Rear Wall decontamination was carried out after approximately two years of KATRIN operation. Prior to this, only extended UV illumination of the Rear Wall had been performed, following KNM2. During that time, 122 days of illumination resulted in a decontamination effect of (16 to 23) %, corresponding to a rate of (0.015 to 0.022) % d^{-1}.

The evolution of the BIXS rate during the dedicated decontamination procedures is shown in Figure 6.8 with the intervals of the respective decontamination procedures marked. Preceding the data shown in the plot the system was evacuated over a period of 35 d, during which a decline of the measured rate of roughly 1.5 % relatively to the previous rate was observed. Additionally, the UV illumination was activated for a duration of 4 d, leading to a reduction of the observed rate by less than 2.5 %. For better visibility those periods are not shown in the plot. Step 1 marks the start of the heating of the system. During continued evacuation (step 2) the heating resulted in a rate decrease of 3 % after a time period of 5 d, with the main effect taking place within the first day of heating.

Subsequent purging of the system with N_2 ($\approx$ 6 mbar) and air ($\approx$ 5 mbar) in step 3 resulted in an prompt decline of count rate which is associated with scattering and absorption of β-electrons in the gas. The decline is completely reversible and upon evacuation of the gas (step 4) the observed rate returns to the previous level. Increase of the exposition time

with ≈ 6 mbar air (steps 5-6) or a change of the medium to D_2 at ≈ 20 mbar (steps 7-10) resulted in the same behavior. Only following the prolonged exposure in step 9 a decline of the rate of less than 5 % can be observed, indicating that no significant decontamination effect has been achieved. The marginal decontamination results of these procedures align with Prediction 4.

Exposing the system to ≈ 40 mbar of filtered air with residual humidity (step 11) resulted in a sudden reduction of the observed count rate, followed by a continuous linear rate decline of roughly 5 % d^{-1}. This decline is credited to the decontamination effect of the residual humidity, as described in Section 5.2.3. Following the initial gas introduction into the system at the beginning of step 11 no exchange of gas took place, implying that no activity was removed from the Rear Wall-chamber. The observed BIXS rate decline is attributed to an increasing amount of tritium being removed from surfaces. The probability of β-electrons being emitted inside of the volume interacting with the Rear Wall and generating X-rays for BIXS to detect is considerably smaller. This effect is further increased by the attenuation by the gas mentioned earlier.

In step 12 additional air was introduced into the system until a pressure of roughly 100 mbar was reached and the UV illumination was activated. This resulted in a steep, continuous decline of the count rate. Upon deactivating the UV illumination in step 13 the rate decline returned to a slower pace comparable to the one observed during step 11. Reactivating the UV illumination in step 14 led to continued decline of the count rate following an exponential trend with a time constant of $t_1 = (14.01 \pm 0.06)$ h. The time offset t_0 was chosen to mark the time the UV illumination was activated. Subsequent evacuation of the system in step 15 led to a ≈ 25 % decrease of the rate alongside with the removal of tritiated gas species. The decontamination with air and UV illumination was then continued with an air pressure of 7 mbar for 9 d (step 16). During this time the rate decreased by further 71 %. Over a time-span of 14 d following the last decontamination step no significant recovery of the count rate was observed.

The high decontamination effect achieved by the UV/ozone cleaning in steps 12 and 14, along with the small but observable isotope exchange effect from residual humidity in step 11, supports prediction Prediction 5. Additionally, the time constant t_1 leads to an activity decrease of approximately 7 % after one hour, which is consistent with the findings of Vennhaus et al. [Ven02], who reported a 5 % decrease under similar conditions.

6.2.2.2 Second Rear Wall decontamination

After KNM6, following the re-accumulation of tritium on the Rear Wall during standard KATRIN operation of roughly one year, the decontamination process was repeated with a 80:20 He/O_2 mixture to exclude any possible contribution of non-oxygen components in the gas mixture. The recorded BIXS rate is depicted in Figure 6.9. The initial count rate was at a comparable level to the previously shown data. Notable is the stronger decontamination effect of the heating. The rate reduction achieved within one day amounts to approximately

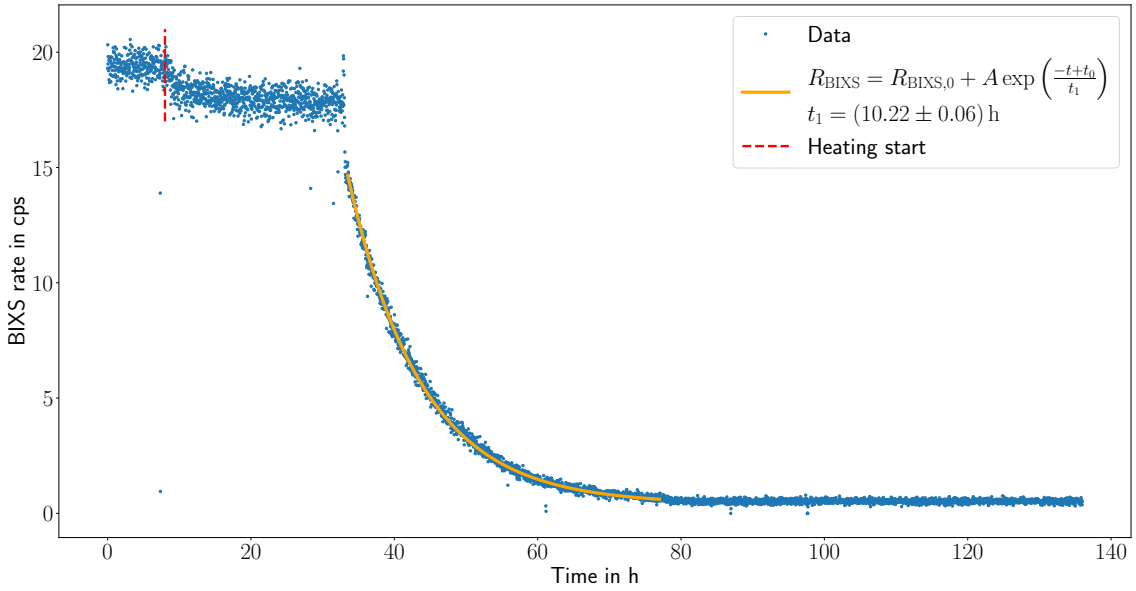

Figure 6.9: Evolution of the BIXS count rate during the second Rear Wall decontamination procedure. The red line marks the time of starting the heating. The beginning of the exponential decay marks the activation of the UV-illumination. As decontamination gas a 80:20 He/O_2 mixture was used.

8 %. Illumination with UV light resulted in an exponential decline of the count rate with a time constant $t_1 = (10.22 \pm 0.06)\,\mathrm{h}$ which is slightly shorter compared to the previous result. This indicating an increased effectiveness of the cleaning procedure. Considering the multiple different decontamination approaches combined in the first process and the absence of humidity in the gas mix this change cannot clearly be attributed to either being caused by the differing process or potential changes in the characteristics of the adsorbent.

6.2.2.3 Third Rear Wall decontamination

A third cleaning of the Rear Wall was performed after KNM7, following about two and a half months of tritium circulation, employing the same procedure as during the second cleaning. The recorded BIXS rate is depicted in Figure 6.10. The initial count rate amounts to approximately 27 % of the rate observed prior to the second cleaning, which is expected, given the short duration of the tritium circulation beforehand. Remarkably, the effect of heating is much more pronounced. It leads to a 30 % reduction in the count rate within just one day, followed by a significant and continuous decline afterward. With this decline continuing during the UV/O_3 cleaning, the function to describe the exponential decline is modified to

$$R_{\mathrm{BIXS}} = R_{\mathrm{BIXS},0} + A \exp\left(\frac{-t+t_0}{t_1}\right) + m\,(t - t_0) \tag{6.4}$$

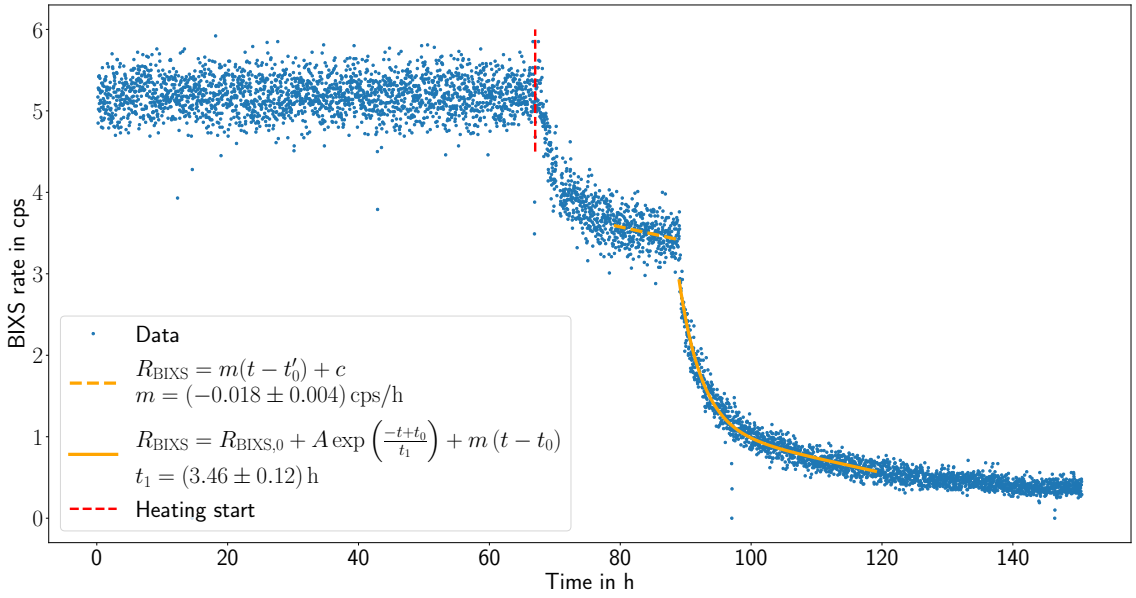

Figure 6.10: Evolution of the BIXS count rate during the third Rear Wall decontamination procedures. The red line marks the time of starting the heating. The beginning of the exponential decay marks the activation of the UV-illumination. As decontamination gas a 80:20 He/O_2 mixture was used. Following the previous cleanings the heating resulted in a more pronounced and continuing decline. This decline was approximated as linear (dashed orange line) and considered in the evaluation of the UV/O_3 decontamination trend (solid orange line).

to accommodate for the overlap of both effects. To facilitate fitting, the decline is approximated to be linear, with the slope being determined in a fit to the last section of the data, before the UV/O_3 cleaning is started, as depicted in the plot by the dashed line. The determined slope is then considered as a fixed parameter in the fit function in Equation (6.4), which yields a time constant $t_1 = (3.46 \pm 0.12)\,\mathrm{h}$, which is notably lower compared to the results of the two previous cleanings. Suggesting a higher decontamination effectiveness for both, the heating and the UV/O_3 cleaning compared to the previous iteration of the process, possibly due to a largely reduced density of aC:T. This scenario is discussed in more detail in Section 7.1.2 and a first indication for Prediction 8 being met.

6.2.3 Comparison of Rear Wall Rate Before and After the UV/O_3 Cleaning Using the FPD

The final achieved decontamination factor of roughly 1300 for the first Rear Wall cleaning was determined by comparing measurements before and after the above described procedure using the KATRIN setup as described in section Section 6.1.2. The assessed lower value for the surface activity of the Rear Wall after the decontamination was $1.1\,\mathrm{kBq\,cm^{-2}}$. In Figure 6.11 the distribution of the activity on the Rear Wall as seen by the FPD is shown for

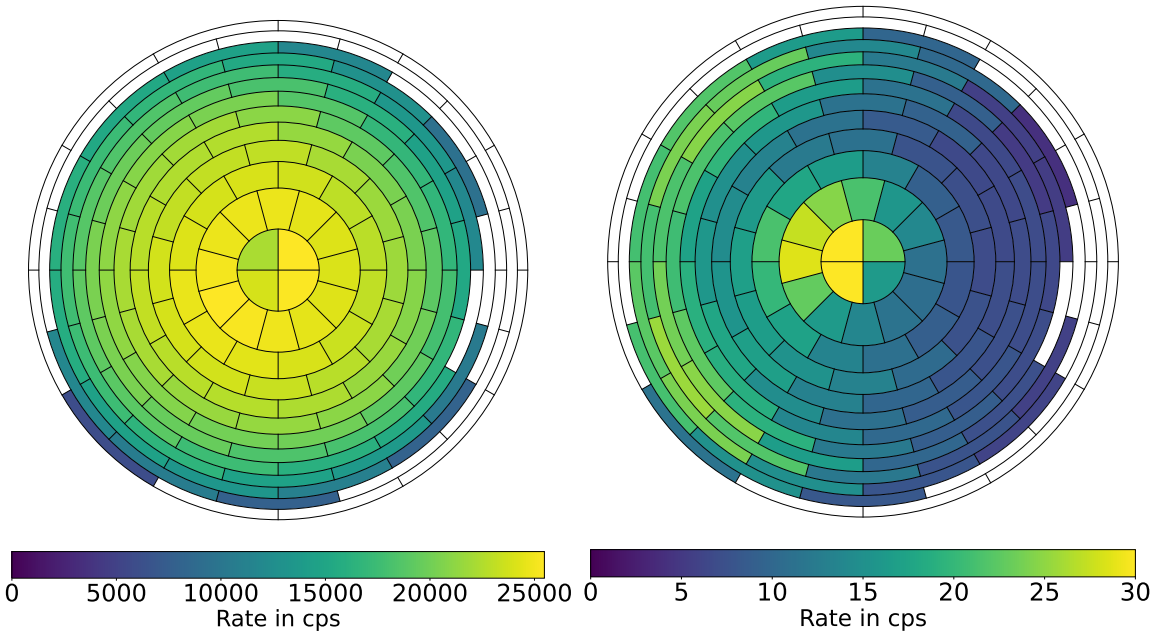

(a) Before cleaning

(b) After cleaning

Figure 6.11: Distribution of the near-surface tritium on the Rear Wall, as seen by the segmented FPD (a) before and (b) after the first UV/ozone decontamination. The total rate was decreased by a factor of roughly 1300. In (b), a rate hot spot in the center is visible. The hot spot is caused by β-electrons being emitted from tritium contamination behind the rear wall and passing its central hole.

those two measurements. While the first measurement shows an azimuthally homogeneous distribution of the activity declining with increasing radius, the second measurement shows a notably lower count rate at the right side. This area coincides with the incoming UV illumination, indicating stronger decontamination effects on areas where a higher UV light intensity or ozone concentration could be expected. It is not entirely clear from literature, whether the UV light directly causes the decontamination [Oya01a] or whether the effect is solely caused by ozone as suggested by Ishikawa [Ish97]. However, the data shown in the previous section demonstrates that the combined UV/ozone approach is significantly more effective, than UV alone.

Figure 6.12 shows the FPD pixelmaps of the Rear Wall rate measurements before and after the second cleaning. While the first cleaning aimed to achieve the highest possible reduction of activity that could still be detected by BIXS, the goal of the second cleaning was to decrease the Rear Wall activity by up to two orders of magnitude. This limitation was set since the reduction is sufficient and the shorter cleaning time minimizes the impact of cleaning on other surfaces, such as the vessel walls of the Rear Wall chamber, whose work function might affect plasma properties [Kel22]. In comparison to both measurements before the cleaning (see Figure 6.11a and Figure 6.12a), the rate distribution appears more homogeneous. A detailed discussion on the distribution of tritium on the Rear Wall

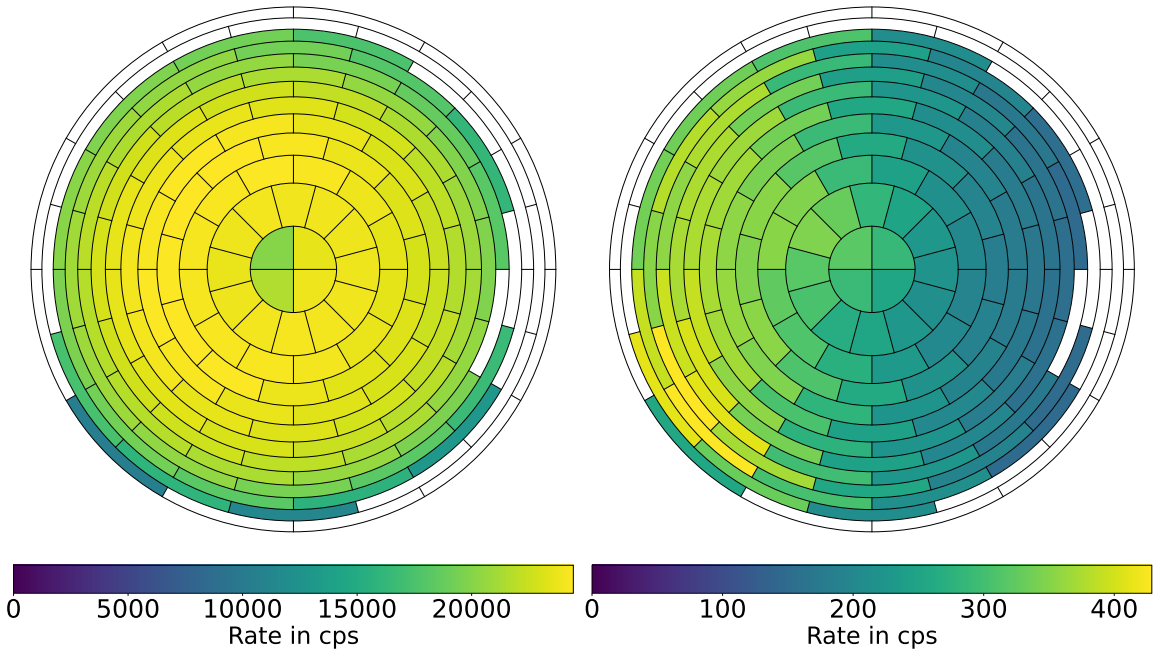

(a) Before cleaning (b) After cleaning

Figure 6.12: Effect of the second Rear Wall cleaning, as seen by the segmented FPD (a) before and (b) after the UV/ozone decontamination. The total rate was decreased by a factor of roughly 80.

and the insights that can be derived from this are provided in Section 7.1.2.5. After the cleaning the pixelmap again exhibits the previously discussed dipole structure regardless of the overall higher rate due to the shortened cleaning. For the third measurement, no decontamination factor can be provided due to technical reasons that prevented prior measurements. Nevertheless, the results of the third cleaning align with the previously discussed findings, showing a lower rate post-cleaning. A summary of the key parameters of all three cleanings is given in Table C.1. The development of the rate due to the accumulation of tritium and the impact of the cleaning procedures on the accumulation characteristics are further elaborated in Section 7.1.2.

6.3 Discussion of the Results

The results presented in the previous sections open up discussions on two key fronts. Firstly, the insights gained from the Rear Wall scans and activity measurements, coupled with the successful development of a cleaning procedure for the Rear Wall, lay the foundation for a comprehensive strategy to mitigate the impact of the residual tritium spectrum on the KATRIN neutrino mass analysis. This discussion forms the first part of this section.

Additionally, these results also offer an opportunity to begin probing the model proposed in Section 5.3.

In the second part, Section 6.3.2, the spectral properties and characteristics of the secondary spectrum determined during the multiple decontamination procedures are discussed regarding the insights they provide of the underlying molecular properties of the bound tritium. Both discussions will be complemented by the results obtained from investigations of the systems dynamics, the findings of which will be presented in Chapter 7.

6.3.1 Pathway to the Mitigation of the Residual Tritium Impact on the m_ν Result

In summary of the previous sections of this chapter, on the formulation of a strategy to mitigate systematic effects on the KATRIN m_ν analysis, three main results come into focus:

1. **Rear Wall scans reveal that the residual tritium spectrum displays a significant different endpoint from the gaseous one, but the spectral shape stays constant over time.**
   While the low rate requires measurements spanning $2 - 4$ days to accumulate sufficient statistics the spectral shape can be characterized using three fit parameters: The endpoint, the FSD-shape parameter and the signal, which changes over time.
2. **Rear Wall rate measurements requiring about one hour including preparatory measures can be performed to supplement the spectral data obtained from Rear Wall scans.**
   Improving the statistics gathered in a short time by measuring the Rear Wall rate at a low $U_{\text{ret}} = 14\,\text{keV}$ allows to intermittently monitor the evolution of the Rear Wall activity. While this enables the extrapolation of the changing signal of the residual spectrum, it comes with a list of challenges. The associated effects with the required, specialized measurement configuration have been identified, investigated and been accounted for in the analysis chain in Section 6.1.2.
3. **Rear Wall cleanings effectively reduce the amount of accumulated tritium on the Rear Wall, achieving a reduction of the activity to $\approx 1\,\%$ ($\approx 1\,‰$) within 1 week (2 weeks) requiring only minor consideration in the measurement schedule when conducted during maintenance phases.**
   The effectiveness was found to increase with each conducted cleaning procedure, increasing the speed of the decontamination process and deteriorating the tritium retention of the Rear Wall.

These three results can be combined in the following procedure to mitigate the impact of the residual tritium on the determination of m_ν with minimal measurement time required.

The residual spectrum shape gets infrequently but regularly characterized by conducting Rear Wall scans before and after each measurement campaign. Rear Wall rate measurements being performed intermittently every 2 to 4 weeks throughout each measurement campaign, allow for modeling the rate evolution. This model is used to inter- and extrapolate the results of the Rear Wall scans to account for the total contribution of electrons emitted by the residual tritium to the β-scan data of the campaign. This first aspect of mitigation, which relies on analytical consideration of the residual tritium background gets supplemented by Rear Wall cleanings. These reduce the systematic uncertainty inherently caused by the analytical background treatment. Additionally the previously presented results suggest that repeated cleanings lead to a long term improvement of the background. This rough sketch of the procedure will be elaborated in more detail in the next chapter, containing information of the evolution of the residual tritium.

6.3.2 Insights on the Molecular State of Tritium on the Rear Wall

Analogous to Section 6.3.1 the results of the previous sections can be probed for information on the underlying processes of tritium sorption and retention onto the Rear Wall.

Insights can be gained from the shape of the secondary spectrum. The overall statistics and resolution are not sufficient to probe the data for characteristics of the underlying FSD and the availability of detailed FSDs in literature is severely limited. In the absence of these inputs, a modification of the available FSD, as discussed in Section 4.3.1 of T_2 is applied to find a best working approximation. The need to modify the FSD suggests that tritium is present in a state different to T_2. This is in agreement with the resulting values for the endpoint of the secondary spectrum, which are found to be higher than those of gaseous T_2, as expected according to Prediction 2.

The results of the Rear Wall rate measurements are most informative in conjecture with their evolution over time and are thus discussed in the upcoming chapter.

The majority of insights from this chapter are gained from the results of the cleaning studies which are discussed in the following paragraphs.

The varying effectiveness of the different performed decontamination procedures allows for an estimation of the nature of the contamination on the Rear Wall. The marginal decline of rate observed during the prolonged evacuation indicates a minimal amount of residual tritium gas present in the recipient and that no significant out-gassing occurred. This explains the lack of decontamination achieved by purging the system with inert N_2 as carrier gas for low concentrations of gaseous tritium [Nis03].

The exact composition of the tritiated molecules on the surface of the Rear Wall cannot be determined with the presented data. However, the results support the working hypothesis that the adsorbed activity primarily consists of tritiated amorphous carbon (aC:T) deposited on the Rear Wall. Additionally, some of the observed activity is likely due to adsorbed HTO, which is present on the Rear Wall as an additional tritiated species. The presence of HTO

is suggested by the observed but limited decontamination of heating and the exposure to ambient air [Oya01b; Tor02]. From the presented data no clear conclusion can be drawn from the lack of decontamination achieved by D_2 exposure - apart from the known fact, that decontamination with humid air is more effective.

The resilience against the initial decontamination processes support Prediction 4 and the subsequent strong decontamination effect achieved by UV/O_3 cleaning suggests strongly bound tritium as e.g. tritiated co-deposited carbon layers [Ven02; Shu01; Oya01a]. This, in combination with the observes decontamination effect due to the exposure to the residual humidity of ambient air confirms Prediction 5.

This leads to aC:T being a possible candidate for the contaminating species removed by this step. The formation under the present conditions is expected as discussed in Section 5.2 and aC:T can be resistant to all the other decontamination procedures performed while UV/ozone cleaning which is widely applied for removal of organic contaminants proofed to be effective.

Additional information can be drawn from the changes observed upon repeated cleanings. An increased efficacy for both, decontamination by heating and by UV/O_2 cleaning, was observed after each iteration. This indicates a modification of the adsorbent with each cleaning, reducing its resistivity to cleaning and reducing its ability to retain tritium.

A possible interpretation of those findings matches with model proposed in Section 5.3. The continued removal of adsorbent, like aC, leads to decreased availability of binding partners to form stable compounds. This results in either additional tritium or tritiated compounds being less likely to be retained on the surface due to weak binding or lack of available partners for restructuring after electron-induced dissociation. Consequently, there is an increased portion of tritium binding through weak bonds or weak physisorption on gold, as the removal of carbon limits the possibility of forming aC:T.

7 Investigation of Tritium Accumulation on the KATRIN Rear Wall

The consideration of the secondary tritium spectrum in the KATRIN analysis chain requires a thorough understanding of the tritium accumulation process on the Rear Wall. This understanding is essential for accurately assessing the Rear Wall rate at any given time during a measurement campaign and for evaluating how adsorbed tritium contributes to the measured β-spectrum.

This chapter discusses the observed tritium accumulation dynamics on the Rear Wall. The chapter begins in Section 7.1 by presenting the tracking of the growth of Rear Wall activity and quantifying its impact on the measured β-spectrum. Following this, Section 7.2 reports on the probing of the underlying processes driving tritium accumulation through dedicated measurements and their corresponding results. The model discussed in Section 5.3 is then evaluated in Section 7.3, where empirical data is used to test the predictions of the model. Finally, Section 7.4 consolidates the findings from this work, providing essential inputs for the analysis chain and formulating recommendations to manage tritium adsorption during the experimental operation of KATRIN.

7.1 Accumulation of Tritium Activity on the Rear Wall Over Time

This section introduces a method to quantitatively describe the temporal evolution of the Rear Wall rate. The rate evolution is expected to be linked to the growth of the aC:T layer on the Rear Wall. Similar to the growth model for aC discussed in Section 5.2.1.2, this growth is expressed as a function of dosage, as outlined in Prediction 1. To effectively describe dosage, the concept of "integral flow" is introduced in Section 7.1.1, which is a measure of the accumulated tritium throughput through the WGTS. In Section 7.1.2, the evolution of the Rear Wall rate relative to the integral flow is detailed, along with an analysis of how intermediate cleaning procedures, discussed in Section 6.2, influence the accumulation behavior.

Additionally, this section tests the model developed for tritium accumulation by examining several predictions outlined in Section 5.3.2.

7.1.1 Integral Flow as Measure of Exposure

As discussed in Section 5.2.1.2, the growth of the aC:T layer - and consequently the increase in the Rear Wall rate - is expected to correlate with the dosage the Rear Wall surface is exposed to. In this context, the integral flow has been selected as a measure for the dosage. This analogy arises from the fact that the dosage on the Rear Wall surface is dependent on the tritium activity within the WGTS, which is regulated by the flow of tritium. Since the β-decay rate in the WGTS is proportional to the tritium flow, the total dosage is proportional to the integrated flow f, making the integral flow an appropriate measure of exposure. Additionally, this metric inherently accounts for the availability of tritium for incorporation into the aC layer.

The integral flow is calculated from slow control data of the KATRIN Loops system, following an analysis provided by A. Marsteller. The data used includes readings from the pressure sensor of the pressure-controlled buffer vessel, temperature and flow sensor data, and valve positions. Other peripheral systems are also considered. BIXS readings are included to account for source activity, and the gas composition, particularly the concentration of tritium and other isotopologues, as determined by the Laser-Raman system, is also taken into account.

Different operation modes are distinguished within the analysis, including the initial "30 K mode," the combined Tritium and Krypton mode, and the "80 K mode" [Mar20; Mar22; Ake24a].

This analysis utilizes a reimplementation of ab initio gas kinetics calculations by F. Sharipov, incorporating the geometry relevant to tritium circulation in the WGTS. The so-determined column density is included to consider the gas amount and throughput recirculating into the WGTS in specific circulation modes. Valve positions in the KATRIN beamline are evaluated regarding their impact on the circulated tritium affecting the Rear Wall. The uncertainty arising from the use of the integral flow for interpolation and extrapolation of the Rear Wall rate is estimated to amount to 0.2 % of the resulting rate.

The cumulative tritium flow over time is shown in Figure 7.1, with corresponding measurement phases indicated. The integral flow is reset to zero after each Rear Wall cleaning following KNM4, KNM6, and KNM7 (as discussed in Section 6.2.2). During measurement phases, tritium circulation leads to a steady increase in the integral flow, which is dependent on the column density and the circulation mode. Conversely, during maintenance phases or special measurements without tritium, the integral flow remains stagnant due to the halt in circulation. The plot clearly illustrates the "burn-in" phase during KNM1, characterized by reduced tritium throughput. During this phase the column density in the WGTS was varied widely with different throughputs being achieved. This phase was especially characterized by the high amount of tritiated methane being formed since it marked the initial tritium exposure to the stainless steel walls of the system.

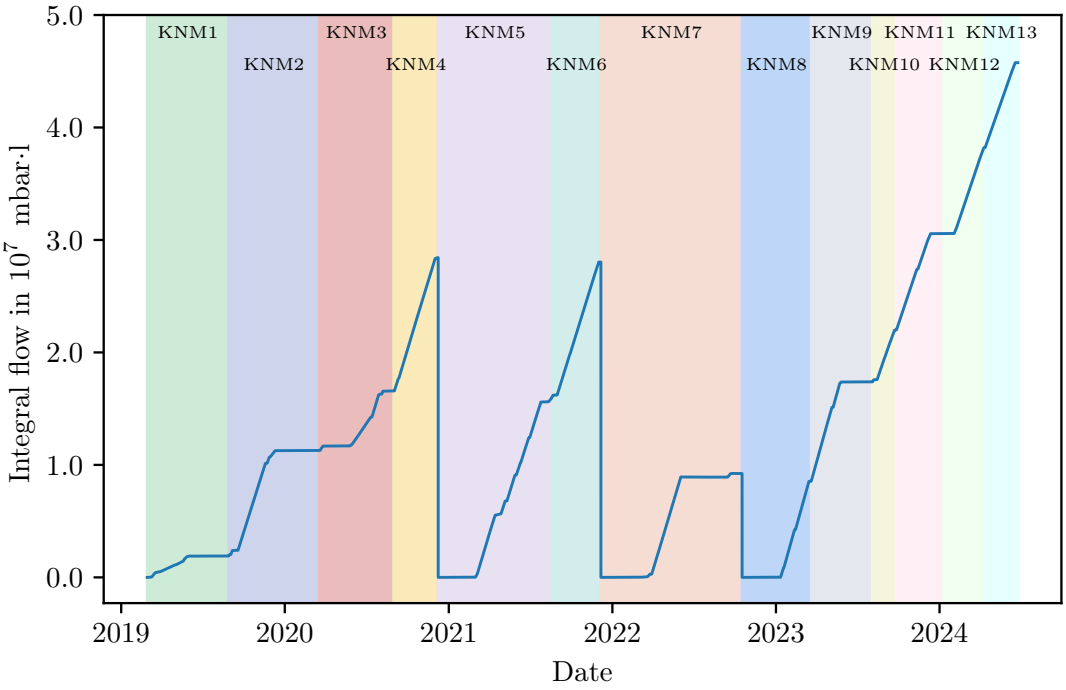

Figure 7.1: Integral tritium throguhtput over KNM1-KNM13. The integral flow accumulates during tritium circulation in the WGTS. To reflect the exposure of the Rear Wall tritium circulated while valve V0 is closed is excluded and the integral flow is set to zero following each UV/ozone cleaning of the Rear Wall as can be seen following KNM4, KNM6 and KNM7.

Starting from KNM4, the standard measurement mode was switched from the "30 K mode" to the "80 K mode," which involves bypassing the permeator within the loops system for part of the gas flow. This change results in a higher tritium throughput at the same column density and reduces the removal of impurities from the circulated gas.

7.1.2 Temporal Evolution of the Rear Wall Activity

Using the relationship between time and integral flow depicted in Figure 7.1, the Rear Wall rate measurements outlined in Section 6.1.2.2 can be plotted as a function of the integral flow. This step, along with understanding the correlation between the Rear Wall rate and the integral flow, is a crucial part of the mitigation strategy presented in Section 6.3.1. It also serves to probe the underlying tritium accumulation process, particularly in relation to Prediction 1 and eventually Prediction 8.

The temporal evolution of the Rear Wall rate will be discussed in several stages. In Section 7.1.2.1, the results from measurement phases KNM1-4 are covered. Phases KNM5 and KNM6 provide insights into tritium accumulation on a freshly cleaned Rear Wall, as discussed in Section 7.1.2.2. The behavior of the Rear Wall rate after multiple cleanings is

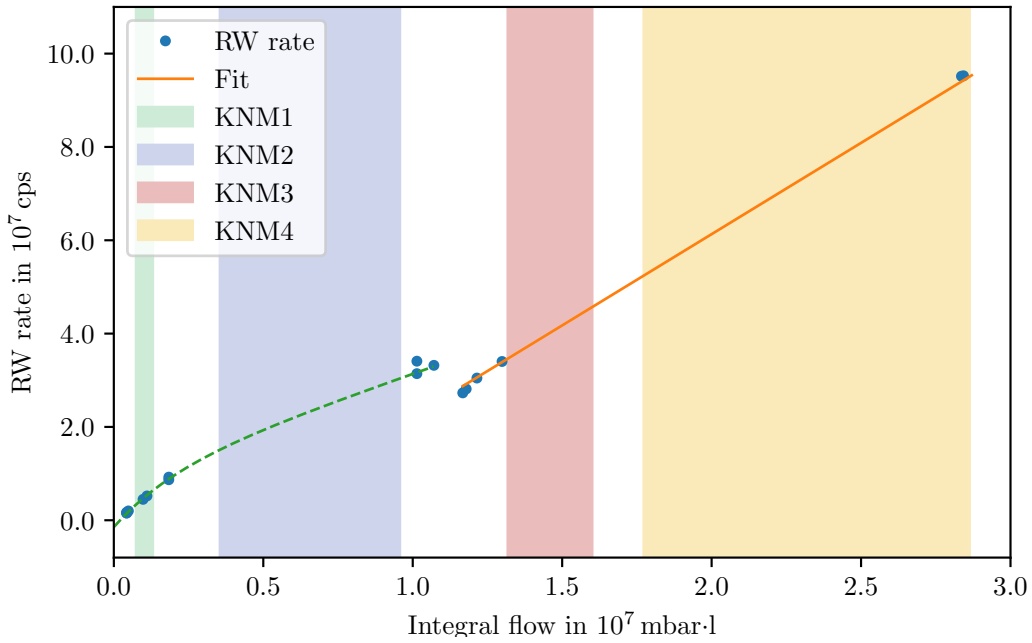

Figure 7.2: Evolution of the Rear Wall rate of KNM1-4 as a function of the integral flow. The respective neutrino mass measurement campaigns are highlighted in the background. Due to unstable conditions during KNM1 no quantitative analysis has been performed for KNM1 and KNM2. The dashed line is a fit result, suggesting that a rate evolution as mentioned in Prediction 1 could be possible.

qualitatively addressed in Section 7.1.2.3, with ongoing work focused on recovering the KNM7 data. While these sections focus on an uniform look at the Rear Wall rate to build a fundamental understanding of accumulation, Section 7.1.2.4 provides a more detailed look at the patchwise development, which is essential for addressing the needs of the KATRIN m_ν analysis, as described in Section 3.3.

7.1.2.1 KNM1-4

Figure 7.2 illustrates the evolution of the Rear Wall rate over the integral flow for the first four KATRIN neutrino measurement phases. The colored background indicates the measurement periods of β-scans. The rate over the course of KNM1 and KNM2 initially shows a growth, which gradually decreases in magnitude, as suggested by the dashed line fit. However, this analysis remains qualitative and does not offer a definitive understanding of the varying parameters during the early circulation, particularly during the "burn-in phase" mentioned earlier. There is also uncertainty regarding the condition of the Rear Wall before its exposure to tritium, as no in-situ cleaning was performed prior to this exposure. While these results hint at affirming Prediction 1, the large number of unconsidered variables

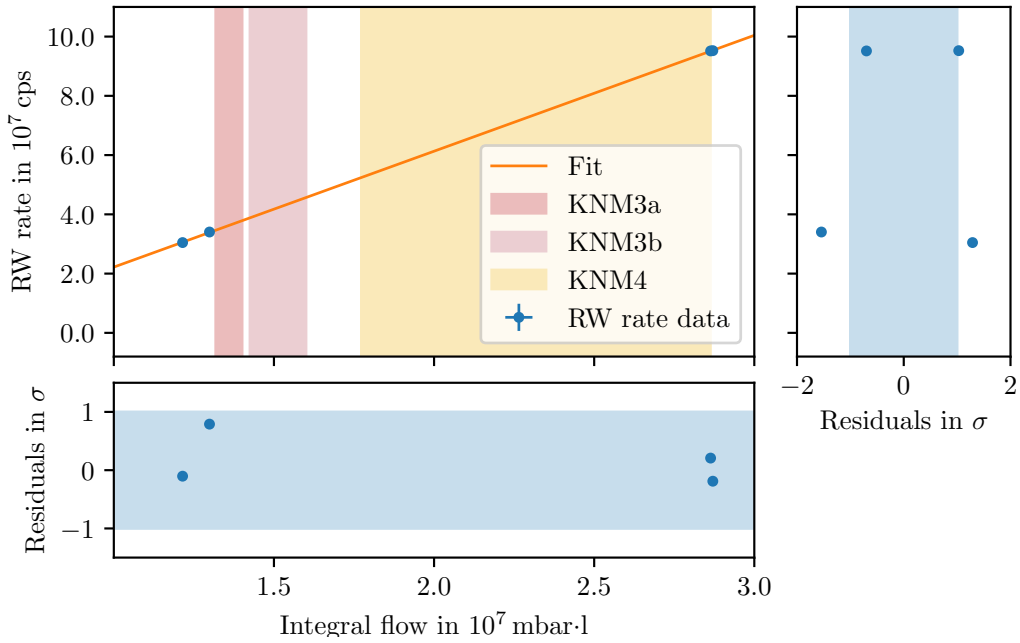

Figure 7.3: Rear Wall rate evolution model of KNM3-4. The model consists of a linear fit with the respective x and y residuals being depicted next to and below the plot. The respective neutrino mass measurement campaigns are highlighted in the background. The error bars are too small to be visible to the eye.

prevents drawing a firm conclusion. Following KNM2, the first decontamination approach was implemented using UV illumination with a Cermax lamp over a period of 122 days, leading to a reduction in the measured rate at the FPD by 16 % and the BIXS rate by 23.5 %, which translates to a decrease of (0.015 to 0.022) % d^{-1}. Additionally, the KATRIN FPD was upgraded with a wafer exchange, which likely altered the alignment and may have affected the detector efficiency in measuring the Rear Wall rate. This changes necessitated treating KNM3 and KNM4 separately from KNM1 and KNM2. Given these uncertainties, along with the limited impact of the Rear Wall rate during KNM1-2 relative to other uncertainties of the KATRIN m_ν analysis, it was deemed negligible for further analysis.

During KNM3-4, the Rear Wall rate exhibits a linear increase, as expected after prolonged exposure, as discussed in Section 5.2.1.2. Initial data points deviate from this trend, likely due to the restart of tritium circulation following the UV decontamination. This led to rapid tritium adsorption that quickly saturated dangling bonds created by UV illumination, which dissociated T-C bonds (as per Prediction 5). The Rear Wall rate quickly returned to pre-UV levels, with no significant long-term impact, affirming Prediction 6. These initial points were therefore excluded from the fit.

A more detailed analysis, including residuals of the linear fit and a breakdown of sub-campaigns within KNM3, is presented in Figure 7.3. These sub-campaigns reflect the switch in MS operation from a symmetric analyzing plane to an asymmetric one, intended to suppress background effects [Lok22].

The resulting parameters of the best fit have the values

- $m = (3.91 \pm 0.02)$ cps/mbar·l for the slope, and
- $c = (-1.69 \pm 0.02) \cdot 10^7$ cps for the offset.

The shift from "30 K mode" to "80 K mode" circulation after KNM3 may have influenced the accumulation behavior as discussed in Section 7.1.1. However, the available data is currently too limited to experimentally verify this impact.

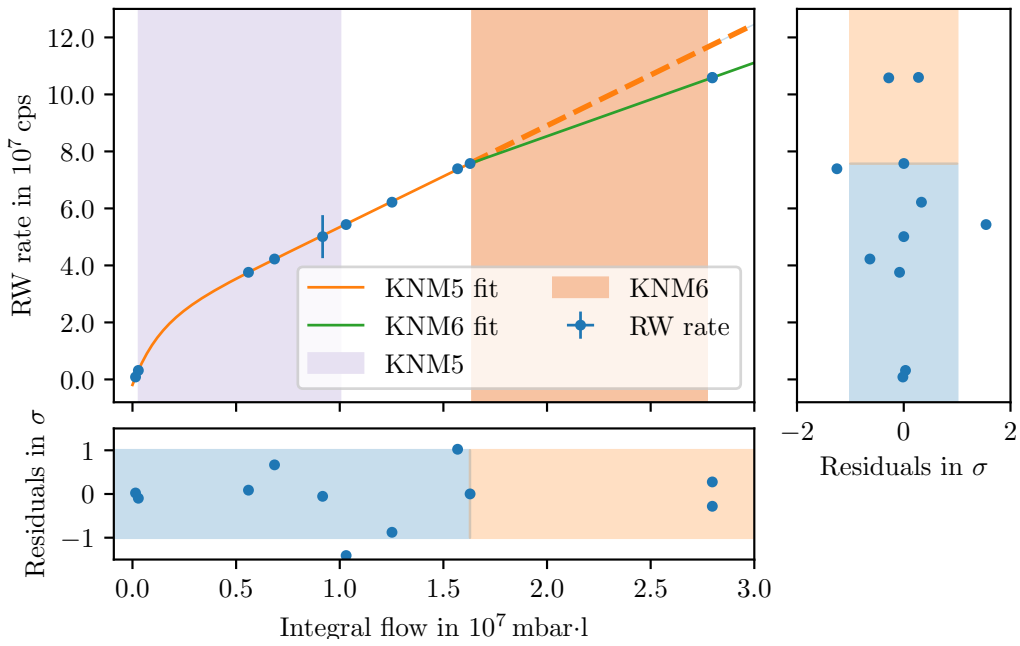

Figure 7.4: Rear Wall rate evolution models of KNM5 and KNM6, with the residuals of the model fits shown alongside the plot. A deviation from the KNM5 model is observable following KNM6, necessitating a distinct linear fit for the rate evolution of KNM6. Data points recorded immediately after the cleaning prior to KNM5 are excluded, as exposure experiments conducted before nominal circulation would distort the model fit. The respective neutrino mass measurement campaigns are highlighted in the background. The error bars are too small to be visible, except for one data point, which was recorded at a deviating retarding potential.

7.1.2.2 KNM5-6

Following the first UV/ozone cleaning of the Rear Wall (see Section 6.2.2.1), the growth model postulated in Prediction 1 can be evaluated through constant exposure of a freshly cleaned Rear Wall in a stable system. Figure 7.4 shows the evolution of the Rear Wall rate, with the colored background indicating the periods of β-scan recordings for the m_ν analysis. Immediately after the cleaning, a dedicated measurement campaign was carried out under non-nominal conditions to expose the pristine Rear Wall. These measurements, discussed in Section 7.2, resulted in minimal tritium accumulation, leading to a slightly above-zero starting point for the data presented in the plot. To avoid skewing the analysis, Rear Wall rate measurements immediately after cleaning are discarded.

The Rear Wall rate initially rises sharply, then transitions to a linear growth phase. This rapid increase at the beginning of KNM5 further confirms prediction Prediction 6. The growth model proposed in Section 5.3.2 accurately describes the data from KNM5, affirming Prediction 1, as the linear rate growth clearly reflects a quasi-steady state. The fit follows Function 7.1

$$R_{\mathrm{RW}}(f) = a \cdot \exp\left(-k \cdot (f + f_0)\right) + b \cdot (f + f_0)\,, \tag{7.1}$$

with the resulting parameters for the best fit

- $a = (-1.189 \pm 0.090) \cdot 10^9$ cps,
- $k = (8.1 \pm 0.2) \cdot 10^{-7}$ mbar·l^{-1},
- $f_0 = (5.02 \pm 0.06) \cdot 10^6$ mbar·l and
- $b = (3.56 \pm 0.02)$ cps/mbar·l.

Though the KNM6 data shows some deviation with a further decrease in the rate of accumulation, this is not unexpected. A potential depletion of a hydrocarbon reservoir could reduce the availability of hydrocarbons migrating to the Rear Wall surface, exposed to impinging β-electrons. This behavior may align with Item Prediction 8. Due to a second UV/ozone cleaning of the Rear Wall immediately following KNM6 (see Section 6.2.2.2), no additional insights could be drawn from subsequent data. The available data is best described by a linear function, yielding:

- $m = (2.58 \pm 0.03)$ cps/mbar·l for the slope, and
- $c = (3.38 \pm 0.08) \cdot 10^7$ cps for the offset.

The difference of the green line, deviating from the orange fit to the continuation of the orange fit (dashed line) reaches 9.4 % at the end of KNM6. The last value recorded in KNM6 represents the highest Rear Wall rate measured in this work. Using the extrapolation factors presented in Section 6.1.2.3, the quantity of aC:T present on the surface can be estimated.

Assuming[1] a density of $\rho_{\mathrm{aC:T}} = 1\,\mathrm{g\,cm^{-3}}$ and considering a perfectly planar Rear Wall, this corresponds to approximately 0.76 to 0.82 monolayers aC:T. For the direct adsorption of atomic T on gold a result of 2.26 to 2.44 monolayers is obtained, based on the calculations from M. Röllig [Röl15]. While aC:T can theoretically form multiple layers, it is unlikely for more than one T atom to occupy a single adsorption site on gold. Adsorption of a second T atom onto an already adsorbed T atom would likely lead to recombination, resulting in the desorption of the newly formed T_2 molecule. This observation further refutes the idea of adsorbed atomic T as the sole contributor to the observed activity, suggesting instead that tritium accumulation could exceed the observed maximum value in cases involving aC:T.

7.1.2.3 KNM8-12

Figure 7.5 presents the evolution of the Rear Wall rate from KNM8 onwards, following the third cleaning after KNM7 (see Section 6.2.2.3), alongside the previously discussed KNM5-6 Rear Wall rate trend for comparison. As observed earlier, the Rear Wall rate initially shows a rapid increase, which then diminishes. This is likely due to the fact that both the second and third cleanings were applied to reduce the Rear Wall rate by a factor of about 20, rather than fully removing the aC:T layer. The decision to stop cleaning earlier was made to minimize the impact on other surfaces, which could potentially alter plasma properties due to changes in work function. The quick increase on basis of possible residual aC:T after a partial cleaning aligns with Prediction 6.

Unlike KNM5-6, however, the Rear Wall rate eventually reaches saturation and remains constant, rather than continuing a linear growth. A further decrease in the Rear Wall rate is observed after KNM9 and KNM11. Following KNM9 the rate decreases 23 % over a timespan of 13 d due to desorption. After KNM11 a 21 % reduction occurs 56 d after the measurement, with roughly four days of tritium circulation between the first measurement and the stop of tritium circulation. This may be attributed to desorption, as weakly adsorbed tritium on the gold surface would likely desorb under such conditions (see Section 5.1.2.2), consistent with the observed cessation of growth. Both of these points align with prediction Prediction 8.

However, it is apparent that the time constants do not match the theoretical expectations quoted in Section 5.1.2.2. This behavior is part of ongoing research, this section offers only a qualitative description at the current stage.

7.1.2.4 Patchwise Growth

To support the patch-wise analysis conducted for the β-scans recorded in the SAP setting, it is necessary to break down the Rear Wall rate evolution into patch-wise inputs. This not

[1] A. von Keudell: "The KATRIN Rear Wall and its surface properties". Personal communication. Department of Physics, Ruhr Universität Bochum, Bochum, GER, 2022

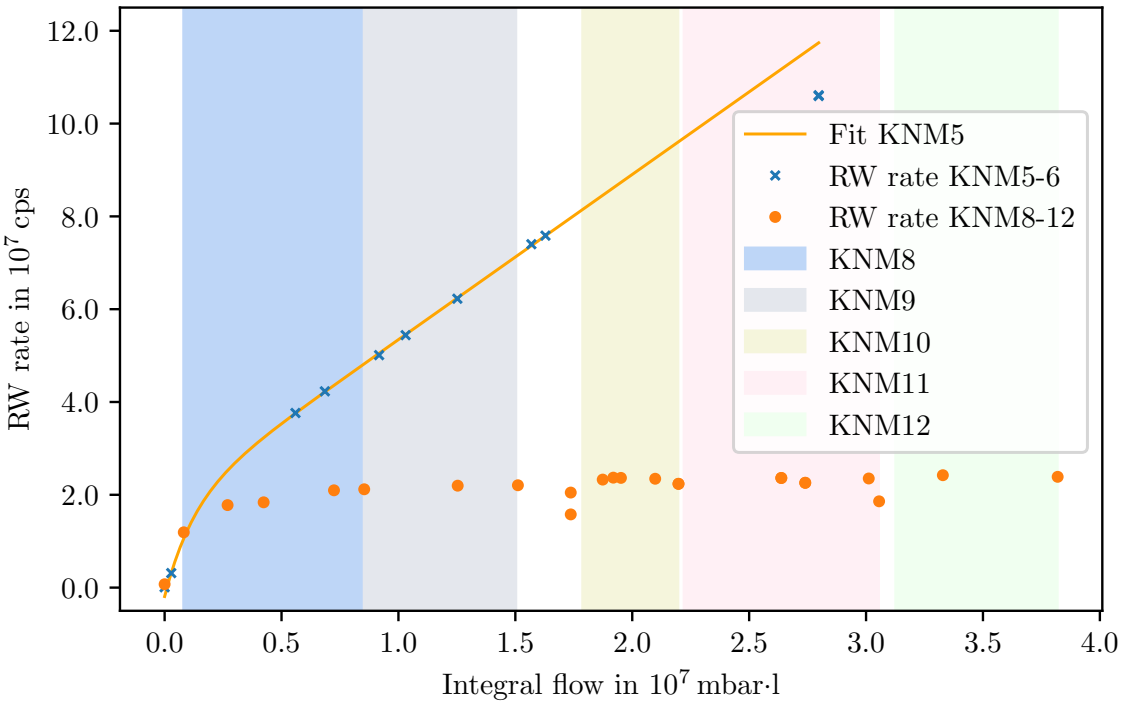

Figure 7.5: Rear Wall rate evolution during KNM8-12, with the KNM5 rate evolution model and data for comparison. Following the second and third Rear Wall UV/ozone cleanings, the Rear Wall rate trends exhibit a saturation behavior after an initial rapid increase. A novel feature is the observable rate decrease due to desorption, particularly visible between KNM9 and KNM10, as well as at the end of KNM11. This desorption is characterized by a rate drop occurring with little to no increase in the integral flow, marking a distinct departure from prior observations.

only aligns with the intrinsic patch-wise characteristics of the SAP setting but also reveals radial effects, as the patches are distributed radially over the FPD (see Section 3.3).

Figure 7.6 illustrates the Rear Wall rate evolution for each patch during KNM3 and KNM4. A clear decline in both rate and slope is observed as the patch number increases, indicating a radial dependency of the aC:T layer growth. The parameters for the corresponding fits are listed in Table B.1.

Similarly, the patch-wise evolution of the Rear Wall rate for KNM5 and KNM6 is shown in Figure 7.7, with fit parameters provided in Table B.2. As with KNM3 and KNM4, the same trend of declining total rate and slope with increasing patch number is observed. However, a notable feature is the increasing deviation between the KNM5 and KNM6 models for each patch. The difference is most pronounced in the innermost patch and diminishes with higher patch numbers, eventually vanishing in the outer patches. This suggests a shift in the growth behavior during KNM6, particularly in the central regions of the Rear Wall, while the outer regions remain unaffected. As discussed in Section 7.1.2.2, this points toward a beginning depletion of the hydrocarbon reservoir, supporting the

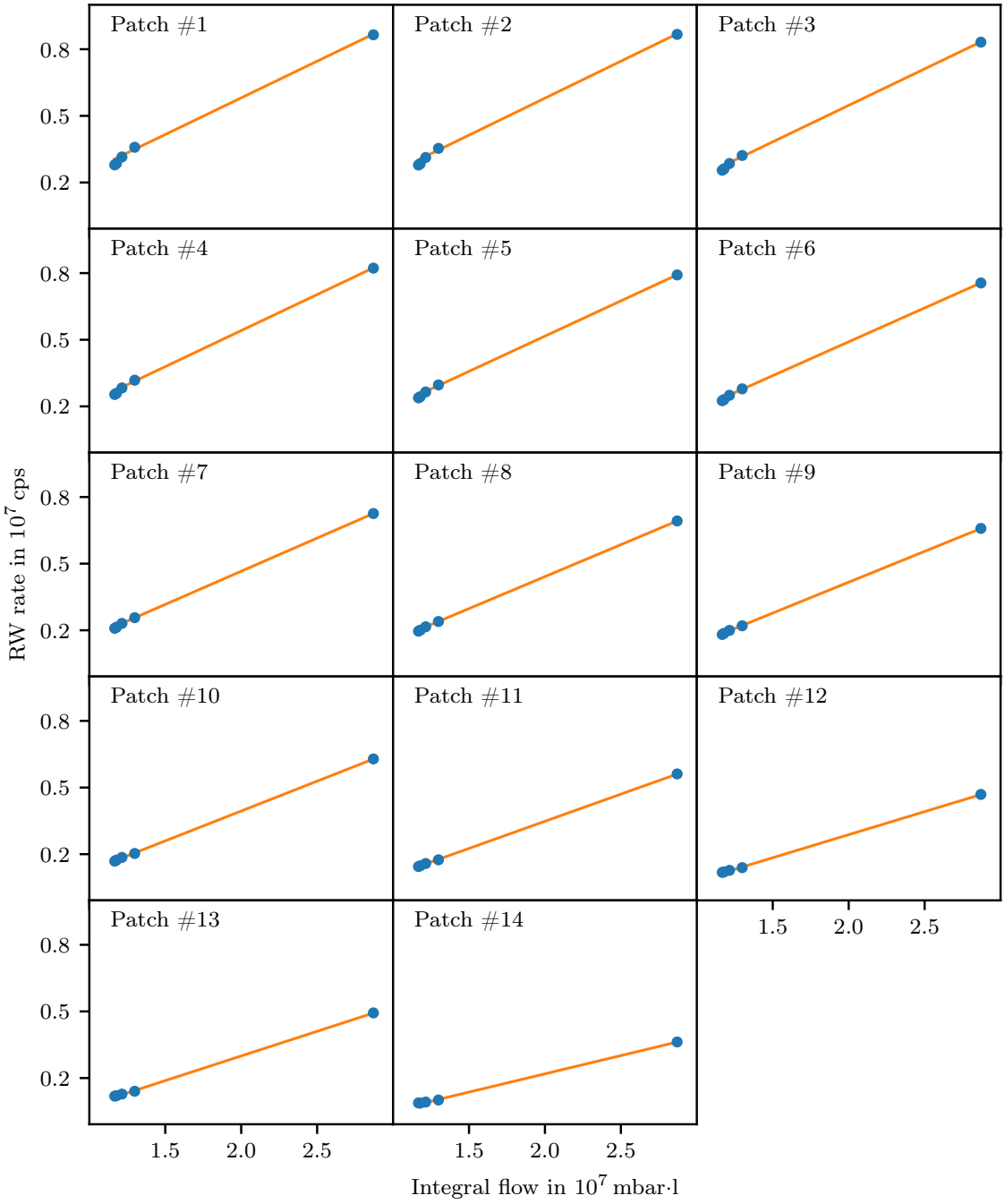

Figure 7.6: Patchwise evolution of the Rear Wall rate for KNM3 and KNM4. The initial data points are excluded from the displayed fit, as they reflect a short-term trend from the rapid re-accumulation of tritium after the UV illumination of the Rear Wall. The error bars are too small to be visible by eye.

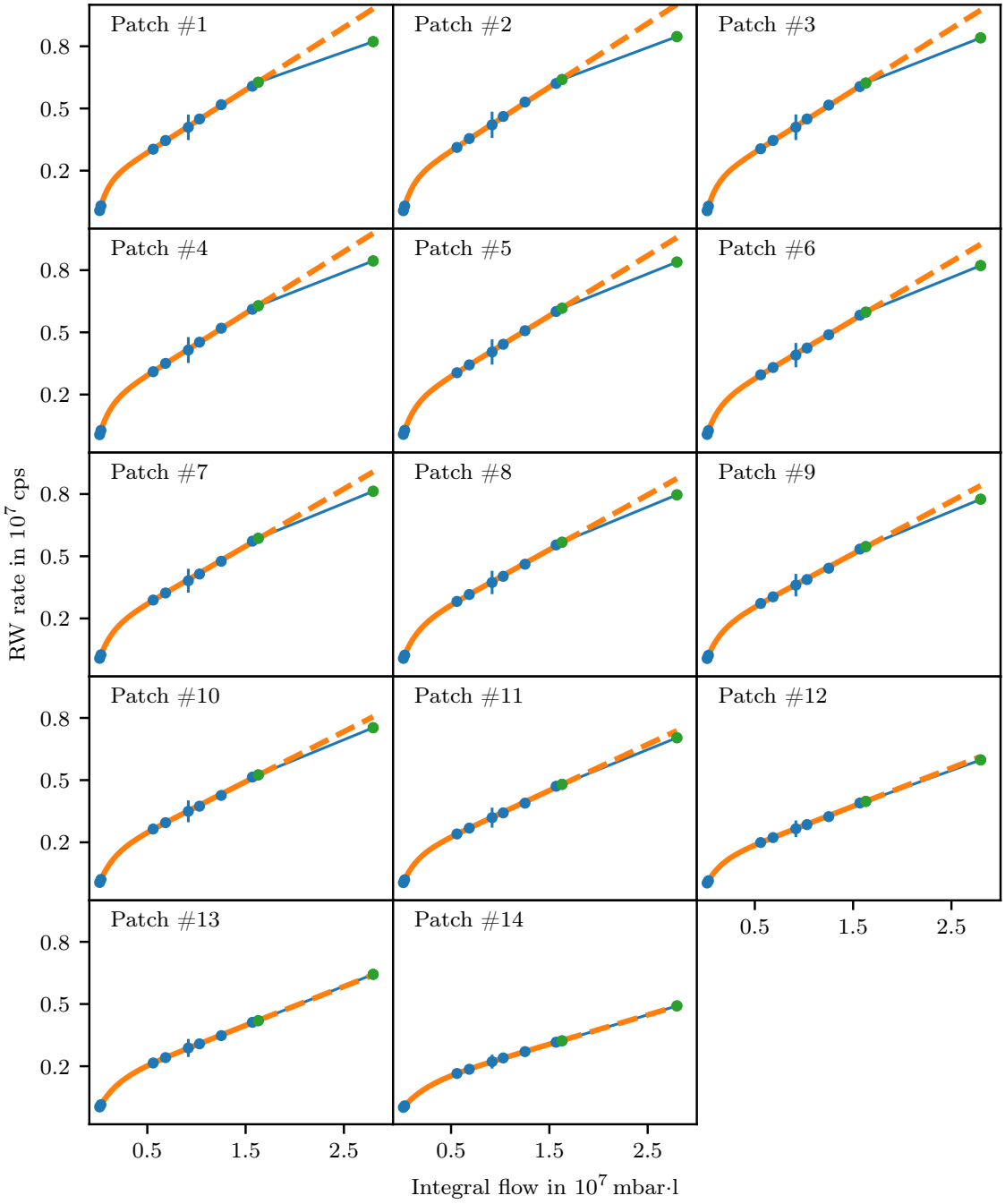

Figure 7.7: Patchwise evolution of the Rear Wall rate for KNM5 and KNM6. For increasing patch number the extrapolation of the KNM5 model (dashed line) and the KNM6 model converge until they eventually overlap.

prediction in Prediction 8. The larger effect in the center may be explained by a reduced migration of precursor hydrocarbons from the back side of the Rear Wall through its central hole. With the depletion of this additional, localized source of hydrocarbons, the growth behavior becomes more homogeneous across the Rear Wall. This results in a more uniform accumulation rate, reducing the previously observed radial dependency. A more detailed analysis of the radial profile of the Rear Wall rate can be found in Section 7.1.2.5.

7.1.2.5 Evolution of the Radial Profile

In addition to the temporal evolution, the spatial distribution of the Rear Wall activity provides crucial insight into the tritium accumulation process. Apart from the requirement of the investigation of the radial Rear Wall rate distribution for the neutrino mass analysis, as discussed in Section 7.1.2.4, it is furthermore particularly informative for understanding the process. Upon closer inspection, the distribution of activity on the Rear Wall is found to be radially symmetric, reflecting either the symmetry of the Rear Wall itself or that of the flux tube carrying electrons and ions toward the Rear Wall. This symmetry allows the description of the spatial activity distribution on the Rear Wall using the so-called radial profile of the Rear Wall rate.

This profile is determined by summing the rate of each pixel in a concentric pixel ring of the FPD. To track changes over time, the profile is compared across different time phases. Figure 7.8 shows a selection of radial profiles from Rear Wall rate measurements, with KNM1-2 in the top left, KNM3-4 in the top right, KNM5-6 in the bottom left, and KNM8-12 in the bottom right. While the time and integral flow intervals between these runs are not equidistant, they were chosen to visualize the transition from one profile shape to another. The rate per ring for each measurement has been extrapolated to the rate expected for 12 pixels, and normalized to the bullseye rate. Changes in the depicted profiles thus reflect the relative shift of activity between different rings. The two outermost rings were excluded due to pixel cuts leading to too few active pixels contributing to the rate.

During KNM1-2, the Rear Wall rate was highly localized in the central rings, with a steep decline towards the outer rings, resembling a Gaussian distribution. Over time, this localization lessened, and the relative activity in the outer rings increased, shifting towards a more parabolic profile. After slight decontamination via UV illumination by the Cermax lamp, the radial profiles in KNM3 and KNM4 continue this trend toward a more even distribution, with the outer rings gaining in relative activity and the curvature decreasing. However, no clear shift in the profile shape is observed during these phases.

KNM5 and KNM6 provided the first data after the UV/ozone cleaning. The profile from run 67437, recorded before any tritium circulation, shows distortions from electrons originating from residual tritium behind the Rear Wall, which the cleaning did not effectively remove. Passing through the central Rear Wall hole those electrons can reach the FPD and are registered as rate coming from the central Rear Wall. Additionally, the directional UV illumination introduced a slight asymmetry in the residual tritium distribution following

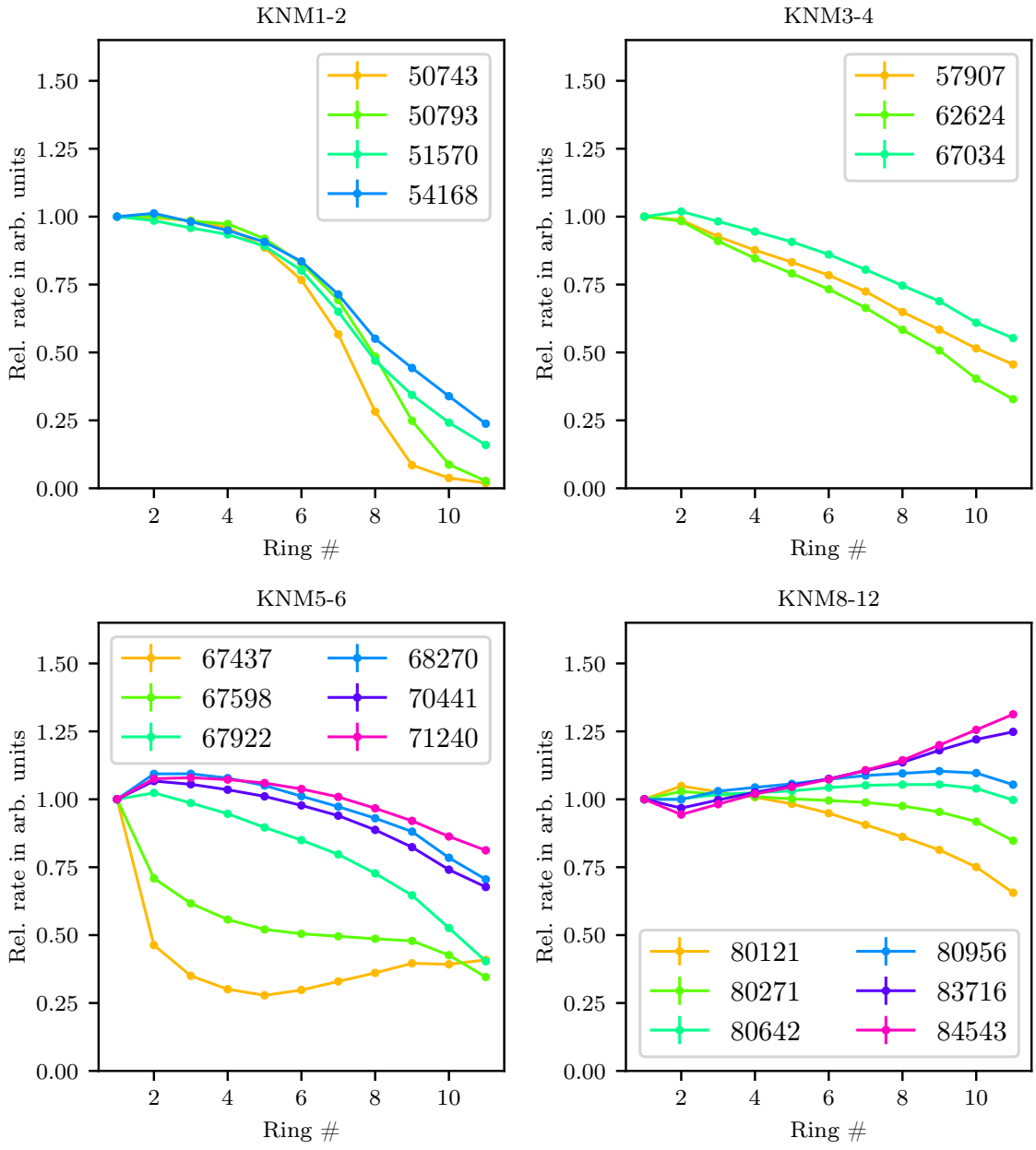

Figure 7.8: Evolution of the radial profile of the Rear Wall rate. The rate of each ring is extrapolated to the expected rate of 12 pixels. Data points are connected by straight lines to guide the eye. Uncertainties are insignificant compared to the displayed differences.

the cleaning (see Section 6.2.3). After less than ten days of tritium circulation, run 67922 shows a profile returning to a roughly parabolic shape. This curvature diminishes further for subsequent runs, with the outer rings approaching near unity in activity compared to the bullseye, with only a slight excess in the middle rings.

Following the second and third cleanings, the Rear Wall rate profiles recorded during KNM8 and KNM12 became significantly more homogeneous. These profiles resembled a horizontal line, with early measurements showing slightly lower activity in the outer rings, which gradually increased until the outer rings surpassed the inner rings in relative activity. This clear trend of homogenization in the Rear Wall rate distribution, along with the overall decrease in accumulated activity after UV/ozone cleanings (see Section 7.1.2.3), is consistent with the findings of Section 7.1.2.4 and meets the expectations of Prediction 7. It suggests a reduced influx of hydrocarbons through the Rear Wall hole, possibly due to an initial localized hydrocarbon deposit in the center of the Rear Wall during KNM1-2, serving as a precursor hydrocarbon source. The lack of such a source in the center after multiple cleanings shifts the migration of precursor hydrocarbons toward the outer regions, where the Rear Wall is in contact with its mount, which now dominates the distribution. This effect may be further amplified by reduced direct gaseous adsorption of hydrocarbons, though this is generally considered to be a minor contributor. In summary, these results clearly demonstrate a significant improvement in the homogeneity of the Rear Wall rate, driven by the depletion of hydrocarbon reservoirs as anticipated in Prediction 8. The depletion initially led to a much more uniform distribution of activity across the Rear Wall. However, with the asynchronous exhaustion of one reservoir, the homogeneity has begun to slightly decline. Despite this recent decrease, the overall homogeneity remains substantially better than prior to the depletion. There is still potential for further improvement if subsequent reservoirs also deplete, leading to a more stable and balanced Rear Wall rate in the future.

7.2 Experimental Investigations of Tritium Accumulation on a Pristine Rear Wall

Following the first Rear Wall cleaning after KNM4, a series of dedicated measurements was conducted to gain deeper insights into the tritium accumulation process. The initially low Rear Wall rate allowed for the detection of small rate changes, enabling the application of short exposure times in non-standard conditions while still yielding measurable results. An overview of these measurements can be found in Section 7.2.1. In Section 7.1.2.5, the contribution of ions to the tritium accumulation is examined, while Section 7.2.2 explores the role of charge carriers as the driving force behind this accumulation. Additionally, short-term tritium exposures are analyzed in Section 7.2.4.

7.2.1 Overview of Measurements

A series of dedicated measurements were performed to investigate the adsorption dynamics of tritium on the Rear Wall. The general procedure involved the following steps:

1. measurement of the initial Rear Wall rate,

2. controlled exposure of the Rear Wall to tritium,
3. subsequent measurement of the Rear Wall rate to observe any changes.

This process was repeated for multiple exposures. The parameters of each exposure, along with the specific aim of the measurements, are detailed in Table 7.1. The exposure order, determined by the column density during the exposure, duration, and special settings, was optimized to minimize the impact on subsequent measurements. The second exposure was performed under nominal source parameters, however, the flux tube, guiding charged particles through the source and onto the Rear Wall was shifted to expose only a quadrant of the Rear Wall to the impinging particles. All exposures were conducted with no bias voltage applied to the Rear Wall.

7.2.2 Tritium Accumulation on the Rear Wall due to Impinging Charged Particles

As discussed in Section 5.2.1, the primary mechanism proposed for the formation of aC:T on the Rear Wall is based on the Electron Beam Induced Deposition (EBID) principle. This process requires secondary electrons, created by the impinging β-electrons from the WGTS, to generate hydrocarbon fragments that subsequently polymerize, forming aC:T. To test Prediction 3, a dedicated measurement was performed on the freshly cleaned Rear Wall, as part of the exposures listed in Table 7.1.

For this investigation, the WGTS dipoles were adjusted to shift the flux tube, which normally covers the entire Rear Wall, to the upper-right quadrant. A simulation performed by G. Li, showing the altered positions of the field lines as they terminate on the Rear Wall under this shifted configuration, is presented in Figure 7.9a. Since the outer rings of the FPD are

Table 7.1: Overview of first tritium exposures after Rear Wall cleaning. Four distinct exposures were carried out, utilizing the low Rear Wall rate to gain sensitivity to small amounts of accumulated tritium. These exposures were performed under different conditions to probe the dynamics of the accumulation processes, offering insight into the various mechanisms responsible for tritium deposition on the Rear Wall.

Exposure no.	Investigation of	CD during exposure	Exposure time
1	Short time exposure	75 %	50 min
2	Charged particle contribution by deflecting them to a single RW quadrant	75 % (WGTS dipoles at 80/80 A)	22:30 h
3	Ion contribution by changing the CD which impacts the radial ion distribution	30 %	18:30 h
4	Reference measurement	75 %	23:30 h

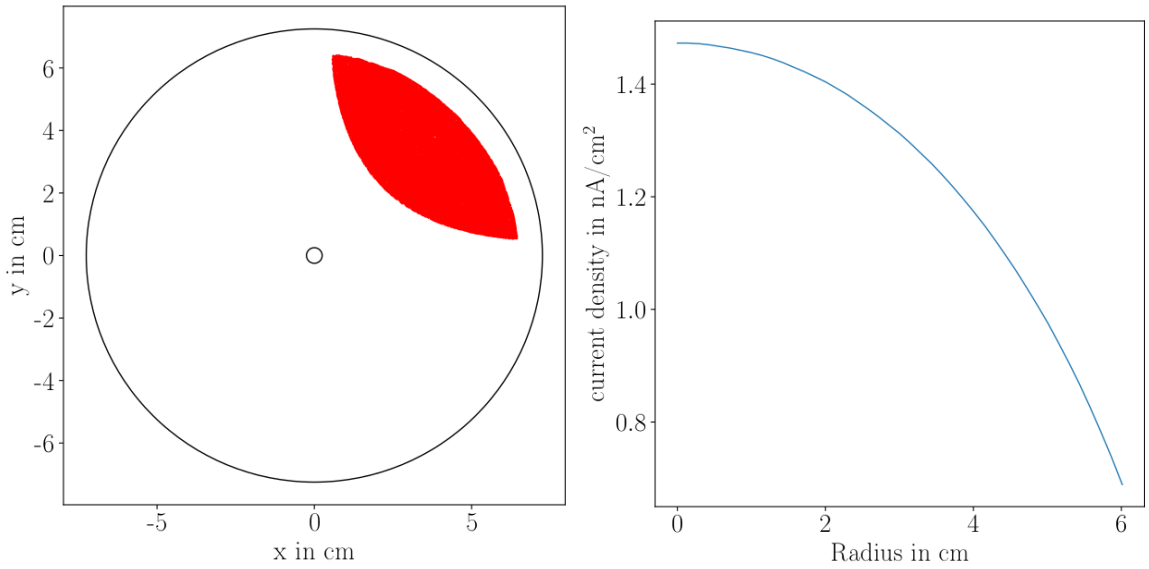

(a) Filed lines on the Rear Wall (b) Distribution of the ion current on the Rear Wall

Figure 7.9: Deflected field lines and ion current distribution on the Rear Wall, according to simulations performed by G. Li und F. Glück. (a) The flux tube was shifted to only cover parts of one Rear Wall quadrant. (b) In the nominal field setting, the ion current exhibits a radially symmetric distribution on the Rear Wall. The current is predominantly caused by cluster ions.

mostly excluded due to pixel cuts, the field lines are only displayed for the portion of the Rear Wall to which the FPD remains sensitive.

This shift in the flux tube directs both electrons and ions to the same spot on the Rear Wall, making it difficult to discern the specific contribution of each to the rate change. However, a quantitative plausibility check can be conducted for the extreme scenarios of either 100 % ion contribution or none, based on simulations by F. Glück. The radial distribution of the ion flux in the WGTS under nominal conditions is displayed in Figure 7.9b.

The analysis of tritium exposure on the Rear Wall with the shifted flux tube is detailed in Section 7.2.2.1, and the calculations for the hypothetical cases of pure ion or pure electron contributions are presented in Section 7.2.2.2.

7.2.2.1 Comparison of Irradiated and Non-Irradiated Rear Wall Sections

Figure 7.10 compares the expected rate distribution, based on simulated data, with the actual measured rate increase following the exposure with the shifted flux tube. In Figure 7.10a, the ion current distribution directed toward the Rear Wall is shown as it would be detected by the FPD. For this, the simulated ion current density inside the WGTS (Figure 7.9b) was convolved with the field line simulation data (Figure 7.9a) to estimate the ion current density on the Rear Wall's surface. This was then mapped to the FPD pixel map to visualize

where the FPD would observe a rate increase due to ion induced tritium accumulation. The assigned current is highest for pixels near the symmetry line of the top-right quadrant in the outer rings, and it drops off rapidly within one or two pixels. While the currents given correspond to ion currents, both ions and β-electrons are equivalently diverted. The key difference lies in the distribution: β-electrons exhibit a more homogeneous distribution within the irradiated area. Unlike ions, which follow the density distribution described above, β-electrons are distributed uniformly in the WGTS.

Figure 7.10b displays the observed rate increase after the shifted flux tube exposure. The rate increase shown is specifically attributed to impinging charged particles. To calculate this, the mean rate increase associated with "neutral processes" (i.e., areas not affected by the guided charged particles) was subtracted from each pixel's rate. This neutral process rate, $\hat{R}_{\text{neutral}} = (15.8 \pm 3.5)\,\text{cps}$, was determined using pixels corresponding to regions of the Rear Wall unaffected by charged particles: The inner two rings and any pixels located 1-2 pixels azimuthally away from the highlighted region (with red borders).

The resulting rate distribution shows a significant accumulation in the top-right quadrant. While the overall shape of the distribution generally matches the simulated ion current distribution, the center of the observed rate distribution is shifted inward by approximately two rings. Additionally, the observed rate distribution features a more pronounced peak that decreases more gradually over a wider area than the ion current distribution, extending the rate increase beyond the highlighted region.

To account for the radial shift, which could potentially result from misalignment in the experimental setup of the magnets that is not properly modeled in the simulation framework, the quantitative analysis takes an integral approach. Here, the ion current and corresponding rates for the pixels within the highlighted area are summed for comparison. The shape of the selected area corresponds to pixels to which an ion current above a threshold of 0.2 nA was mapped. Additionally, the selection is expanded to account for the observed shift by adding the area that is covered, if those pixels were moved two rings toward the center.

The results of this measurement strongly support Prediction 3, which postulates that aC:T formation is driven by impinging charged particles, particularly β-electrons from the source. This is evidenced by the pronounced contrast in the rate increase between the Rear Wall areas irradiated by these electrons and those that are not. The mean rate increase in pixels outside the shifted flux tube, $\hat{R}_{\text{neutral}}$, equals to about 7 % of the mean rate increase observed in Figure 7.10b.

The accumulation process attributed to "neutral processes" remains uncertain. A potential explanation for the rate increase outside the irradiated area is the migration of (tritiated) hydrocarbon fragments from the irradiated regions, which could then recombine elsewhere on the Rear Wall. This process also explains the gradually diminishing extension of the rate increase outside of the highlighted region. Assuming a stochastic recombination behavior,

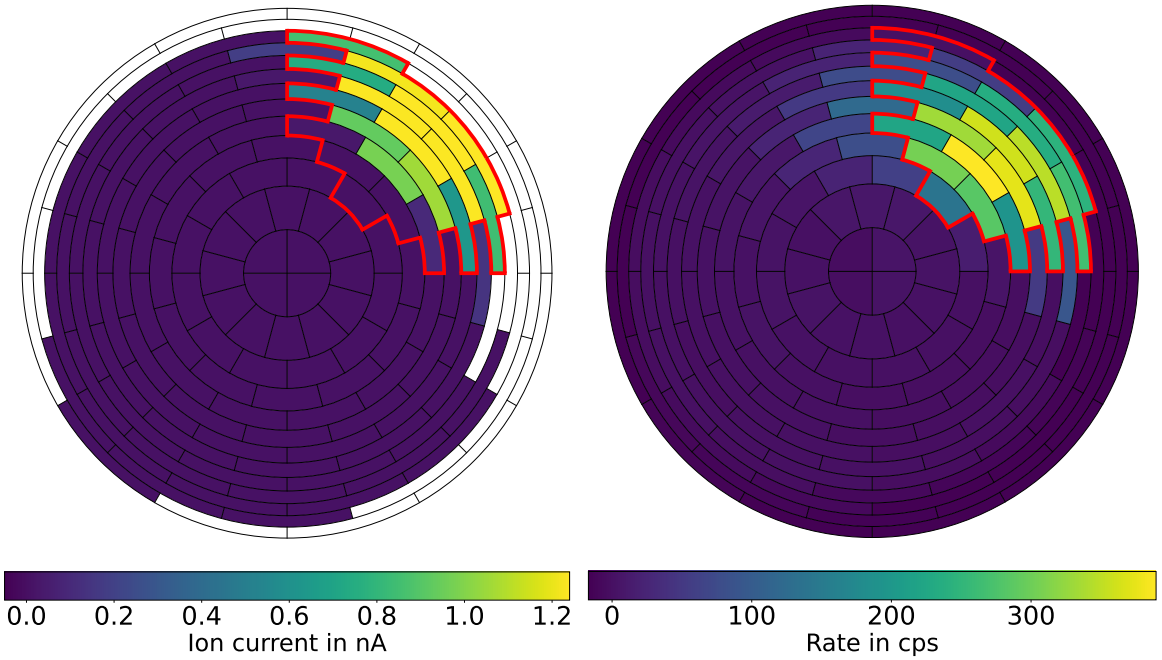

(a) Simulated ion current mapped to the FPD.

(b) Observed rate increase.

Figure 7.10: Comparison of expected and measured Rear Wall rate increase following the exposure with the shifted flux tube. The distribution of ion current impinging on the Rear Wall mapped onto the FPS pixel map (a) is positioned approximately two rings outward compared to the rate increase attributed to charged particles (b). Apart from this shift, both distributions are similar, with the rate distribution being less sharply pronounced. The area marked in red defines the pixels used to compare integral current and rates. The rate shown in (b) is corrected for the mean rate increase observed on pixels that were not impacted by the flux tube.

these fragments might migrate across the entire Rear Wall surface, contributing to the observed background rate increase, $\hat{R}_{\text{neutral}}$.

Additionally, some irradiation resulting from tritium decay outside the flux tube could promote aC:T formation in areas not directly exposed to the shifted flux tube. Since neutral tritium molecules are not influenced by the shifted magnetic field, they could contribute uniformly to tritium accumulation across the Rear Wall through processes that do not rely on activation or dissociation by secondary electrons.

7.2.2.2 Quantitative Investigation of Possible Ion or Electron Contribution

Putting the results of Section 7.2.2.1 into perspective, the implied effectiveness of tritium accumulation for either fully ion-driven or fully electron-driven processes can be calculated. The total rate increase in the considered area (highlighted area in Figure 7.10) amounted to $R_{\text{I}} = 4482\,\text{cps}$. Using the conversion factor r_{act} calculated in Section 6.1.2.3 this can

be converted into the corresponding activity on the Rear Wall, which in turn can be converted into the total number of accumulated tritium atoms N_{T} considering there are $N_{1\,\mathrm{Bq}} = 5.62 \cdot 10^{8}$ tritium atoms per Becquerel:

$$N_{\mathrm{T}} = R \cdot r_{\mathrm{act}} \cdot N_{1\,\mathrm{Bq}} = 1 \cdot 10^{15}\,\mathrm{atoms}.$$

This calculation is based on the conversion factor for a 20 nm carbon layer on the Rear Wall surface. Next, the total ion current $I_{\mathrm{Ion}} = 14\,\mathrm{nA}$, determined by the simulation and the circulation time $t_{\mathrm{circ}} = 22{:}30\,\mathrm{h}$ can be used to calculate the total number of ions

$$N_{\mathrm{Ions}} = \frac{I_{\mathrm{Ion}}}{e} \cdot t_{\mathrm{circ}},$$

where e is the elementary charge. This allows the determination of the number of tritium atoms bound per impinging cluster ion:

$$\frac{N_{\mathrm{T}}}{N_{\mathrm{Ions}}} = 1.4 \cdot 10^{-1}\,\mathrm{atoms/ion}.$$

This is a relatively high probability for the creation of a bond, but it is not entirely unrealistic. For comparison, the sticking coefficient of CH_3 radicals impinging on an aC:H surface in conjunction with H atoms can reach values around 10^{-2}[Von02]. The cluster ions reaching the Rear Wall are thermal and dissociate upon recombination with electrons, which are readily available on the surface of the Rear Wall. Leaving a reactive tritium atom with some energy from the dissociation to surpass required activation energies. However, caution is advised with this result, as the ion profile simulation includes some assumptions that may not fully reflect reality. For instance, the boundary conditions for the plasma, in which the ions are created, may not be accurate given the partial flux tube shift, for which no adaption regarding surface potentials could be provided. Furthermore assumptions regarding surface work functions were made without the possibility of verification.

In contrast, the tritium accumulation induced by electron irradiation is considered. Here, neutral T_2 molecules are taken as the source of tritiation, and $\hat{R}_{\mathrm{neutral}}$ is ignored for direct comparability, focusing on induced effects that don't occur outside of the flux tube on the Rear Wall. The inflow of tritium molecules can be estimated from the reduction factor of the last pump port between the WGTS and the RS. The gas flux towards the pump port $f_{\mathrm{T_2}} = 0.9\,\mathrm{mbarl/s}$, and the reduction factor $p_{\mathrm{red}} = 400$ at the pump port based on pressure differences, provide the foundation for calculating the tritium influx density:

$$I_{\mathrm{T_2}} = \frac{f_{\mathrm{T_2}}}{p_{\mathrm{red}} \cdot A_{\mathrm{pump}}} \cdot A_{\mathrm{eff,\,RW}},$$

where A_{pump} is the cross-sectional area of the pump port which has a diameter of 250 mm, and $A_{\mathrm{eff,\,RW}}$ is the effective area on the Rear Wall, calculated using the number of FPD pixels

N_{pixel} that correspond to the area highlighted in Figure 7.10b. The area of each pixel on the wafer is $A_{\text{pixel}} = 43\,\text{mm}^2$ and the effective area is given by:

$$A_{\text{eff, RW}} = N_{\text{pixel}} \cdot A_{\text{pixel}} \frac{B_{\text{FPD}}}{B_{\text{RW}}},$$

where B_{FPD} and B_{RW} are the magnetic field strengths at the FPD and the Rear Wall respectively. From this the number of tritium atoms bound per impinging T_2 molecule is calculated as:

$$\frac{N_{\text{T}}}{N_{\text{T}_2}} = \frac{N_{\text{T}}}{I_{\text{T}_2} \cdot t_{\text{circ}}} = 1.0 \cdot 10^{-6}\,\text{atoms/T}_2$$

This analysis shows that for the tritium accumulation to be solely ion-driven a high bonding cross section would be required, while a purely electron-driven accumulation profits from the abundant T_2 molecules, requiring only a comparatively low cross-section. The data does not clearly distinguish between ion- and electron-driven processes, but the high binding probability disfavors a completely ion-driven process. Further measurements are needed to resolve this, which will be proposed in Section 7.4.2

7.2.3 Impact of Different Column Densities on the Radial Profile

The conditions within the WGTS play a crucial role in determining both the amount and the density profile of ions traveling towards the Rear Wall. The formation of cluster ions, which scales quadratically with gas density, is of particular interest. These cluster ions are the dominant species reaching the Rear Wall, as other ions tend to recombine before making contact. This fact opens up further ways to investigate the tritium accumulation process, specifically regarding the contribution of ions.

With a lower column density-such as the 30 % level used during the third exposure (see Table 7.1)-a smaller radial dependence of the Rear Wall activity is expected if ions play a crucial role in tritium accumulation. The rationale lies in the radial ion density profile in the WGTS, as shown in Figure 7.9b, which could cause the pronounced radial profile observed in the Rear Wall activity.

To explore this hypothesis, the radial profiles of the Rear Wall activity were compared across three exposures conducted during the dedicated measurements after the first Rear Wall cleaning. In order to mitigate the asymmetry in the profile caused by the shifted flux tube exposure (discussed in Section 7.2.2), which took place between the exposure measurements, pixels within the area marked in Figure 7.10 were excluded from the analysis. The background from the previous measurement was subtracted, ensuring that only the rate changes due to the new exposure were considered. The radial profile was then examined analogously to Section 7.1.2.5.

The resulting radial profiles of the rate growth due to initial Exposure 1 at 75 % column density, Exposure 2 at 30 %, and Exposure 3 at 75 % are depicted in Figure 7.11. Each

exposure resulted in a rate increase with a clear radial profile, and no significant deviations can be observed between them. While the uncertainty of each data point-below 0.35 %-is insufficient to fully account for the differences, no structural changes in the profiles are noticeable. Small deviations could be attributed to the high dynamic range in the early stages of tritium accumulation on the freshly cleaned Rear Wall, as seen in the steep rate increase and sharp changes in the early KNM5 circulation (see Figure 7.4). There may be a possible effect on the outer rings, where the exposure at 30 % column density led to a lower relative rate increase compared to both exposures at 75 %. However, the difference between the two high column density exposures was larger than that between the low and high column density exposures, pointing towards a general change in the radial activity distribution discussed earlier.

Ultimately, no definitive conclusions can be drawn from this data regarding the contribution of ions to Rear Wall tritium accumulation. The observed results may suggest that either ions do not contribute significantly, or that the effect of the changed column density was too weak compared to other factors, such as growth variations during ongoing accumulation, as discussed in Section 6.1.2.

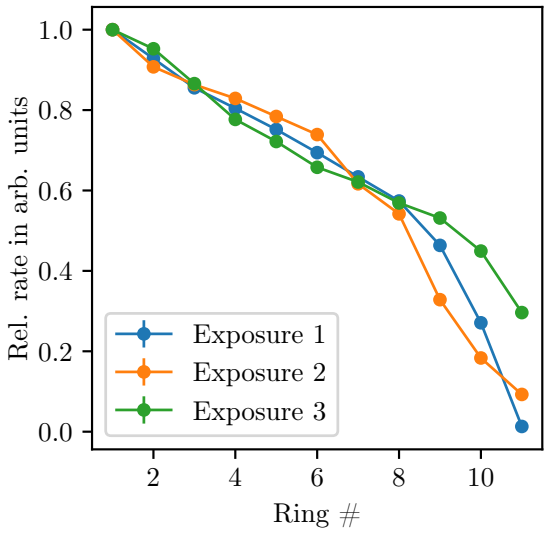

Figure 7.11: Radial profiles of the rate increase due to exposures at different column densities. Only the rate changes due to the respective exposure are considered. The data points are normalized to the rate of the bullseye. Pixels affected by the exposure with shifted flux tube are exempt from this analysis. The error bars are to small to be seen by the eye. The data points are connected by straight lines to guide the eye.

7.2.4 Observed Rate Increase Following Tritium Exposure

The fine meshed observation of the Rear Wall rate evolution and the use of different circulation parameters in the dedicated measurement campaign following the first Rear Wall cleaning provide insight into the correlation between tritium accumulation and tritium throughput. While the exposure time of Exposure 1 (see Table 7.1) was too short to guarantee a fully stabilized gas distribution in the system leading to an oscillating CD during the exposure time, Exposures 3 and 4 provide a more stable basis for analysis. The pixels impacted by the exposure during the shifted flux tube are excluded, analogously to the approach used in Section 7.2.3. The exposures were short and close in time, minimizing major differences in growth behavior. However, since these measurements occurred during the highly dynamic initial growth phase, some influence on the results is still possible, as noted in Section 7.2.3. By comparing the rate increases following Exposures 3 and 4, and normalizing them by the amount of circulated tritium, a difference in rate growth per tritium flow is observed:

- $\dot{R}_{30\,\%} = (11.66 \pm 0.07)$ cps/mbarl for Exposure 3 with a CD of 30 %, and
- $\dot{R}_{75\,\%} = (17.20 \pm 0.04)$ cps/mbarl for Exposure 4 with a CD of 75 %.

Despite normalizing for dosage, a significant difference remains, indicating a correlation between rate accumulation and gas density. However, this relationship is not quadratic, as might be expected for the ion production. A decrease in growth would be expected for the later measurement based on the trend observed during KNM5. However, an increase occurred instead. A possible explanation could be that at a lower CD, a higher relative amount of T_2 passes through the first pump port. Since this pump port operates in the transition flow regime, stronger beaming at lower CD could lead to deteriorated pump performance, resulting in a higher availability of T_2 molecules relative to the same dosage at lower CD values.

7.3 Empirical Model of the Tritium Accumulation on the Rear Wall

This section aims to help digest the results of Chapters 6 and 7 by consolidating individual findings into a unified model of the processes on the Rear Wall that lead to tritium accumulation on its surface. The goal is twofold: first, to understand the fundamental processes driving the observed results, and second, to create a model that can guide strategies for mitigating the impact of tritium accumulation on KATRIN's m_ν analysis. While not fully comprehensive, as it doesn't delve deeply into the complex surface physics occurring on microscopic scales, the model will be customized to the specific needs of the KATRIN experiment, with a primary focus on surface-near activity - tritium decays leading to counts detected by the FPD near the endpoint of the primary spectrum.

The fundamentals of this model were initially presented as a working hypothesis in Section 5.3.1.

The model posits that hydrocarbon precursors from reservoirs within the system migrate to the Rear Wall via surface diffusion. Beta-electrons impinging on the Rear Wall generate secondary electrons, which dissociate these hydrocarbons. The dissociated fragments then recombine and polymerize into an amorphous carbon layer (aC:T) that accumulates and retains tritium on the Rear Wall surface. Over time, this leads to increasing activity observable by the FPD. The tritium in aC:T produces a secondary beta spectrum distinct from the primary gaseous tritium spectrum in the WGTS, forming a time-evolving background that distorts the measurement results.

In Section 5.3.2 a series of predictions were derived from this model. Those predictions were probed by the results presented throughout Chapters 6 and 7.To synthesize an overall understanding of the model's validity and implications, those predictions are revisited below, in light of the corresponding experimental findings, providing an evaluation of how well the results support or challenge the proposed model:

Prediction 1 **Tritium Accumulation:** An increase of tritium activity on the Rear Wall was observed correlated with tritium throughput, as outlined in Section 7.1.2.

The observed rate evolution is the central result and aligns with the model's core hypothesis by following the functional form

$$R_{\mathrm{RW}}(f) = a \cdot \exp\left(k \cdot (f + f_0)\right) + b \cdot (f + f_0)\,, \tag{7.2}$$

as discussed in Section 7.1.2.2. This function holds after several Rear Wall cleanings, though the linear component's slope diminishes, as discussed in Section 7.1.2.3. In contrast to the EBID process discussed in Section 5.2.1.2, on which the rate growth model is based, it is found that tritium availability is critical alongside dosage (see Section 7.2.4), with the integral tritium flow serving as a suitable proxy for dosage. However, some dependence on the CD remains.

Prediction 2 **Shift of the β-Spectrum:** The endpoint of the secondary β-spectrum was found to be (2.5 ± 0.4) eV higher compared to the primary spectrum, which aligns with the expectation for carbon-bound tritium.

Prediction 3 **Electron-Induced Tritium Accumulation:** Dedicated measurements demonstrated that tritium accumulation is predominantly driven by irradiation of the Rear Wall with charged particles (see Section 7.2.2.1). While the differentiation between electrons and ions as the responsible particle species could not be conclusively determined to verify the EBID process as the fundamental accumulation mechanism, several results, as discussed in Sections 7.1.2.5 and 7.2.3 indicate that the electron induced process is favored.

Prediction 4 **Tritium retention:** The accumulated tritium was found to be firmly bound on the Rear Wall and resistant decontamination procedures, except for UV/ozone cleaning, as reported in Sections 6.2.2 and 6.2.3. This behavior aligns with the expectations for aC:T. Illumination with UV light resulted in some reduction of the accumulated tritium amount, though the process was slow Section 6.2.2.

Prediction 5 **Tritium removal:** Cleaning procedures that either extract tritium from the aC:T matrix or directly remove the aC:T layer were found to effectively and durably reduce the Rear Wall rate, as discussed in Sections 6.2.2 and 6.2.3. However, the effectiveness of isotope exchange using D_2 as an exchange gas was limited. Greater impact was observed when exposing the tritiated surface to air with residual moisture, which is also attributed to isotope exchange reactions. UV/ozone cleaning proved to be the most effective decontamination method. The decontamination factor of roughly 1300 achieved with this surface cleaning procedure indicates that the observed tritium activity is located on the surface and the contribution of tritium migrated into the bulk material is insignificant.

Prediction 6 **Quick Regeneration After Cleaning:** After each cleaning procedure, a rapid initial re-accumulation of tritium was observed. This regeneration was fastest following cleaning methods that likely leave aC with dangling bonds on the Rear Wall, such as decontamination with UV light (Section 7.1.2.1). The effectiveness of regeneration decreased with more thorough cleaning, which reduced the amount of precursor hydrocarbons available for regeneration processes, as discussed in Sections 7.1.2.2 and 7.1.2.3.

Prediction 7 **Activity Distribution:** Changes in the spatial activity distribution on the Rear Wall have been observed as discussed in Section 7.1.2.5. These changes show a general trend towards homogenization following cleaning, which is presumed to be influenced by the local availability of precursor hydrocarbons.

Prediction 8 **Exhaustion of Hydrocarbon Reservoir:** An upper level of saturation for tritium accumulation was reached after extensive cleaning, as detailed in Section 7.1.2.3. During this stage, desorption of tritium during system evacuation was observed, suggesting the presence of a previously not observed type of tritium bonding, possibly weak bonding on gold.

In conclusion, all predictions derived from the underlying model for the observed Rear Wall rate growth have been validated. Further, dedicated studies are needed to determine the relative contributions of tritium cluster ions versus electrons to the tritium accumulation. The temporal evolution of the Rear Wall rate is expected to maintain its current stagnating trend. Given the observed desorption dynamics, it is likely that the currently saturated Rear Wall rate is due to a residual aC:T layer, which could be reduced further

with additional UV/ozone cleaning. The disproportionate growth of the rate on the outer rings is anticipated to continue, albeit slowly, until the hydrocarbon reservoir is depleted, which could potentially be accelerated by further UV/ozone treatments.

This model has facilitated the development of a targeted strategy to mitigate the impact of accumulated tritium on the KATRIN m_ν determination, which is outlined in Section 7.4.

7.4 Mitigation Strategy for Tritium Accumulation on the Rear Wall and its Impact on the KATRIN m_ν Analysis

This section revolves around the central goal of this work: the **development and implementation of a comprehensive strategy to mitigate the impact of tritium accumulated on the Rear Wall on the KATRIN m_ν analysis**. Based on insights gained from the model describing tritium accumulation on the Rear Wall, this strategy consists of three procedures, each addressing different aspects of the Rear Wall activity:

1. **Decontamination Procedure:** As outlined in Section 6.2, this involves cleaning the Rear Wall between measurement phases to reduce the total contribution of the secondary spectrum to the measured data.
2. **Measurement Procedure:** As detailed in Section 6.3.1, this involves regularly measuring the Rear Wall rate throughout the measurement phases and conducting Rear Wall scans between measurement campaigns to monitor any accumulation.
3. **Analysis Procedure:** This merges both the Rear Wall rate measurements and the spectral information from the Rear Wall scans to provide input for the KATRIN m_ν analysis, allowing for consideration of the secondary spectrum in the analysis.

The analysis procedure is outlined in detail in this section.

7.4.1 An Analysis Procedure for KATRIN to Consider Tritium Accumulated on the Rear Wall

The measurement and analysis of the secondary spectrum, described in Section 6.1.1, lay the foundation to quantify the contribution of the secondary spectrum to the measured data for neutrino mass analysis. This quantification is done using three key input parameters:

1. **Endpoint E_0 and Shape parameter $w_{GR,RW}$**: Both are determined through fitting and are used to describe the shape of the secondary spectrum, allowing it to be considered as background. The endpoint, E_0, is linearly adapted for RW bias using the time-weighted RW bias from the corresponding measurement campaign. No

further adjustments are required, as the endpoint and shape parameter have been shown to be stable over time, as reported in Section 6.1.1.

2. **Signal Amplitude**: This parameter quantifies the impact of the secondary spectrum on the measured data by describing the amplitude of the secondary spectrum. Since it varies over time and the Rear Wall scans require long measurement durations, extrapolation is necessary, as discussed in Section 6.3.1. The extrapolation process will be detailed in the following[2].

The focus here is to ensure these parameters accurately describe the secondary spectrum for proper integration into the neutrino mass analysis.

Since the signal parameter depends on the CD by definition, a virtual CD for the Rear Wall scans is introduced, and the signal parameter is scaled accordingly, as noted in Section 4.3.2. This allows for a direct comparison between the Rear Wall signal and the signal from the corresponding beta scans of a measurement campaign.

The mean Rear Wall signal per patch is required as input for the KATRIN m_ν analysis. Since the signal parameter represents the amplitude of the beta spectrum, it is proportional to the Rear Wall rate. Therefore, tracking the signal evolution relative to the RW rate and integral flow is essential for accurately representing the impact of the secondary spectrum in the neutrino mass analysis.

For multiple Rear Wall scans recorded at different times, a fixed growth model $R(f)$ is fitted to the data with a free amplitude parameter s to determine the mean signal for each patch

$$\mathrm{Sig}(s, f) = s \cdot R(f). \tag{7.3}$$

To estimate uncertainties on the mean signal, a set of input parameters for the growth model is sampled using a multivariate normal distribution. The fit is then performed as mentioned above for each sample, with 10 000 samples leading to fit results for s and σ_{fit}. The uncertainty on s is calculated by combining the mean of the fit uncertainties $\bar{\sigma}_{\mathrm{fit}}$ with the error on the mean of s, $\sigma_{\mathrm{eom}} = \sigma_{\mathrm{std}}/\sqrt{n_{\mathrm{samples}}}$ by adding them in quadrature. This signal value is then extrapolated by applying the patchwise growth models shown in this chapter (see Section 7.1.2.4). To compute the impact of the Rear Wall rate on recorded beta scan data, the mean signal value for each beta scan run i during a campaign is calculated for each patch as an integral mean:

$$\overline{\mathrm{Sig}}_i = \frac{1}{\mathrm{f_{End}} - \mathrm{f_{Start}}} \int_{\mathrm{f_{Start}}}^{\mathrm{f_{End}}} \mathrm{Sig}(s, f) df \tag{7.4}$$

The correlation between the growth model and the scaling parameters across all i runs is accounted for by drawing values from a shared distribution for all runs and sampling

[2] Details of this work were conceptualized in the Masters thesis "Investigation of spectral characteristics of the rear wall background and systematic inputs for the neutrino mass analysis" by Simon Tirolf, 2022, KIT

the growth model parameters from a multivariate Gaussian distribution. To calculate the total contribution of the secondary spectrum to the data analyzed for a given measurement campaign, a time-weighted mean signal for the campaign is computed as follows:

$$\overline{\mathrm{Sig}} = \sum_i \frac{\overline{\mathrm{Sig}}_i \cdot t_i}{t_{\mathrm{total}}}, \tag{7.5}$$

where t_i represents the duration of each run, and t_{total} is the total run length of all considered runs. This process is repeated 10 000 times, and the final input value for the KATRIN m_ν analysis is obtained by computing the mean of all $\overline{\mathrm{Sig}}$ values. The uncertainties are estimated by taking the standard deviation of the distribution of all samples from these iterations.

7.4.2 Conclusive Remarks

This work laid the foundation to mitigate the impact of tritium accumulated on the Rear Wall on the KATRIN m_ν determination. The strategy and procedures developed have been implemented in the measurement operations and analysis chain of KATRIN. This has contributed to the comprehensive analysis of the KNM1-5 measurement runs and yielded recently published results on the upper m_ν limit [Ake24a]. Due to the mitigation strategy implemented in the scope of this work, the total uncertainty from the secondary spectrum on this result was limited to $0.004\,\mathrm{eV}^2/\mathrm{c}^4$. Omitting this approach would have led to an estimated shift in m_ν^2 of up to $0.073\,\mathrm{eV}^2/\mathrm{c}^4$ for a single measurement campaign, with this value possible increasing further, without cleaning of the Rear Wall.

For the upcoming analysis of the Rear Wall activity in campaigns from KNM8 onwards, the model developed here can be applied. It should be expanded to account for desorption during circulation stops, which follows a hyperbolic trend as discussed in Section 5.1.2.2.

To deepen the understanding of the tritium accumulation process, ion contributions can be explored through a proposed experiment. Similar to the procedure discussed in Section 7.2, the Rear Wall should be cleaned to low tritium levels, and the flux tube deflected using WGTS dipoles to expose the Rear Wall to tritium. This step should be repeated in a second exposure of a different Rear Wall quadrant while a low positive Rear Wall bias voltage is applied to deflect cluster ions. By comparing the differences in accumulation, the role of ions in the process can be better understood.

8 Summary and Outlook

Neutrinos have been a source of intrigue since their discovery, posing challenges to our understanding of particle physics. The discovery of neutrino oscillations revealed they must possess mass, contradicting their originally assumed massless nature in the SM. This breakthrough sparked some of the most pressing questions in neutrino physics today: What is the absolute value of this mass? Do sterile neutrinos exist, potentially giving insight to the process of neutrino mass generation?

The
acrlongKATRIN (KATRIN) experiment is one of the major efforts in neutrino physics, aiming to determine the effective electron antineutrino mass m_ν with an unprecedented sensitivity of better than 0.3 eV/c^2 at 90 % CL. To achieve this, KATRIN employs the model-independent approach of high-precision β-spectroscopy. By measuring the tritium β-decay spectrum near its endpoint and analyzing its shape for the characteristic signature of neutrino mass, KATRIN has set the most stringent limit to date on the effective neutrino mass using a direct kinematic method. From the data of its first five measurement campaigns, KATRIN has established the upper limit: [Ake24a]:

$$m_\nu < 0.45 \text{ eV/c}^2 \text{ at } 90 \text{ \% CL.} \tag{8.1}$$

The gold-coated Rear Wall is a vital component of the KATRIN experiment, serving as the termination of the flux-tube. hence defining the starting potential of the β-electrons. Positioned at the end of the source, it interacts with the full magnetic flux tube that adiabatically guides the β-electrons from the tritium source, through the pumping and transport sections, and onward to the main spectrometer and detector. As such, the Rear Wall is exposed to tritium, as well as tritium ions and electrons originating from the source, which are guided towards it.

Over time, an increasing amount of tritium was observed accumulating on the surface of the Rear Wall. This accumulation of activity leads to the creation of a secondary β-spectrum, distinct from the primary β-spectrum produced by tritium decay in the Windowless Gaseous Tritium Source (WGTS). The secondary spectrum has a different shape and endpoint energy ($E_{0,\text{RW}}$), and acts as a background. This results in KATRIN measuring a superposition of the primary and secondary spectra, causing a distorted overall spectrum.

The distortion impacts the spectral shape in the endpoint region, where the signature of the neutrino mass is probed, leading to a bias in the determination of m_ν^2. To address this,

a comprehensive strategy to mitigate the impact of tritium accumulated on the Rear Wall on the KATRIN m_ν analysis was developed and implemented in the KATRIN operation and the analysis chain within the scope of this thesis.

This strategy involved five key sub-tasks:

1. Understanding the accumulation process,
2. Development of characterization methods,
3. Direct mitigation of tritium accumulation,
4. Characterization of the evolution of the secondary spectrum and
5. Providing inputs for the m_ν analysis.

Understanding the Accumulation Process

Clarifying the fundamental processes responsible for tritium accumulation on the Rear Wall is essential for addressing the issue effectively. Two key questions need to be answered to develop appropriate mitigation procedures: In what form is tritium bound to the Rear Wall and how can it be removed efficiently?

Previous studies concluded that the direct adsorption of tritium onto the gold coating of the Rear Wall is insufficient to explain the observed accumulation and retention capabilities, suggesting the involvement of an intermediary that facilitates tritium binding. Amorphous carbon (aC) has emerged as a likely candidate, as it is known to effectively bind tritium, forming aC:T. The formation of aC has been documented in systems under conditions similar to those in KATRIN, particularly in fusion-related research. Additionally, the formation of aC is extensively studied in electron microscopy, specifically in the context of Electron Beam Induced Deposition (EBID).

In EBID, electrons with energies of a few keV generate secondary electrons that fragment surface-bound hydrocarbons. These fragments subsequently recombine to form aC, which can be tritiated through various processes, resulting in aC:T. This insight allowed the construction of a working hypothesis for the tritium accumulation observed on the Rear Wall.

Based on this hypothesis, several cleaning procedures aimed at removing tritium from the Rear Wall were developed. Additionally, a series of predictions were derived from the hypothesis - including a model describing the accumulation dynamics - and tested, providing validation for the proposed mechanism.

Development of Characterization Methods

To mitigate the impact of the secondary spectrum on the m_ν determination, it is crucial to thoroughly characterize the secondary spectrum. This characterization allows the

secondary spectrum to be treated as a background signal in the KATRIN analysis chain. A two-fold approach was developed for this purpose.

First, the secondary spectrum is measured while the tritium source is evacuated, providing key parameters such as the endpoint energy $E_{0,\mathrm{RW}}$, shape parameter $w_{\mathrm{GS,RW}}$ and signal amplitude $A_{s,\mathrm{RW}}$ of the secondary spectrum. This so-called Rear Wall-scan offers a detailed description of the shape of the secondary spectrum but requires significant measurement time - on the order of days. However, it was found that while the endpoint and shape parameter of the secondary spectrum remain constant over time, only the signal amplitude increases as more tritium accumulates.

This consistency in shape allows the Rear Wall-scan to be complemented by a second, faster measurement known as the Rear Wall-rate measurement. By measuring the rate at electron energies as low as 14 keV, where the electron rate is higher, measurement times can be reduced to a few minutes. This provides a fast option to monitor the changing signal amplitude while maintaining the statistics needed for the m_ν analysis. It also allows Rear Wall scans to be limited to maintenance phases, optimizing measurement efficiency.

Direct Mitigation of Tritium Accumulation

The approach of mitigation within the KATRIN data analysis is complemented by a reduction of the activity on the Rear Wall. Decontaminating the Rear Wall reduces the contribution of the secondary spectrum to the measured data by lowering the overall rate. Given the resilience of aC:T to many conventional decontamination techniques different methods were tested and compared. Among these, UV/ozone cleaning emerged as by far the most effective, achieving a rate reduction of about three orders of magnitude in just over three days. The high decontamination factor achieved through a surface cleaning technique suggests that the tritium responsible for the secondary spectrum resides primarily near the surface, with tritium absorbed deeper into the material playing only a negligible role.

The UV/ozone cleaning showed increased effectiveness with repeated applications, and there were indications that hydrocarbon reservoirs, which act as precursors for further aC:T formation, were becoming exhausted. There is some concern that UV/ozone cleaning might negatively affect the work function of the Rear Wall, potentially altering the effective starting potential of the β-electrons in the source. However, this risk can be minimized by keeping the decontamination times short due to the high efficiency of the cleaning process.

Characterization of the Evolution of the Secondary Spectrum

The parameters describing the shape of the secondary spectrum, $E_{0,\mathrm{RW}}$ and $w_{\mathrm{GS,RW}}$, were observed to remain stable over time, with the signal amplitude A_s being the only variable

parameter. To track these changes, intermittent Rear Wall rate measurements were conducted throughout measurement campaigns. Cleaning the Rear Wall surface allowed for accurate monitoring of the temporal evolution of the Rear Wall rate, enabling repeated testing of the accumulation model under controlled conditions. The outcomes consistently reproduced the qualitative behavior predicted by the model, with observed changes in accumulation rate and spatial distribution understood in the context of the model as environmental shifts resulting from cleaning.

The model derived from the working hypothesis describes the Rear Wall rate R_{RW} as a limited growth function of the integral tritium flow f circulated through the WGTS. This function converges toward a linear growth, with the integral tritium flow acting as a combined measure of both the dosage and the availability of tritium for accumulation. The function has the form:

$$R_{\mathrm{RW}}(f) = a \cdot \exp\left(-k \cdot (f + f_0)\right) + b \cdot (f + f_0)\,. \tag{8.2}$$

Recorded data aligned well with this model, with R_{RW} stabilizing at a constant rate after repeated cleanings, showing a vanishing slope for the linear component. The information from these measurements is critical for assessing the contribution of the secondary spectrum to the data recorded by KATRIN, enabling interpolation and extrapolation of its impact on the measured spectrum.

Additionally, these studies - complemented by dedicated measurements - provided further validation of predictions from the working hypothesis:

- Analysis of tritium accumulation under partial deflection of the flux tube supported the hypothesis of an electron-beam-induced aC:T formation process.
- The expected initial rapid regeneration of the Rear Wall rate post-cleaning, attributed to residual aC remaining on the Rear Wall surface, was observed.
- After each cleaning, the spatial distribution of the activity on the Rear Wall was found to homogenize, consistent with the hypothesis for pre-existing hydrocarbons being present on the Rear Wall and acting as precursor molecules for aC:T.
- The saturation of the Rear Wall rate at a low value after multiple cleanings, along with the changes in spatial distribution, support the proposed exhaustion of hydrocarbon reservoirs on the Rear Wall surface.

Providing Inputs for the m_ν Analysis

The final step combines the Rear Wall rate evolution model with data from Rear Wall scans taken between measurement campaigns to accurately quantify the total contribution of the secondary spectrum during each campaign. The rate evolution model tracks the amplitude of the secondary spectrum over time, and with the parameters describing the shape of the spectrum, this enables computation of inputs for the KATRIN analysis. By integrating the

secondary spectrum as a background signal into the fit model, the analysis chain mitigates its impact. Together with repeated Rear Wall cleanings to directly reduce the secondary spectrum, this approach limits the effect on the determined $m_u pnu^2$ to an uncertainty of 0.004 eV^2/c^4, which is well within the uncertainty budget of the experiment. Without these measures, a shift Δm_ν^2 would result, which was estimated on a campaign-wise basis and reaches up to 0.073 eV^2/c^4. Without the cleaning applied this impact could grow even larger. Especially effective was the combination of Rear Wall rate measurements and Rear Wall scans. Between KNM5 and KNM12, a total of 33 Rear Wall rate measurements were conducted, each lasting about 10 min, compared to two to four days required for a single measurement with Rear Wall scans, depending on accumulated activity. Over this period, roughly 485 days were dedicated to β-scans. This comparison emphasizes the efficiency of combining both Rear Wall rate measurements and Rear Wall scans, as obtaining equivalent data through Rear Wall scans alone would be impractical within the operational timeframe.

Outlook

With the strategy developed and implemented in this work, KATRIN is well-prepared to address the tritium accumulation on the Rear Wall through the completion of the current neutrino mass measurement program, expected to run until late 2025. The methods developed can be applied across all remaining data-taking phases, with minor adjustments to account for observed desorption dynamics. These dynamics have emerged following significant removal of aC:T and probable exhaustion of accessible hydrocarbon reservoirs. While this model adjustment is straightforward, an open question remains regarding the evolution of hydrocarbon reservoirs within the systems of KATRIN: will they eventually deplete entirely, or will migration of hydrocarbons from more remote regions substitute those in proximity to the Rear Wall over time?

Another open question could further deepen the understanding of aC-facilitated tritium accumulation on surfaces: what role do tritium (cluster-)ions play in aC:T formation? While findings in this work suggest that the process is primarily electron-induced, a clear distinction between contributions from electrons and ions was not achieved in one of the critical measurements. An additional measurement, as proposed in Section 7.4.2, could provide clarity on this mechanism. While not essential for the main objectives of KATRIN, this insight could offer valuable information on the underlying processes at play. As upcoming tritium-based neutrino experiments progress in planning and target even higher sensitivity. Gaining a more detailed understanding of the accumulation process could support the early development of additional strategies to mitigate potential systematic effects from tritium adsorption.

This understanding is particularly relevant for the future experimental program of KATRIN, which aims to search for sterile neutrinos with masses in the keV range. To achieve this, the TRISTAN detector upgrade will be installed, enabling measurements of the tritium

β-spectrum at greater depth and with significantly reduced source activity [Sie24; Ake22b]. For these measurements, mitigating background from residual tritium is even more critical. Although a lower column density may reduce activity buildup, any tritium remaining on the Rear Wall will represent a proportionally higher background due to lower source activity. Addressing this will be crucial for accurate measurements.

The KATRIN collaboration plans to replace the current Rear Wall with a beryllium (Be) disk, to reduce backscattering of electrons on the Rear Wall, which poses as a more significant systematic effect for measurements deep in the tritium β-spectrum. This change will necessitate studies to determine how effectively the findings from this work can be applied, including an evaluation of the compatibility of a Be Rear Wall with UV/ozone cleaning and potential aC formation on Be surfaces. These investigations are currently ongoing.

Appendices

Appendix A

Overview of MS Field Settings

Table A.1: Applied currents and voltages for the MAX and SAP setting. The MAX and SAP setting primarily differ in the currents applied to the LFCS system. For the MAX setting different configurations in of the steep and flat cone (IE rings) were used.

	MAX-Setting			SAP-Setting
	130/130	40/40	SAP-like	
Coil #		Air coil current in A		
1		120		120
2		120		-4
3		120		116
4		120		70
5		110		70
6		110		70
7		110		70
8		110		110
9		110		110
10		110		110
11		110		-60
12		110		-28
13		120		58
14		120		5
15		120		120
16		120		120
17		120		-120
18		120		-119
19		120		-120
20		120		-120
Ring #		IE ring voltage in V		
2,3	130	40	125	125
4,6	130	40	25	25
15	130	40	45	45
16	130	40	105	105

Appendix B

Patch-Wise Fit Results for the Rear Wall Rate Evolution

Table B.1: Patchwise fit results of the KNM3-4 Rear Wall rate model, showing a decreasing slope with increasing patch numbers, indicating that the rate growth diminishes towards higher radii. This suggests a spatial dependence of the tritium accumulation process, with outer regions of the Rear Wall exhibiting slower growth compared to the inner regions.

Patch no.	m in $1 \cdot 10^5$ cps/mbar·l	c in $1 \cdot 10^6$ cps
1	3.30 ± 0.18	−0.79 ± 0.26
2	3.33 ± 0.15	−0.86 ± 0.21
3	3.29 ± 0.10	−1.10 ± 0.14
4	3.25 ± 0.09	−1.08 ± 0.13
5	3.17 ± 0.06	−1.18 ± 0.09
6	3.05 ± 0.05	−1.19 ± 0.06
7	2.99 ± 0.02	−1.32 ± 0.02
8	2.88 ± 0.02	−1.34 ± 0.02
9	2.78 ± 0.04	−1.39 ± 0.05
10	2.69 ± 0.06	−1.43 ± 0.08
11	2.44 ± 0.05	−1.41 ± 0.07
12	2.08 ± 0.07	−1.27 ± 0.09
13	2.22 ± 0.07	−1.45 ± 0.10
14	1.64 ± 0.06	−1.10 ± 0.08

Table B.2: Patchwise fit results of the KNM5 and KNM6 Rear Wall rate models, with a clear trend visible of the slope in the KNM5 model b approaching the values of the KNM6 model slope m at higher patch numbers.

Patch no.	a in 10^8 cps	k in 10^6 mbar·l^{-1}	f_0 in 10^6 mbar·l	b in 10^{-1} cps/mbar·l	m in 10^{-1} cps/mbar·l	c in 10^7 cps
1	−2.44 ± 0.65	1.11 ± 0.07	4.52 ± 0.13	3.02 ± 0.04	1.68 ± 0.03	3.53 ± 0.05
2	−1.86 ± 0.67	1.02 ± 0.09	4.64 ± 0.15	3.07 ± 0.04	1.77 ± 0.03	3.51 ± 0.06
3	−1.81 ± 0.36	1.00 ± 0.05	4.71 ± 0.11	2.98 ± 0.03	1.86 ± 0.03	3.19 ± 0.05
4	−1.36 ± 0.13	0.90 ± 0.03	4.90 ± 0.06	2.97 ± 0.02	1.85 ± 0.02	3.27 ± 0.04
5	−1.17 ± 0.11	0.87 ± 0.03	4.95 ± 0.05	2.91 ± 0.02	1.90 ± 0.03	3.06 ± 0.05
6	−0.93 ± 0.17	0.84 ± 0.05	4.91 ± 0.15	2.81 ± 0.04	1.92 ± 0.02	2.84 ± 0.04
7	−0.72 ± 0.24	0.80 ± 0.08	4.87 ± 0.21	2.76 ± 0.05	1.94 ± 0.03	2.71 ± 0.05
8	−0.64 ± 0.20	0.74 ± 0.08	5.12 ± 0.22	2.64 ± 0.05	1.96 ± 0.02	2.48 ± 0.04
9	−0.63 ± 0.18	0.73 ± 0.07	5.18 ± 0.26	2.54 ± 0.06	1.96 ± 0.02	2.28 ± 0.03
10	−0.59 ± 0.16	0.69 ± 0.07	5.41 ± 0.29	2.41 ± 0.06	1.95 ± 0.02	2.08 ± 0.04
11	−0.65 ± 0.17	0.75 ± 0.06	5.26 ± 0.25	2.22 ± 0.05	1.92 ± 0.02	1.66 ± 0.03
12	−0.40 ± 0.07	0.69 ± 0.04	5.28 ± 0.18	1.84 ± 0.03	1.71 ± 0.02	1.18 ± 0.03
13	−0.38 ± 0.04	0.55 ± 0.02	6.18 ± 0.14	1.87 ± 0.03	1.91 ± 0.02	1.08 ± 0.03
14	−0.18 ± 0.02	0.43 ± 0.02	6.73 ± 0.20	1.41 ± 0.02	1.44 ± 0.02	0.88 ± 0.03

Appendix C

Overview of Decontamination Results

Table C.1: Overview of the OV/ozone decontamination procedures. The decontamination time is determined on the duration of the UV illumination t_{UV}. For both measurement methods, FPD and BIXS the rates before R_0 and after R_1 the procedure are given. The uncertainties on the rates are negligible. The time constant t_1 is determined from the BIXS rate evolution during UV illumination. Furthermore the previously cumulative throughput f of tritium circulated through the source prior to the cleaning and the time since the last cleaning are given.

Cleaning #	t_{UV} in h	$R_{\mathrm{FPD,0}}$ in cps	$R_{\mathrm{FPD,1}}$ in cps	$R_{\mathrm{BIXS,0}}$ in cps	$R_{\mathrm{BIXS,1}}$ in cps	t_1 in h	f in mbar·l	Δt in days
1	80	$2.4 \cdot 10^6$	$1.8 \cdot 10^3$	17.1	0.2	14.01 ± 0.06	$2.8 \cdot 10^7$	-
2	45	$2.7 \cdot 10^6$	$3.3 \cdot 10^4$	19.3	0.5	10.22 ± 0.06	$2.8 \cdot 10^7$	317
3	49	-	$1.8 \cdot 10^4$	5.3	0.4	3.46 ± 0.12	$0.9 \cdot 10^7$	314

Akronyms

ADC Analog-to-Digital Converter. 27

BIXS Beta-Induced X-ray Spectrometry. 31, 32, 33, 34, 70, 75, 76, 86, 87, 88, 89, 90, 91, 92, 93, 99, 102

CD Column Density. 30, 39, 119, 120, 123

CPS Cryogenic Pump Section. 19, 23, 24

DAQ Data Acquisition. 26

DPS Differential Pumping Section. 19, 23

EBID Electron Beam Induced Deposition. 55, 58, 65, 67, 112, 120, 126

FPD Focal Plane Detector. 1, 19, 24, 25, 28, 70, 75, 76, 77, 79, 83, 84, 86, 92, 93, 94, 102, 106, 109, 112, 113, 114, 115, 116, 117, 119, 120

FSD Final-State Distribution. 17, 36, 38, 39, 40, 41, 42, 71, 72, 73, 95, 96

IE Inner Electrodes. 24, 133

KATRIN Karlsruhe Tritium Neutrino. 1, 2, 3, 16, 19, 20, 21, 23, 24, 25, 30, 34, 35, 41, 43, 44, 45, 52, 54, 55, 56, 57, 58, 64, 66, 67, 68, 69, 70, 71, 73, 74, 77, 79, 82, 84, 86, 89, 90, 92, 94, 95, 98, 99, 101, 102, 119, 122, 123, 124, 125, 126, 127, 128, 129, 130

LFCS Low Field Correction System. 24, 133

MAC-E Magnetic Adiabatic Collimation with an Electrostatic filter. 1, 19, 24, 26

MS Main Spectrometer. 19, 24, 25

MTD Measurement Time Distribution. 19, 71

PAE Post-Acceleration Electrode. 26

PS Pre-Spectrometer. 24

RS Rear Section. 19, 29, 30, 33, 34, 55, 116

RSCM Re-Condenser Superconducting Magnet. 30, 33

SAP Shifted Analyzing Plane. 25, 28, 71, 79, 80, 81, 105, 106, 133

SDD Silicon Drift Detector. 31, 32, 33, 75

SDS Spectrometers and Detector Section. 19, 23, 24, 29

SM Standard Model. 1, 4, 5, 6, 7, 11, 12

STS Source and Transport Section. 19, 24

TLK Tritium Laboratory Karlsruhe. 19

TMP Turbomolecular Pump. 23

WGTS Windowless Gaseous Tritium Source. 1, 19, 21, 22, 23, 29, 30, 33, 34, 71, 72, 76, 77, 78, 83, 86, 87, 98, 99, 100, 112, 113, 114, 116, 117, 120, 124, 125, 128

Bibliography

[Aad12] G. Aad, T. Abajyan, B. Abbott, J. Abdallah, S. A. Khalek et al.: 'Observation of a new particle in the search for the Standard Model Higgs boson with the ATLAS detector at the LHC'. In *Physics Letters B* (2012), volume 716(1): pages 1–29. doi: 10.1016/j.physletb.2012.08.020.

[Abb18] T. M. Abbott, F. B. Abdalla, A. Alarcon, J. Aleksić, S. Allam et al.: 'Dark Energy Survey year 1 results: Cosmological constraints from galaxy clustering and weak lensing'. In *Physical Review D* (2018), volume 98(4): page 043526. doi: 10.1103/physrevd.98.043526.

[Abb22] T. M. Abbott, M. Aguena, A. Alarcon, S. Allam, O. Alves et al.: 'Dark Energy Survey Year 3 results: Cosmological constraints from galaxy clustering and weak lensing'. In *Physical Review D* (2022), volume 105(2): page 023520. doi: 10.1103/physrevd.105.023520.

[Abe08] S. Abe, T. Ebihara, S. Enomoto, K. Furuno, Y. Gando et al.: 'Precision Measurement of Neutrino Oscillation Parameters with KamLAND'. In *Physical Review Letters* (2008), volume 100(22). doi: 10.1103/physrevlett.100.221803.

[Abe23] S. Abe, S. Asami, M. Eizuka, S. Futagi, A. Gando et al.: 'Search for the Majorana Nature of Neutrinos in the Inverted Mass Ordering Region with KamLAND-Zen'. In *Physical Review Letters* (2023), volume 130(5). doi: 10.1103/physrevlett.130.051801.

[Ada22] D. Adams, C. Alduino, K. Alfonso, F. Avignone III, O. Azzolini et al.: 'New direct limit on neutrinoless double beta decay half-life of te 128 with cuore'. In *Physical Review Letters* (2022), volume 129(22): page 222501. doi: 10.1103/PhysRevLett.129.222501.

[Ade14] P. A. Ade, N. Aghanim, M. Alves, C. Armitage-Caplan, M. Arnaud et al.: 'Planck 2013 results. I. Overview of products and scientific results'. In *Astronomy & Astrophysics* (2014), volume 571: A1. doi: 10.1051/0004-6361/201321529.

[Agh20] N. Aghanim, Y. Akrami, M. Ashdown, J. Aumont, C. Baccigalupi et al.: 'Planck 2018 results. VI. Cosmological parameters'. In (2020), volume. doi: 10.1051/0004-6361/201833910.

[Ago03] S. Agostinelli, J. Allison, K. a. Amako, J. Apostolakis, H. Araujo et al.: 'GEANT4—a simulation toolkit'. In *Nuclear instruments and methods in physics research section A: Accelerators, Spectrometers, Detectors and Associated Equipment* (2003), volume 506(3): pages 250–303. doi: 10.1016/s0168-9002(03)01368-8.

[Ago20] M. Agostini, G. R. Araujo, A. M. Bakalyarov, M. Balata, I. Barabanov et al.: 'Final Results of GERDA on the Search for Neutrinoless Double-β Decay'. In *Phys. Rev. Lett.* (25 2020), volume 125: page 252502. DOI: 10.1103/PhysRevLett.125.252502.

[Agr24] A. Agrawal, V. V. Alenkov, P. Aryal, J. Beyer, B. Bhandari et al.: *Improved limit on neutrinoless double beta decay of ^{100}Mo from AMoRE-I.* 2024. DOI: 10.48550/ARXIV.2407.05618.

[Aha05] B. Aharmim, S. N. Ahmed, A. E. Anthony, E. W. Beier, A. Bellerive et al.: 'Electron energy spectra, fluxes, and day-night asymmetries of ^{8}B solar neutrinos from measurements with NaCl dissolved in the heavy-water detector at the Sudbury Neutrino Observatory'. In *Phys. Rev. C* (5 2005), volume 72: page 055502. DOI: 10.1103/PhysRevC.72.055502.

[Ahm01] Q. R. Ahmad, R. C. Allen, T. C. Andersen, J. D. Anglin, G. Bühler et al.: 'Measurement of the Rate of $\nu_e + d \rightarrow p + p + e^-$ Interactions Produced by ^8B Solar Neutrinos at the Sudbury Neutrino Observatory'. In *Phys. Rev. Lett.* (7 2001), volume 87: page 071301. DOI: 10.1103/PhysRevLett.87.071301.

[Ake20a] M. Aker, K. Altenmüller, A. Beglarian, J. Behrens, A. Berlev et al.: 'Quantitative Long-Term Monitoring of the Circulating Gases in the KATRIN Experiment Using Raman Spectroscopy'. In *Sensors* (2020), volume 20(17): page 4827. DOI: 10.3390/s20174827.

[Ake20b] M. Aker and M. Röllig: 'Material studies to reduce the tritium memory effect in BIXS analytic systems'. In *Fusion Science and Technology* (2020), volume 76(3): pages 373–378. DOI: 10.1080/15361055.2020.1712989.

[Ake21a] M. Aker, K. Altenmüller, J. Amsbaugh, M. Arenz, M. Babutzka et al.: 'The design, construction, and commissioning of the KATRIN experiment'. In *Journal of Instrumentation* (2021), volume 16(08): T08015. DOI: 10.1088/1748-0221/16/08/t08015.

[Ake21b] M. Aker, K. Altenmüller, A. Beglarian, J. Behrens, A. Berlev et al.: 'Analysis methods for the first KATRIN neutrino-mass measurement'. In *Physical review D* (2021), volume 104(1): page 012005. DOI: 10.1103/physrevd.104.012005.

[Ake22a] M. Aker, K. Altenmüller, D. Batzler, A. Beglarian, J. Behrens et al.: 'Direct neutrino-mass measurement with sub-electronvolt sensitivity'. In *Nature Physics* (2022), volume 18(2): pages 160–166. DOI: 10.1038/s41567-021-01463-1.

[Ake22b] M. Aker, M. Balzer, D. Batzler, A. Beglarian, J. Behrens et al.: 'KATRIN: status and prospects for the neutrino mass and beyond'. In *Journal of Physics G: Nuclear and Particle Physics* (2022), volume 49(10): page 100501. DOI: 10.1088/1361-6471/ac834e.

[Ake23] M. Aker, M. Sturm, F. Priester, S. Tirolf, D. Batzler et al.: 'In Situ Tritium Decontamination of the KATRIN Rear Wall Using an Ultraviolet/Ozone Treatment'. In *Fusion Science and Technology* (2023), volume 80(3–4): pages 303–310. doi: 10.1080/15361055.2023.2214695.

[Ake24a] M. Aker, D. Batzler, A. Beglarian, J. Behrens, J. Beisenkötter et al.: *Direct neutrino-mass measurement based on 259 days of KATRIN data.* 2024. doi: 10.48550/ARXIV.2406.13516.

[Ake24b] M. Aker, D. Batzler, A. Beglarian, J. Behrens, J. Beisenkötter et al.: 'Measurement of the electric potential and the magnetic field in the shifted analysing plane of the KATRIN experiment'. In *The European Physical Journal C* (2024), volume 84(12). doi: 10.1140/epjc/s10052-024-13596-7.

[Ala21] S. Alam, M. Aubert, S. Avila, C. Balland, J. E. Bautista et al.: 'Completed SDSS-IV extended Baryon Oscillation Spectroscopic Survey: Cosmological implications from two decades of spectroscopic surveys at the Apache Point Observatory'. In *Physical Review D* (2021), volume 103(8): page 083533. doi: 10.1103/physrevd.103.083533.

[ALE06] ALEPH Collaboration, DELPHI Collaboration, L3 Collaboration, OPAL Collaboration, SLD Collaboration et al.: 'Precision electroweak measurements on the Z resonance'. In *Physics Reports* (2006), volume 427(5-6): pages 257–454. doi: 10.1016/j.physrep.2005.12.006.

[All06] J. Allison, K. Amako, J. Apostolakis, H. Araujo, P. A. Dubois et al.: 'Geant4 developments and applications'. In *IEEE Transactions on nuclear science* (2006), volume 53(1): pages 270–278. doi: 10.1109/tns.2006.869826.

[All10] M. J. Allen, V. C. Tung and R. B. Kaner: 'Honeycomb carbon: a review of graphene'. In *Chemical reviews* (2010), volume 110(1): pages 132–145. doi: 10.1021/cr900070d.

[All16] J. Allison, K. Amako, J. Apostolakis, P. Arce, M. Asai et al.: 'Recent developments in Geant4'. In *Nuclear instruments and methods in physics research section A: Accelerators, Spectrometers, Detectors and Associated Equipment* (2016), volume 835: pages 186–225. doi: 10.1016/j.nima.2016.06.125.

[Alt20] K. Altenmüller, M. Arenz, W. Baek, M. Beck, A. Beglarian et al.: 'High-resolution spectroscopy of gaseous 83mKr conversion electrons with the KATRIN experiment'. In *Journal of Physics G: Nuclear and Particle Physics* (2020), volume 47(6): page 065002.

[Aly17] M. M. Alyobi, C. J. Barnett and R. J. Cobley: 'Effects of thermal annealing on the properties of mechanically exfoliated suspended and on-substrate few-layer graphene'. In *Crystals* (2017), volume 7(11): page 349. doi: 10.3390/cryst7110349.

[Ams15] J. Amsbaugh, J. Barrett, A. Beglarian, T. Bergmann, H. Bichsel et al.: 'Focal-plane detector system for the KATRIN experiment'. In *Nuclear Instruments and Methods in Physics Research Section A: Accelerators, Spectrometers, Detectors and Associated Equipment* (2015), volume 778: pages 40–60. doi: https://doi.org/10.1016/j.nima.2014.12.116.

[Ang05] J. Angrik, T. Armbrust, A. Beglarian, U. Besserer, J. Blumer et al.: *KATRIN design report 2004.* Technical report. Forschungszentrum Jülich, 2005. 245 pages. doi: 10.5445/IR/270060419.

[Ase11] V. Aseev, A. Belesev, A. Berlev, E. Geraskin, A. Golubev et al.: 'Upper limit on the electron antineutrino mass from the Troitsk experiment'. In *Physical Review D—Particles, Fields, Gravitation, and Cosmology* (2011), volume 84(11): page 112003. doi: 10.1103/physrevd.84.112003.

[Atk13] P. W. Atkins and J. De Paula: *Physikalische Chemie.* 5. Aufl. Weinheim: Wiley-VCH, 2013.

[Bab14] M. Babutzka: 'Design and development for the Rearsection of the KATRIN experiment'. PhD thesis. Karlsruhe Institute of Technology, 2014. doi: 10.5445/IR/1000045598.

[Bah82] J. N. Bahcall, W. F. Huebner, S. H. Lubow, P. D. Parker and R. K. Ulrich: 'Standard solar models and the uncertainties in predicted capture rates of solar neutrinos'. In *Reviews of Modern Physics* (1982), volume 54(3): page 767. doi: 10.1103/revmodphys.54.767.

[Bah92] J. N. Bahcall and M. Pinsonneault: 'Standard solar models, with and without helium diffusion, and the solar neutrino problem'. In *Reviews of Modern Physics* (1992), volume 64(4): page 885. doi: 10.1103/revmodphys.64.885.

[BAH86] N. A. BAHCALL: 'The Hubble Space Telescope'. In *Annals of the New York Academy of Sciences* (1986), volume 470(1): pages 331–337. doi: 10.1111/j.1749-6632.1986.tb47983.x.

[Bar11] G. Barnes and I. Gentle: *Interfacial science : an introduction.* 2. ed. Oxford: Oxford University Press, 2011. doi: 10.1093/hesc/9780199571185.001.0001.

[Bar95] L. Bartlein, S. Konishi, R. Carlson, M. Enoeda, R. Willms et al.: 'Decontamination Studies of Japan Atomic Energy Research Institute Fuel Cleanup System and Glovebox Installed at the Tritium Systems Test Assembly'. In *Proceedings of 16th International Symposium on Fusion Engineering.* Volume 1. IEEE. 1995: pages 292–296. doi: 10.1109/FUSION.1995.534225.

[Bea80] G. Beamson, H. Porter and D. Turner: 'The collimating and magnifying properties of a superconducting field photoelectron spectrometer'. In *Journal of Physics E: Scientific Instruments* (1980), volume 13(1): page 64. doi: 10.1088/0022-3735/13/1/018.

[Beh17] J. Behrens: 'Design and commissioning of a monoenergetic photoelectron source and active background reduction by magnetic pulse at the KATRIN experiment'. PhD thesis. Westfälische Wilhelms-Universität Münster, 2017.

[Ber71] K.-E. Bergkvist: 'On some atomic effects in the tritium β-spectrum'. In *Physica Scripta* (1971), volume 4(1-2): page 23. doi: 10.1088/0031-8949/4/1-2/004.

[Bet32] H. Bethe: 'Bremsformel für elektronen relativistischer geschwindigkeit'. In *Zeitschrift für Physik* (1932), volume 76(5): pages 293–299. doi: 10.1007/bf01342532.

[Bil10] S. Bilenky: *Introduction to the Physics of Massive and Mixed Neutrinos*. Springer Berlin Heidelberg, 2010. doi: 10.1007/978-3-642-14043-3.

[Blo36] F. Bloch: 'On the Continuous γ-Radiation Accompanying the β-Decay'. In *Physical Review* (1936), volume 50(4): page 272. doi: 10.1103/PhysRev.50.272.

[Bod15] L. Bodine, D. Parno and R. Robertson: 'Assessment of molecular effects on neutrino mass measurements from tritium β decay'. In *Physical Review C* (2015), volume 91(3): page 035505. doi: 10.1103/PhysRevC.91.035505.

[Bol83] K. Boller, R.-P. Haelbich, H. Hogrefe, W. Jark and C. Kunz: 'Investigation of carbon contamination of mirror surfaces exposed to synchrotron radiation'. In *Nuclear instruments and methods in physics research* (1983), volume 208(1-3): pages 273–279. doi: 10.1016/0167-5087(83)91134-1.

[Bon10] F. Bonaccorso, Z. Sun, T. Hasan and A. Ferrari: 'Graphene photonics and optoelectronics'. In *Nature photonics* (2010), volume 4(9): page 611. doi: 10.1038/nphoton.2010.186.

[Bon18] M. Bonfanti, S. Achilli and R. Martinazzo: 'Sticking of atomic hydrogen on graphene'. In *Journal of Physics: Condensed Matter* (2018), volume 30(28): page 283002. doi: 10.1088/1361-648x/aac89f.

[Bor05] B. Bornschein, M. Glugla, K. Günther, T. Le and K. Simon: 'Experimental validation of a method for performance monitoring of the front-end permeators in the TEP system of ITER'. In *Fusion engineering and design* (2005), volume 75: pages 645–650. doi: 10.1016/j.fusengdes.2005.06.038.

[Bor23] M. Borghesi, B. Alpert, M. Balata, D. Becker, D. Bennet et al.: 'An updated overview of the HOLMES status'. In *Nuclear Instruments and Methods in Physics Research Section A: Accelerators, Spectrometers, Detectors and Associated Equipment* (2023), volume 1051: page 168205. doi: 10.1016/j.nima.2023.168205.

[Bra12] O. Braginsky, A. Kovalev, D. Lopaev, E. Malykhin, T. Rakhimova et al.: 'Removal of amorphous C and Sn on Mo: Si multilayer mirror surface in Hydrogen plasma and afterglow'. In *Journal of Applied Physics* (2012), volume 111(9). doi: 10.1063/1.4709408.

[Bri22] S. Brieden, H. Gil-Marín and L. Verde: 'Model-agnostic interpretation of 10 billion years of cosmic evolution traced by BOSS and eBOSS data'. In *Journal of Cosmology and Astroparticle Physics* (2022), volume 2022(08): page 024. doi: 10.1088/1475-7516/2022/08/024.

[Car18] M. A. Caro, A. Aarva, V. L. Deringer, G. Csányi and T. Laurila: 'Reactivity of Amorphous Carbon Surfaces: Rationalizing the Role of Structural Motifs in Functionalization Using Machine Learning'. In *Chemistry of Materials* (2018), volume 30(21): pages 7446–7455. doi: 10.1021/acs.chemmater.8b03353. eprint: https://doi.org/10.1021/acs.chemmater.8b03353.

[Cha10] M. Chaigneau, G. Picardi and R. Ossikovski: 'Tip enhanced Raman spectroscopy evidence for amorphous carbon contamination on gold surfaces'. In *Surface science* (2010), volume 604(7-8): pages 701–705. doi: 10.1016/j.susc.2010.01.018.

[Cha12] S. Chatrchyan, V. Khachatryan, A. M. Sirunyan, A. Tumasyan, W. Adam et al.: 'Observation of a new boson at a mass of 125 GeV with the CMS experiment at the LHC'. In *Physics Letters B* (2012), volume 716(1): pages 30–61. doi: 10.1016/j.physletb.2012.08.021.

[Cha14] J. Chadwick: 'The intensity distribution in the magnetic spectrum of beta particles from radium (B+ C)'. In *Verh. Phys. Gesell* (1914), volume 16(383-391): page 3.

[Cha32a] J. Chadwick: 'Possible existence of a neutron'. In *Nature* (1932), volume 129(3252): pages 312–312. doi: 10.1038/129312a0.

[Cha32b] J. Chadwick: 'The existence of a neutron'. In *Proceedings of the Royal Society of London. Series A, Containing Papers of a Mathematical and Physical Character* (1932), volume 136(830): pages 692–708. doi: 10.1098/rspa.1932.0112.

[Che20] H. Chen, W. Ding, Z. An, J. Zhu, M. Liu et al.: 'BIXS for tritium analysis with Ar gas and Al thin film as β-ray stopping layers and comparison with EBS'. In *Radiation Physics and Chemistry* (2020), volume: page 108931. doi: 10.1016/j.radphyschem.2020.108931.

[Che22] L. Chen, Y. Huang, Y. Xue, Z. Jia and W. Wang: 'Oligomer formation from the gas-phase reactions of Criegee intermediates with hydroperoxide esters: mechanism and kinetics'. In *Atmospheric Chemistry and Physics* (2022), volume 22(22): pages 14529–14546. doi: 10.5194/acp-22-14529-2022.

[Che24] Y.-C. Chen, A. Sihag, R. Sarkar, T.-Y. Chen, M. S. Dyer et al.: 'Hydrogen adsorption, migration and desorption on amorphous carbon: A DFT and AIMD study'. In *Materials Chemistry and Physics* (2024), volume 325: page 129711. doi: 10.1016/j.matchemphys.2024.129711.

[Che75] M. Chesters and G. Somorjai: 'The chemisorption of oxygen, water and selected hydrocarbons on the (111) and stepped gold surfaces'. In *Surface Science* (1975), volume 52(1): pages 21–28. doi: 10.1016/0039-6028(75)90004-7.

[Chr88] K. Christmann: 'Interaction of hydrogen with solid surfaces'. In *Surface Science Reports* (1988), volume 9(1-3): pages 1–163. doi: 10.1016/0167-5729(88)90009-x.

[Cla92] T. Claxton, S. Schafroth and P. Meier: 'Molecular final states after β decay of tritium-substituted molecules'. In *Physical Review A* (1992), volume 45(9): page 6209. doi: 10.1103/physreva.45.6209.

[Cle98] B. T. Cleveland, T. Daily, R. Davis Jr, J. R. Distel, K. Lande et al.: 'Measurement of the solar electron neutrino flux with the Homestake chlorine detector'. In *The Astrophysical Journal* (1998), volume 496(1): page 505. doi: 10.1086/305343.

[Com24] W. Commons: *File: Standard Model of Elementary Particles.svg - Wikimedia Commons, the free media repository.* [Online; accessed 16-October-2024]. 2024.

[Coo12] D. R. Cooper, B. D'Anjou, N. Ghattamaneni, B. Harack, M. Hilke et al.: 'Experimental review of graphene'. In *ISRN Condensed Matter Physics* (2012), volume 2012. doi: 10.5402/2012/501686.

[Cow56] C. L. Cowan Jr, F. Reines, F. Harrison, H. Kruse and A. McGuire: 'Detection of the free neutrino: a confirmation'. In *Science* (1956), volume 124(3212): pages 103–104. doi: 10.1016/b978-0-08-006509-0.50008-9.

[Cre98] D. Cremer, E. Kraka and P. G. Szalay: 'Decomposition modes of dioxirane, methyldioxirane and dimethyldioxirane—A CCSD (T), MR-AQCC and DFT investigation'. In *Chemical physics letters* (1998), volume 292(1-2): pages 97–109. doi: 10.1016/s0009-2614(98)00678-2.

[Cri75] R. Criegee: 'Mechanism of ozonolysis'. In *Angewandte chemie international edition in english* (1975), volume 14(11): pages 745–752. doi: 10.1002/anie.197507451.

[Dan10] K. M. Daniels, B. Daas, R. Zhang, I. Chowdhury, A. Obe et al.: *Graphene to Graphane: Novel Electrochemical Conversion.* 2010. doi: 10.48550/ARXIV.1010.5458.

[Dan12] K. M. Daniels, B. Daas, N. Srivastava, C. Williams, R. Feenstra et al.: 'Evidences of electrochemical graphene functionalization and substrate dependence by Raman and scanning tunneling spectroscopies'. In *Journal of Applied Physics* (2012), volume 111(11): page 114306. doi: 10.1063/1.4725489.

[Dan62] G. Danby, J. M. Gaillard, K. Goulianos, L. M. Lederman, N. Mistry et al.: 'Observation of high-energy neutrino reactions and the existence of two kinds of neutrinos'. In *Physical Review Letters* (1962), volume 9(1): page 36. doi: 10.1103/physrevlett.9.36.

[Das91] D. Dasgupta, F. Demichelis and A. Tagliaferro: 'Electrical conductivity of amorphous carbon and amorphous hydrogenated carbon'. In *Philosophical Magazine B* (1991), volume 63(6): pages 1255–1266. doi: 10.1080/13642819108205558.

[Dav68] R. Davis Jr, D. S. Harmer and K. C. Hoffman: 'Search for neutrinos from the sun'. In *Physical Review Letters* (1968), volume 20(21): page 1205. doi: 10.1103/physrevlett.20.1205.

[Dem17] W. Demtröder: *Experimentalphysik 4 : Kern-, Teilchen- und Astrophysik*. 5. Aufl. 2017. Berlin, Heidelberg: Springer Spektrum, 2017.

[Di 21] E. Di Valentino, O. Mena, S. Pan, L. Visinelli, W. Yang et al.: 'In the realm of the Hubble tension—a review of solutions'. In *Classical and Quantum Gravity* (2021), volume 38(15): page 153001. doi: 10.1088/1361-6382/ac086d.

[Di 24] E. Di Grezia, S. Esposito and A. Naddeo: 'Measuring a Mass: The Puzzling History of an Elusive Particle'. In *Universe* (2024), volume 10(8): page 317. doi: 10.3390/universe10080317.

[Día24] D. Díaz Barrero: 'The catalytic generation of tritium-substituted methanes and their analysis using Raman spectroscopy and mass spectrometry'. PhD thesis. Universidad Autónoma de Madrid, 2024.

[Din05] W. Ding, D. Dikin, X. Chen, R. Piner, R. Ruoff et al.: 'Mechanics of hydrogenated amorphous carbon deposits from electron-beam-induced deposition of a paraffin precursor'. In *Journal of Applied Physics* (2005), volume 98(1). doi: 10.1063/1.1940138.

[Dok24] N. V. Dokhlikova, M. V. Grishin and S. V. Doronin: 'Hydrogen diffusion on (100),(111),(110) and (211) gold faces'. In *International Journal of Quantum Chemistry* (2024), volume 124(1): e27242. doi: 10.1002/qua.27242.

[Don15] L. Dong, Y. Xie, L. Du, W. Li and Z. Tan: 'Theoretical investigation of isotope exchange reaction in tritium-contaminated mineral oil in vacuum pump'. In *Journal of Hazardous Materials* (2015), volume 287: pages 42–50. doi: 10.1016/j.jhazmat.2015.01.030.

[Dos06] N. Doss, J. Tennyson, A. Saenz and S. Jonsell: 'Molecular effects in investigations of tritium molecule β decay endpoint experiments'. In *Physical Review C—Nuclear Physics* (2006), volume 73(2): page 025502. doi: 10.1103/physrevc.73.025502.

[Dre13] G. Drexlin, V. Hannen, S. Mertens and C. Weinheimer: 'Current direct neutrino mass experiments'. In *Advances in High Energy Physics* (2013), volume 2013(1): page 293986. doi: 10.1155/2013/293986.

[Duś93] R. Duś: 'Hydrogen adsorption on group 1 B metals'. In *Progress in surface science* (1993), volume 42(1-4): pages 231–243. doi: 10.1016/0079-6816(93)90072-4.

[Eli09a] D. C. Elias, R. R. Nair, T. Mohiuddin, S. Morozov, P. Blake et al.: 'Control of graphene's properties by reversible hydrogenation: evidence for graphane'. In *Science* (2009), volume 323(5914): pages 610–613. doi: 10.1126/science.1167130.

[Eli09b] D. C. Elias, R. R. Nair, T. Mohiuddin, S. Morozov, P. Blake et al.: 'Control of graphene's properties by reversible hydrogenation: evidence for graphane'. In *Science* (2009), volume 323(5914): pages 610–613. doi: 10.1126/science.1167130.

[Enn53] A. Ennos: 'The origin of specimen contamination in the electron microscope'. In *British Journal of Applied Physics* (1953), volume 4(4): page 101. doi: 10.1088/0508-3443/4/4/302.

[Enn54] A. Ennos: 'The sources of electron-induced contamination in kinetic vacuum systems'. In *British Journal of Applied Physics* (1954), volume 5(1): page 27. doi: 10.1088/0508-3443/5/1/307.

[Est19] I. Esteban, M. C. González-García, A. Hernandez-Cabezudo, M. Maltoni and T. Schwetz: 'Global analysis of three-flavour neutrino oscillations: synergies and tensions in the determination of $\theta 23$, δCP, and the mass ordering'. In *Journal of High Energy Physics* (2019), volume 2019(1): pages 1–35. doi: 10.1007/jhep01(2019)106.

[Est24] I. Esteban, M. C. Gonzalez-Garcia, M. Maltoni, I. Martinez-Soler, J. P. Pinheiro et al.: *NuFit-6.0: Updated global analysis of three-flavor neutrino oscillations*. 2024. doi: 10.48550/ARXIV.2410.05380.

[Fer34] E. Fermi: 'Versuch einer Theorie der β-Strahlen. I'. In *Zeitschrift für Physik* (1934), volume 88(3): pages 161–177. doi: 10.1007/bf01351864.

[Fie92] A. Fiege: *Tritium*. Technical report. Kernforschungszentrum Karlsruhe GmbH (Germany). Projekt Kernfusion, 1992.

[For21] J. A. Formaggio, A. L. C. de Gouvêa and R. H. Robertson: 'Direct measurements of neutrino mass'. In *Physics Reports* (2021), volume 914: pages 1–54. doi: 10.1016/j.physrep.2021.02.002.

[Fri20] F. R. Friedel: 'Ion and plasma systematics during the first KATRIN neutrino mass measurements'. PhD thesis. Karlsruher Institut für Technologie (KIT), 2020. doi: 10.5445/IR/1000126837.

[Fuk98a] Y. Fukuda, T. Hayakawa, E. Ichihara, K. Inoue, K. Ishihara et al.: 'Measurements of the solar neutrino flux from Super-Kamiokande's first 300 days'. In *Physical review letters* (1998), volume 81(6): page 1158. doi: 10.1103/physrevlett.81.1158.

[Fuk98b] Y. Fukuda, T. Hayakawa, E. Ichihara, K. Inoue, K. Ishihara et al.: 'Evidence for Oscillation of Atmospheric Neutrinos'. In *Physical Review Letters* (1998), volume 81(8): pages 1562–1567. doi: 10.1103/physrevlett.81.1562.

[Ful20] A. Fulst: 'A novel quasi-differential method for MAC-E filters and determination and control of the electric potentials of the KATRIN experiment with a stabilized condensed krypton source and a UV illumination system'. PhD thesis. Westfälische Wilhelms-Universität Münster, 2020.

[Fur39] W. H. Furry: 'On transition probabilities in double beta-disintegration'. In *Physical Review* (1939), volume 56(12): page 1184. doi: 10.1103/physrev.56.1184.

[Gas14] L. Gastaldo, K. Blaum, A. Dörr, C. E. Düllmann, K. Eberhardt et al.: 'The Electron Capture^ 163 163 Ho Experiment ECHo'. In *Journal of Low Temperature Physics* (2014), volume 176: pages 876–884. doi: 10.1007/s10909-014-1187-4.

[Gel98] C. Geletneky and S. Berger: 'The mechanism of ozonolysis revisited by 17O-NMR spectroscopy'. In *European journal of organic chemistry* (1998), volume 1998(8): pages 1625–1627. doi: 10.1002/(sici)1099-0690(199808)1998:8<1625::aid-ejoc1625>3.0.co;2-l.

[Gen02] C. A. Gentile, J. J. Parker, G. L. Guttadora and L. P. Ciebiera: 'Oxidative Tritium Decontamination System'. In *Proceedings of the 19th IEEE/IPSS Symposium on Fusion Engineering. 19th SOFE (Cat. No. 02CH37231)*. IEEE. 2002: pages 159–163. doi: 10.2172/796125.

[Gil09] W. Gil, J. Bonn, B. Bornschein, R. Gehring, O. Kazachenko et al.: 'The cryogenic pumping section of the KATRIN experiment'. In *IEEE transactions on applied superconductivity* (2009), volume 20(3): pages 316–319. doi: 10.1109/tasc.2009.2038581.

[Giu12] A. Giuliani and A. Poves: 'Neutrinoless Double-Beta Decay'. In *Advances in High Energy Physics* (2012), volume 2012: pages 1–38. doi: 10.1155/2012/857016.

[Gol58] M. Goldhaber, L. Grodzins and A. W. Sunyar: 'Helicity of neutrinos'. In *Physical review* (1958), volume 109(3): page 1015. doi: 10.1016/b978-0-08-006509-0.50013-2.

[Got70] R. Goto: 'Hyperpure hydrogen from palladium alloy membrane permeation'. In *Chem. Econ. Eng. Rev.* (1970), volume 2(11).

[Gro15] S. Groh: 'Modeling of the response function and measurement of transmission properties of the KATRIN experiment'. PhD thesis. 2015. doi: 10.5445/IR/1000046546.

[Hak01] H. Haken and H. C. Wolf: *Atom- und Quantenphysik : Einführung in die experimentellen und theoretischen Grundlagen*. 7. Auflage. Berlin: Springer, 2001.

[Har00] A. Hart, A. Flewitt, J. Robertson and W. Milne: 'Effect of work function and surface microstructure on field emission of tetrahedral amorphous carbon'. In *Journal of Applied Physics* (2000), volume 88(10): pages 6002–6010. doi: 10.1063/1.1314874.

[Har70] R. Hart, T. Kassner and J. Maurin: 'The contamination of surfaces during high-energy electron irradiation'. In *Philosophical Magazine* (1970), volume 21(171): pages 453–467. doi: 10.1080/14786437008238431.

[Har86] J. Harris, S. Andersson, C. Holmberg and P. Nordlander: 'The interaction of H2 with metal surfaces'. In *Physica Scripta* (1986), volume 1986(T13): page 155. doi: 10.1088/0031-8949/1986/T13/026.

[Har88] J. Harris: 'On the adsorption and desorption of H 2 at metal surfaces'. In *Applied Physics A* (1988), volume 47: pages 63–71. doi: 10.1007/bf00619699.

[Hay64] D. O. Hayward and B. M. W. Trapnell: *Chemisorption*. London: Butterworths, 1964.

[Het17] S. Hettler, M. Dries, P. Hermann, M. Obermair, D. Gerthsen et al.: 'Carbon contamination in scanning transmission electron microscopy and its impact on phase-plate applications'. In *Micron* (2017), volume 96: pages 38–47. doi: 10.1016/j.micron.2017.02.002.

[Hig64] P. W. Higgs: 'Broken symmetries and the masses of gauge bosons'. In *Physical review letters* (1964), volume 13(16): page 508. doi: 10.1103/physrevlett.13.508.

[Hol92] E. Holzschuh: 'Measurement of the neutrino mass from tritium beta-decay'. In *Reports on Progress in Physics* (1992), volume 55(7): page 1035. doi: 10.1088/0034-4885/55/7/004.

[Hop05] C. Hopf, W. Jacob and A. Von Keudell: 'Ion-induced surface activation, chemical sputtering, and hydrogen release during plasma-assisted hydrocarbon film growth'. In *Journal of applied physics* (2005), volume 97(9). doi: 10.1063/1.1883729.

[Hoy11] D. Hoyle, M. Malac, M. Trudeau and P. Woo: 'UV treatment of TEM/STEM samples for reduced hydrocarbon contamination'. In *Microscopy and Microanalysis* (2011), volume 17(S2): pages 1026–1027. doi: 10.1017/s1431927611006003.

[Hub21] A. Huber: 'Analysis of first KATRIN data and searches for keV-scale sterile neutrinos'. PhD thesis. Karlsruher Institut für Technologie (KIT), 2021. doi: 10.5445/IR/1000128344.

[Iba06] H. Ibach: *Physics of surfaces and interfaces*. Berlin: Springer, 2006.

[Iku77] S. Ikuta, S. Iwata and M. Imamura: 'Ab initio studies of the β–decay in OHT, NH2T, CH3T, and 14CH4'. In *The Journal of Chemical Physics* (1977), volume 66(10): pages 4671–4676. doi: 10.1063/1.433676.

[Ily11] A. Ilyin, N. Guseinov, I. Tsyganov and R. Nemkaeva: 'Computer simulation and experimental study of graphane-like structures formed by electrolytic hydrogenation'. In *Physica E: Low-dimensional Systems and Nanostructures* (2011), volume 43(6): pages 1262–1265. doi: 10.1016/j.physe.2011.02.012.

[Ish97] Y. Ishikawa and H. Y. Hirose: 'Etching of nondiamond carbon in diamond thin films synthesized by hot-filament chemical vapor deposition with ultraviolet irradiation'. In *Japanese journal of applied physics* (1997), volume 36(3R): page 1233. doi: 10.1143/jjap.36.1233.

[Jac93] W. Jacob and W. Möller: 'On the structure of thin hydrocarbon films'. In *Applied Physics Letters* (1993), volume 63(13): pages 1771–1773. doi: 10.1063/1.110683.

[Jan85] F. Jansen, M. Machonkin, S. Kaplan and S. Hark: 'The effects of hydrogenation on the properties of ion beam sputter deposited amorphous carbon'. In *Journal of Vacuum Science & Technology A: Vacuum, Surfaces, and Films* (1985), volume 3(3): pages 605–609. doi: 10.1116/1.572960.

[Jan15] A. Jansen: 'The Cryogenic Pumping Section of the KATRIN Experiment - Design Studies and Experiments for the Commissioning'. PhD thesis. 2015. doi: 10.5445/IR/1000047146.

[Jar09] B. N. Jariwala, C. V. Ciobanu and S. Agarwal: 'Atomic hydrogen interactions with amorphous carbon thin films'. In *Journal of Applied Physics* (2009), volume 106(7). doi: 10.1063/1.3238305.

[Jia19] H. Jiang, M. Kammler, F. Ding, Y. Dorenkamp, F. R. Manby et al.: 'Imaging covalent bond formation by H atom scattering from graphene'. In *Science* (2019), volume 364(6438): pages 379–382. doi: 10.1126/science.aaw6378.

[Jo12] G. Jo, M. Choe, S. Lee, W. Park, Y. H. Kahng et al.: 'The application of graphene as electrodes in electrical and optical devices'. In *Nanotechnology* (2012), volume 23(11): page 112001. doi: 10.1088/0957-4484/23/11/112001.

[Jon99] S. Jonsell, A. Saenz and P. Froelich: 'Neutrino-mass determination from tritium β decay: Corrections to and prospects of experimental verification of the final-state spectrum'. In *Physical Review C* (1999), volume 60(3): page 034601. doi: 10.1103/PhysRevC.60.034601.

[Jon49] W. Jones: 'Thermodynamic functions for tritium deuteride. The dissociation of tritium deuteride. Equilibria among the isotopic hydrogen molecules'. In *The Journal of Chemical Physics* (1949), volume 17(11): pages 1062–1064. doi: 10.1063/1.1747113.

[Kap88] I. Kaplan and V. Smutny: 'β-Decay-Induced Rearrangement of the Molecular Electron Shell and the Problem of Determining the Neutrino Rest Mass'. In *Advances in Quantum Chemistry*. Volume 19. Elsevier, 1988: pages 289–348. doi: 10.1016/s0065-3276(08)60618-8.

[Kaz08] O. Kazachenko, B. Bornschein, L. Bornschein, F. Eichelhardt, N. Kernert et al.: 'TRAP—a cryo-pump for pumping tritium on pre-condensed argon'. In *Nuclear Instruments and Methods in Physics Research Section A: Accelerators, Spectrometers, Detectors and Associated Equipment* (2008), volume 587(1): pages 136–144. DOI: 10.1016/j.nima.2007.12.024.

[Kel22] J. Kellerer: 'Simulation of the KATRIN Source Plasma using Monte Carlo and Particle in Cell Methods'. PhD thesis. Karlsruher Institut für Technologie (KIT), 2022. 181 pages. DOI: 10.5445/IR/1000143868.

[Keu03] A. von Keudell and W. Jacob: 'Growth of polymer-like a-C films'. In *Amorphous Carbon*. INSPEC, The Institution of Electrical Engineers, London, United Kingdom, 2003.

[Kin08] S. F. King: 'Neutrino mass models: A road map'. In *Journal of Physics: Conference Series* (2008), volume 136(2): page 022038. DOI: 10.1088/1742-6596/136/2/022038.

[Kle19] M. Kleesiek, J. Behrens, G. Drexlin, K. Eitel, M. Erhard et al.: 'β-Decay spectrum, response function and statistical model for neutrino mass measurements with the KATRIN experiment'. In *The European Physical Journal C* (2019), volume 79(3): page 204. DOI: 10.1140/epjc/s10052-019-6686-7.

[Kle19] M. Klein: 'Tritium ions in KATRIN: blocking, removal and detection'. PhD thesis. Karlsruher Institut für Technologie (KIT), 2019. DOI: 10.5445/IR/1000093526.

[Kod01] K. Kodama, N. Ushida, C. Andreopoulos, N. Saoulidou, G. Tzanakos et al.: 'Observation of tau neutrino interactions'. In *Physics Letters B* (2001), volume 504(3): pages 218–224. DOI: 10.1016/s0370-2693(01)00307-0.

[Kog84] Y. Koga and L. Harrison: 'Reactions of solids with gases other than oxygen'. In *Comprehensive chemical kinetics*. Volume 21. Elsevier, 1984: pages 119–149. DOI: 10.1016/S0069-8040(08)70007-4.

[Köl] L. Köllenberger: 'Combined neutrino-mass analysis of the first five KATRIN science runs'. PhD thesis. Karlsruhe Institute of Technology (KIT).

[Kon16] E. A. Konshina: 'Amorphous hydrogenated carbon films with diamond-like and polymer-like properties'. In *Crystalline and Non-crystalline Solids* (2016), volume: pages 125–146. DOI: 10.5772/62704.

[Kra05] C. Kraus, B. Bornschein, L. Bornschein, J. Bonn, B. Flatt et al.: 'Final results from phase II of the Mainz neutrino mass searchin tritium decay'. In *The European Physical Journal C-Particles and Fields* (2005), volume 40(4): pages 447–468. DOI: 10.1140/epjc/s2005-02139-7.

[Kra23] H. A. Kramers: 'XCIII. On the theory of X-ray absorption and of the continuous X-ray spectrum'. In *The London, Edinburgh, and Dublin Philosophical Magazine and Journal of Science* (1923), volume 46(275): pages 836–871. DOI: 10.1080/14786442308565244.

[Kuc16] L. Kuckert: 'The Windowless Gaseous Tritium Source of the KATRIN Experiment - Characterisation of Gas Dynamical and Plasma Properties'. PhD thesis. Karlsruher Institut für Technologie (KIT), 2016. DOI: 10.5445/IR/1000065077.

[Küp95] J. Küppers: 'The hydrogen surface chemistry of carbon as a plasma facing material'. In *Surface Science Reports* (1995), volume 22(7-8): pages 249–321. DOI: 10.1016/0167-5729(96)80002-1.

[Lag77] D. Laguitton and W. Parrish: 'Experimental spectral distribution versus Kramers' law for quantitative X-ray fluorescence by the fundamental parameters method'. In *X-Ray Spectrometry* (1977), volume 6(4): pages 201–203. DOI: 10.1002/xrs.1300060409.

[Lar22] G. K. Larsen, K. Nguyen and S. E. H. Murph: 'Preventing Tritium Memory Effects in Ion Chambers Using Ultraviolet LEDs'. In *IEEE Transactions on Nuclear Science* (2022), volume 69(5): pages 1092–1097. DOI: 10.1109/tns.2022.3163630.

[Les08] J. Lesgourgues, W. Valkenburg and E. Gaztañaga: 'Constraining neutrino masses with the integrated-Sachs-Wolfe-galaxy correlation function'. In *Physical Review D* (2008), volume 77(6). DOI: 10.1103/physrevd.77.063505.

[Leu21] D. van Leuken, C. de Meijere, R. Van der Horst, V. Banine, E. Osorio et al.: 'An atomic hydrogen etching sensor for H2 plasma diagnostics'. In *Review of Scientific Instruments* (2021), volume 92(6). DOI: 10.1063/5.0033518.

[Li22] Y. Li, Y. Jiang, X. Liu, Q. Bai, H. Liu et al.: 'Influence of reactive oxygen species concentration and ambient temperature on the evolution of chemical bonds during plasma cleaning: a molecular dynamics simulation'. In *RSC advances* (2022), volume 12(47): pages 30754–30763. DOI: 10.1039/d2ra05901k.

[Lin20] Y.-T. Lin, T. Burritt, C. Claessens, G. Holman, M. Kallander et al.: 'Beta decay of molecular tritium'. In *Physical review letters* (2020), volume 124(22): page 222502. DOI: 10.1103/physrevlett.124.222502.

[Liu13] J. Liu, M. Notarianni, G. Will, V. T. Tiong, H. Wang et al.: 'Electrochemically exfoliated graphene for electrode films: effect of graphene flake thickness on the sheet resistance and capacitive properties'. In *Langmuir* (2013), volume 29(43): pages 13307–13314. DOI: 10.1021/la403159n.

[Lob85] V. Lobashev and P. Spivak: 'A method for measuring the electron antineutrino rest mass'. In *Nuclear Instruments and Methods in Physics Research Section A: Accelerators, Spectrometers, Detectors and Associated Equipment* (1985), volume 240(2): pages 305–310. DOI: 10.1016/0168-9002(85)90640-0.

[Lok22] A. Lokhov, B. Bieringer, G. Drexlin, S. Dyba, K. Gauda et al.: 'Background reduction at the KATRIN experiment by the shifted analysing plane configuration'. In *The European Physical Journal C* (2022), volume 82(3): pages 1–11. doi: 10.1140/epjc/s10052-022-10220-4.

[Luc00] L. L. Lucas and M. P. Unterweger: 'Comprehensive review and critical evaluation of the half-life of tritium'. In *Journal of research of the National Institute of Standards and Technology* (2000), volume 105(4): page 541. doi: 10.6028/jres.105.043.

[Luo06] X. Luo, C. Day, V. Hauer, O. Malyshev, R. Reid et al.: 'Monte Carlo simulation of gas flow through the KATRIN DPS2-F differential pumping system'. In *Vacuum* (2006), volume 80(8): pages 864–869. doi: 10.1016/j.vacuum.2005.11.044.

[Mac21] M. B. Machatschek: 'A Phenomenological Theory of KATRIN Source Potential Systematics and its Application in Krypton-83m Calibration Measurements'. PhD thesis. Karlsruher Institut für Technologie (KIT), 2021. doi: 10.5445/IR/1000132391.

[Mad24] M. S. Madhavacheril, F. J. Qu, B. D. Sherwin, N. MacCrann, Y. Li et al.: 'The Atacama Cosmology Telescope: DR6 gravitational lensing map and cosmological parameters'. In *The Astrophysical Journal* (2024), volume 962(2): page 113. doi: 10.3847/1538-4357/acff5f.

[Mak62] Z. Maki, M. Nakagawa and S. Sakata: 'Remarks on the unified model of elementary particles'. In *Progress of Theoretical Physics* (1962), volume 28(5): pages 870–880. doi: 10.1143/PTP.28.870.

[Mao11] L. Mao, Z. An, J. Liang, X. Long, S. Peng et al.: 'Effects of internal bremsstrahlung of tritium β-decay and surface roughness in the BIXS method'. In *Nuclear Instruments and Methods in Physics Research Section B: Beam Interactions with Materials and Atoms* (2011), volume 269(2): pages 105–110. doi: 10.1016/j.nimb.2010.10.024.

[Mar22] A. Marsteller, M. Böttcher, B. Bornschein, S. Enomoto, C. Fengler et al.: 'Operation modes of the KATRIN experiment Tritium Loop System using 83mKr'. In *Journal of Instrumentation* (2022), volume 17(12): P12010. doi: 10.1088/1748-0221/17/12/P12010.

[Mar20] A. C. Marsteller: 'Characterization and Optimization of the KATRIN Tritium Source'. PhD thesis. Karlsruher Institut für Technologie (KIT), 2020. doi: 10.5445/IR/1000127553.

[Mat07] M. Matsuyama, Y. Torikai, M. Hara and K. Watanabe: 'New technique for non-destructive measurements of tritium in future fusion reactors'. In *Nuclear fusion* (2007), volume 47(7): S464. doi: 10.1088/0029-5515/47/7/s09.

[Mat85] M. Matsuyama, K. Ichimura, K. Ashida, K. Watanabe and H. Sato: 'Contamination of Ionization Chamber Due to Tritium Exposure'. In *Fusion Technology* (1985), volume 8(2P2): pages 2461–2466. doi: 10.13182/fst85-a24648.

[McD02] A. McDonald, Q. Ahmad, R. Allen, T. Andersen, J. Anglin et al.: 'Direct Evidence for Neutrino Flavor Transformation from Neutral-Current Interactions in SNO'. In *AIP Conference Proceedings*. Volume 646. AIP, 2002: pages 43–58. doi: 10.1063/1.1524553.

[McL73] R. McLellan: 'Solid solutions of hydrogen in gold, silver and copper'. In *Journal of Physics and Chemistry of Solids* (1973), volume 34(6): pages 1137–1141. doi: 10.1016/s0022-3697(73)80022-8.

[Med23] M. Medina Restrepo and E. G. Myers: 'Mass difference of tritium and helium-3'. In *Physical Review Letters* (2023), volume 131(24): page 243002. doi: 10.1103/physrevlett.131.243002.

[Mik86] S. P. Mikheyev and A. Y. Smirnov: 'Resonant amplification of ν oscillations in matter and solar-neutrino spectroscopy'. In *Il Nuovo Cimento C* (1986), volume 9(1): pages 17–26. doi: 10.1007/bf02508049.

[Mil06] B. Mildner, E. Hasselbrink and D. Diesing: 'Electronic excitations induced by surface reactions of H and D on gold'. In *Chemical physics letters* (2006), volume 432(1-3): pages 133–138. doi: 10.1016/j.cplett.2006.10.048.

[Miy19a] T. Miyazawa, Y. Kano, Y. Nakayama, K. Ozawa, T. Iga et al.: 'Improved pumping speeds of oxygen-free palladium/titanium nonevaporable getter coatings and suppression of outgassing by baking under oxygen'. In *Journal of Vacuum Science & Technology A: Vacuum, Surfaces, and Films* (2019), volume 37(2): page 021601. doi: 10.1116/1.5074160.

[Miy19b] T. Miyazawa, Y. Sugawara, I. Yoshikawa, Y. Sato, S. Ohno et al.: 'Surface analysis and pumping speed measurements of oxygen-free palladium/titanium nonevaporable getter after heating at 100–450° C'. In *Journal of Vacuum Science & Technology B, Nanotechnology and Microelectronics: Materials, Processing, Measurement, and Phenomena* (2019), volume 37(6): page 062923. doi: 10.1116/1.5111879.

[Mün19] G. Münster: *Von der Quantenfeldtheorie zum Standardmodell: eine Einführung in die Teilchenphysik*. Walter de Gruyter GmbH & Co KG, 2019. doi: 10.1515/9783110638547.

[Mye15] E. Myers, A. Wagner, H. Kracke and B. Wesson: 'Atomic masses of tritium and helium-3'. In *Physical review letters* (2015), volume 114(1): page 013003. doi: 10.1103/physrevlett.114.013003.

[Nak01] N. Nakashio, J. Yamaguchi, R. Kobayashi and M. Nishikawa: 'Rate of isotope exchange reaction between tritiated water in a gas phase and water on the surface of piping materials'. In *Fusion technology* (2001), volume 39(2P1): pages 189–197. doi: 10.13182/fst39-189.

[Nav24] S. Navas, C. Amsler, T. Gutsche, C. Hanhart, J. J. Hernández-Rey et al.: 'Review of Particle Physics'. In *Phys. Rev. D* (3 2024), volume 110: page 030001. doi: 10.1103/PhysRevD.110.030001.

[Nde24] W. M. Ndeke: 'Molecular Effects in Nuclear β Decay'. PhD thesis. Humboldt-Universität zu Berlin, 2024.

[Nis03] M. Nishikawa, T. Takeishi and K. Katayama: 'Tritium Decontamination from Various Materials (Experiment with Used Tritium Gas Cylinder)'. In *Materials For Advanced Energy Systems And Fission & Fusion Engineering*. World Scientific, 2003: pages 111–120. doi: 10.1142/9789812705198_0012.

[Nis89] M. Nishikawa, T. Takeishi, Y. Matsumoto and I. Kumabe: 'Ionization chamber system to eliminate the memory effect of tritium'. In *Nuclear Instruments and Methods in Physics Research A* (1989), volume 278(2): pages 525–531. doi: 10.1016/0168-9002(89)90875-9.

[Ope10] L. A. Openov and A. I. Podlivaev: 'Thermal desorption of hydrogen from graphane'. In *Technical Physics Letters* (2010), volume 36(1): pages 31–33. doi: 10.1134/s1063785010010104.

[Ott08] E. Otten and C. Weinheimer: 'Neutrino mass limit from tritium β decay'. In *Reports on Progress in Physics* (2008), volume 71(8): page 086201. doi: 10.1088/0034-4885/71/8/086201.

[Oya01a] Y. Oya et al.: 'A study of tritium decontamination of deposits by UV irradiation'. In *Journal of nuclear materials* (2001), volume 290: pages 469–472. doi: 10.1016/s0022-3115(00)00440-2.

[Oya01b] Y. Oya et al.: 'Tritium contamination and decontamination study on materials for ITER remote handling equipment'. In *Fusion engineering and design* (2001), volume 55(4): pages 449–455. doi: 10.1016/s0920-3796(01)00217-4.

[Pan11] S. Pang, Y. Hernandez, X. Feng and K. Müllen: 'Graphene as transparent electrode material for organic electronics'. In *Advanced Materials* (2011), volume 23(25): pages 2779–2795. doi: 10.1002/adma.201100304.

[Pan05] N. Panagia: 'A Geometric Determination of the Distance to SN 1987A and the LMC'. In *International Astronomical Union Colloquium*. Volume 192. Cambridge University Press. 2005: pages 585–592. doi: 10.1017/s0252921100009702.

[Pau08] W. Pauli: *Wissenschaftlicher Briefwechsel mit Bohr, Einstein, Heisenberg ua Band IV, Teil I: 1950–1952/Scientific Correspondence with Bohr, Einstein, Heisenberg ao Volume IV, Part I: 1950–1952*. Volume 14. Springer-Verlag, 2008.

[Pau20] W. Pauli: 'Theoretische Bemerkungen über den Diamagnetismus einatomiger Gase'. In *Zeitschrift für Physik* (1920), volume 2(3): pages 201–205. doi: 10.1007/bf01328724.

[Pau64] W. Pauli: *letter to a physicists' gathering at Tübingen, December 4, 1930. Reprinted in Wolfgang Pauli, Collected Scientific Papers, ed. R. Kronig and V. Weisskopf, Vol. 2.* 1964.

[Pen00] R. Penzhorn, U. Berndt, C. Caldwell-Nichols, S. Grünhagen, E. Kirste et al.: 'Radiochemistry of an equimolar deuterium–tritium mixture or of T2 with CO'. In *Fusion Engineering and Design* (2000), volume 49-50: pages 927–937. doi: 10.1016/s0920-3796(00)00343-4.

[Pic92a] A. Picard, H. Backe, H. Barth, J. Bonn, B. Degen et al.: 'A solenoid retarding spectrometer with high resolution and transmission for keV electrons'. In *Nuclear Instruments and Methods in Physics Research Section B: Beam Interactions with Materials and Atoms* (1992), volume 63(3): pages 345–358. doi: 10.1016/0168-583x(92)95119-c.

[Pic92b] A. Picard, H. Backe, H. Barth, J. Bonn, B. Degen et al.: 'A solenoid retarding spectrometer with high resolution and transmission for keV electrons'. In *Nuclear Instruments and Methods in Physics Research Section B: Beam Interactions with Materials and Atoms* (1992), volume 63(3): pages 345–358. doi: 10.1016/0168-583x(92)95119-c.

[Poh12] H. L. Poh, F. Šaněk, Z. Sofer and M. Pumera: 'High-pressure hydrogenation of graphene: towards graphane'. In *Nanoscale* (2012), volume 4(22): pages 7006–7011. doi: 10.1039/c2nr31962d.

[Pon58] B. Pontecorvo: 'Mesonium and antimesonium'. In *Soviet Journal of Experimental and Theoretical Physics* (1958), volume 6: page 429.

[Pov15] B. Povh, K. Rith, C. Scholz, F. Zetsche and W. Rodejohann: *Particles and Nuclei: An Introduction to the Physical Concepts*. Springer Berlin Heidelberg, 2015. doi: 10.1007/978-3-662-46321-5.

[Pra12] M. Prall, P. Renschler, F. Glück, A. Beglarian, H. Bichsel et al.: 'The KATRIN pre-spectrometer at reduced filter energy'. In *New Journal of Physics* (2012), volume 14(7): page 073054. doi: 10.1088/1367-2630/14/7/073054.

[Pra11] M. Prall: 'Transmission Function of the Pre-Spectrometer and Systematic Tests of the Main-Spectrometer Wire Electrode (PHD thesis)'. PhD thesis. Dissertation, Münster, Universität Münster, 2011, 2011.

[Pri63] J. Pritchard: 'Surface-potential study of the chemisorption of hydrogen and carbon monoxide on evaporated copper and gold films'. In *Transactions of the Faraday Society* (1963), volume 59: pages 437–452. doi: 10.1039/tf9635900437.

[Rob02a] J. Robertson: 'Diamond-like amorphous carbon'. In *Materials Science and Engineering: R: Reports* (2002), volume 37(4): pages 129–281. doi: https://doi.org/10.1016/S0927-796X(02)00005-0.

[Rob02b] J. Robertson: 'Diamond-like amorphous carbon'. In *Materials science and engineering: R: Reports* (2002), volume 37(4-6): pages 129–281. doi: 10.1016/s0927-796x(02)00005-0.

[Rob03] J. Robertson: 'Hydrogen in a-C'. In *Amorphous Carbon*. INSPEC, The Institution of Electrical Engineers, London, United Kingdom, 2003.

[Rob86] J. Robertson: 'Amorphous carbon'. In *Advances in physics* (1986), volume 35(4): pages 317–374. doi: 10.1016/s1359-0286(96)80072-6.

[Rod23] C. Rodenbeck: 'Inelastic electron scattering in tritium gas and ppm-precise energy scale at the KATRIN experiment'. PhD thesis. Münster (Westfalen), Univ., Diss., 2023, 2023.

[Röl15] M. Röllig: 'Tritium analytics by beta induced X-ray spectrometry'. PhD thesis. Karlsruher Institut für Technologie (KIT), 2015. doi: 10.5445/IR/1000054050.

[Röt23] C. Röttele, M. Steidl, M. Sturm, M. Röllig, A. Marsteller et al.: 'Characterization of the KATRIN cryogenic pumping section'. In *Vacuum* (2023), volume 208: page 111699. doi: 10.1016/j.vacuum.2022.111699.

[Röt19] C. Röttele: 'Tritium suppression factor of the KATRIN transport section'. PhD thesis. Karlsruher Institut für Technologie (KIT), 2019. doi: 10.5445/IR/1000096733.

[Sac67] R. K. Sachs and A. M. Wolfe: 'Perturbations of a Cosmological Model and Angular Variations of the Microwave Background'. In *The Astrophysical Journal* (1967), volume 147: page 73. doi: 10.1086/148982.

[Sac20] R. Sack: 'Measurement of the energy loss of 18.6 keV electrons on deuterium gas and determination of the tritium Q-value at the KATRIN experiment'. PhD thesis. Westfälische Wilhelms-Universität Münster, 2020.

[Sae00] A. Saenz, S. Jonsell and P. Froelich: 'Improved molecular final-state distribution of HeT+ for the β-decay process of T 2'. In *Physical review letters* (2000), volume 84(2): page 242. doi: 10.1103/PhysRevLett.84.242.

[Sch12] C. Scheu and W. D. Kaplan: 'Introduction to scanning electron microscopy'. In *In-situ electron microscopy: Applications in physics, chemistry and materials science. Weinheim, DEU: Wiley-VCH Verlag* (2012), volume: pages 3–37. doi: 10.1002/9783527652167.ch1.

[Sch14] H. Schmidbaur, H. G. Raubenheimer and L. Dobrzańska: 'The gold–hydrogen bond, Au–H, and the hydrogen bond to gold, Au$\cdots$H–X'. In *Chemical Society Reviews* (2014), volume 43(1): pages 345–380. doi: 10.1039/c3cs60251f.

[Sch24a] S. Schneidewind, J. Schürmann, A. Lokhov, C. Weinheimer and A. Saenz: 'Improved treatment of the T 2 molecular final-states uncertainties for the KATRIN neutrino-mass measurement'. In *The European Physical Journal C* (2024), volume 84(5): page 494. doi: 10.1140/epjc/s10052-024-12802-w.

[Sch24b] C. Schweiger, M. Brass, V. Debierre, M. Door, H. Dorrer et al.: 'Penning-trap measurement of the Q value of electron capture in 163Ho for the determination of the electron neutrino mass'. In *Nature Physics* (2024), volume 20(6): pages 921–927. doi: 10.1038/s41567-024-02461-9.

[Sch06] P. Schneider: *Einführung in die extragalaktische Astronomie und Kosmologie*. Springer-Verlag, 2006. doi: 10.1007/3-540-30589-0.

[Sch16] K. Schönung: 'Development of a Rear Wall for the KATRIN Rear Section and investigation of tritium compatibility of Rear Section components'. PhD thesis. Karlsruher Institut für Technologie (KIT), 2016. doi: 10.5445/IR/1000056077.

[Sch21] L. Schimpf: 'Characterisation of energy loss processes of 18.6 keV electrons inside the windowless tritium source of KATRIN'. PhD thesis. Karlsruher Institut für Technologie (KIT), 2021. doi: 10.5445/IR/1000131810.

[Sco18] D. M. Scolnic, D. Jones, A. Rest, Y. Pan, R. Chornock et al.: 'The complete light-curve sample of spectroscopically confirmed SNe Ia from Pan-STARRS1 and cosmological constraints from the combined pantheon sample'. In *The Astrophysical Journal* (2018), volume 859(2): page 101. doi: 10.3847/1538-4357/aab9bb.

[Shu01] W. M. Shu et al.: 'Tritium decontamination of TFTR carbon tiles employing ultra violet light'. In *Journal of nuclear materials* (2001), volume 290: pages 482–485. doi: 10.1016/s0022-3115(00)00441-4.

[Shu12] A. D. Shugard, R. T. Walters and P. Van Blarigan: 'Titanium tritide radioisotope heat source development: Palladium-coated titanium hydriding kinetics and tritium loading tests'. In *Energy conversion and management* (2012), volume 64: pages 371–377. doi: 10.1016/j.enconman.2012.06.011.

[Sie24] D. Siegmann, F. Edzards, C. Bruch, M. Biassoni, M. Carminati et al.: 'Development of a silicon drift detector array to search for keV-scale sterile neutrinos with the KATRIN experiment'. In *Journal of Physics G: Nuclear and Particle Physics* (2024), volume. doi: 10.1088/1361-6471/ad4bf8.

[Sil03] S. Silva: 'Microstructure of a-C'. In *Amorphous Carbon*. INSPEC, The Institution of Electrical Engineers, London, United Kingdom, 2003.

[Sto92] L. Stobiński and R. Duś: 'Atomic hydrogen adsorption on thin gold films'. In *Surface science* (1992), volume 269: pages 383–388. doi: 10.1016/0039-6028(92)91279-k.

[Sto99] L. Stobiński, L. Zommer and R. Duś: 'Molecular hydrogen interactions with discontinuous and continuous thin gold films'. In *Applied surface science* (1999), volume 141(3-4): pages 319–325. doi: 10.1016/s0169-4332(98)00517-0.

[Str71] A. Streitwieser Jr, W. Hollyhead, A. Pudjaatmaka, P. Owens, T. Kruger et al.: 'Acidity of hydrocarbons. XXXVII. Broensted correlation and hydrogen isotope exchange kinetics of fluorenes, benzfluorenes, and indene with methanolic sodium methoxide'. In *Journal of the American Chemical Society* (1971), volume 93(20): pages 5088–5096. doi: 10.1021/ja00749a022.

[Stu21] M. Sturm, F. Priester, M. Röllig, C. Röttele, A. Marsteller et al.: 'Kilogram scale throughput performance of the KATRIN tritium handling system'. In *Fusion Engineering and Design* (2021), volume 170: page 112507. doi: 10.1016/j.fusengdes.2021.112507.

[Stu10] M. Sturm: 'Aufbau und Test des Inner-Loop-Systems der Tritiumquelle von KATRIN'. PhD thesis. 2010. doi: 10.5445/IR/1000019355.

[Tan17] T. Tanabe: *Tritium: Fuel of fusion reactors*. Springer, 2017. doi: 10.1007/978-4-431-56460-7.

[Tom78] F. C. Tompkins: *Chemisorption of Gases on Metals*. London: Academic Press, 1978.

[Ton12] J. L. Tonry, C. W. Stubbs, K. R. Lykke, P. Doherty, I. S. Shivvers et al.: 'THE Pan-STARRS1 PHOTOMETRIC SYSTEM'. In *The Astrophysical Journal* (2012), volume 750(2): page 99. doi: 10.1088/0004-637x/750/2/99.

[Tor02] Y. Torikai et al.: 'Effect of water vapor on tritium decontamination of stainless steel 316'. In *Fusion science and technology* (2002), volume 41(3P2): pages 736–740. doi: 10.13182/fst02-2.

[Uda92] T. Uda, K. Okuno and Y. Naruse: 'Hydrogen isotope exchange reaction rate in tritium and methane mixed gas'. In *Journal of radioanalytical and nuclear chemistry* (1992), volume 159(1): pages 145–154. doi: 10.1007/bf02041027.

[Vel19] C. Velte, F. Ahrens, A. Barth, K. Blaum, M. Brass et al.: 'High-resolution and low-background^ 163 163 Ho spectrum: interpretation of the resonance tails'. In *The European Physical Journal C* (2019), volume 79: pages 1–8. doi: 10.1016/j.nima.2023.168564.

[Ven02] T. J. Venhaus et al.: 'The effect of UV light irradiation on the removal of tritium from the codeposited carbon–tritium layer in fusion reactors'. In *Journal of nuclear materials* (2002), volume 302(2-3): pages 224–226. doi: 10.1016/s0022-3115(02)00808-5.

[Ver00] V. Verbetsky and S. Mitrokhin: 'Copper-silver-and gold-hydrogen'. In *Solid State Phenomena* (2000), volume 73: page 503. doi: 10.4028/www.scientific.net/ssp.73-75.503.

[Vig85] J. R. Vig: 'UV/ozone cleaning of surfaces'. In *Journal of Vacuum Science & Technology A: Vacuum, Surfaces, and Films* (1985), volume 3(3): pages 1027–1034. doi: 10.21236/ada169024.

[Von02] A. Von Keudell, M. Meier and C. Hopf: 'Growth mechanism of amorphous hydrogenated carbon'. In *Diamond and Related Materials* (2002), volume 11(3-6): pages 969–975. doi: 10.1016/s0925-9635(01)00553-2.

[Von96] A. Von Keudell and W. Jacob: 'Growth and erosion of hydrocarbon films investigated by in situ ellipsometry'. In *Journal of Applied Physics* (1996), volume 79(2): pages 1092–1098. doi: 10.1063/1.360796.

[Wad80] N. Wada, P. Gaczi and S. Solin: '"Diamond-like" 3-fold coordinated amorphous carbon'. In *Journal of Non-Crystalline Solids* (1980), volume 35: pages 543–548. doi: 10.1016/0022-3093(80)90651-1.

[Wel17] S. Welte, E. Fanghänel, S. Fischer, F. Kramer, T. Le et al.: 'Experimental performance test of key components of the KATRIN outer tritium loop'. In *Fusion Science and Technology* (2017), volume 71(3): pages 316–320. doi: 10.1080/15361055.2017.1291233.

[Wex63] S. Wexler: 'On the mechanism of the isotopic exchange of tritium with methane'. In *Journal of the American Chemical Society* (1963), volume 85(3): pages 272–277.

[Wil91] J. Wilkerson, T. Bowles, J. Friar, R. Robertson, G. Stephenson et al.: 'Limit on νe mass from observation of the beta decay of molecular tritium'. In *Nuclear Physics B - Proceedings Supplements* (1991), volume 19: pages 215–224. doi: 10.1016/0920-5632(91)90202-p.

[Wit96] M. Wittmann and J. Küppers: 'A model of hydrogen impact induced chemical erosion of carbon based on elementary reaction steps'. In *Journal of nuclear materials* (1996), volume 227(3): pages 186–194. doi: 10.1016/0022-3115(95)00150-6.

[Wol78] L. Wolfenstein: 'Neutrino oscillations in matter'. In *Physical Review D* (1978), volume 17(9): pages 2369–2374. doi: 10.1103/physrevd.17.2369.

[Wu57] C.-S. Wu, E. Ambler, R. W. Hayward, D. D. Hoppes and R. P. Hudson: 'Experimental test of parity conservation in beta decay'. In *Physical review* (1957), volume 105(4): page 1413. doi: 10.1016/b978-0-08-006509-0.50011-9.

[Yam14] Y. Yamada, K. Murota, R. Fujita, J. Kim, A. Watanabe et al.: 'Subnanometer vacancy defects introduced on graphene by oxygen gas'. In *Journal of the American Chemical Society* (2014), volume 136(6): pages 2232–2235. doi: 10.1021/ja4117268.

[Yor00] D. G. York, J. Adelman, J. E. Anderson Jr, S. F. Anderson, J. Annis et al.: 'The sloan digital sky survey: Technical summary'. In *The Astronomical Journal* (2000), volume 120(3): page 1579. DOI: 10.1086/301513.

[Zan88] A. Zangwill: *Physics at surfaces*. Cambridge: Cambridge university press, 1988. DOI: 10.1017/cbo9780511622564.

[Zel24] G. Zeller: 'Raman spectroscopy for KATRIN: monitoring of continuous tritium gas flows and tritium-graphene interactions'. PhD thesis. Karlsruher Institut für Technologie (KIT), 2024. DOI: 10.5445/IR/1000168486.

[Zub20] K. Zuber: *Neutrino physics*. Taylor & Francis, 2020. DOI: 10.1201/9781315195612.

[Zyl20] P. A. Zyla, R. M. Barnett, J. Beringer, O. Dahl, D. A. Dwyer et al.: 'Review of Particle Physics'. In *Progress of Theoretical and Experimental Physics* (2020), volume 2020(8): page 083C01. DOI: 10.1093/ptep/ptaa104. eprint: https://academic.oup.com/ptep/article-pdf/2020/8/083C01/34673722/ptaa104.pdf.

Danksagung

An dieser Stelle möchte ich all jenen herzlich danken, die zum Gelingen dieser Arbeit beigetragen haben - sei es durch tatkräftige Unterstützung, hilfreiche Tipps oder Worte, leckeren Süßkram oder andere Arten der Aufmunterung.

Zunächst möchte ich mich herzlich bei Prof. Dr. Guido Drexlin bedanken - für die Möglichkeit, diese Arbeit zu realisieren, für den nötigen Freiraum, den er mir dabei gelassen hat, und besonders für die Unterstützung, die er mir stets gewährt hat, wann immer ich sie gebraucht habe.

Ebenfalls herzlicher Dank gebührt JProf. Dr. Loredana Gastaldo. Sie hatte stets ein offenes Ohr für mich und hat mich mit viel Verständnis durch diese Arbeit hinweg unterstützt - trotz aller bürokratischer und oft zeitraubender Hindernisse.

Dr. Magnus Schlösser möchte ich für die abschließenden Kommentare, die diese Arbeit abrundeten und mit besonderem Einsatz innerhalb kürzester Zeit erstellt wurden, danken.

Besonderer Dank geht an Dr. Michael Sturm und Dr. Robin Größle, von denen ich stets eine hilfreiche Antwort auf meine Fragen erhalten habe. Von euch habe ich viel lernen können, insbesondere was die Vakuumtechnik, die Eigenheiten von Tritium oder die Feinheiten von Datenanalysen angeht. Aber auch aus den vielen, darüber hinaus gehenden Diskussionen konnte ich einiges für mich mitnehmen. In diese Zuge möchte ich auch Stefan Welte danken, der stets mit gutem Rat bei der Planung von Experimenten half und von dem ich viel über die Arbeit mit Tritium lernen konnte.

Dr. Florian Priester und Dr. Marco Röllig gebührt mein Dank ebenfalls - für all die Ratschläge und die Gewissheit, dass ich mich bei fachlichen Fragen an sie wenden kann.

Nicht genug danken kann ich meinen Mitstreitern auf den letzten Metern. Johanna Wydra, unter anderem für die vielen Kekse und vorallem für die anspornende Konkurrenz beim Pferderennen auf der Pinwand zum Ziel der fertig gestellten Dissertation und Dr. Alexander Marsteller für das stetige Antreiben beider Pferdchen, damit bloß keines unterwegs schlapp macht. Mit euch beiden hat die ganze Sache deutlich mehr Spaß gemacht!

Dr. Genrich Zeller, Dr. Alexander Marsteller sowie Dominic Batzler danke ich von Herzen für das gründliche Durchlesen einzelner Kapitel und teilweise der gesamten Dissertation sowie für die wertvollen Verbesserungsvorschläge, die sie mir bereitgestellt haben. Generell wart ihr stets für hilfreiche oder unterhaltsame Diskussionen zur Stelle!

Dr. Simon Niemes danke ich in diesem Zug ebenfalls, für all die Unterstützung und die stets hilfreichen Antworten wenn ich mit Fragen zu dir kommen bin.

Für tatkräftige Unterstützung vorallem im Labor danke ich Nancy Tuchscherer, Dirk Osenberg, David Hillesheimer und Tobias Falke. Auf euch kann man sich immer verlassen!

Bernhard Heinle danke ich für seine wachsamen Augen, wenn ich im Labor mit Tritium umging und das reichhaltige Wissen über den praktischen Strahlenschutz, das er im Laufe der Jahre mit mir teilte.

Viel Unterstützung und viele heitere Momente verdanke ich auch meinen Freunden und Kommilitonen, mit denen ich mein gesamtes Studium verbringen durfte. Dafür möchte ich Stefan und Ida Eisele, Sebastian Schulz, Dr. Jan Brehm und Dr. Andreas Will danken. Danke in diesem Zug auch an Marcus Schmitt, mein langjähriger Mitbewohner. Die Zeit zusammen mit euch war besonders und ist gespickt mit wunderbaren Erinnerungen!

All die Zeit wäre undenkbar gewesen ohne meine Familie. Ich möchte meinem Vater Erich danken, dass er mir alles was ich erreicht habe ermöglicht hat. Meine Mutter Annette verdient den größtmöglichen Dank, auch wenn sie die letzten Jahre meines Werdegangs leider nicht mehr mitverfolgen konnte. Ohne ihre unbegrenzte Liebe und Förderung, wäre ich niemals so weit gekommen.

Mein innigster Dank gebührt meiner Frau Anna und meinem Sohn Aaron. Danke für die Liebe, die Aufheiterungen und Ermutigungen, all das Verständnis, die grenzenlose Unterstützung und die Tatsache, dass ich immer, wenn ich nach Hause komme, liebevolle Menschen vorfinde, die sich freuen mich zu sehen.